UNIVERSITY OF CALIFORNIA

Los Angeles

Aero-Structural Design Investigations for Biplane Wind Turbine Blades

A dissertation submitted in partial satisfaction of the requirements for the degree Doctor of Philosophy in Aerospace Engineering

by

Perry Moses Sablan Roth-Johnson

ABSTRACT OF THE DISSERTATION

Aero-Structural Design Investigations for Biplane Wind Turbine Blades

by

Perry Moses Sablan Roth-Johnson

Doctor of Philosophy in Aerospace Engineering University of California, Los Angeles, 2014 Professor Richard E. Wirz, Chair

Large wind turbine blades are being developed at lengths of 85–125 meters, in order to improve energy capture and reduce the cost of wind energy. Bending loads in the inboard region of the blade make large blade development challenging. The "biplane blade" design was proposed to use a biplane inboard region to improve the design of the inboard region and improve overall performance of large blades. This work uses a "structures-first" approach with aero-structural analyses to (1) examine the feasibility of the biplane blade, (2) determine how the dimensions of the biplane inboard region affect performance, and (3) compare the aero-structural performance of a 100-meter biplane blade to the Sandia SNL100-00 reference blade. Two-dimensional CFD simulations were used to compare the aerodynamic performance of a biplane with a thick monoplane. The lift-to-drag ratio and the maximum lift coefficient is significantly greater for the biplane than the thick monoplane for angles of attack of 0–15 degrees. Analytical methods and beam finite elements with cross-sectional analysis were both used to examine the performance of biplane blade structures. These structures varied in complexity from isotropic spars to composite spars to composite full blades. In each case, biplane blade structures were compared to monoplane blade structures of the same length, mass, and complexity. Simple load cases were applied to each structure and their displacements, bending moments, axial forces, and stresses were compared. Similar performance trends are identified with both the analytical and computational models. Parametric analyses show that gap-to-chord ratios bewteen 1.0–1.2 and joint length-to-span ratios of about 0.5 give good aero-structural performance. At the tip, the biplane blade increases flapwise structural efficiency by 20-40%, depending on the load. Edgewise structural efficiency was decreased by 27-35% at the tip. The benefits for the inboard region could lead to mass reductions in wind turbine blades. Innovations that create lighter blades can make large blades a reality, suggesting that the biplane blade is an attractive design for large (100-meter) blades.

The dissertation of Perry Moses Sablan Roth-Johnson is approved.

Oddvar O. Bendiksen

Ertugrul Taciroglu

Xiaolin Zhong

Richard E. Wirz, Committee Chair

University of California, Los Angeles 2014

 $Dedicated\ to\ my\ wife,\ Lizzie.$

TABLE OF CONTENTS

Li	st of	figure	S	X
Li	st of	tables	5	xiv
N	omer	ıclatur	re	xv
1	Intr	roduct	ion	1
	1.1	Curre	nt status of wind energy	1
	1.2	Motiv	ation	3
	1.3	Design	n approaches for improving the inboard region	7
	1.4	Signif	icance of this work	9
	1.5	Outlin	ne of the thesis	10
2	Ana	atomy	of a wind turbine and its components	11
	2.1	Wind	turbine components	11
	2.2	Conve	entional blades and their substructures	14
		2.2.1	External (aerodynamic) geometry	16
		2.2.2	Internal (structural) geometry	19
	2.3	Biplar	ne blades and their substructures	23
		2.3.1	Blade regions and substructures	23
		2.3.2	External (aerodynamic) geometry for the inboard biplane region	24
		2.3.3	Internal (structural) geometry for the inboard biplane region	26
3	Aer	o-stru	ctural investigation of biplane wind turbine blades	29
	3.1	Introd	luction	30

	3.2	Appro	ach	34
		3.2.1	Cross-sectional properties of a thick monoplane and biplane	35
		3.2.2	Aerodynamic comparison of a thick monoplane and biplane cross-section	36
		3.2.3	Structural comparison of monoplane beams and biplane beams	39
	3.3	Result	s	46
		3.3.1	Cross-sectional properties of a thick monoplane and biplane	46
		3.3.2	Aerodynamic comparison of a thick monoplane and biplane cross-section	46
		3.3.3	Structural comparison of monoplane beams and biplane beams	48
	3.4	Conclu	sion	51
		3.4.1	Outlook & future work	52
4	Stru	ıctural	design of spars for 100-meter biplane wind turbine blades	54
	4.1	Introd	uction	55
	4.2	Metho	ds	59
		4.2.1	Analytical model	59
		4.2.2	Computational model	64
	4.3	Result		80
			S	
		4.3.1	Analytical model: comparison of biplane beam and monoplane beam	80
	4.4	4.3.1 4.3.2	Analytical model: comparison of biplane beam and monoplane beam	80
	4.4	4.3.1 4.3.2	Analytical model: comparison of biplane beam and monoplane beam Computational model	80 82
	4.4	4.3.1 4.3.2 Discus	Analytical model: comparison of biplane beam and monoplane beam Computational model	80 82 88
	4.4	4.3.1 4.3.2 Discus 4.4.1	Analytical model: comparison of biplane beam and monoplane beam Computational model	80 82 88 88
	4.4	4.3.1 4.3.2 Discus 4.4.1 4.4.2	Analytical model: comparison of biplane beam and monoplane beam Computational model	80 82 88 88 90

		4.4.6	Outlook & future work	. 92
5	Aer	o-struc	ctural analysis of a full 100-meter biplane wind turbine blade	101
	5.1	Introd	uction	. 101
	5.2	Metho	ods	. 102
		5.2.1	Blade geometry	. 105
		5.2.2	2D cross-sectional analysis	. 106
		5.2.3	1D beam finite element models	. 110
		5.2.4	Load cases	. 111
	5.3	Result	SS	. 112
		5.3.1	Blade geometry	. 112
		5.3.2	Cross-sectional analysis	. 113
		5.3.3	Load cases	. 114
	5.4	Discus	ssion	. 124
6	Con	clusio	ns and recommendations	. 131
\mathbf{A}	Der	ivation	of analytical model for biplane beams	. 136
	A.1	Kinem	natic assumptions and essential boundary conditions	. 136
	A.2	Potent	tial energy	. 137
	A.3	Minim	num total potential energy	. 139
	A.4	Equilil	brium equations	. 143
	A.5	Natura	al boundary conditions	. 144
	A.6	Assum	nptions for engineering properties	. 144
	A.7	Solutio	on of equilibrium equations	. 146
R	Lan	ninate	schedules for spars	148

\mathbf{C}	Spanwise properties of spars	152
D	Blade definition for 100-meter biplane blade	156
Re	eferences	161

LIST OF FIGURES

1.1	Land-based and offshore wind energy resource of the United States	2
1.2	Height, size, and power of wind turbines over time	4
1.3	Historical trend of the levelized cost of energy for wind	6
1.4	Schematic of the inboard and outboard regions on a wind turbine blade	6
1.5	"Multi-element blades" are a new class of blade designs	8
1.6	Artistic rendering of a biplane blade	8
2.1	Components of wind turbines	12
2.2	Schematic of a typical wind turbine rotor in operation	13
2.3	Nomenclature for blade coordinate directions	15
2.4	Blade designs are defined by a set of cross-section geometries	15
2.5	External geometry of a conventional blade cross-section	16
2.6	A view down the pitch axis of a conventional blade	18
2.7	Flap and edge load distributions on a wind turbine blade in operation	19
2.8	Flap and edge loads lead to compression and tension in different areas	20
2.9	Internal geometry of a conventional blade cross-section	21
2.10	Stacking sequences for uniaxial, biaxial, and triaxial layups	22
2.11	Outboard monoplane and inboard biplane regions of the biplane blade	24
2.12	Four substructures make up the inboard region of the biplane blade	24
2.13	Gap and stagger dimensions for a biplane cross-section	25
2.14	The external geometry of a biplane cross-section for a biplane blade	27
2.15	Internal geometry of a biplane blade cross-section	28
3.1	Schematic of the inboard and outboard regions on a wind turbine blade	30

3.2	Thick airfoil cross-sections used in the inboard region	31
3.3	Artistic rendering for several views of a biplane blade	32
3.4	For the biplane blade, loads manifest themselves on the beam flanges	33
3.5	Schematic of a biplane and a thick monoplane airfoil cross-section	35
3.6	Geometry of the biplane cross-section	37
3.7	Computational grids for preliminary aerodynamic analysis	38
3.8	Model beams for preliminary structural analysis	40
3.9	Load profiles applied to model beams	41
3.10	Computational meshes used for finite element analysis	44
3.11	Comparison of lift and drag coefficients for the FFA-W3-301 thick monoplane	47
3.12	Aerodynamic performance of a thick monoplane and a biplane cross-section.	48
3.13	Comparison of beam deflections under various load profiles	49
3.14	Effect of three design parameters on the tip deflection of a biplane beam	50
4.1	Two major design parameters for the biplane blade	57
4.2	Design approaches for conventional and biplane blades	58
4.3	Schematic of the biplane beam structure used for the analytical model	60
4.4	Schematics for the kinematic assumptions at the rigid joint	60
4.5	Surface geometry of spars used for the computational model	64
4.6	Components used to define the spar	66
4.7	All spars were assumed to have rectangular cross-sections	66
4.8	All cross-sections had equal areas, so all spars had the same mass	69
4.9	Design and analysis procedure for the monoplane spar	70
4.10	Design and analysis procedure for the biplane spar	71
4.11	Edgewise views of half-height and full-height biplane spars	72

4.12	1D representations of biplane spars	74
4.13	Fifteen biplane spar configurations were designed and analyzed in this study.	75
4.14	Load profiles applied to spars	75
4.15	Tip loads applied to spars: flapwise (top) and torsional (bottom)	76
4.16	Computational meshes used for finite element analysis	77
4.17	Comparison of deflections, bending moments, and axial forces	81
4.18	Flapwise bending stiffness distributions	83
4.19	Comparison of spar deflections and bending moments	94
4.20	Comparison of edgewise deflections of spars under a torsional tip load	95
4.21	Comparison of cross-sectional stresses along the span of three spars \dots	96
4.22	Normal stresses in selected cross-sections of the monoplane spar $\ \ldots \ \ldots$	97
4.23	Normal stresses in selected cross-sections of the half-height biplane spar	98
4.24	Normal stresses in selected cross-sections of the full-height biplane spar $\ .$	99
4.25	Effect of two parameters on the structural performance of a biplane spar $$	100
5.1	CAD rendering of rotor with biplane blades	103
5.2	Technology stack for design and analysis of a full biplane blade	104
5.3	Wireframe representation of the full biplane blade	105
5.4	The biplane blade reused cross-section properties from the Sandia blade	107
5.5	Example cross-sectional mesh	109
5.6	Computational meshes used for finite element analysis	110
5.7	Four surface views of the biplane blade	111
5.8	Stiffness properties along the span of the Sandia blade	115
5.9	Mass properties along the span of the Sandia blade	116
5.10	Sandia and biplane blades under a flapwise tip load	119

5.11	Structural efficiency of biplane blade under a flapwise tip load	120
5.12	Sandia and biplane blades under a flapwise uniform distributed load	121
5.13	Structural efficiency of biplane blade under a flap uniform distributed load $$.	122
5.14	Sandia and biplane blades under a flapwise BEM distributed load	123
5.15	Structural efficiency of biplane blade under a flapwise BEM distributed load	124
5.16	Sandia and biplane blades under an edgewise tip load	125
5.17	Structural efficiency of biplane blade under an edgewise tip load	126
5.18	Sandia and biplane blades under an edgewise uniform distributed load	127
5.19	Structural efficiency of biplane blade under an edge uniform load	128
5.20	Mode 1: The biplane blade vibrates in edge	128
5.21	Mode 2: The biplane blade vibrates in flap	129
5.22	Mode 6: The biplane blade shows torsion/edgewise coupling	129
6.1	CAD rendering of flapwise asymmetric, no stagger biplane blade	133
6.2	CAD rendering of flapwise asymmetric, staggered biplane blade	134
6.3	CAD rendering of flapwise symmetric, staggered biplane blade	134
D 1	Selected cross-sections of the biplane blade	157

LIST OF TABLES

3.1	Definition of design parameters for the biplane blade	39
4.1	Definition of design parameters for the biplane blade	57
4.2	Material property data for glass fiber composites and structural foam	68
4.3	Scaling factors for the engineering properties of the biplane beam	80
4.4	Structural efficiency factors for biplane spars under three different load cases	85
5.1	Material property data for full blade	109
5.2	Flapwise distributed load from BEM	112
5.3	Modal analysis to inform future designs	122
В.1	Laminate schedule for the monoplane spar	149
B.2	Laminate schedule for a half-height biplane spar	150
В.3	Laminate schedule for a full-height biplane spar	151
C.1	Key for translating column entries to VABS matrix entries	152
C.2	Spanwise properties for the monoplane spar	153
C.3	Spanwise properties for a half-height biplane spar	154
C.4	Spanwise properties for a full-height biplane spar	155
D.1	Geometry of a full 100-meter biplane blade	158
D.2	Laminate schedule for a full 100-meter biplane blade	159
D.3	Spanwise properties for a full biplane blade	160

Nomenclature

c	chord length	$V_{ m wind}$	incoming wind velocity
$c_{ m lower}$	lower chord length	LBNL	Lawrence Berkeley National Lab-
$c_{ m total}$	total chord length		oratory
$c_{ m upper}$	upper chord length	NREL	National Renewable Energy Labo-
$f_{ m lower}$	lower chord fraction		ratory
$f_{ m upper}$	upper chord fraction	PTC	Production Tax Credit
g	gap	RPS	Renewable Portfolio Standards
g/c	gap-to-chord ratio	α	angle of attack
R	span	η	gap fraction
r_{j}	joint length	ϕ	structural efficiency
r_j/R	joint length-to-span ratio	θ	angle between chord line and rotor
r_t	transition length		plane
s	stagger	θ_p	blade pitch angle
s/c	stagger-to-chord ratio	θ_t	local twist angle
$V_{ m relative}$	relative wind velocity	φ	local inflow angle
$V_{ m rotor}$	linear velocity from rotor rotation	ξ	pitch axis fraction

ACKNOWLEDGMENTS

First of all, I am grateful to my advisor, Prof. Richard Wirz. Thank you for taking me into the lab in the summer before I started grad school, and for guiding me patiently through this unique project. By challenging me to make this project my own, you taught me how to think for myself to become a better engineer and researcher. Looking back now, it is exciting to see how we took a conceptual idea from five years ago and developed it into a well-defined design today. Thank you for sending me to Mesalands Community College in Tucumcari, New Mexico to climb their wind turbine and get some hands-on experience with real hardware—it provided me with valuable context, considering that my research is entirely computational. In addition to my research, thank you for encouraging me to pursue my engineering education work, first by founding BEAM at UCLA, and now by starting a new position at the California Science Center.

I am thankful for the insight, support, and time of my committee. Prof. Ertugrul Taciroglu, when the focus of my project shifted from aerodynamics to structures, thank you for patiently helping me deepen my knowledge of structural mechanics. Prof. Xiaolin Zhong, thank you for introducing me to the world of computational aerodynamics. Prof. Oddvar Bendiksen, your series of dynamics courses formed the first two years of my grad school experience and introduced me to aeroelasticity. Thank you for your insightful discussions about this project, as well as all of your wonderful stories.

Two other faculty members also graciously offered their expertise to me. Prof. Stanley Dong, thanks for sitting down with me to talk at length about cross-sectional analysis (and about your time at Berkeley!). Prof. Bill Klug, I deeply enjoyed learning from you in class, and appreciate your help with the analytical model for my research. I was thrilled when I discovered how energy methods could help me understand my computational results.

To all of the former and current members of the Wirz Research Group (Hann, Emily, Monica, Sebastian, Reza, Taylor, Jun, Phil, Lauren, Ben D., Ryan, Marlene, Louis, Ben F., Gaby, Chris, Cesar, Mac, Ed, Christos, Sennan, Alex, Joseph, and Tom): thank you for your friendship and support. I have fond memories of our canyoneering adventures, foosball

tournaments, pub trivia teams, trips to SEAS Cafe, and siestas after lunch at Indian buffet. I'm particularly grateful to the wind energy researchers who made this dissertation possible. Phil, thank you for sharing all your valuable insights with me. (Team Biplane!) You made many contributions to my work, and I am deeply grateful to have had you as my partner on this research project. Ed and Christos, thank you for all your assistance towards the end of my tenure at UCLA—it was a privilege to mentor you, and I wish you all the best going forward. Sennan, thank you for getting DYMORE working at the beginning of this research. Sebastian, thank you for graciously passing this project along to me.

I got my first taste of research as an undergraduate at Berkeley. Prof. Lisa Pruitt, thank you for giving me the opportunity to work in your biomaterials lab for a year, and for continuing to advise me at important moments in my grad school career. Sara Atwood and Eli Patten, thank you for patiently mentoring me in the lab.

I am eternally grateful to my family and friends. To my smart and beautiful wife, Lizzie thank you for all your love and support. I had no idea what I was getting myself into five years ago when we made the jump together from Berkeley to UCLA, but I'm so happy I got to go on this journey with you. I could always count on your encouragement and patience when I needed it most. We made it! To my parents, Moses and Genny, thank you for teaching me the value of a good education, and for your unending love and encouragement. To my sister, Isabel, it has been wonderful watching you grow up to become a scholar in your own right. Good luck at Berkeley! And to my new family: Jim, Molly, and Tim, thank you for welcoming me into your lives and supporting me as one of your own. To my Nina and Nino, thank you for always supporting my education, especially when you generously hosted me, Jun, and Hann at your home in Hawaii while we attended a conference. Chris, Andrea, Mike, Pedro, Bat, Amy, Christina, and JB: thanks for getting me out of the lab once in a while to have some fun. Finally, thank you to everyone else who supported me as I found my way towards an engineering education career: Jessica, Emily, and Zhihao (the amazing undergrads now running BEAM at UCLA); Prof. Adrienne Lavine, Prof. Greg Carman, and Lynn Kim-John at UCLA, along with Prof. George Youssef at CSUN; John Coate and Kristy Sherrer at the UCLA Career Center, and the entire Versatile PhD community.

I thank my co-authors and collaborators for all their contributions to this work. The research in Chapter 3 was originally published in *Wind Energy*. Roth-Johnson, P. and Wirz, R. E. (2014), "Aero-structural investigation of biplane wind turbine blades," *Wind Energ.*, 17: 397411. doi: 10.1002/we.1583. Copyright © 2012 John Wiley & Sons, Ltd. The research in Chapter 4 originally appeared in *Renewable Energy*. Roth-Johnson P., Wirz R. E., and Lin E. (2014), "Structural design of spars for 100-m biplane blades," *Renewable Energy*. doi: 10.1016/j.renene.2014.05.030. Thanks are due to Phillip Chiu for valuable discussions, the artistic renderings, and for calculating load distributions with WT.Perf. Thanks are also due to Sebastian Aspe, Sennan Sulaiman, and Joseph Pan for their assistance with CFD, DYMORE, and VABS, respectively. Thank you also to Edward Lin for his assistance with structural analyses, and to Christos Voutsaras for creating CAD models of the 100-meter biplane blade. Thanks are due to Prof. William Klug from UCLA for his guidance with the analytical model. Thank you also to Prof. Ertugrul Taciroglu and Prof. Stanley Dong from UCLA for valuable discussions on the computational model.

This research was made possible by the developers of each of the software packages used in my work. I am grateful to Prof. Olivier A. Bauchau from the Georgia Institute of Technology for providing DYMORE to me as free and open source. I thank Prof. Wenbin Yu from Purdue University for his assistance with VABS. Thanks also to Dr. Robert Rainsberger for providing me with an academic version of TrueGrid. Finally, a big thank you to the Python developers of IPython, Matplotlib, Mayavi, Shapely, and SymPy, which were all essential to my work.

This work was generously supported by UCLA Graduate Division through a Eugene V. Cota-Robles Fellowship, a Malcolm R. Stacey Memorial Scholarship, and a Dissertation Year Fellowship. I also gratefully acknowlege the additional support from the California Energy Commission through an Energy Innovations Small Grant (EISG grant #56536A/09-15), from UCLA Mechanical & Aerospace Engineering through two Departmental Fellowships, from the Communities Foundation of Texas through a General James H. Doolittle Scholarship, and from the National Science Foundation IGERT at UCLA through a Clean-Green Summer Fellowship.

VITA

2006	Member & Outreach Program Coordinator, Pi Tau Sigma, Mechanical Engineering Honor Society, UC Berkeley
2008	Founder, Building Engineers & Mentors, UC Berkeley beam.berkeley.edu
2008	Undergraduate Researcher, Medical Polymer Group, UC Berkeley
2009	B.S., Mechanical Engineering, UC Berkeley
2009	Eugene V. Cota-Robles Fellow, Graduate Division, UCLA
2010	Teaching Assistant, Elementary Fluid Mechanics, UCLA
2011	Founder, Building Engineers & Mentors, UCLA beam.ucla.edu
2011	Honorable Mention, Graduate Research Fellowship, NSF
2011	M.S., Aerospace Engineering, UCLA
2012	General James H. Doolittle Scholar, Communities Foundation of Texas
2013	Teaching Assistant, Basic Mechanical Engineering Lab, UCLA
2013	Clean Energy for Green Industry Fellow, NSF IGERT at UCLA
2013	Malcolm R. Stacey Memorial Scholar, Graduate Division, UCLA
2013	Dissertation Year Fellow, Graduate Division, UCLA
2014	Air and Space Exhibit Researcher, California Science Center

Publications and Presentations

- P. Roth-Johnson, R. Wirz, E. Lin, "Structural design of spars for 100-m biplane wind turbine blades," *Renewable Energy*, 2014. doi: 10.1016/j.renene.2014.05.030
- P. Roth-Johnson, R. Wirz, "Aero-structural investigation of biplane wind turbine blades," Wind Energy, 2014, 17: 297-411. doi: 10.1002/we.1583
- P. Roth-Johnson, R. Wirz, "Wind turbine blade with biplane section," U.S. Patent Application, 2014 (patent pending).
- P. Roth-Johnson, E. Roth-Johnson, K. Alvarez, J. Choi, R. Wirz, G. Carman, "Building Engineers and Mentors: Bringing science and engineering to Los Angeles schools," *TANMS NSF Annual Review*, Los Angeles, CA, (poster) May 7, 2013.
- P. Johnson, R. Wirz, "Structural design of spars for 100-m biplane wind turbine blades," *AWEA Windpower*, Atlanta, GA, (presentation) June 5, 2012.
- R. Wirz, P. Johnson, "Aero-structural performance of multiplane wind turbine blades," 29th AIAA Applied Aerodynamics Conference, AIAA 2011-3025, Honolulu, HI, June 27, 2011. doi: 10.2514/6.2011-3025

CHAPTER 1

Introduction

1.1 Current status of wind energy

Sparked by concerns over domestic energy security during the 1970s oil crisis, the U.S. government began investing in wind energy research in the 1980s. These investments, along with concerns about climate change, helped grow the wind industry over the past 35 years. Today, wind energy generates 4% of the electricity used in the U.S. [1].

Several renewable energy policies have been put in place to encourage this growth at both the federal and state levels [2]. At the federal level, the Production Tax Credit (PTC) provides subsidies to wind farms. Along with the PTC, the federal government also sets long-term goals for wind energy. In 2008, the U.S. Department of Energy set a goal to produce 20% wind energy by 2030 [3]. In 2013, President Obama described his national Climate Action Plan, part of which would aim to double U.S. wind energy capacity in the next 4 years [4]. At the state level, Renewable Portfolio Standards (RPS) mandate how much electricity must be generated from renewable sources. In 2013, California produced 23% of its electricity from renewable energy sources; its current RPS mandates 33% renewables by 2020 [5].

The U.S. wind resource is large, both on land and offshore (Figure 1.1). Land-based winds are generally strongest in the middle of the country. As a result, Iowa, South Dakota, and Kansas produced more than 20% of their electricity from wind in 2012 [6]. By contrast, California produced 5% from its wind farms in Altamont Pass (east of the Bay Area) and in Tehachapi Pass (east of Bakersfield).

Although land-based winds are plentiful, offshore winds are even more attractive. Off-

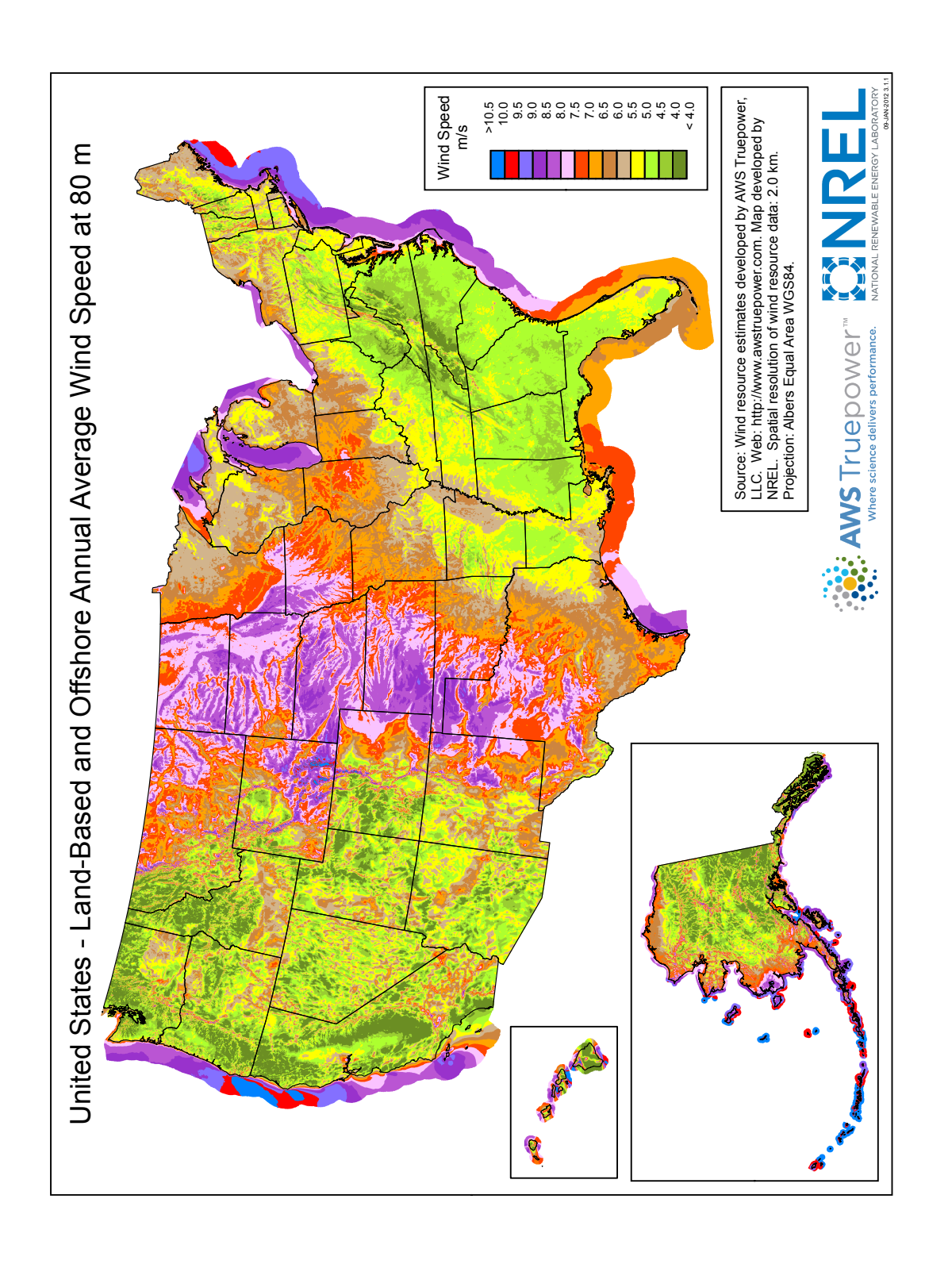


Figure 1.1: Land-based and offshore wind energy resource of the United States. Source: National Renewable Energy Laboratory, http://www1.eere.energy.gov/wind/pdfs/wind_speed_map_hi-res.pdf

shore winds tend to be faster and less turbulent than land-based winds, which have to pass over rough terrain and buildings. Stronger offshore winds are also located near many large coastal cities with a high demand for energy, reducing transmission costs. However, offshore wind farms need to overcome numerous technical challenges (deep waters, harsh environmental conditions, difficult to access for maintenance) and policy challenges (leasing government lands), which often lead to higher costs than land-based wind farms. In the U.S., several offshore wind farms have been proposed (such as Cape Wind, off the coast of Massachussetts), but none have been built [6]. By contrast, in Europe in 2011, 9% of wind capacity was installed offshore [7]. In order for wind energy to continue growing, researchers are continually looking for ways to reduce its costs, both on land and offshore.

1.2 Motivation

To reduce costs and increase energy capture, wind turbines have grown dramatically over time. From 1980–2013, the rotor diameter of wind turbines increased more than tenfold, from 15 meters to 171 meters (Figure 1.2). Longer blades are being developed to enable large, multi-MW wind turbines to increase their rated power and capture more energy. In 2013, SSP Technology manufactured an 83.5 meter blade for a 7-MW offshore wind turbine [8], and blades are expected to grow even larger in the future. Current research is focused on developing 100+ meter blades [9, 10].

The equation for rotor power (Equation (1.1)) explains the benefits of large turbines. The power extracted from the wind by the rotor is determined by the power coefficient of the rotor C_p , air density ρ , the radius of the rotor R, and the velocity of the wind V. Rotor power increases with R^2 (larger rotors have more area to capture more wind) and V^3 (taller hub heights can access faster winds out of the terrestrial boundary layer).

$$P_{\text{rotor}} = \frac{1}{2} C_p \rho \pi R^2 V^3 \tag{1.1}$$

There are four main challenges with the development of large rotor blades: (1) manufac-

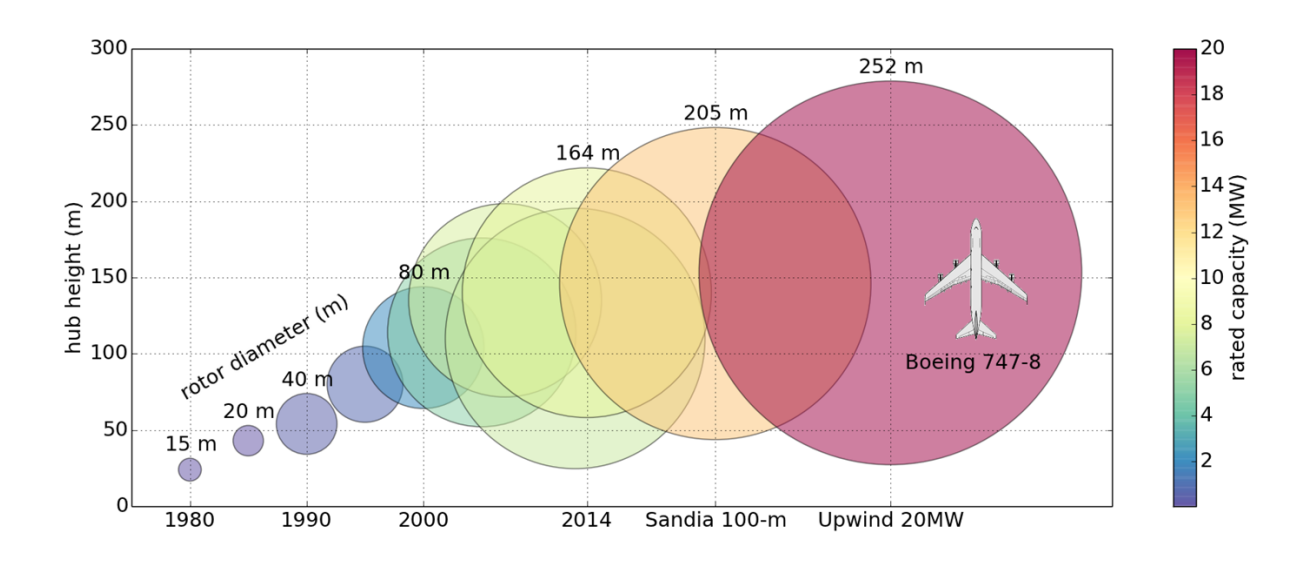


Figure 1.2: Height, size, and power of wind turbines over time: hub height (y-axis position of circle centers), rotor diameter (size of circles), and rated capacity (color of circles). Wind turbines have grown dramatically from 1980 to 2014 [3, 11, 12, 13, 14, 15, 16]. Researchers are focused on developing even larger tubine concepts for the future: the Sandia 100-m blade [9] and the Upwind 20MW turbine [10]. Taller hub heights can access faster winds and larger rotor diameters can capture more wind, both of which increase turbine power.

turing^{*}, (2) transportation[†], (3) limiting the growth of blade mass, and (4) supporting large blade loads. This dissertation focuses on the last two challenges.

To discuss the growth of blade mass, consider the following scenario. Assuming geometric similarity as a rotor grows in size, its power (revenue) scales with R^2 , but the volume of its material (and hence, its mass and cost) scales with R^3 . This implies that cost will increase linearly with scale, and at some size, the extra cost of a larger blade will exceed the extra revenue it can generate. This concept is commonly known as the "square-cube law" [3]. However, if design improvements are applied to a large blade, then its mass (and cost) will grow more slowly than R^3 . In practice, engineers and blade manufacturers have been able to improve blade designs as they have upscaled them, to keep mass growth closer to R^2 [18, 19]. Cost reductions in blades can significantly reduce the cost of the whole turbine, since blades are estimated to account for roughly 18% of the total turbine cost [20]. Furthermore, reducing blade mass will also reduce the costs of other turbine support structures [21].

Clearly, the goal of large blade development is to reduce the cost of energy by limiting the growth of blade mass. Historically, this has reduced the levelized cost of energy (LCOE) threefold (Figure 1.3) [21]. LCOE is the price at which electricity from wind has to be sold to break even over the lifetime of the project. More recently, LCOE has started increasing again (to about \$80/MWh in 2009), due to increases in the price of wind turbines, which were driven by turbine upscaling, and increases in material prices.[‡] This suggests that the square-cube law is getting harder to beat, and motivates further improvements in blade

^{*}Manufacturing constraints limit the dimensions and shapes of blades. Blades are built with composite materials, which consist of woven glass or carbon fibers suspended in a cured plastic resin. In a typical manufacturing process called resin infusion, dry fibers are placed in a mold and sealed off, liquid resin is injected into the fiber package, and the component is cured to produce a hardened composite material [17]. As blades become longer, it becomes more difficult to ensure component quality. Furthermore, manufacturing considerations tend to discourage large changes in shape along the blade length, because when the dry fibers are placed inside a mold with a complex shape, the fibers tend not to lay flat. These crooked fibers result in a weakened component.

[†]Transportation constraints limit the maximum dimensions of the blade. These dimensions depend on the width of roads, the height of bridges, and the dimensions of railcars or truck trailers used for transportation. Most conventional blades are built as monolithic, one-piece structures, which are usually thickest near the root. Sometimes the root needs to be designed for transportation constraints, at the expense of optimal structural or aerodyanmic performance considerations.

[‡]This is somewhat complicated by the 2008 financial crisis, which may have also increased prices. Many other forms of electricity generation besides wind energy also had higher costs over the timeframe of 2004-2009 [21].

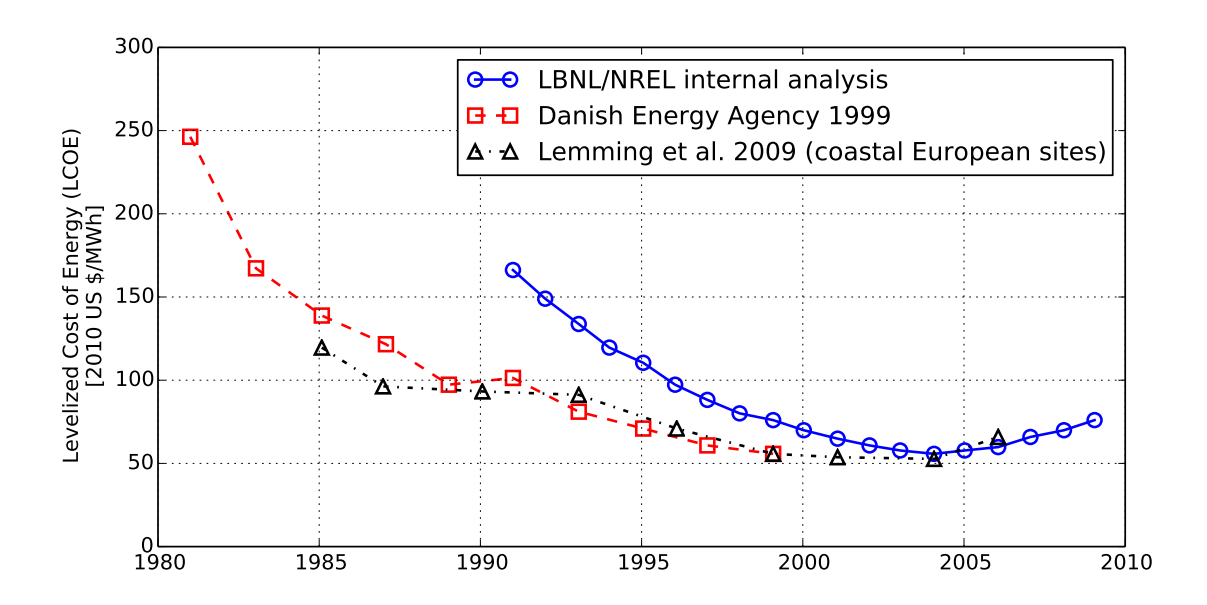


Figure 1.3: From 1980–2004, the levelized cost of energy (LCOE) for wind decreased threefold, but from 2004–2009, LCOE increased slightly [21, 22, 23].

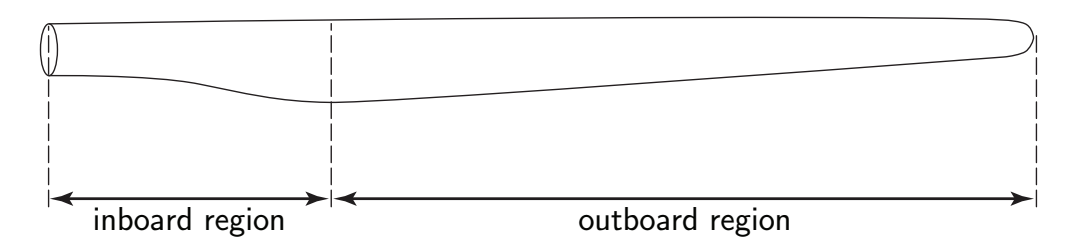


Figure 1.4: Schematic of the inboard and outboard regions on a wind turbine blade.

design to bring LCOE back down again.

On the other hand, large blades must support large loads. For a simple geometric upscaling of a blade and assuming a constant tip speed ratio, the bending moments due to aerodynamic forces scale with R^3 , and the bending moments due to gravitational forces scale with R^4 [9]. These bending moments are highest in the inboard region, near the root of the blade (Figure 1.4). Hence, the inboard region needs an efficient structure that can support the bending loads, provide favorable aerodynamic performance, but also limit overall blade mass (and cost). The blade cannot be too heavy, because excess blade mass increases inertial fatigue loads, which decrease the blade lifetime. Heavier blades also tend to cost more to manufacture and transport, which limits the economic benefits of large wind turbines.

1.3 Design approaches for improving the inboard region

Recent research suggests that design improvements to the inboard region may improve the overall blade performance. Conventionally, the inboard region used thick airfoils to support large flapwise bending loads [24, 20, 25]. While the aerodynamic efficiency of thick airfoils is generally poor, this is the standard compromise between structures and aerodynamics in blade design. The inboard region is primarily designed for structural efficiency: thick cross-sections (with a large second moment of area in the flapwise direction) support the large flapwise bending loads. The inboard region design is also influenced by manufacturing constraints related to the root attachment, as well as transportation requirements that limit the maximum allowable dimensions.

To improve the performance of the inboard region within the context of these constraints, blunt trailing-edge "flatback" airfoils have been designed to address both the structural and aerodynamic performance challenges of the inboard region [26, 27]. For a given sectional maximum thickness, structural advantages include a larger sectional area and increased sectional moment of inertia; aerodynamic advantages include a larger maximum lift coefficient and reduced sensitivity to surface soiling [28]. Known challenges include large base drag and vortex shedding noise [29]. Essentially, flatbacks are state-of-the-art thick airfoils for wind turbine blades, and they have been recently used on commercial blades [30].

More recently, several unconventional blade concepts have proposed using multiple airfoils in the inboard region to improve blade performance. These blade concepts form a new class of "multi-element" blade designs (Figure 1.5).

Wirz proposed a conceptual design for wind turbine blades that has the potential to improve the structural and aerodynamic performance of the inboard region: the biplane blade [34]. The biplane blade design uses a biplane inboard region that transitions into a mid-blade joint, which is connected to a monoplane outboard region (Figure 1.6). At the blade root, it was also envisioned that the biplane inboard region could transition into a root joint, which is connected to a conventional root cylinder that can bolt into a conventional hub. Analytical and computational structural analysis of the internal spar of the biplane

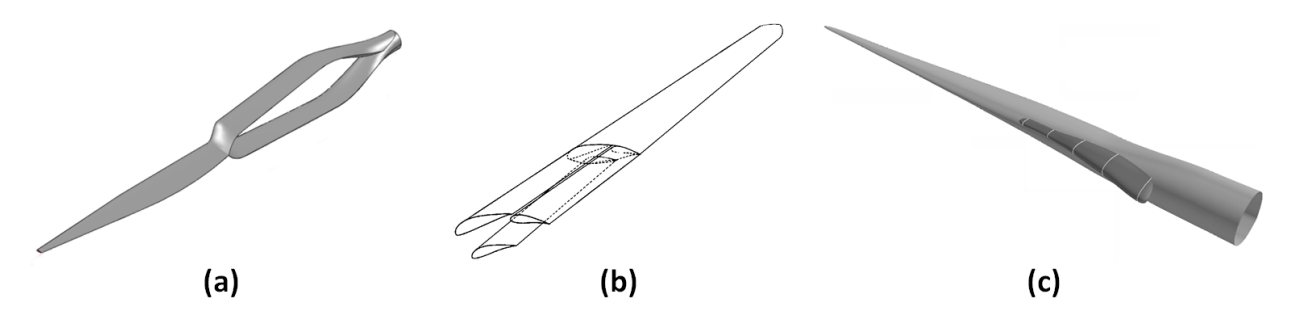


Figure 1.5: "Multi-element blades" are a new class of unconventional blade designs, which use multiple airfoils in the inboard region: (a) the biplane blade [31], (b) multi-element airfoils [32], and (c) leading edge slats [33].

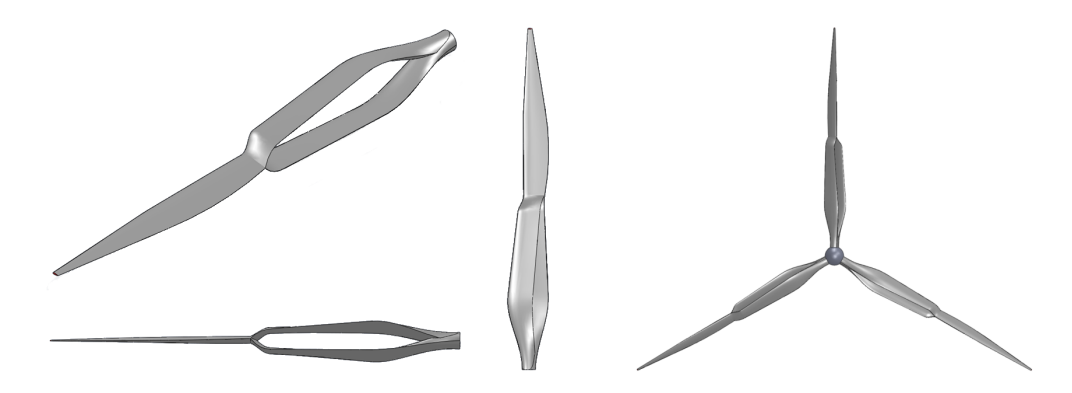


Figure 1.6: Artistic rendering of a biplane blade for next-generation wind turbine blades. Image credit: Phillip Chiu.

blade showed an increase in structural efficiency in the flapwise direction [35, 31, 36]. Two-dimensional computational aerodynamic analysis also showed that biplane airfoils increase the maximum lift coefficient [31, 37]. These benefits can lead directly to weight and cost reductions for large blades. A similar design was independently proposed by Grabau [38], but did not include a root joint; instead the biplane airfoils were bolted directly into the hub. Another study [39] used basic structural and aerodynamic analyses to examine the feasibility of a biplane blade without a root joint, but the structural analyses were not as detailed as the results presented here. This study also recommended a configuration with a small gap§ between the biplane airfoils, which seemed to limit the stiffness of the biplane blade in the chosen configuration.

 $[\]S$ The recommended gap-to-chord ratio for the biplane inboard region ranged from 0.3 at the mid-blade joint to 0.7 at the root.

Other aerodynamic studies [40, 41] have shown that multi-element airfoils have greater lift-to-drag ratios and maximum lift coefficients compared to standard thick airfoils for wind turbines. Another study examined a 10-MW turbine with a leading edge slat fitted to the inboard region, which obtained an 8% increase in the power coefficient (at the cost of a 12% increase in thrust coefficient) and a 1% increase in the annual energy production [42]. Hence, it may be possible to increase the maximum power production, improve start-up performance, and improve overall efficiency of blades for MW-size turbines. These studies showed aerodynamic improvements, but did not explicitly examine the structural considerations for large multi-element blades.

This dissertation focuses on the biplane blade, and uses a "structures-first" approach with aero-structural investigations to move the biplane blade from a conceptual idea to a well-defined design. The following research questions were considered:

- 1. Is the biplane blade a feasible design?
- 2. How do the dimensions of the biplane inboard region affect blade performance?
- 3. How does the aero-structural performance of the biplane blade compare to a conventional "monoplane" blade?

1.4 Significance of this work

While its potential benefits are interesting, the unconventional configuration of the biplane blade makes it challenging to design and analyze. It is not initially apparent exactly how the biplane should be incorporated into the overall blade structure, because several design parameters need to be specified for the inboard biplane region. This work provides the following contributions to the wind energy research community:

- 1. a feasibility study of the biplane blade, which demonstrates its basic aerodynamic and structural improvements
- 2. an analytical model for the displacement field of simple biplane spars, which reveals

[¶]These multi-element airfoils are specifically designed for wind turbines, and are usually thick airfoils with thickness-to-chord ratios of 15-30%. This differs from prior investigations of thinner multi-element airfoils, which focused on aircraft applications.

how they carry loads differently from conventional cantilevered monoplane spars

- 3. an approach to model the biplane blade with beam finite elements, which was carried out on 3 types of structures, each with increasing complexity: isotropic biplane beams, composite biplane spars, and a composite biplane blade
- 4. a blade definition for a 100-meter biplane wind turbine blade, with detailed cross-sectional geometries and a laminate schedule
- 5. an open-source technology stack and methodology for biplane blade design and analysis

This dissertation finds that the biplane blade improves flapwise structural efficiency, relative to a conventional monoplane blade of the same mass and length. Therefore, it may be possible to construct a *lighter* biplane blade with an *equal* structural efficiency. These benefits can lead directly to weight and cost reductions for large blades.

1.5 Outline of the thesis

The main objective of this dissertation is to develop and document the design of a large (100-meter) biplane blade, and compare its performance to the conventional 100-meter Sandia SNL100-00 reference blade [9]. Chapter 2 defines the nomenclature used to describe the external (aerodynamic) and internal (structural) geometry of both conventional monoplane blades and the biplane blade. Chapters 3 to 5 describe three studies of the biplane blade, carried out in order of increasing complexity:

<u>Chapter 3</u> analyzes the aerodynamic and structural performance of the biplane blade separately, in a proof-of-concept manner. The work in this chapter was published in [35, 31].

<u>Chapter 4</u> uses analytical and computational methods to compare the structural performance of composite biplane spars to a composite monoplane spar from the Sandia reference blade. The work in this chapter originally appeared in [36].

<u>Chapter 5</u> gives a detailed blade definition for a full 100-meter biplane blade, and compares its structural performance to the Sandia reference blade.

Finally, Chapter 6 gives concluding remarks and recommendations for future research.

CHAPTER 2

Anatomy of a wind turbine and its components

This chapter will introduce the names and functions of the major components found in modern wind turbines. These component names will be reused throughout this dissertation. Because this dissertation focuses on blade design, this chapter will also briefly discuss the components of conventional ("monoplane") blades. Finally, some new nomenclature will be introduced for biplane blades.

2.1 Wind turbine components

Modern wind turbines are large machines made of many components (Figure 2.1). Overall, these components can be grouped into three main systems: (1) a rotor, (2) a nacelle, and (3) a tower. The rotor is attached to the front of the nacelle, which sits on top of a tower, which is fixed to the ground.

First, the rotor converts the kinetic energy of the wind into useful torque for the wind turbine. The rotor is made up of three blades and a hub. The root of each blade is bolted into the hub. As the wind rushes by, aerodynamic lift forces develop on each blade; these aerodynamic forces turn the rotor.

As the rotor turns, it sweeps out a circular area called the "rotor plane" (Figure 2.2). The turning rotor provides large amounts of torque to a rotor shaft connected to the hub. The rotor shaft turns at a low speed (typically about 10 rpm) and transmits the torque to the nacelle.

The wind speed often varies in time, which changes the lift forces on the blade. The angle between the incoming wind and a blade can be changed to alter the lift forces on the blade.

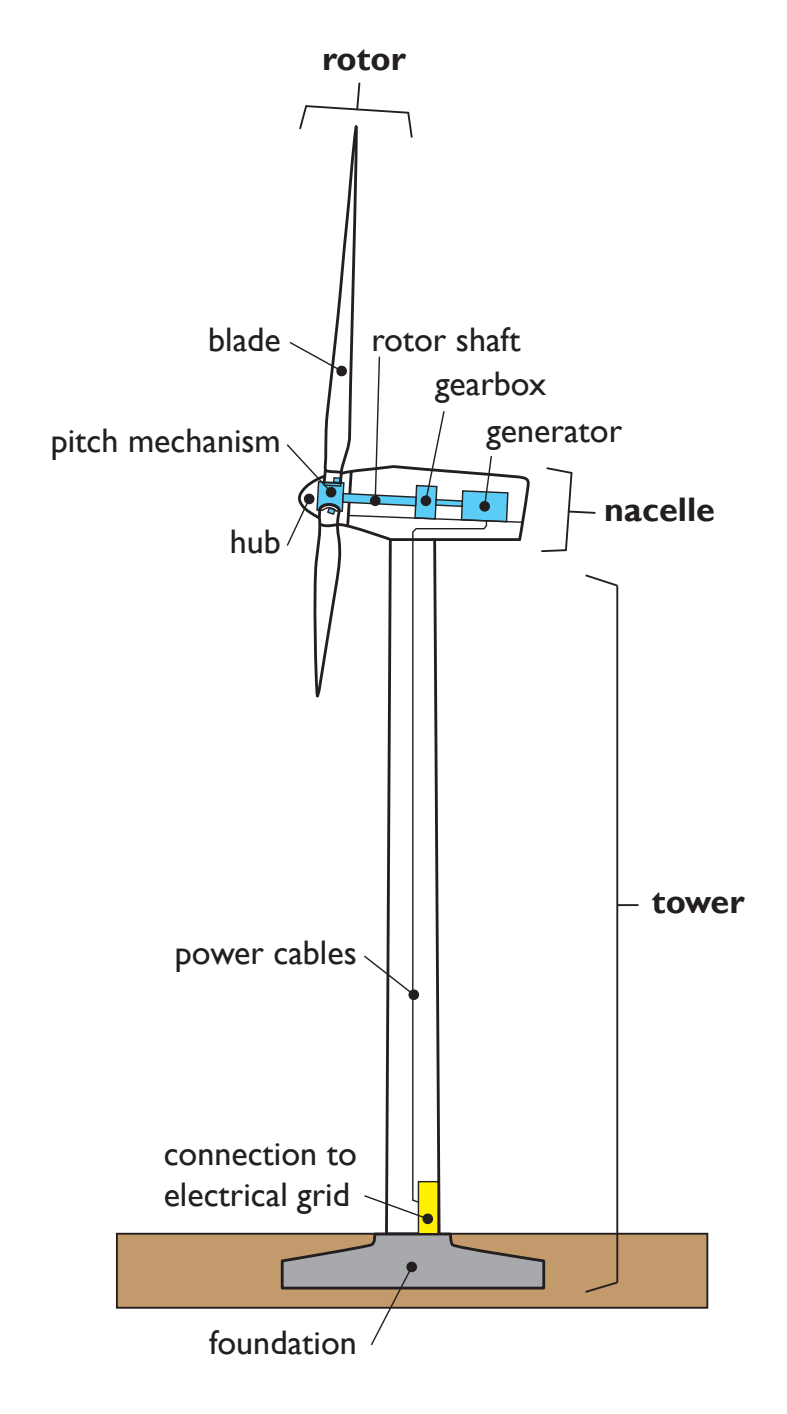


Figure 2.1: Components of wind turbines. Adapted from [43].

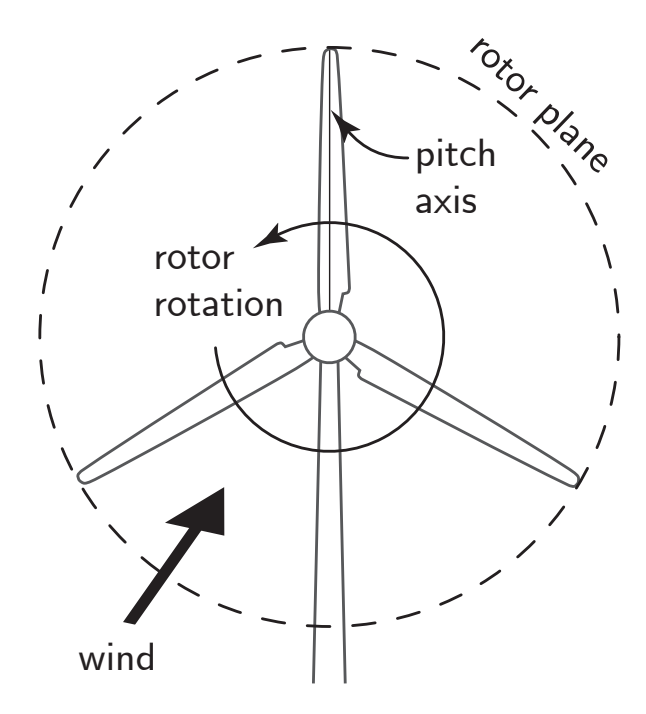


Figure 2.2: Schematic of a typical wind turbine rotor in operation.

In the hub, pitch mechanisms attached to each blade root can rotate individual blades about their "pitch axis" (Figure 2.2). This rotation, or "pitching," changes the angle between the wind and the blade, and alters the lift forces on the blade. This can be used to optimize rotor performance during normal operation, or to slow and stop the rotor during a storm.

Second, the nacelle houses the machinery that converts torque into electricity. The rotor shaft passes through the front of the nacelle and delivers its torque to a gearbox. The gearbox converts the low speed from the rotor shaft to a higher speed for the generator. Many generators typically require a high speed of rotation to efficiently convert torque into electricity.* Power cables transmit the electricity out the bottom of the nacelle, through the tower, and to the electrical grid on the ground.

Third, the tower holds up the entire wind turbine. The tower resists thrust loads from the wind that develop on the rotor and nacelle. For land-based turbines, the bottom of the

^{*}New "direct-drive" generators have been developed that do not require a high speed of rotation for efficient operation, thus eliminating the need for a gearbox. In this case, the rotor shaft is directly connected to the generator. Since gearboxes are usually heavy and prone to failure, many manufacturers are moving towards direct-drive generators to reduce overall turbine cost. However, these cost reductions may be limited by the large quantities of expensive rare earth metals that are used in direct-drive generators.

tower sits on a concrete foundation, which anchors the turbine into the ground. For offshore turbines, the tower sits on a substructure that connects it to the ocean floor.

2.2 Conventional blades and their substructures

Conventional ("monoplane") blades are long slender structures. Three coordinate directions are used to describe a blade's geometry (Figure 2.3). The maximum dimensions of a blade in each of these direction are its span (along the spanwise coordinate), its maximum chord length (along the edgewise coordinate), and its maximum thickness (along the flapwise coordinate). The root and tip of the blade are located at the minimum and maximum spanwise coordinates, respectively. The spanwise coordinate runs along the pitch axis of the blade (Figure 2.2). These three coordinates are also used to describe the displacements, forces, and bending moments of the blade under applied loads. For example, when a load is applied to the blade in the flapwise direction, a flapwise bending moment develops about the edgewise axis to resist flapwise deflection of the blade.

Since the maximum dimension in the spanwise direction is so much larger than its dimensions in the edgewise and flapwise directions, blade designs are usually defined by a set of cross-section geometries that are distributed along the span at "blade stations" (Figure 2.4). In turn, each of these cross-section geometries are specified with an external and internal geometry. Generally, aerodynamic considerations inform the selection of the external geometry, while structural considerations inform the selection of the internal geometry.

Since wind turbine blades are pre-twisted, it is important to clearly define the edgewise and flapwise directions. In this dissertation, the "edgewise" direction refers to the direction that is in-the-rotor-plane. In helicopter rotors, this is also referred to as the "lead-lag" direction. In this dissertation, the "flapwise" direction refers to out-of-the-rotor-plane.

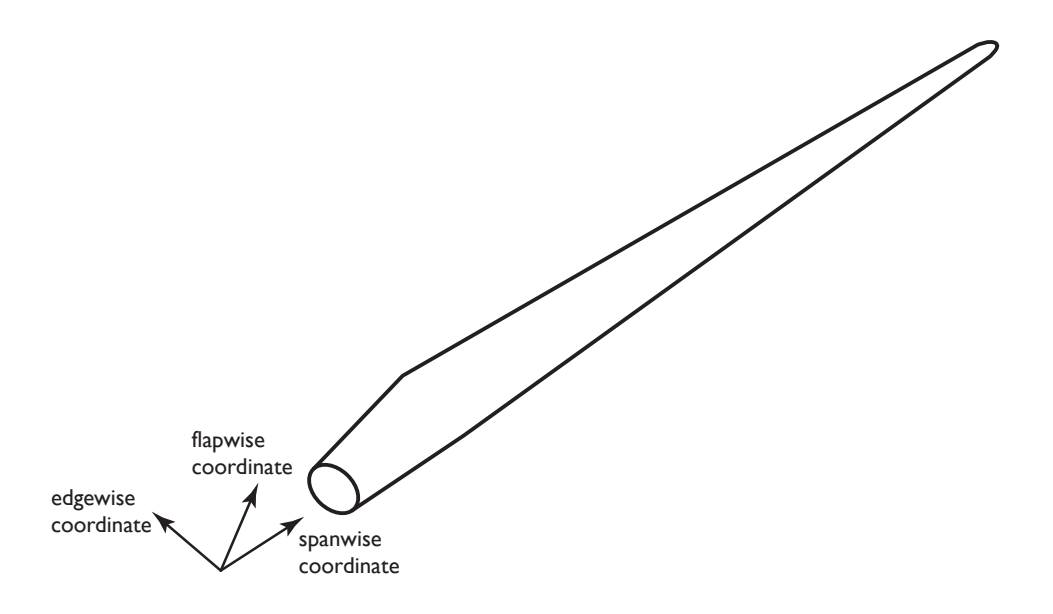


Figure 2.3: Nomenclature for blade coordinate directions: flapwise, edgewise, and spanwise. When bending loads are applied to the blade, bending moments develop in the blade to resist bending in the direction of the applied load. When loads are applied in the *flapwise* direction, bending moments that develop about the edgewise axis are called *flapwise* bending moments. Similarly, when loads are applied in the *edgewise* direction, bending moments that develop about the flapwise axis are called *edgewise* bending moments.

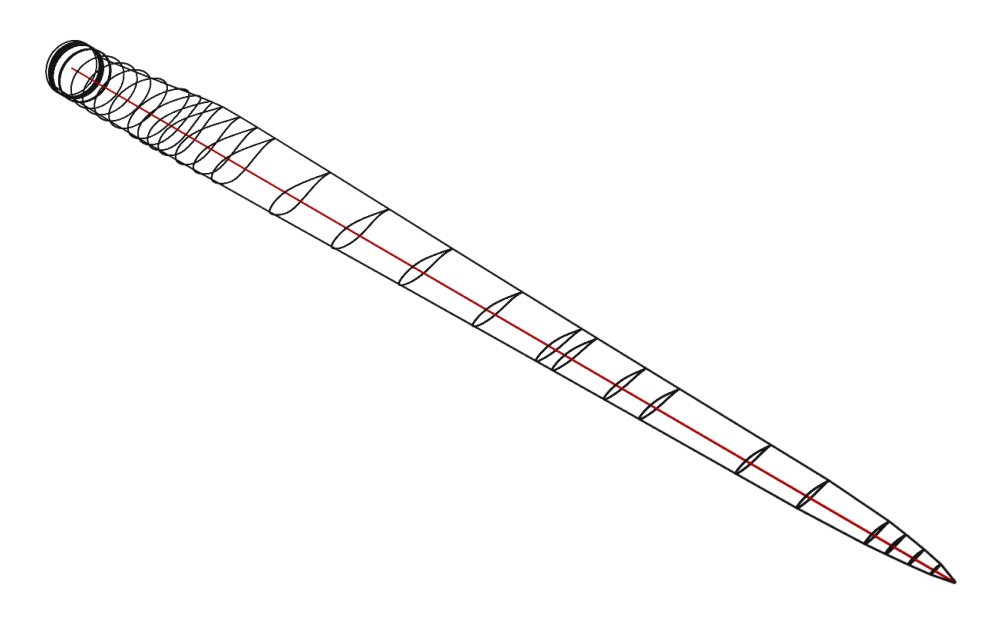


Figure 2.4: Blade designs are defined by a set of cross-section geometries at "blade stations" distributed along the spanwise coordinate (red line).

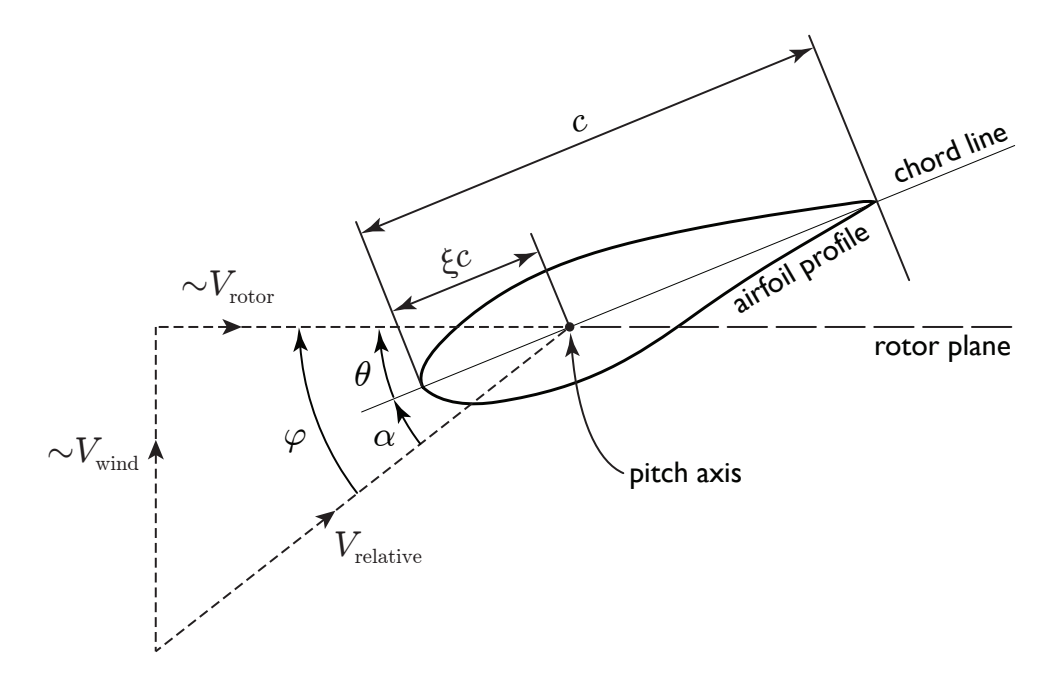


Figure 2.5: External geometry of a conventional blade cross-section. This cross-section is viewed from the edge of the rotor plane (the dashed line), looking down the pitch axis (the point on the dashed line). Both the rotor plane and pitch axis were shown earlier, from the perspective of the entire rotor, in Figure 2.2.

2.2.1 External (aerodynamic) geometry

The external shape of a cross-section (Figure 2.5) is determined by an airfoil profile, which has a chord length c. Thick airfoil profiles (which can fit over tall spars with good structural performance) are typically chosen for the inboard blade region. Thin airfoil profiles (which have better aerodynamic performance) are usually chosen for the outboard blade region.

The pitch axis is located along the chord line, at a distance ξc behind the leading edge of the airfoil. The parameter ξ is the *pitch axis fraction*, where $0 < \xi < 1$. In other words, the pitch axis fraction ξ is a nondimensional length, normalized by the chord length c. Depending on the airfoil profile and spanwise location along the blade, typical values for the pitch axis fraction range between $0.3 < \xi < 0.5$. The pitch axis can be used as a reference point for positioning the shear webs (see Section 2.2.2), typically with one shear web forward of the pitch axis, and another aft of the pitch axis.

The relative wind velocity "seen" by the cross-section, V_{relative} , is broken up into two

components: the velocity of the incoming wind, V_{wind} ; and the linear velocity of the cross-section V_{rotor} , which comes from the rotation of the rotor, and is seen as a right-to-left motion of the cross-section along the rotor plane.[†] The local inflow angle φ (measured between the rotor plane and the relative wind velocity) is also broken up into two smaller angles: the angle of attack, α ; and the angle between the local chord line and the rotor plane, θ .

The angle θ typically varies along the span of the blade, so that during normal operation, each cross-section will "see" the wind at an appropriate angle of attack α for good aerodynamic performance. In other words, θ describes the local rotation of the cross-section about the blade's pitch axis. Although it is not shown on Figure 2.5, θ is the sum of the local twist angle θ_t and the blade pitch angle θ_p .

In a typical blade design, the local twist angle θ_t varies along the span of the blade, with maximum twist near at the root ($\approx 15\text{-}20^\circ$), and minimum twist at the tip (Figure 2.6). During normal operation, the blade twist allows each cross-section to "see" the wind at the appropriate angle of attack α for optimum aerodynamic performance. While the value of θ_t changes along the span of a twisted blade, it is fixed for each cross-section once the blade is built.

During the turbine's operation, the blade pitch angle is set by the pitch mechanism attached to the blade root. As described in Section 2.1, the pitch mechanism can rotate the entire blade around its pitch axis, which collectively changes the pitch angle θ_p for all the cross-sections at once.[‡] This in turn changes the angles θ , α , and ϕ in order to regulate the lift forces on the blade, hence, regulating the power produced by the blade.[§]

[†]In Figure 2.5, V_{wind} and V_{rotor} are shown as approximate values because the solid rotor blades slow down the incoming wind, leading to slight changes of these velocities. Momentum theory, which models the actuator disc can be used to describe this phenomenon in more detail [44].

[‡]If the blade pitch angle θ_p is set to zero, then $\theta = \theta_t$, since $\theta = \theta_t + \theta_p$.

 $[\]S$ A control algorithm chooses the appropriate pitch angle in response to changes in the incoming wind velocity, V_{wind} .

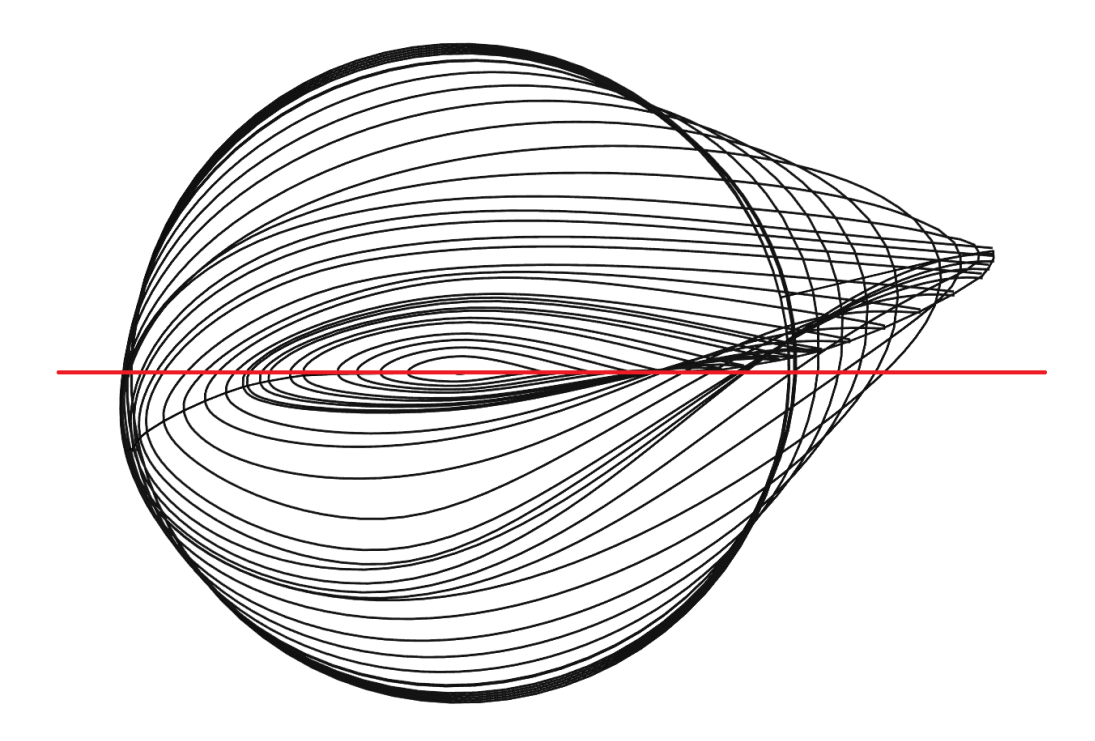


Figure 2.6: A view down the pitch axis of a conventional blade shows maximum twist for thick airfoil profiles at the root, and minimum twist for thin airfoil profiles at the tip. The red line represents horizontal (zero twist).

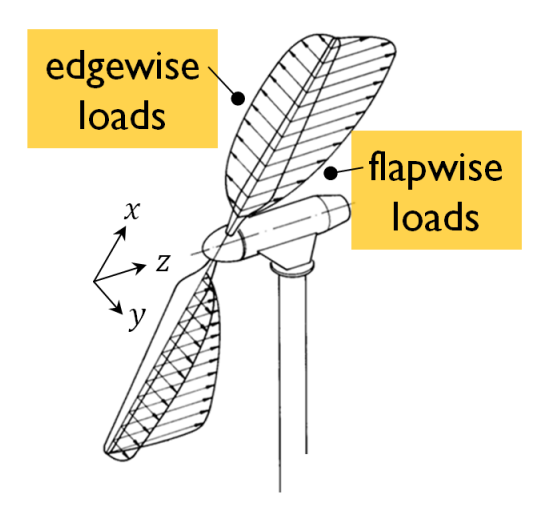


Figure 2.7: Flapwise and edgewise load distributions on a wind turbine blade in operation. Adapted from [25].

2.2.2 Internal (structural) geometry

The blades are subjected to external loads, which come from (1) the wind, which generates aerodynamic forces in the flapwise direction, and (2) gravity, which generates gravitational and inertial forces in the edgewise direction (Figure 2.7). Inside the blade, several structural parts are used to stiffen the blade to support the loads in each of these directions. Parts placed on the top and bottom surfaces help resist flapwise loads, while parts placed on the forward and aft surfaces help resist edgewise loads (Figure 2.8). Figure 2.9 shows a schematic of the internal structure for a typical blade.

Each part of the internal structure is made of different materials, depending on the type of load it is designed to support. Most of these parts are made of glassfiber-reinforced plastic (GFRP), more commonly known as "fiberglass" or "glass fiber". The high strength-to-weight ratio of GFRP makes it ideal for large wind turbine blades, as compared to other materials like wood, aluminum, or steel.§ GFRP is a composite material made of strong fibers, which are suspended in a plastic resin matrix that has been cured and hardened. Usually, GFRP is manufactured in thin sheets (plies). These plies are laid on top of each other in a specific orientation and order (a layup) to constuct a laminate. Uniaxial, biaxial, and triaxial GFRP

[§]Newer blades are also made of carbon fiber, which is stronger and lighter (but also about 10 times more expensive) than glass fiber.

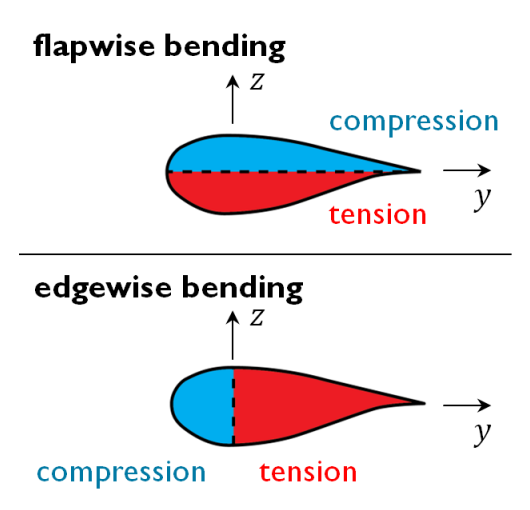


Figure 2.8: Flapwise bending loads lead to compression and tension on the upper and lower parts of a cross-section (top). Edgewise bending loads lead to compression and tension on the forward and aft parts of a cross-section (bottom).

laminates are made by using different layups of GFRP plies (Figure 2.10).

In general, GFRP is strongest when loads are applied along the direction of the fibers in the GFRP. In uniaxial GFRP, all the fibers are aligned in one direction (0°). In biaxial GFRP, half the plies have fibers pointing in one direction (+45°), and the other half point in an orthogonal direction (-45°). Triaxial GFRP has fibers pointing in three directions (0°, +45°, and -45°).

Uniaxial GFRP is only designed to take loads in one direction, along its fibers. Spar caps, located at the top and bottom of the cross-section, are made of uniaxial GFRP to support the largest tensile and compressive stresses from flapwise bending loads. The trailing edge reinforcement, located at the aft of the cross-section, is also made of uniaxial GFRP to support the largest tensile and compressive stresses from edgewise bending loads.

Biaxial GFRP can take loads in the same plane as the laminate, but is weak at supporting out-of-plane loads. Shear webs, which connect the top and bottom spar caps, are made of biaxial GFRP to resist the shear loads that can slide one spar cap past the other in the spanwise direction.

Triaxial GFRP is the most "multipurpose" laminate, and can take loads in most directions, but it is weaker than uniaxial GFRP at supporting tensile loads in one direction.

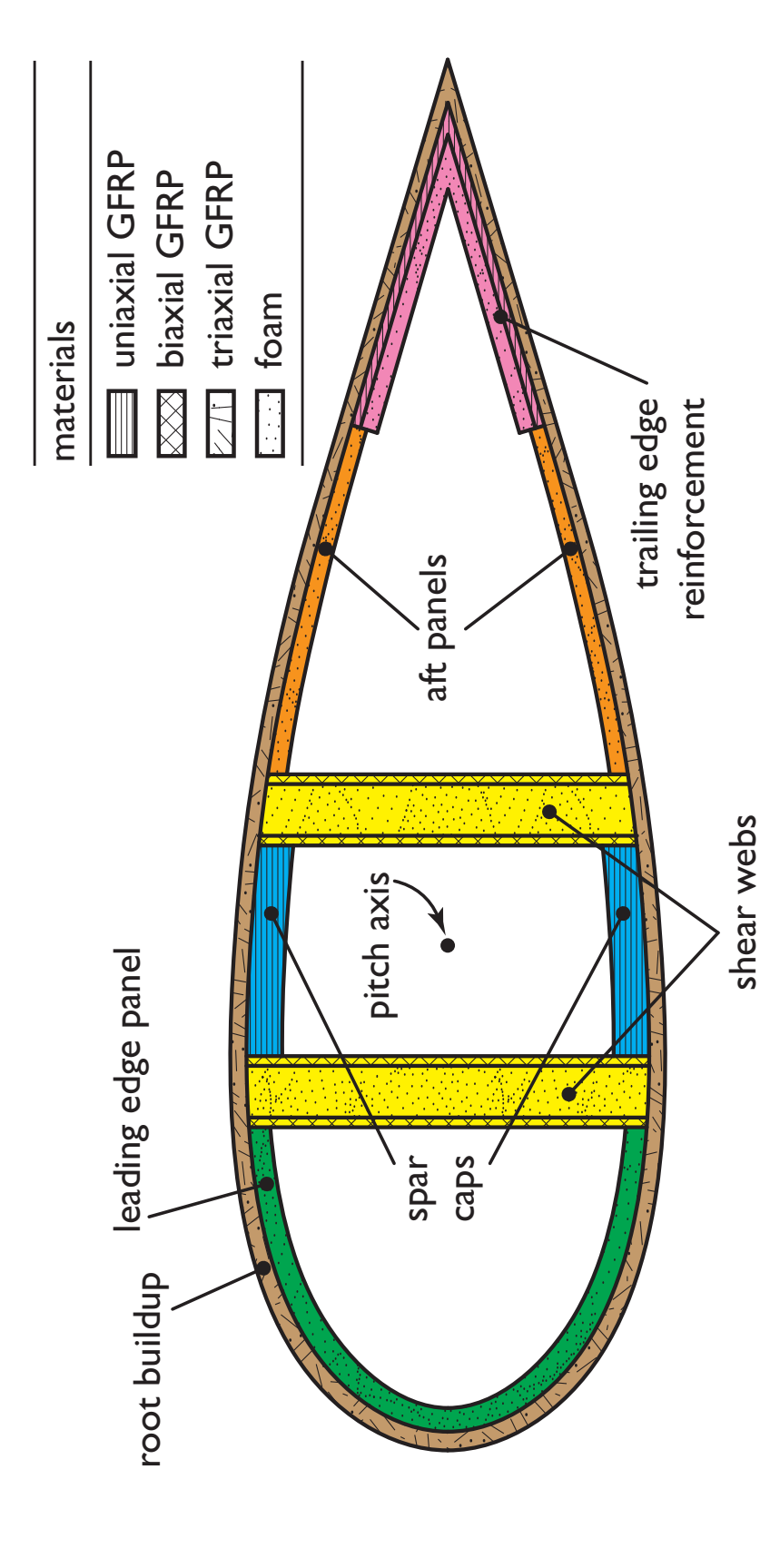


Figure 2.9: Internal geometry of a conventional blade cross-section made with glassfiber-reinforced plastics (GFRP). Adapted from [9]. Note: figure not to scale.

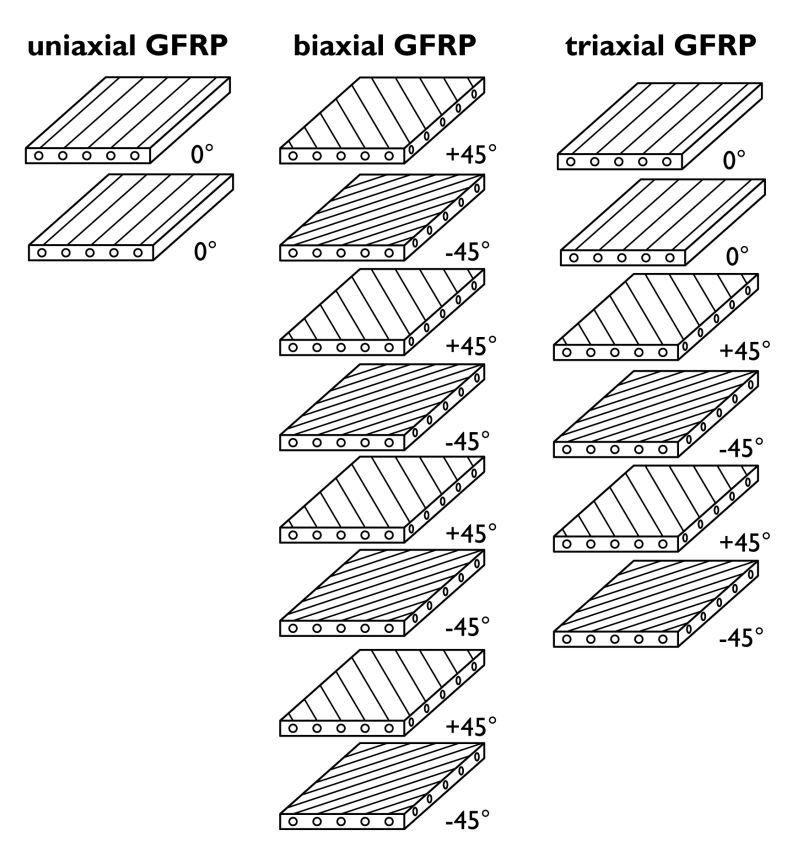


Figure 2.10: Example stacking sequences for uniaxial, biaxial, and triaxial layups of glassfiber-reinforced plastics (GFRP).

Hence, triaxial GFRP is used heavily in the root buildup (near the blade root), as well as along the airfoil skin, where loads are applied in many directions.

Foam is also used to provide buckling resistance to the shear webs, leading edge panel, and aft panels. It is usually sandwiched between GFRP laminates. For example, shear webs are made of foam sandwiched between two thin layers of biaxial GFRP. This leads to a stiff, lightweight structure for structural parts that do not need to support the largest flapwise or edgewise bending loads.

2.3 Biplane blades and their substructures

Like conventional blades, biplane blade designs can be defined by a set of cross-section geometries along the span at blade stations. However, since the inboard region of the blade uses biplane cross-sections, some new parameters need to be defined to specify the external (aerodynamic) shape of each airfoil in the biplane cross-section. Furthermore, substructures like *joints* are present in the biplane blade, which do not exist in conventional blades. This section introduces some new nomenclature for the substructures and cross-section geometries that are unique to the biplane blade.

2.3.1 Blade regions and substructures

A biplane blade can be divided up into two main regions (Figure 2.11). The *outboard* monoplane region of a biplane blade is essentially the same as the outboard region of a conventional blade (for example, see Figure 1.4). However, the *inboard biplane region* of a biplane blade is much different from a conventional blade.

The inboard biplane region is made up of four substructures (Figure 2.12): a mid-blade joint, an upper biplane element, a lower biplane element, and a root joint. The mid-blade joint connects the outboard monoplane region to the outboard ends of the upper and lower biplane elements. The root joint connects the hub to the inboard ends of the upper and lower biplane elements. Both of these joints provide a transition between monoplane cross-

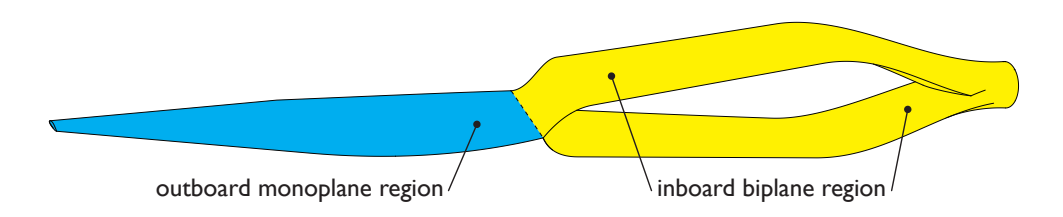


Figure 2.11: The biplane blade has an outboard monoplane region and an inboard biplane region. (Image outline courtesy of Phillip Chiu.)

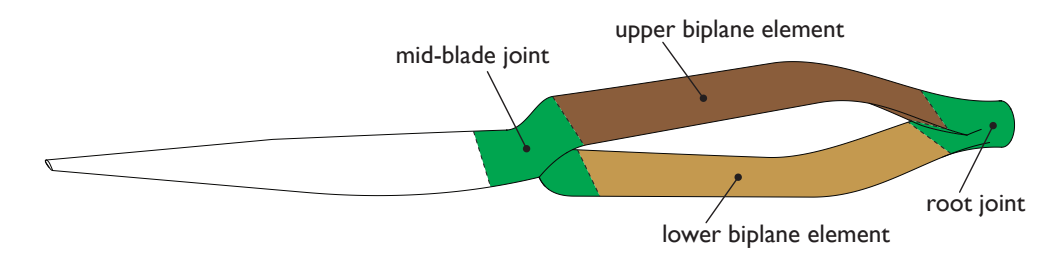


Figure 2.12: Four substructures make up the inboard region of the biplane blade. (Image outline courtesy of Phillip Chiu.)

sections (in the outboard monoplane region and at the root) and biplane cross-sections (in the inboard biplane region).

2.3.2 External (aerodynamic) geometry for the inboard biplane region

A biplane cross-section is made up of two airfoils; the relative position of each airfoil is specified by a gap g and a stagger s (Figure 2.13). The gap is the distance between each chord line. The stagger is the distance from the leading edge of the upper airfoil to the leading edge of the lower airfoil. Stagger can be positive, zero, or negative; it is defined as positive if the upper airfoil is placed forward of the lower airfoil. \P

In general, the upper and lower airfoil profiles can be different, and the upper and lower chord lengths (c_{upper} and c_{lower}) can also be different. However, in this study, both profiles and chord lengths were chosen to be the same at each blade station. This choice was made

[¶]Note: the chord lines of each airfoil do not have to be parallel, as they are drawn in Figure 2.13. The angle between each chord line is called *decalage*, which is sometimes used to fine-tune the aerodynamic performance of a biplane cross-section. A review of the literature showed that the effect of decalage on aerodynamic performance is small compared to the effects of gap and stagger. Therefore, decalage was not considered in this study. However, it may be a useful parameter to consider in future studies of the biplane blade.

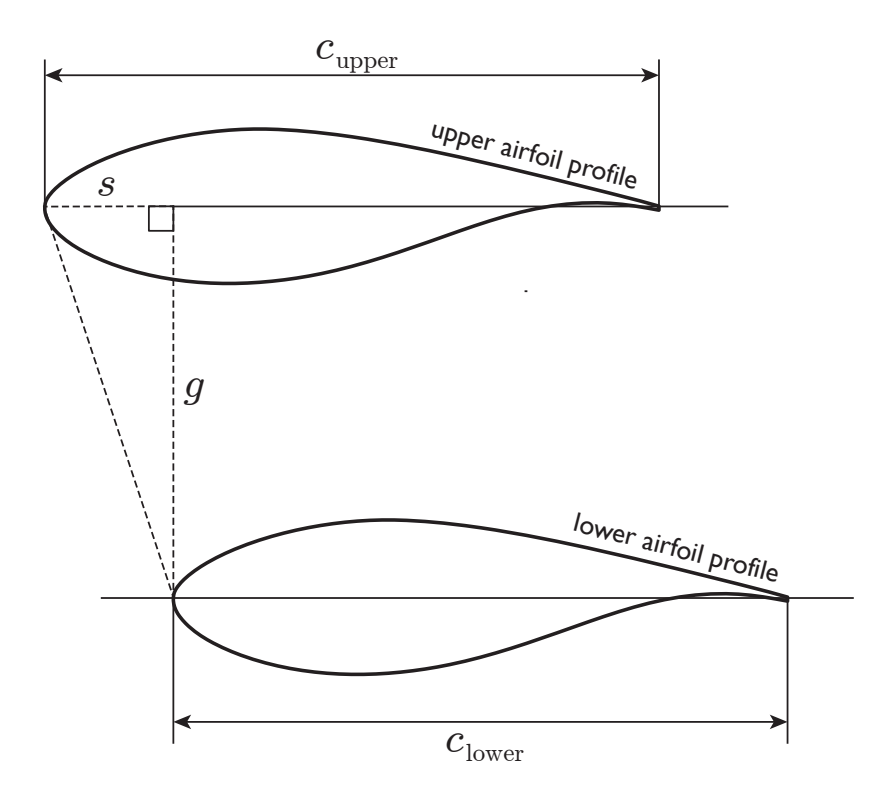


Figure 2.13: Gap (g) and stagger (s) dimensions for a biplane cross-section.

to limit the design space for the biplane blade. However, different airfoil profiles and chord lengths could be considered in future studies.

Different configurations of biplane cross-sections can be compared with two nondimensional parameters: the gap-to-chord ratio g/c and the stagger-to-chord ratio s/c. In each of these ratios, c is chosen to be the lower chord length.

In a conventional blade, the pitch axis is located inside the airfoil profile, along the chord line (Figure 2.5). In a biplane blade, however, the pitch axis may be located outside both airfoil profiles (Figure 2.14). The chordwise position of the pitch axis is specified by ξc_{total} . Here, ξ is the pitch axis fraction (as defined earlier in Section 2.2.1), and c_{total} is the total chord length (the distance from the leading edge of the upper airfoil to the trailing edge of the lower airfoil). The flapwise position of the pitch axis is specified by ηg . Here, η is the gap fraction, where $0 < \eta < 1$.

The total chord length depends on the stagger. If there is no stagger, then $c_{\text{total}} = c_{\text{upper}} = c_{\text{lower}}$ in this study.

Once the pitch axis location has been specified, the twist angle θ can be determined by rotating the biplane cross-section about the pitch axis. This definition of θ is similar to a monoplane cross-section. In fact, the local flow angle φ and the angle of attack α for a biplane are also defined similarly to a monoplane.

In a monoplane cross-section, the pitch axis is used as a reference point to position the shear webs, with one shear web forward of the pitch axis, and another aft of the pitch axis. In a biplane cross-section, it is convenient to define two new reference points to place shear webs in the upper and lower airfoils (see Figure 2.15). The upper reference point is located at a distance $f_{\text{upper}}c_{\text{upper}}$ along the upper chord line. Similarly, the lower reference point is at a distance f_{lower} along the lower chord line. Here, f_{upper} and f_{lower} are chord length fractions for each airfoil, where $0 < f_{\text{upper}} < 1$ and $0 < f_{\text{lower}} < 1$.

2.3.3 Internal (structural) geometry for the inboard biplane region

In this study, the internal (structural) geometry of each biplane cross-section was chosen to be identical for the upper and lower airfoils (Figure 2.15). If we consider one of the airfoils in a biplane cross-section by itself, then the discussion presented in Section 2.2.2 can be applied to size each of the structural parts inside that individual airfoil. Then, the structural parts inside the other individual airfoil can be sized in a similar way. Therefore, the internal dimensions for a biplane will not be discussed further in this section.

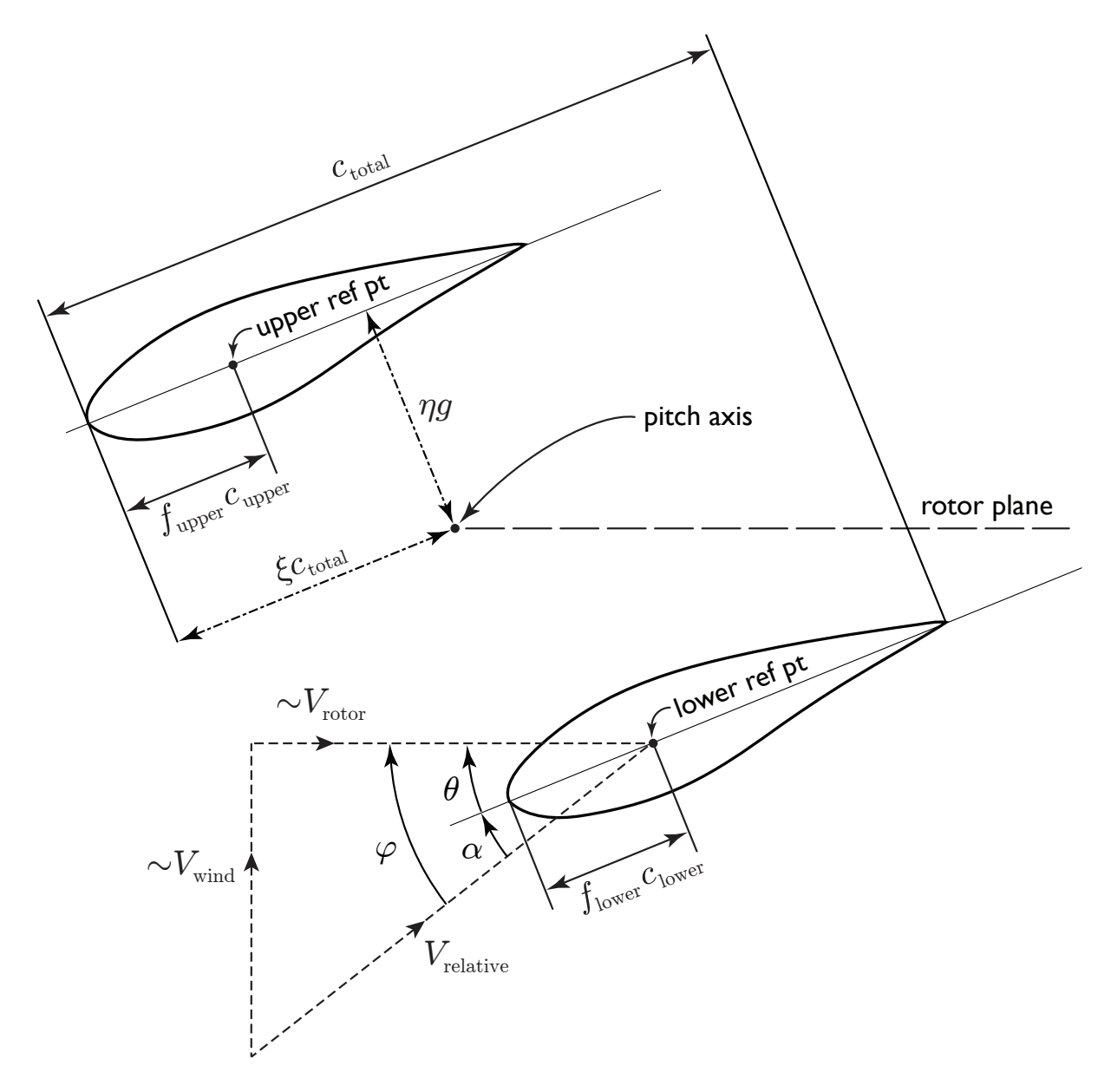


Figure 2.14: The external geometry of a biplane cross-section for a biplane blade. The upper and lower reference points (used to position the shear webs in each airfoil) are abbreviated as *upper ref pt* and *lower ref pt*, respectively.

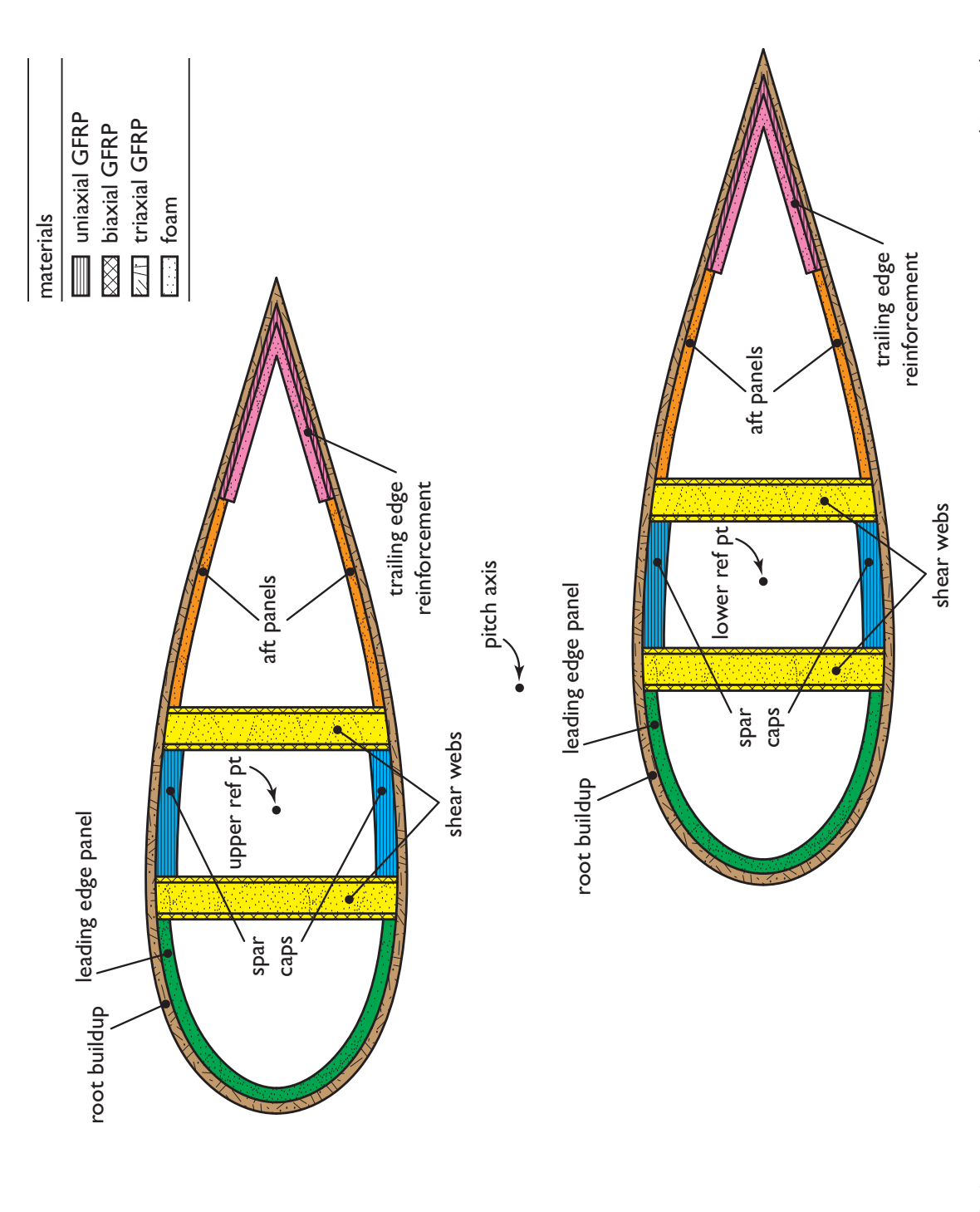


Figure 2.15: Internal geometry of a biplane blade cross-section made with glassfiber-reinforced plastics (GFRP). The upper and lower reference points (used to position the shear webs in each airfoil) are abbreviated as upper ref pt and lower ref pt, respectively. Note: figure not to scale.

CHAPTER 3

Aero-structural investigation of biplane wind turbine blades

As wind turbines grow larger, loads increase dramatically, particularly in the inboard region of the blade. A key problem is to design a strong inboard region that supports these loads without sacrificing too much aerodynamic performance. A new design is proposed: a biplane inboard region that transitions into a joint, which connects to a monoplane outboard region. The objective is to develop biplane inboard configurations that improve the aerostructural performance of blades. To approximately compare a conventional inboard region with a biplane inboard region, cross-sectional properties of a thick monoplane and a biplane were measured. Numerical simulations were used to explicitly compare the aerodynamic performance of a thick monoplane to a biplane. Then, several model beams were designed to be simple approximations of a conventional blade ("monoplane beam") and the biplane blade ("biplane beam"). Canonical bending loads were applied to each model beam and their deflections were compared. Numerical simulations show that the lift-to-drag ratio is significantly greater for the biplane than the thick monoplane for $0^{\circ} < \alpha < 15.5^{\circ}$. A parametric analysis of biplane beam configurations shows that their tip deflections are smaller than monoplane beams of the same length. These benefits for the inboard region of (1) improved aerodynamics and (2) improved strength could lead to weight reductions in wind turbine blades. Innovations that create lighter blades can make large blades a reality. These results suggest that the biplane blade is an attractive design for large blades.

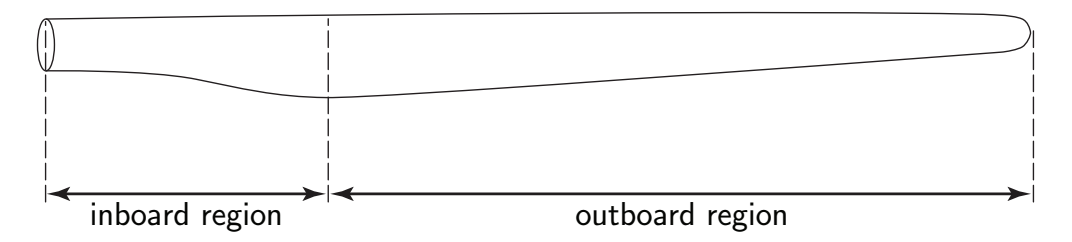


Figure 3.1: Schematic of the inboard and outboard regions on a wind turbine blade.

3.1 Introduction

Structural loads in wind turbine blades have increased dramatically as commercial turbines have grown in size [19]. The greatest bending loads are sustained in the inboard region of the blade, near the blade root (Figure 3.1). The structural design of the inboard region is driven by these large loads. Hence, the key problem for the blade designer today is to construct lighter blades with a strong inboard region to limit blade mass and support blade loads.

Conventionally, the inboard region used thick airfoils to support large bending loads [24, 20, 25] (Figure 3.2). While the aerodynamic performance of thick airfoils is generally poor, this is the standard compromise between structures and aerodynamics in blade design. The inboard region is primarily designed for structures: thick cross-sections (with a large second moment of area in the flapwise direction) support the large flapwise bending loads. The outboard region is primarily designed for aerodynamics: thin airfoils with high lift and low drag supply torque to turn the rotor. Normally, this compromise is sufficient for small- and mid-size turbines, because the aerodynamics of the inboard region are assumed to be minor. However, large turbines currently use airfoils in the inboard region that are approaching thickness-to-chord ratios of 45% [41]. Much thicker airfoils would likely be needed for the inboard region on longer blades. For very long blades, this approach is infeasible.

While many have developed airfoils for the mid- and outboard regions of wind turbine blades [24, 45, 46, 47, 48, 49], less work has focused on the improving the inboard region. Prior efforts in flow control attempted to improve the poor aerodynamics of the thick inboard region. Separation of the boundary layer was delayed to a certain extent with aerodynamic

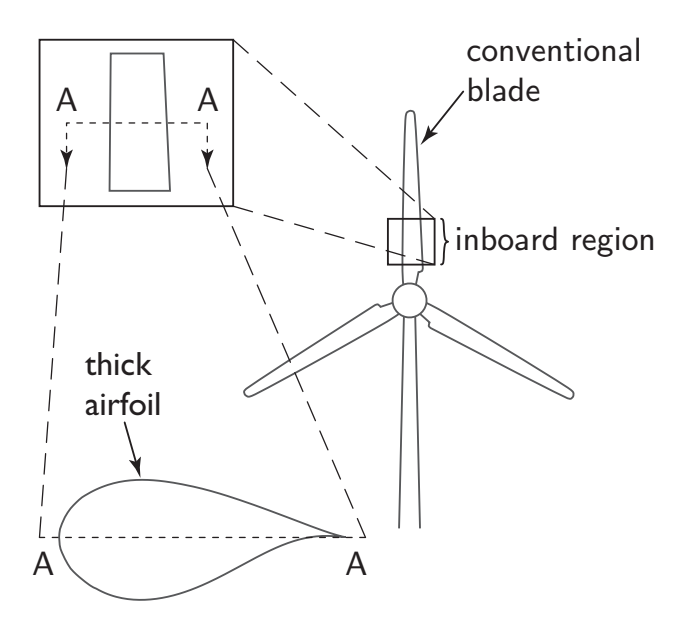


Figure 3.2: Thick airfoil cross-sections used in the inboard region of conventional wind turbine blades.

devices (e.g. flaps, wedges, stall strips, and vortex generators) installed on the surface of the inboard region [50]. However, this approach does not explicitly address the structural requirements for the inboard region. Therefore, it is unlikely to help drive the design of longer blades. More recently, blunt trailing-edge "flatback" airfoils have been designed to address both the structural and aerodynamic performance of the inboard region [26, 27]. Structural advantages of flatback airfoils include a larger sectional area and increased sectional moment of inertia; aerodynamic advantages include a larger sectional maximum lift coefficient, increased lift curve slope, and reduced sensitivity to surface soiling [28].

Wirz proposed a new conceptual design for wind turbine blades that has the potential to improve the structural and aerodynamic performance of the inboard region: the biplane blade [34]. This design uses a biplane inboard region that transitions into a joint, which is connected to a monoplane outboard region. Improved structural performance of the biplane blade could allow the blade to be stiffer and lighter. It is expected that this design will be most applicable to large (3-7 megawatt) and ultra-large (8-10 megawatt) turbines for both land-based and offshore applications. An artist's conception of a biplane blade is shown in Figure 3.3.

The aero-structural advantages of this design are summarized in Figure 3.4. The slen-

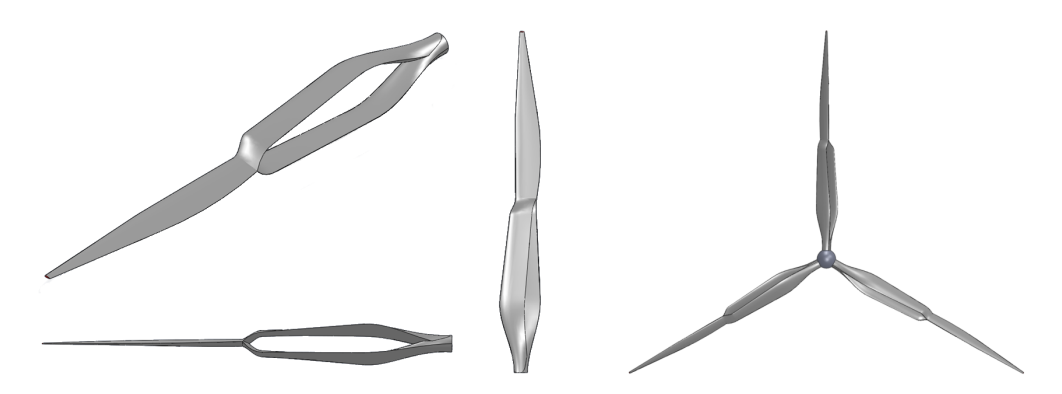


Figure 3.3: Artistic rendering for several views of a biplane blade for next-generation wind turbine blades.

der biplane airfoils improve the aerodynamic performance of the inboard region, which can increase the power produced by the blade. While the flow in the inboard region is known to be highly complex and three-dimensional [51, 52], initial two-dimensional studies have shown that biplane airfoils demonstrate improved lift-to-drag ratios, larger sectional maximum lift coefficients, and gentler stall characteristics than comparable thick monoplane airfoils [35, 37]. Other researchers also found that multi-element airfoils designed for wind turbine blades offered similar improvements [41]. If considering a cross-section, the gap between the biplane airfoils also greatly improves the second moment of area of the inboard region, which can improve the flapwise bending stiffness of the blade. Compared to a large conventional blade, a biplane blade of the same length could offer (1) less weight and cost in the rotor, as well as (2) less demand for rotor overhang, a major cost in nacelle structure. The first benefit is subject to the evaluation of material costs, as well as manufacturing costs for the biplane blade. The second benefit is subject to the evaluation of the stiffness of the biplane blade. All of these aero-structural advantages have the potential to increase the annual energy production of wind turbine blades.

While its potential benefits are compelling, the radical configuration of the biplane blade makes it challenging to design and analyze. One challenge with the concept is the design of the mid-blade joint between the inboard biplane region and the outboard monoplane region. The geometry near the joint is complex, and the flow around the joint may be highly three-dimensional. This makes it difficult to calculate the aerodynamic drag on the joint without

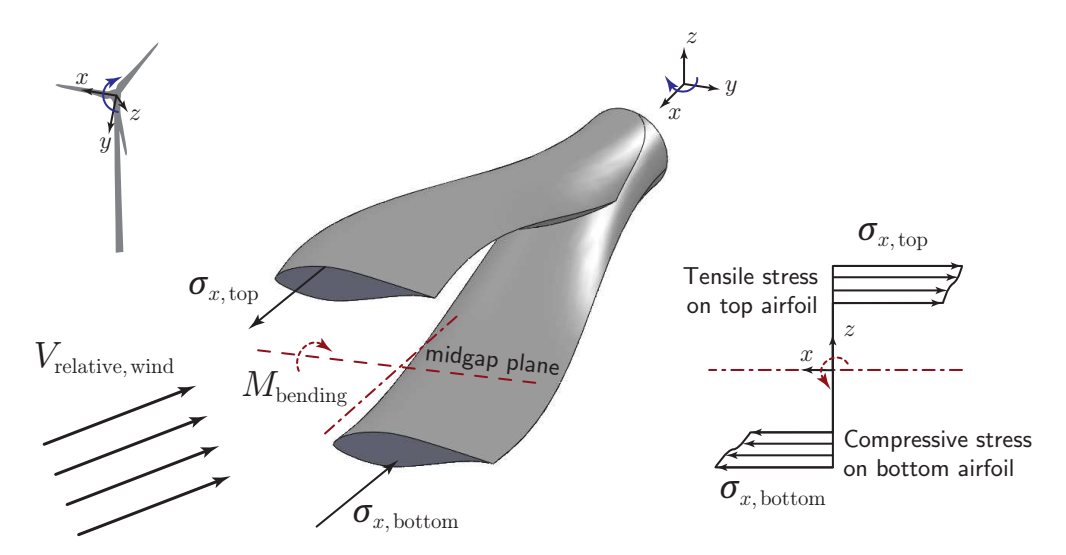


Figure 3.4: For the biplane blade, loads manifest themselves on the beam flanges similar to the behavior of an I-beam. These diagrams show a downwind view of a wind turbine rotor rotating clockwise about the z-axis (upper left), a biplane section cutout (middle), and an illustrative stress diagram resulting from bending moments about the y-axis (right). Wind is in the positive z-direction.

detailed three-dimensional computational fluid dynamics simulations. The drag forces near the joint of the biplane blade may be high; similar results were found for aerodynamic analyses of joined-wing aircraft [53]. However, for biplane wind turbine blades, this is an open research question that needs to be addressed with future studies. Another challenge with the concept is the manufacture of the blade, particularly near the mid-blade joint and the root, where the ends of the biplane region merge together. It may be possible to combine some of the design elements from (1) segmented blades [10], and (2) blades with pre-bend [54] and/or swept blades [55] to design the biplane blade for manufacturing. However, these considerations are outside the scope of this paper, but they should also be treated in future studies.

More generally, Wirz proposed that this design opens up a new paradigm for the design of large multiplane blades, as a natural extension of the concept for biplane blades. Here, "multiplane blade" refers to any blade with an inboard region that uses more than one airfoil (e.g. biplane, triplane, quadplane, etc.). If the advantages of the biplane blade are realized, then triplane blades or quadplane blades could also be investigated in the future.

It should also be noted that a key challenge with upscaling blades is that the mass of the blades increases faster than the rotor power. Assuming geometric similarity, material similarity, and constant tip speed ratio, blade mass scales with length cubed, while rotor power scales with length squared. According to these scaling laws, the edgewise bending moments (due to gravitational loads from blade mass) grow with length raised to the fourth power; flapwise bending moments (due to aerodynamic loads) grow with length raised to the third power [9]. Considering today's blades (typically about 50 meters long), aerodynamic loads are usually larger than gravitational loads. For much longer blades, edgewise bending moments due to gravitational loads will become important. Blade design innovations may be able to reduce the growth rate of blade mass and edgewise bending moments; however this is an open question for research that should be investigated in future studies. This paper focuses on the scale of 50-meter blades, where flapwise bending moments are still the principal design driver.

The objective of this effort is to develop biplane inboard configurations that improve the aero-structural performance of wind turbine blades. This paper reveals their basic aerodynamic and structural benefits separately using simple techniques.

3.2 Approach

To compare the performance of a conventional inboard section with a biplane inboard section, the structural and aerodynamic performance of a thick monoplane cross-section was compared to a biplane cross-section. As discussed in Section 3.2.1, cross-sectional properties were measured to approximately characterize the structural and aerodynamic performance. Next, as presented in Section 3.2.2, computational fluid dynamics (CFD) simulations were used to explicitly compare the aerodynamic performance of a thick monoplane to a biplane. Finally, Section 3.2.3 describes how several model beams were designed to be simple, first-order approximations of a conventional wind turbine blade and a biplane blade. Three canonical bending loads were applied to each of these model beams and the deflection of each beam was compared.

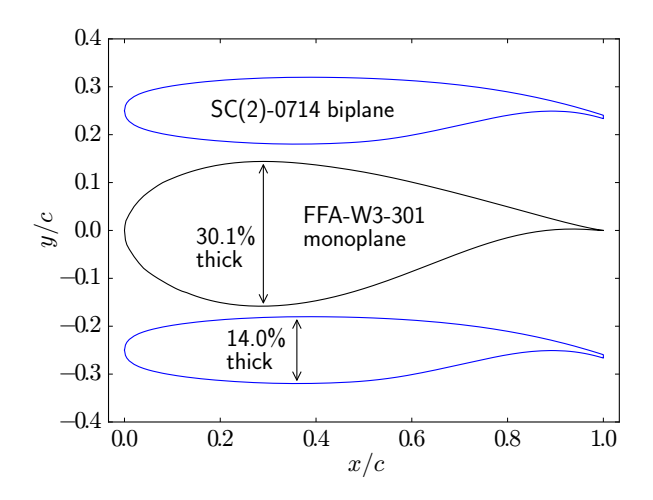


Figure 3.5: Schematic of a biplane airfoil cross-section and a thick monoplane airfoil cross-section.

3.2.1 Cross-sectional properties of a thick monoplane and biplane

To approximately characterize the structural and aerodynamic characteristics of a thick monoplane and a biplane cross-section, several cross-sectional properties were measured for two model airfoils. An FFA-W3-301 airfoil (Figure 3.5) was chosen as the thick monoplane cross-section. This airfoil has a thickness-to-chord ratio of 30.1% and is similar to those used near the root in conventional wind turbine blades [56]. An SC(2)-0714 airfoil (Figure 3.5) was used in the biplane cross-section. This airfoil has a thickness-to-chord ratio of 14.0%; thus, an SC(2)-0714 biplane using two of these airfoils has a total thickness-to-chord ratio of 28.0%, roughly equal to that of an FFA-W3-301 monoplane. In this preliminary analysis, however, the SC(2)-0714 airfoil was not chosen for its aerodynamic properties, but instead for its structural shape. This airfoil is designed to operate in the transonic regime [57], which is well beyond the subsonic regime of wind turbine aerodynamics in the inboard region. However, because the box-like profile of the SC(2)-0714 airfoil is more similar to the rectangular shape of I-beam flanges than other airfoils, it was expected that this airfoil would have large principle area moments of inertia. It was also expected that the smaller thickness-to-chord ratio of the SC(2)-0714 airfoil would create less pressure drag than the thicker FFA-W3-301 airfoil. Therefore, this airfoil was used in both this cross-sectional analysis, as well as a comparative aerodynamic analysis described in Section 3.2.2.

Three cross-sectional properties were measured for the thick monoplane and the biplane cross-sections: the second moments of area in the flapwise and edgewise directions ($I_{\rm flap}$ and $I_{\rm edge}$, respectively), the projected frontal area, and the wetted surface area. Because a cross-section's bending stiffness is proportional to its second moment of area, the second moment of area gives an approximate measure of the structural stiffness of a cross-section when subjected to bending loads. Similarly, a cross-section's pressure and viscous drag are roughly proportional to its projected frontal area and wetted surface area, respectively. Thus, the projected frontal area and wetted surface area give an approximate measure of the pressure and viscous aerodynamic drag of a cross-section. The chord length of each cross-section was c=1 m. The airfoils in the biplane cross-section were not staggered and were separated by a gap-to-chord ratio of g/c=0.5. The SolidWorks 2010 software [58] was used to calculate these properties, assuming the airfoils in each cross-section were made of a solid material with density $\rho=2.0\times 10^3$ kg/m³. Results from this analysis are given in Section 3.3.1.

3.2.2 Aerodynamic comparison of a thick monoplane and biplane cross-section

In order to quantify the comparative aerodynamic performance of the thick monoplane cross-section and the biplane cross-section, a two dimensional (2D) CFD analysis was performed using O-grid computational domains (Figure 3.6). As before, the chord length of each cross-section was c=1 m; the airfoils in the biplane cross-section were not staggered and were separated by a gap-to-chord ratio of g/c=0.5. Both domains had a diameter of 21 chord lengths, so that incompressible viscous calculations could accurately model the flow far away from the cross-section. A velocity-inlet boundary condition was used along the left edge of each domain to define the upstream flow velocity. An outflow boundary condition was used along the right edge of each domain to extrapolate the downstream flow properties from the domain interior. Wall boundary conditions were used along each airfoil.

Two structured grids were generated for each domain with Gridgen 15.06 (Figure 3.7). The thick monoplane used an O-grid with 131,072 cells. The biplane used an H-grid between

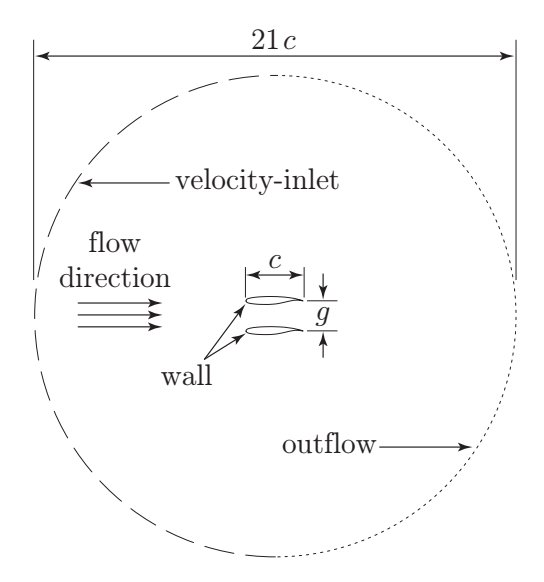


Figure 3.6: Geometry of the biplane cross-section, shown with numerical boundary conditions. Note: figure not to scale.

each airfoil and an O-grid for the surrounding far-field region; the entire grid used 151,500 cells. In both grids, cells were concentrated near the airfoil walls, where large gradients in the flow exist from the boundary layer.

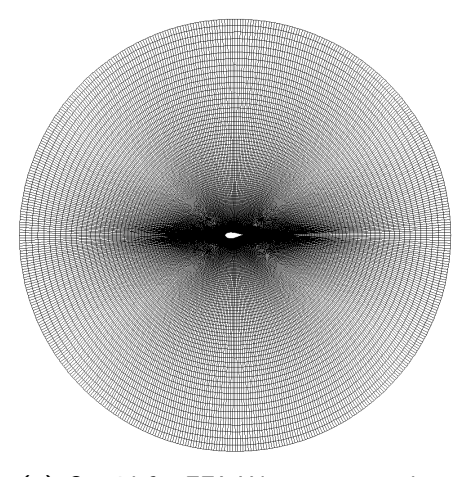
Steady-state, incompressible viscous CFD calculations were performed with the Fluent 6.3.26 software [59]. CFD was used to implicitly solve the pressure-based Navier-Stokes equations in 2D, such that

$$\nabla \cdot \mathbf{V} = 0 \tag{3.1}$$

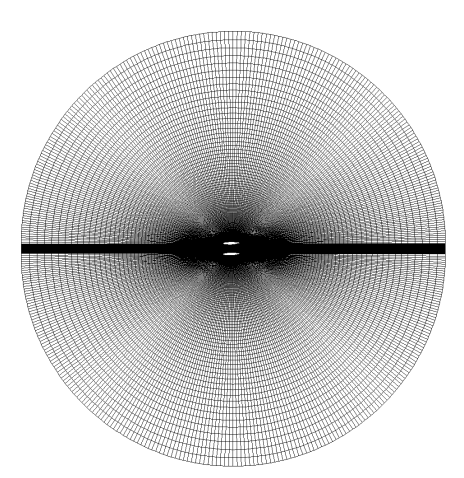
$$\rho\left(\mathbf{V}\cdot\nabla\mathbf{V}\right) = -\nabla p + \mu\nabla^{2}\mathbf{V},\tag{3.2}$$

where V is the velocity vector, p is the pressure, and μ is the dynamic viscosity of the fluid. Turbulent viscosity was modeled with the one-equation Spalart-Allmaras model [60]. The solution scheme was second-order accurate in space.

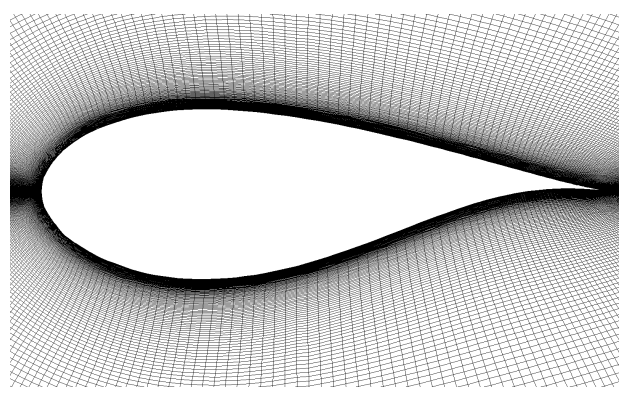
All flow conditions in the numerical simulation were for air at atmospheric pressure $p_{\rm atm} = 1.01325 \times 10^5$ Pa, density $\rho = 1.225$ kg/m³, and viscosity $\mu = 1.7894 \times 10^{-5}$ kg/(m·s). All simulations had a Reynolds number of $Re = 1.479 \times 10^6$ and a freestream velocity of $V_{\infty} = 21.6$ m/s. The flow over the thick monoplane was computed at angles of attack



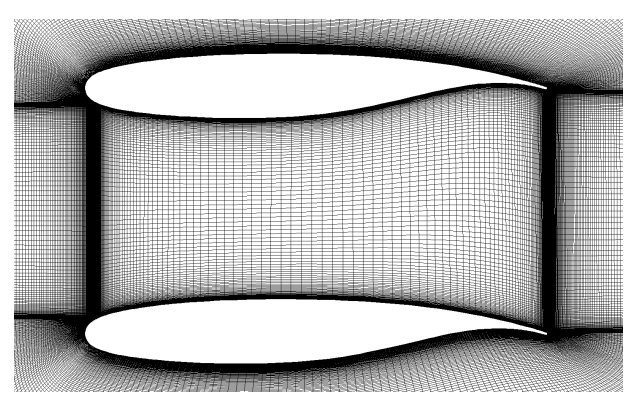
(a) O-grid for FFA-W3-301 monoplane.



(c) O-grid for SC(2)-0714 biplane.



(b) Clustered grid points near FFA-W3-301 monoplane.



(d) Clustered grid points and H-grid between SC(2)-0714 biplane.

Figure 3.7: Computational grids for preliminary aerodynamic analysis.

Table 3.1: Definition of design parameters for the biplane blade.

Parameter name	Symbol	Description
Chord	c	Length from leading edge to trailing edge
Gap	g	Length between upper and lower chord lines
Span	R	Length from blade root to tip
Joint length	r_{j}	Length from blade root to joint
Transition length	r_t	Length of transition from biplane to monoplane

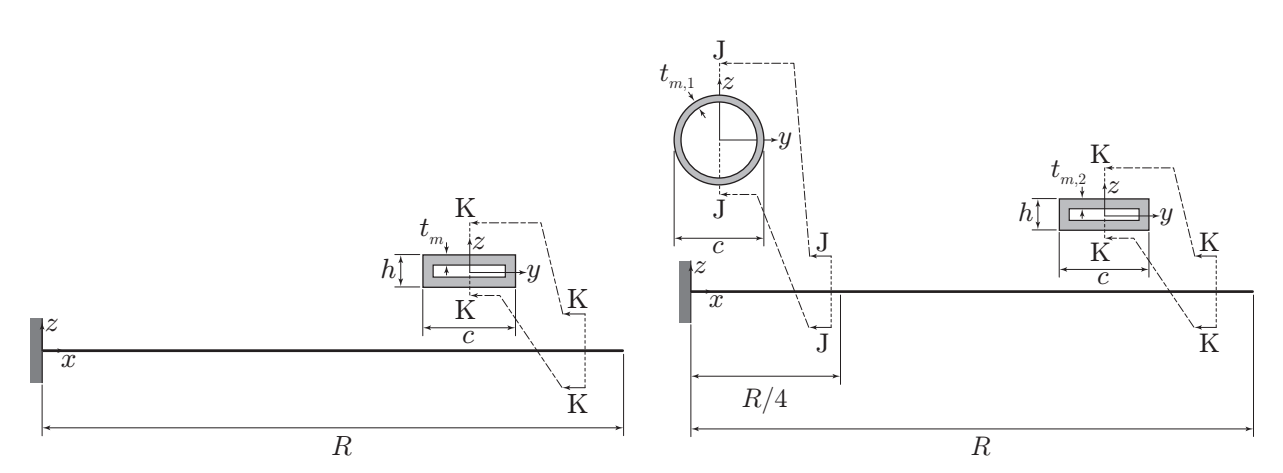
between $0^{\circ} \leq \alpha \leq 15.5^{\circ}$; the flow over the biplane was computed between $0^{\circ} \leq \alpha \leq 15.3^{\circ}$. Convergence criteria of 10^{-3} were used for all computed solutions.

3.2.3 Structural comparison of monoplane beams and biplane beams

Several model beams (Figure 3.8) were designed to be simple, first-order approximations of a conventional wind turbine blade ("monoplane beam") and a biplane blade ("biplane beam"). Design parameters for the biplane beam are defined in Table 3.1. Three canonical types of bending load profiles were applied to the model beams (Figure 4.14), and the deflection of each beam was calculated. These deflections were calculated with a 1D beam finite element analysis, and validated with a fully 3D finite element analysis. The 1D analysis was used to quickly explore the effect of three non-dimensional design parameters (referring to Figure 3.8(c): the joint length-to-span ratio r_j/R , the transition length-to-joint length ratio r_t/r_j , and the gap-to-chord ratio g/c) on the tip deflection of the biplane beam. The results from this parametric analysis are given in Section 4.3.2.3.

3.2.3.1 Design of model beams

In order to quickly evaluate the effect of several design parameters on structural performance, simplified representations of a biplane blade were designed. For this initial study, tapering of the cross-section along the span of the beam was not considered (the cross-sectional area, chord length c=1 m, and height h=0.35 m were kept constant from root to tip). Composite materials were also not considered. An isotropic material that approximated aluminum was



(a) Monoplane beam, rectangular cross-section (1D (b) Monoplane beam, 25% circular - 75% rectangular schematic).

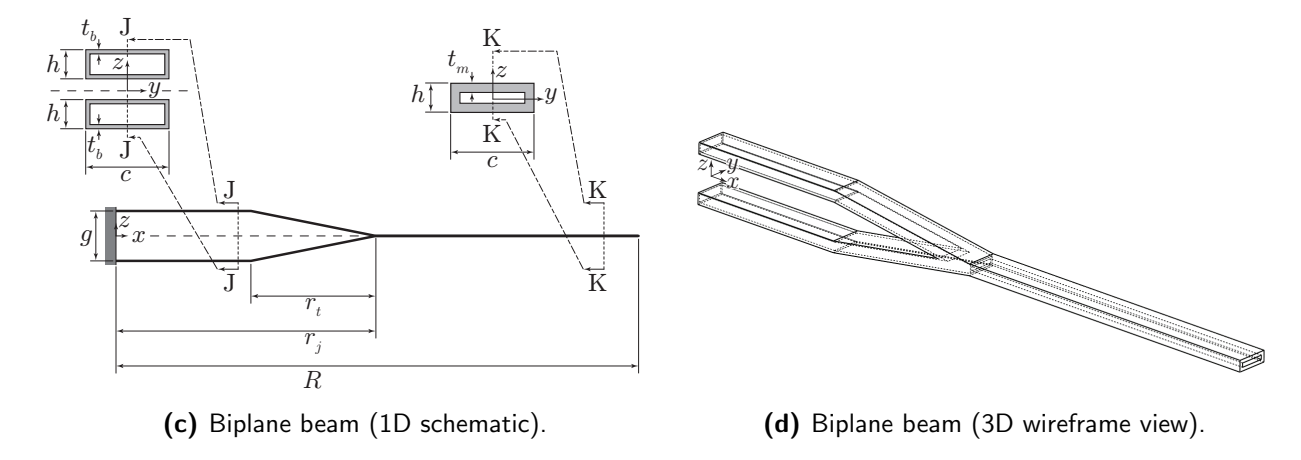


Figure 3.8: Model beams for preliminary structural analysis.

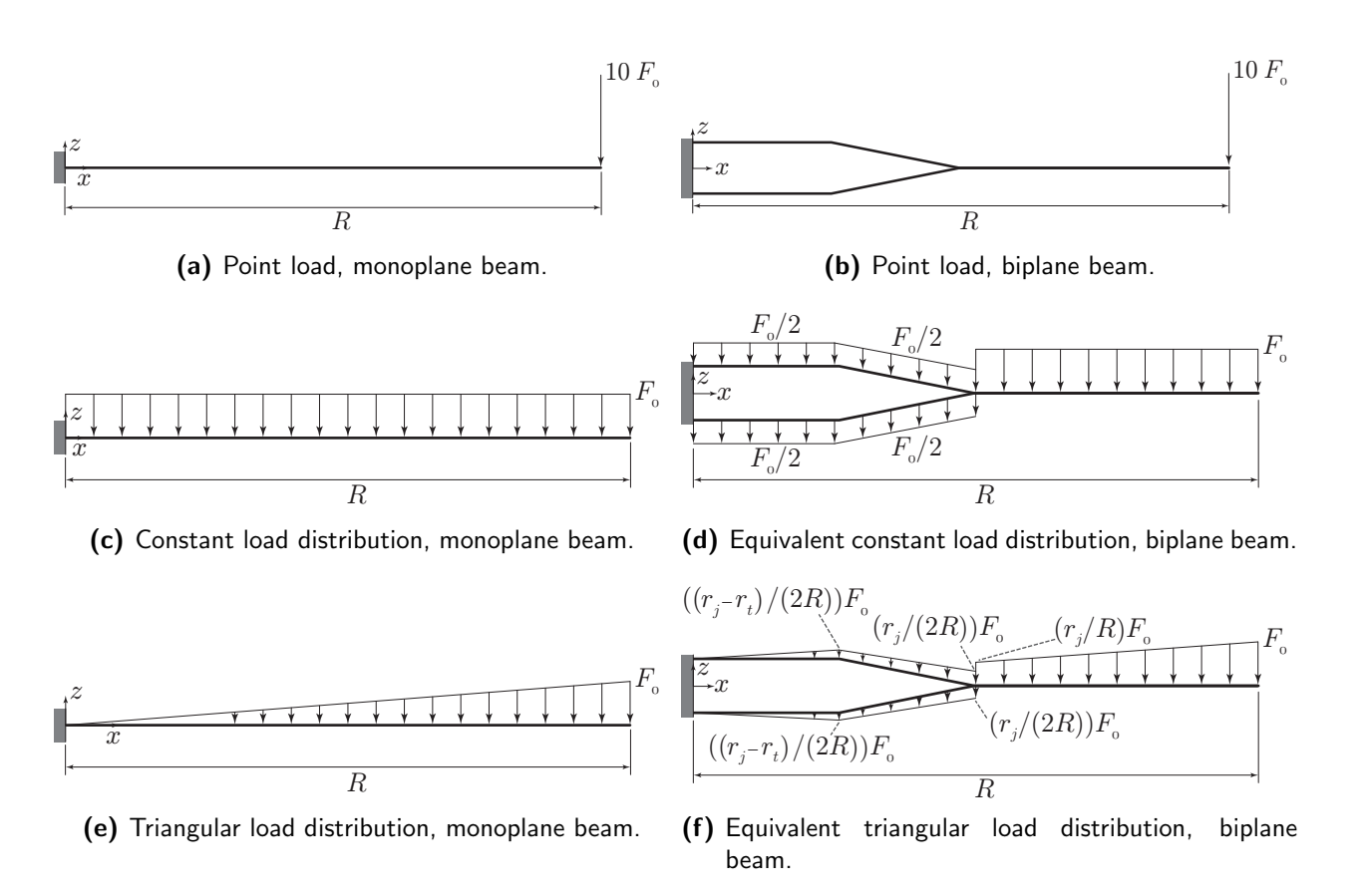


Figure 3.9: Load profiles applied to model beams.

used for all beams (Young's modulus $E = 5.0 \times 10^{10}$ Pa, Poisson's ratio $\nu = 0.3$, and density $\rho = 2.0 \times 10^3$ kg/m³). Because weight is one of the important limiting parameters that determines the length of wind turbine blades [19], all beams had equal cross-sectional areas, and hence, equal mass per unit length. This allowed for a self-consistent comparison between their structural performance.

Monoplane beam, hollow rectangular cross-section: A monoplane beam with a hollow rectangular cross-section (Figure 3.8(a)) was constructed to mimic the "box beam" structure typically used for the spars in conventional wind turbine blades [9]. The rectangular cross-section had a wall thickness-to-chord ratio of $t_m/c = 11.08\%$.

Monoplane beam, 25% circular - 75% rectangular cross-section: Another monoplane beam (Figure 3.8(b)) with a hollow circular cross-section in the inboard region ($0 \le x \le R/4$) and the same rectangular cross-section in the outboard region ($R/4 \le x \le R$) was constructed to mimic the cylindrical root section of conventional blades. The circular cross-section had a wall thickness-to-chord ratio of $t_{m,1}/c = 8.72\%$; the rectangular cross-section had $t_{m,2}/c = 11.08\%$.

Biplane beam: A biplane beam (Figures 3.8(c) and 3.8(d)) was also constructed to mimic the "box beam" structure that would be used in a biplane blade. For this analysis, the beam was symmetric about the xy-plane. The monoplane outboard region ($r_j < x < R$) used the same rectangular cross-section ($t_m/c = 11.08\%$) as the first monoplane beam. The biplane inboard region ($0 < x < r_j$) used a rectangular cross-section with thinner walls ($t_b/c = 5.0\%$ wall thickness-to-chord ratio). The area of this thinner-walled cross-section was half of the area of the thicker-walled cross-section. This kept the weight of the biplane beam equal to the weight of both monoplane beams.

3.2.3.2 Load profiles and boundary conditions

To approximate the flapwise bending moment (the primary load on wind turbine blades [51]), three canonical bending load profiles were applied to the model beams: a point load, a constant load distribution, and a triangular load distribution (Figure 4.14). The point

load magnitude was 10,000 N ($F_o = 1000$). The maximum magnitude of the constant and triangular load distributions was 1,000 N/m. In particular, the triangular load distribution was chosen to approximate the load distribution that develops on a wind turbine blade during operation (largest loads near the tip and smallest loads near the root). To load the monoplane beams and the biplane beam in an equivalent manner, it was assumed that the loads on the biplane inboard region of the biplane beam were equally distributed among the upper and lower beams (Figures 3.9(f) and 4.14(b)). All beams were cantilevered at the root (x = 0 m) and free at the tip (x = R = 50 m).

3.2.3.3 Validation of 1D beam finite element analysis

Both 1D beam and 3D tetrahedral finite elements were used to carry out a linear static analysis on both monoplane beams and one biplane beam configuration. This validation study was conducted to determine if the 1D models of these beams (Figure 3.10(a)) were accurate, when compared to the 3D models of these beams (Figure 3.10(b)). In particular, the authors wanted to ensure that the region near the joint of the biplane beam could be modeled accurately with 1D beam elements. The biplane beam used for this validation study had a joint length-to-span ratio of $r_j/R = 0.6$, a transition length-to-joint length ratio of $r_t/r_j = 0.6$, and a gap-to-chord ratio of g/c = 2.0. Each of the load profiles described in Section 3.2.3.2 was applied to each beam. In the 1D models, the 3D structure of each beam was approximated with 1D beam finite elements. In the 3D models, the 3D structure of each beam was approximated with 3D tetrahedral finite elements. Results from this validation study are given in Section 3.3.3.1.

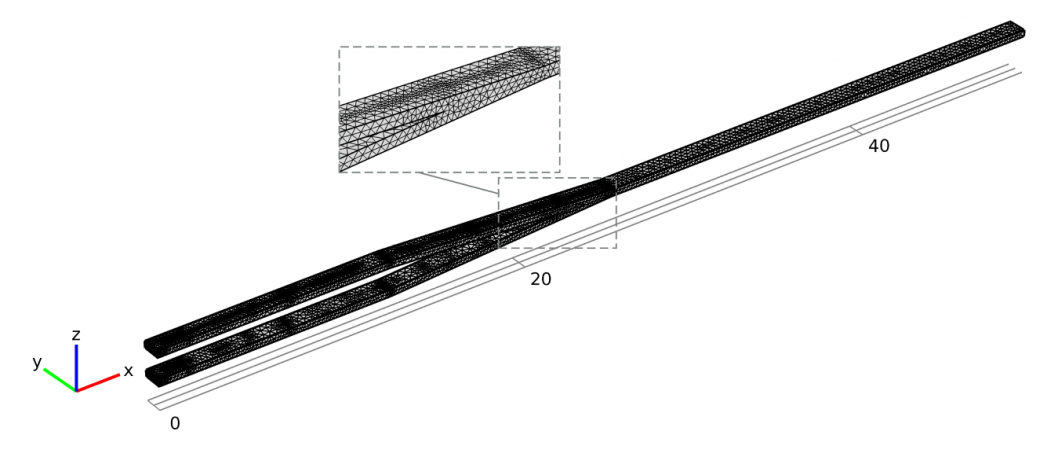
For the 1D models, each beam was modeled with 3rd-order 1D Timoshenko beam finite elements (Figure 3.10(a)) in DYMORE 3.0, a flexible multibody dynamics finite element program [61, 62]. For this linear static analysis, DYMORE solved the equation

$$[S]\{\mathbf{q}\} = \{\mathbf{f}\},\tag{3.3}$$

where q is the vector of all the degrees of freedom, and f is the vector of externally applied



(a) Biplane beam discretized with 1D beam finite elements.



(b) Biplane beam discretized with 3D tetrahedral finite elements.

Figure 3.10: Computational meshes used for finite element analysis.

forces.

The 2D cross-sectional properties of these beam elements were calculated with the VABS 3.4 software [63, 64], also known as Variational Asymptotic Beam Sectional analysis. VABS uses the variational asymptotic method [65, 66] to accurately calculate the mass and stiffness matrices for arbitrary beam cross-sections. The 6×6 mass matrix [M] can be determined from the equation for the kinetic energy density K, such that

where K is the kinetic energy density, V is the linear velocity, Ω is the angular velocity, $\tilde{\mu}$ is the mass per unit length, x is the distance from the root, y is the distance from the leading

edge, z is the distance from the chord line, and i is the mass moment of inertia. Symbols with a subscripted 1, 2, or 3 refer to properties along the beam reference line, the chord line in the cross-sectional plane, or the thickness line in cross-sectional plane, respectively.

VABS uses a generalized Timoshenko beam model [67], whose 6×6 stiffness matrix [S] can be determined from the equation for the strain energy density U, such that

$$U = \frac{1}{2} \left\{ \begin{array}{c} \gamma_{11} \\ 2\gamma_{12} \\ 2\gamma_{13} \\ \kappa_{1} \\ \kappa_{2} \\ \kappa_{3} \end{array} \right\} \left\{ \begin{array}{c} S_{11} & S_{12} & S_{13} & S_{14} & S_{15} & S_{16} \\ S_{12} & S_{22} & S_{23} & S_{24} & S_{25} & S_{26} \\ S_{13} & S_{23} & S_{33} & S_{34} & S_{35} & S_{36} \\ S_{14} & S_{24} & S_{34} & S_{44} & S_{45} & S_{46} \\ S_{15} & S_{25} & S_{35} & S_{45} & S_{55} & S_{56} \\ S_{16} & S_{26} & S_{36} & S_{46} & S_{56} & S_{66} \end{array} \right\} \left\{ \begin{array}{c} \gamma_{11} \\ 2\gamma_{12} \\ 2\gamma_{13} \\ \kappa_{1} \\ \kappa_{2} \\ \kappa_{3} \end{array} \right\}, \tag{3.5}$$

where U is the strain energy density, γ is the strain, κ is the curvature, and S_{ij} are the entries in the generalized Timoshenko stiffness matrix.

DYMORE and VABS were selected as structural analysis tools because they are fast [67, 68], and they have successfully modeled helicopter blades [69, 61, 70] and wind turbine blades [71, 72, 73, 68]. Furthermore, several researchers have also used 1D beam finite elements to model a joined wing structure [74, 75, 76, 77].

For the 3D models, each beam was modeled with 3D tetrahedral finite elements (Figure 3.10(b)) in the Structural Mechanics module of COMSOL Multiphysics 4.1.0.88 [78]. For this linear static analysis, COMSOL also solved Equation (3.3). Again, note that this 3D analysis was conducted to validate the 1D analysis, so that DYMORE and VABS could be confidently used to quickly analyze several different biplane beam configurations (as described in Section 4.3.2.3).

3.3 Results

3.3.1 Cross-sectional properties of a thick monoplane and biplane

The FFA-W3-301 thick monoplane cross-section has second moments of area $I_{\rm flap}=8.202\times 10^{-4}~{\rm m}^4$ and $I_{\rm edge}=7.848\times 10^{-3}~{\rm m}^4$, a projected frontal area of 0.301 square meters per unit span, and a wetted surface area of 2.168 square meters per unit span. The SC(2)-0714 biplane cross-section has second moments of area $I_{\rm flap}=1.165\times 10^{-2}~{\rm m}^4$ and $I_{\rm edge}=1.288\times 10^{-2}~{\rm m}^4$, a projected frontal area of 0.280 square meters per unit span, and a wetted surface area of 4.134 square meters per unit span. In the flapwise direction, the second moment of area for the biplane is about one order of magnitude (1320%) greater than the thick monoplane. In the edgewise direction, the second moment of area for the biplane is about 64% greater than the thick monoplane. The projected frontal area of the biplane is slightly less than the frontal area of the thick monoplane. Finally, the wetted surface area of the biplane is nearly twice that of the thick monoplane. Two of the three cross-sectional properties for the biplane are better than those for the thick monoplane; this motivates further comparisons of the two cross-sections with CFD, as well as a structural comparison of monoplane and biplane beams.

3.3.2 Aerodynamic comparison of a thick monoplane and biplane cross-section

Lift and drag coefficients of both the thick monoplane and biplane were calculated from the integrated pressure force along each of the airfoil walls. The lift and drag coefficients calculated with CFD for the FFA-W3-301 thick monoplane were then compared to experimental data [56]. The pressure and viscous parts of the lift and drag data were also reported from CFD to study the effect of the biplane's increased surface area on viscous drag. Finally, the lift-to-drag ratio at each angle of attack was calculated to compare the aerodynamic efficiency of the thick monoplane and the biplane.

Numerical and experimental results for the FFA-W3-301 thick monoplane match well for angles of attack between $0^{\circ} < \alpha \lesssim 10^{\circ}$ (Figure 3.11). Above this range, CFD calculations

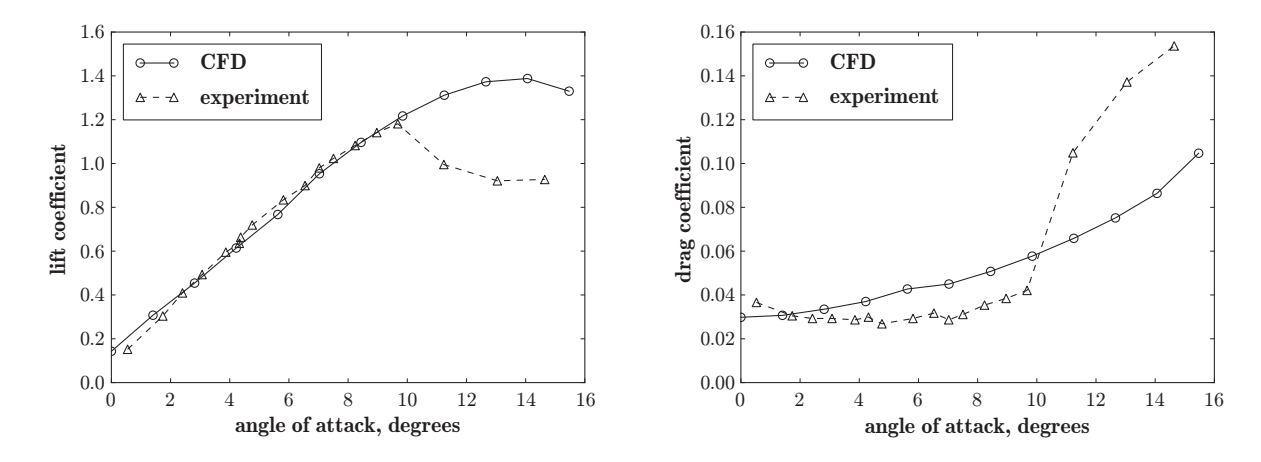
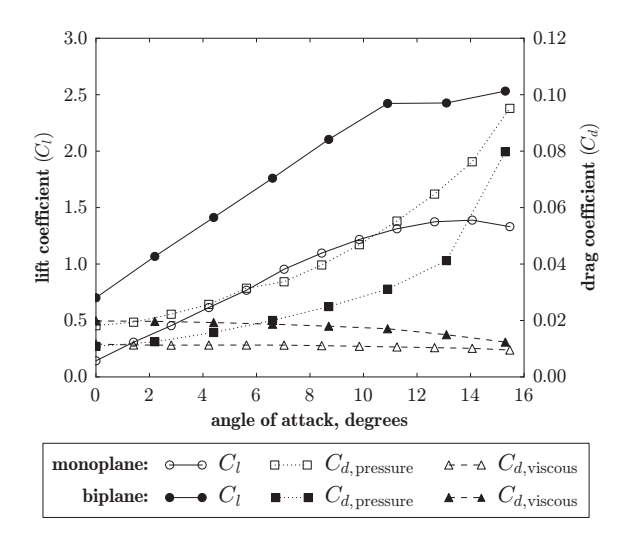
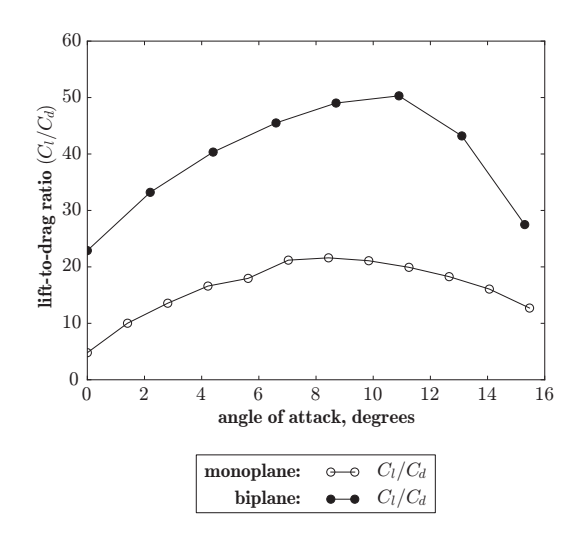


Figure 3.11: Comparison of lift and drag coefficients for the FFA-W3-301 thick monoplane, calculated by CFD and measured from experiments conducted by Fuglsang et al. [56].

did not predict lift and drag coefficients measured in wind tunnel experiments [56]. The CFD results predict that the FFA-W3-301 thick monoplane would stall near $\alpha \approx 14^{\circ}$, while experimental measurements show an earlier stall near $\alpha \approx 10^{\circ}$. Thus, the CFD results overpredict the lift and underpredict the drag when $\alpha \gtrsim 10^{\circ}$. CFD also slightly overpredicts the drag when $3^{\circ} \lesssim \alpha \lesssim 10^{\circ}$.

Overall, CFD calculations show that the SC(2)-0714 biplane outperforms the FFA-W3-301 thick monoplane for angles of attack between $0^{\circ} \leq \alpha \leq 15.5^{\circ}$ (Figure 3.12). The lift generated by the biplane for each angle of attack is always greater than the lift generated by the thick monoplane (Figure 3.12(a)). The pressure drag on the biplane is always smaller than the pressure drag on the thick monoplane. Although the viscous drag on the biplane is always greater than the viscous drag on the thick monoplane, the total drag for the biplane is always less than the total drag for the thick monoplane. As a result, the lift-to-drag ratio of the biplane is always greater than the lift-to-drag ratio of the thick monoplane (Figure 3.12(b)). However, the results for angles of attack $\alpha \gtrsim 10^{\circ}$ in Figure 3.12 may be inaccurate because, as mentioned earlier, numerical and experimental results for the thick monoplane only match well for angles of attack between $0^{\circ} \leq \alpha \lesssim 10^{\circ}$ (Figure 3.11).





- (a) Coefficients for lift, pressure drag, and viscous drag of a thick monoplane and biplane at different angles of attack.
- **(b)** Lift-to-drag ratios of a thick monoplane and biplane at different angles of attack.

Figure 3.12: Aerodynamic performance of a thick monoplane and a biplane cross-section. Forces on each cross-section were integrated with Fluent CFD.

3.3.3 Structural comparison of monoplane beams and biplane beams

3.3.3.1 Validation of 1D beam finite element analysis

Both monoplane beams and one biplane beam configuration (joint length-to-span ratio of $r_j/R=0.6$, transition length-to-joint length ratio of $r_t/r_j=0.6$, and gap-to-chord ratio of g/c=2.0) were used to validate the 1D beam finite element analysis against a 3D finite element analysis for each of the load profiles described in Section 3.2.3.2. Figure 3.13 shows the deflections calculated by both analyses. For the point load, the tip deflections calculated by each approach for the point load differ by 0.27% (monoplane beam, hollow rectangular cross-section), 8.48% (monoplane beam, 25% circular - 75% rectangular cross-section), and 2.76% (biplane beam). For the constant load distribution, the tip deflections differ by 0.64% (monoplane beam, rectangular cross-section), 10.17% (monoplane beam, 25% circular - 75% rectangular cross-section), and 3.42% (biplane beam). For the triangular load distribution, the tip deflections differ by 0.38% (monoplane beam, rectangular cross-section), 9.79% (monoplane beam, 25% circular - 75% rectangular cross-section), and 3.31% (biplane beam). Although the tip deflections of the monoplane beam with 25% circular - 75% rect-

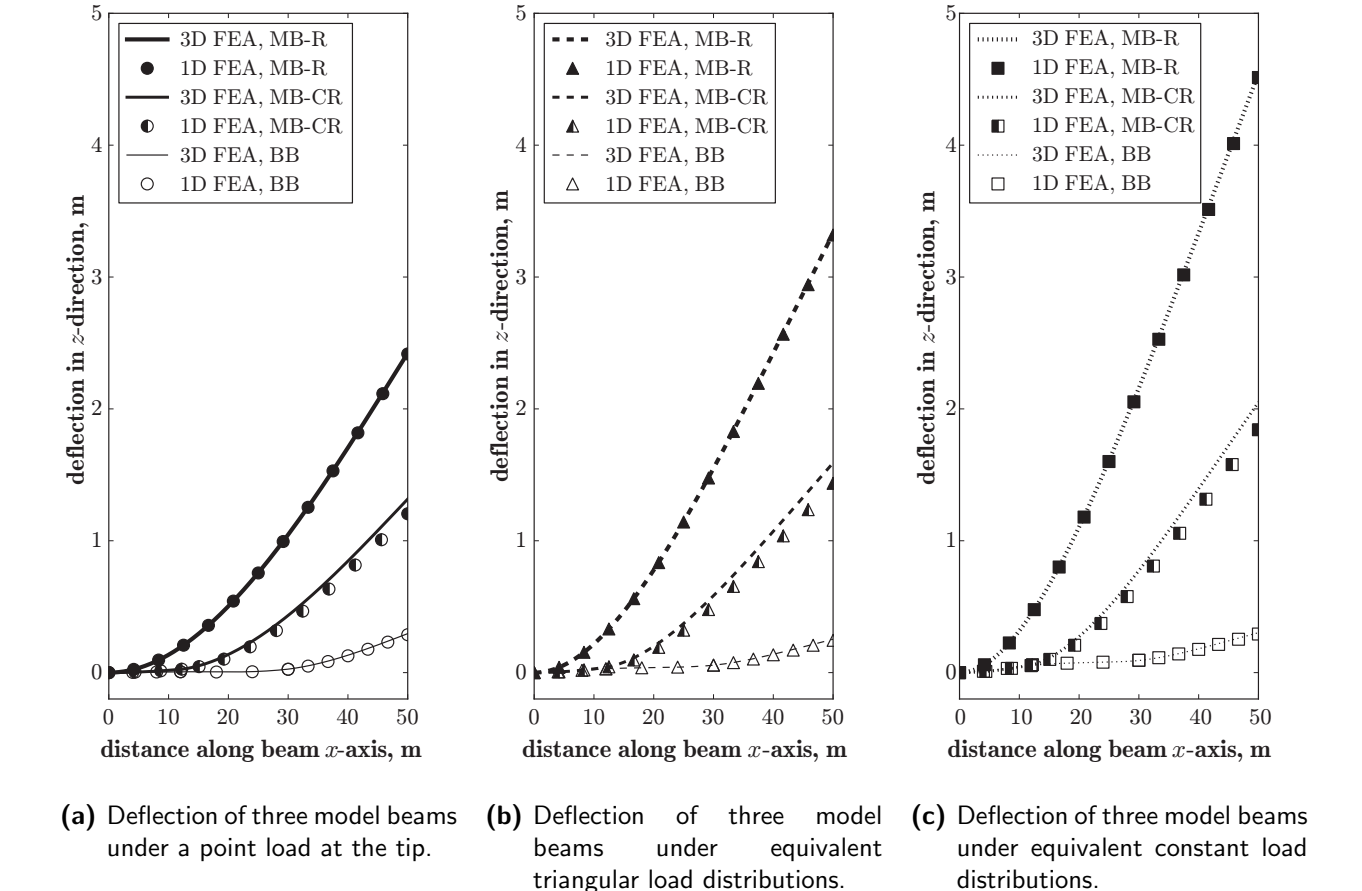


Figure 3.13: Comparison of beam deflections under various load profiles, calculated with DY-MORE (1D FEA) and COMSOL (3D FEA): a monoplane beam with a rectangular cross-section (MB-R); a monoplane beam with 25% circular - 75% rectangular cross-section (MB-CR); and a biplane beam with design parameters g/c=2.0, $r_j/R=0.6$, and $r_t/r_j=0.6$ (BB).

angular cross-section have higher errors than the other two model beams, the results still show decent agreement between the 1D and 3D approaches. The disagreement is likely due to the sharp gradient in this beam's cross-sectional properties at x = R/4, which cannot be resolved well by the mesh of 1D beam elements. For a triangular load distribution, which approximates the loading on a wind turbine blade during operation, the tip deflection of the biplane blade is less than 30% of the tip deflection of a monoplane blade (Figure 3.13(b)).

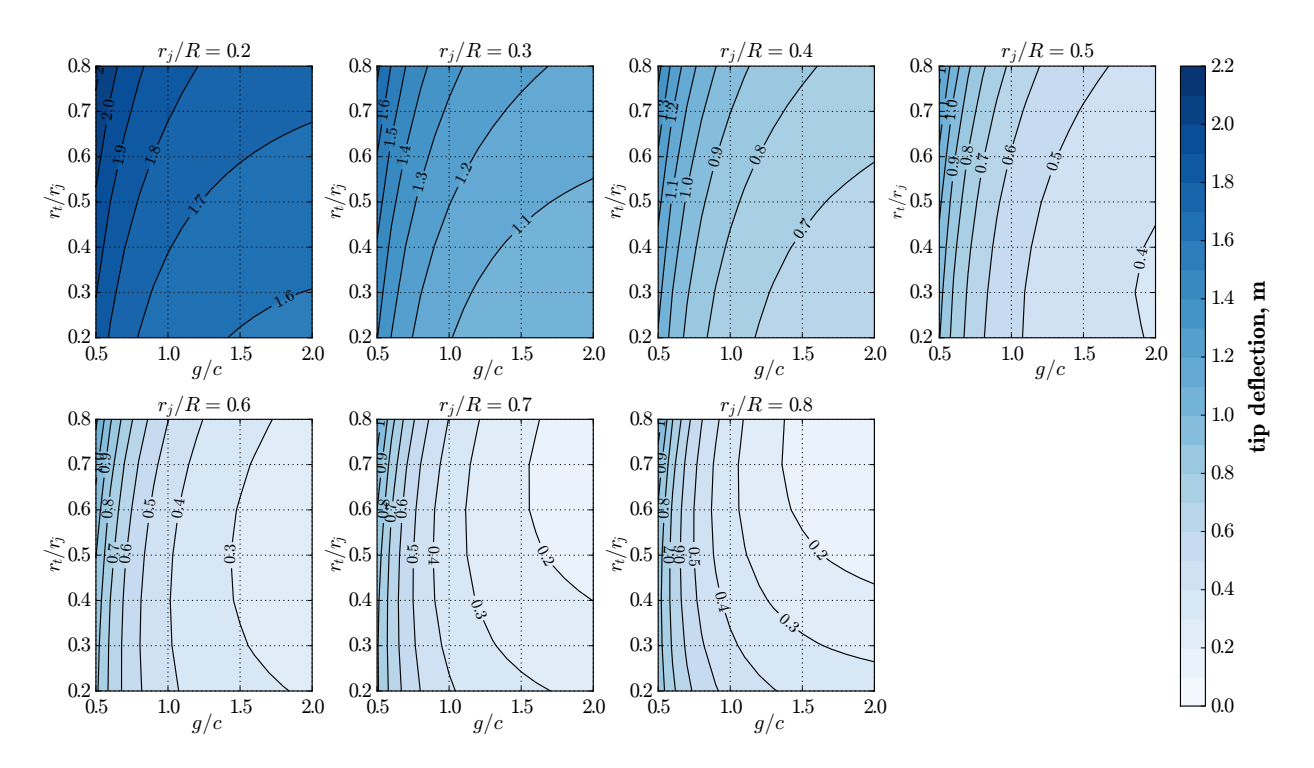


Figure 3.14: Effect of three design parameters (joint length-to-span ratio r_j/R , transition length-to-joint length ratio r_t/r_j , and gap-to-chord ratio g/c) on the tip deflection of a biplane beam under a triangular load distribution. Lighter filled contours show smaller tip deflections.

3.3.3.2 Parametric analysis of different biplane beam configurations

Several biplane beam configurations were constructed by varying three non-dimensional design parameters (joint length-to-span ratios of $r_j/R = 0.2, 0.3, \dots 0.8$; transition length-to-joint length ratios of $r_t/r_j = 0.2, 0.3, \dots 0.8$; and gap-to-chord ratios of $g/c = 0.5, 0.6, \dots 2.0$), while the span R = 50 m was held constant. From all the permutations of these three parameters, 784 biplane beam configurations were constructed. Three load profiles (described in Section 3.2.3.2) were applied to each biplane beam configuration, and DY-MORE was used to calculate the tip deflections. The effect of three non-dimensional design parameters (joint length-to-span ratio r_j/R , transition length-to-joint length ratio r_t/r_j , and gap-to-chord ratio g/c) on the tip deflection of all 784 biplane beam configurations was evaluated (Figure 4.25).

Overall, tip deflections decrease as the joint length-to-span ratio r_j/R increases. For

a given joint length-to-span ratio r_j/R , tip deflections always decrease as the gap-to-chord ratio g/c increases. When $0.2 \le r_j/R \le 0.4$, tip deflections decrease as the transition length-to-joint length ratio r_t/r_j decreases. However, for $0.5 \le r_j/R \le 0.8$, tip deflections show a dependence on both the transition length-to-joint length ratio r_t/r_j and the gap-to-chord ratio g/c. When the gap-to-chord ratio g/c is small (≈ 0.5), tip deflections decrease slightly as the transition length-to-joint length ratio r_t/r_j decreases. When the gap-to-chord ratio g/c is large (≈ 2.0), tip deflections sometimes increase as the transition length-to-joint length ratio r_t/r_j decreases. As the joint length-to-span ratio r_j/R increases, the tip deflection is more likely to depend on the transition length-to-joint length ratio r_t/r_j across a wider range of gap-to-chord ratios g/c. For example, at a joint length-to-span ratio of $r_j/R = 0.5$, this behavior is seen when $1.9 \lesssim g/c \le 2.0$, but at $r_j/R = 0.8$, this behavior is seen for a much wider range of $0.75 \lesssim g/c \le 2.0$. Only results from the triangular load distribution are shown in Figure 4.25. Results from other load profiles gave similar results and are not shown.

3.4 Conclusion

The results show that the biplane blade significantly improves both the aerodynamic and structural characteristics of the blade. As discussed in Section 3.3.1, it was expected that the smaller thickness-to-chord ratio of the SC(2)-0714 airfoil would create less pressure drag than the thicker FFA-W3-301 airfoil. This aerodynamic benefit was confirmed in Section 3.3.2, where CFD calculations show that the lift-to-drag ratio of the biplane is much greater than the lift-to-drag ratio of the thick monoplane for the angles of attack investigated (0–15.5°). Although the projected frontal areas of the biplane and thick monoplane are about equal, the biplane has less pressure drag than the thick monoplane because the biplane configuration splits the frontal area between two separate airfoils. The biplane also has less total drag than the thick monoplane, despite having nearly twice the wetted surface area of the thick monoplane and more viscous drag. As presented in Section 3.3.1, the second moment of area for the biplane was about one order of magnitude greater than those for the thick monoplane in the flapwise direction. This structural benefit was confirmed in Section 3.3.3

through a comparison of monoplane and biplane beams. For a triangular load distribution, which approximates the loading on a wind turbine blade during operation, the tip deflection of the biplane beam is less than 30% of the tip deflection of a monoplane beam. A parametric analysis of different biplane beam configurations shows that tip deflections of biplane beams are reduced overall as each of the design parameters (joint length-to-span ratio r_j/R , transition length-to-joint length ratio r_t/r_j , and gap-to-chord ratio g/c) are increased.

The aerodynamic and structural benefits described above suggest that the biplane blade is an attractive design for the next generation of large wind turbine blades. Aerodynamic performance improvements to the inboard region can lower the cut-in wind speed at which a needed to start rotating a wind turbine rotor. Structural performance improvements indicate that for a monoplane blade of fixed length, it is likely possible to construct a *lighter* biplane blade with an *equal* tip deflection. These benefits can lead directly to weight reductions for large blades that can reduce the cost of the blades, the gravitational loads on the blades, as well as the inertial loads on the rest of the wind turbine. Thus, it is likely that this design will be significant for large (3-7 megawatt) and ultra-large (8-10 megawatt) turbines for both land-based and offshore applications.

3.4.1 Outlook & future work

Aerodynamic work will continue with CFD to obtain validated results up through high angles of attack. The differences between the results from CFD and experiments at high angles of attack are likely due to the choice of the Spalart-Allmaras turbulence model. It has been shown that this model is prone to give nonphysical results at high angles of attack when the flow becomes separated from the airfoil surface [59]. In the future, wind tunnel experiments will also be conducted on biplane cross-sections up through high angles of attack. This paper only considered one biplane configuration (gap-to-chord ratio g/c = 0.5, without stagger), but further work is needed to explore the effects of varying gap and stagger on biplane performance across a range of angles of attack; at the time of writing, the authors' colleagues are performing this work with both computational and experimental methods.

This work will allow for a more accurate evaluation of the aerodynamic performance of the biplane-monoplane transition region near the mid-blade joint of the biplane blade, where the gap-to-chord ratio varies from $2.0 \le g/c \le 0.0$. The flow around the joint is also expected to be highly complex and three-dimensional. The drag forces near the joint of the biplane blade may be high because similar results were found for aerodynamic analyses of joined-wing aircraft [53]. However, effect of the joint's drag on the performance of the biplane blade is not yet clear and needs to be addressed with 3D CFD studies in the future.

Structural work will be extended to construct more accurate models of monoplane and biplane blades with realistic geometries and composite layups, and to load these models under actual operating conditions (including loads in both the flapwise and edgewise directions). These loads can be obtained from wind turbine Blade Element Momentum codes [51]. The finite element analysis can also be extended to measure internal stresses, perform dynamic simulations, calculate buckling modes, and analyze centrifugal loading under rotation of the biplane beam. Overall, this paper lays a foundation for future side-by-side comparisons of monoplane and biplane blades at a fixed multi-megawatt scale and rotor diameter, which will include loads, structural design, materials, and manufacturing aspects.

CHAPTER 4

Structural design of spars for 100-meter biplane wind turbine blades

Large wind turbine blades are being developed at lengths of 75-100 meters, in order to improve energy capture and reduce the cost of wind energy. Bending loads in the inboard region of the blade make large blade development challenging. The "biplane blade" design was proposed to use a biplane inboard region to improve the design of the inboard region and improve overall performance of large blades. This paper focuses on the design of the internal "biplane spar" structure for 100-meter biplane blades. Several spars were designed to approximate the Sandia SNL100-00 blade ("monoplane spar") and the biplane blade ("biplane spar"). Analytical and computational models are developed to analyze these spars. The analytical model used the method of minimum total potential energy; the computational model used beam finite elements with cross-sectional analysis. Simple load cases were applied to each spar and their deflections, bending moments, axial forces, and stresses were compared. Similar performance trends are identified with both the analytical and computational models. An approximate buckling analysis shows that compressive loads in the inboard biplane region do not exceed buckling loads. A parametric analysis shows biplane spar configurations have 25-35% smaller tip deflections and 75% smaller maximum root bending moments than monoplane spars of the same length and mass per unit span. Root bending moments in the biplane spar are largely relieved by axial forces in the biplane region, which are not significant in the monoplane spar. The benefits for the inboard region could lead to weight reductions in wind turbine blades. Innovations that create lighter blades can make large blades a reality, suggesting that the biplane blade may be an attractive design for large (100-meter) blades.

4.1 Introduction

In order to improve energy capture and reduce the cost of wind energy, wind turbines have grown dramatically over time. Longer blades are being developed to enable large, multimegawatt wind turbines capture more energy. The rated power of wind turbines has grown almost linearly for the past 30 years [3, 10]. At the time of writing, a 73.5-meter blade had been manufactured for a 6-megawatt offshore wind turbine [79, 80]. Blades are expected to grow even larger in the future; current investigations include the development of a 20megawatt turbine [10] and the design of a 100-meter blade [9]. However, the development of large blades at this scale is challenging. For a simple geometric upscaling of a blade and assuming a constant tip speed ratio, the bending stresses due to aerodynamic forces are independent of blade length, and the bending stresses due to gravitational forces increase linearly as blades get longer [9]. These bending loads are highest in the inboard region, near the root of the blade. Hence, the inboard region needs an efficient structure that can support the bending loads, provide favorable aerodynamic performance, but also limit overall blade mass (and cost). The blade cannot be too heavy, because excess blade mass increases inertial fatigue loads, which decrease the blade lifetime. Heavier blades also tend to cost more to manufacture and transport, which limits the economic benefits of large wind turbines. This paper investigates a new biplane structural design of the inboard region for large wind turbine blades.

Recent research suggests that improving performance in the inboard region of the blade may improve the overall blade performance. Conventionally, the inboard region used thick airfoils to support large flapwise bending loads [24, 20, 25]. While the aerodynamic performance of thick airfoils is generally poor, this is the standard compromise between structures and aerodynamics in blade design. The inboard region is primarily designed for structures: thick cross-sections (with a large second moment of area in the flapwise direction) support the large flapwise bending loads. (The inboard region design is also influenced by manufacturing constraints related to the root attachment, as well as transportation requirements that limit the maximum allowable dimensions.) In order to improve the performance of the inboard

region within the context of these constraints, blunt trailing-edge "flatback" airfoils have been designed to address both the structural and aerodynamic performance of the inboard region [26, 27]. Structural advantages of flatback airfoils include a larger sectional area and increased sectional moment of inertia for a given airfoil maximum thickness; aerodynamic advantages include a larger sectional maximum lift coefficient, increased lift curve slope, and reduced sensitivity to surface soiling [28].

Multi-element airfoils for the inboard region have also been proposed as an alternative concept that may improve performance. Recent aerodynamic investigations [40, 41] have shown that multi-element airfoils (which are specifically designed for wind turbines, and are usually thick airfoils with thickness-to-chord ratios of 15–30%) have greater lift-to-drag ratios and maximum lift coefficients compared to standard thick airfoils for wind turbines. Another study found that multi-element airfoils fitted to the inboard region improved the annual energy production of a 10-megawatt turbine [42]. Hence, it may be possible to increase the maximum power production, improve start-up performance, and improve overall efficiency of blades for megawatt-size turbines. These studies showed aerodynamic improvements, but did not explicitly examine the structural considerations for large blade designs.

Wirz proposed a conceptual design for wind turbine blades that has the potential to improve the structural and aerodynamic performance of the inboard region: the biplane blade [34]. A similar design was independently proposed by Grabau [38]. The biplane blade design uses a biplane inboard region that transitions into a joint, which is connected to a monoplane outboard region. Preliminary structural analysis suggests that a biplane blade could be expected to achieve a 30% decrease in blade tip deflection [31, 35]. This indicates that for a monoplane blade of fixed length, it may be possible to construct a *lighter* biplane blade with an *equal* tip deflection. These benefits can lead directly to weight and cost reductions for large blades. Preliminary aerodynamic analysis showed that biplane airfoils can also achieve significant increases in lift [37], similar to the multi-element airfoils discussed above.

While its potential benefits are interesting, the unconventional configuration of the biplane blade makes it challenging to design and analyze. Hence, a new method is needed to

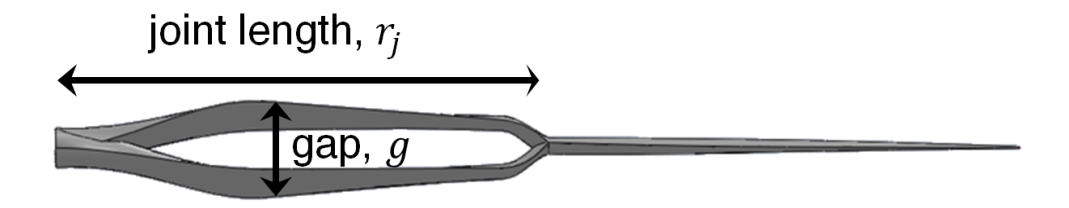


Figure 4.1: Two major design parameters for the biplane blade: joint length (the spanwise distance between the blade root and the mid-blade joint), and the gap (the flapwise distance between the upper and lower elements of the biplane).

Table 4.1: Definition of design parameters for the biplane blade.

Parameter name	Symbol	Description
joint length	r_j	length from blade root to joint
span	\check{R}	length from blade root to tip
joint length-to-span ratio	r_j/R	fraction of blade span containing the inboard biplane region
gap	g	length between the upper and lower chord lines of the biplane
chord	c	length from the leading edge to trailing edge
gap-to-chord ratio	g/c	gap between biplane elements, normalized by chord

design and analyze the biplane blade. It is not initially apparent exactly how the biplane should be incorporated into the overall blade structure, because several design parameters need to be specified for the inboard biplane region. This paper focuses on two important design parameters (see Figure 4.1 and Table 4.1): the joint length r_j (the spanwise distance between the blade root and the mid-blade joint), and the gap g (the flapwise distance between the upper and lower elements of the biplane).

To design the biplane blade, the authors used a "structures-first" design approach: (1) design the internal "biplane spar" structure, and (2) fit the airfoil exterior over that spar (Figure 4.2). (This approach is the reverse of the design process used for the Sandia SNL100-00 reference blade [9], an example of a conventional "monoplane blade." The Sandia blade was designed by first choosing an airfoil family for the aerodynamic exterior of the blade, and then fitting a "monoplane spar" structure inside these airfoils.) For the biplane blade, the two-step structures-first approach will give an initial design for the biplane blade. This design will be refined later by iterating through these two steps several times, in order to arrive at a final design for the biplane blade that provides desirable aero-structural performance. In some respects, the structures-first approach is similar to the "Aerosolve" design process proposed for designing conventional monoplane blades [28]. No aerodynamic analysis of

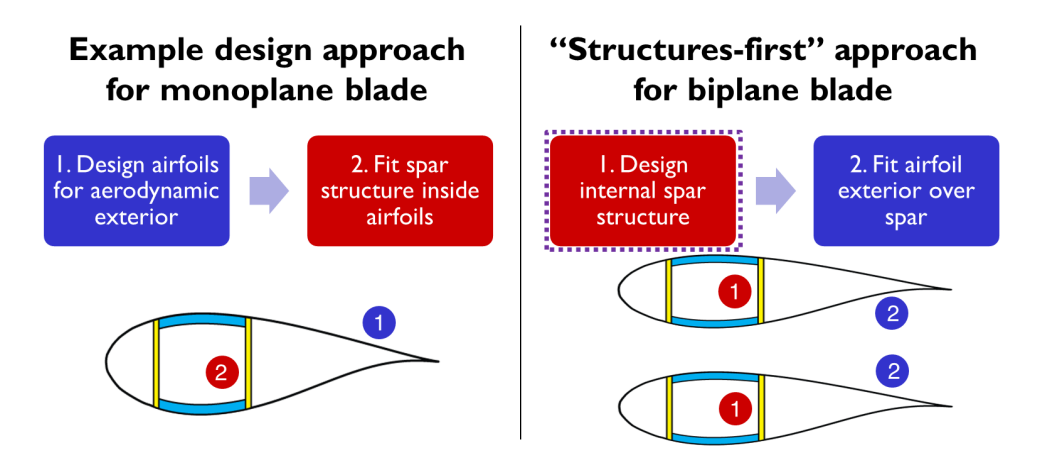


Figure 4.2: Example design approach for a conventional wind turbine blade (left), and the "structures-first" approach to design biplane blades (right). This paper focuses on the first step of the structures-first approach.

the biplane blade is presented here. Instead, this paper focuses on the first step of the structures-first approach (structural design of biplane spars), which lays the foundation for future studies of biplane blades.

Following on from the preliminary investigations, this work aims to show that 100-meter biplane spars can provide improved flapwise structural performance, relative to a conventional 100-meter monoplane spar. First, this work introduces a new analytical model for the displacement field of simplified biplane spars ("biplane beams"), which reveals how biplane spars carry loads differently from conventional cantilevered monoplane spars. Second, a computational model is developed to investigate the design of 100-meter biplane spars made of composite (anisotropic) materials and use realistic cross-sections that taper the spar thickness from root to tip. An approximate buckling analysis is used to verify that compressive loads in the inboard region do not exceed critical buckling loads. This extends earlier research [31, 35] that considered simplified 50-meter biplane spars made of isotropic materials and used uniform rectangular cross-sections (which did not taper the spar thickness from root to tip). Earlier research did not consider buckling. Last, the computational model is used to perform a parametric study of different biplane spar configurations. Fifteen biplane spar configurations were constructed by varying two design parameters (the joint length r_j and the gap g), while the blade span was held constant. This parametric study investigated

the effect of these design parameters on the flapwise structural performance of biplane spars.

4.2 Methods

Both analytical and computational models were used to investigate the structural design of biplane spars. The analytical model gives physical insights into the structural behavior of the biplane spar, which are not clear from the computational model alone. The analytical model used the method of minimum total potential energy [81] to derive the displacement field of a biplane beam (a simplified structure that approximates a biplane spar, using three Euler-Bernoulli beams and a rigid joint). The computational model used beam finite elements and cross-sectional analysis to create more complex models of monoplane and biplane spars made with composite materials and realistic cross-sections that taper the spar thickness from root to tip. These computational models were used in two ways: (1) to compare the structural performance of a monoplane spar to biplane spars, and (2) to perform a parametric study of different biplane spar configurations.

4.2.1 Analytical model

The method of minimum total potential energy [81] was used to derive the displacement field of a simplified biplane spar, or "biplane beam" (Figure 4.3). This method is often used for structures that are difficult or cumbersome to analyze with free body diagrams, because it offers a systematic framework to obtain the equilibrium equations and boundary conditions for the structure. The resulting boundary value problem can be solved analytically for the displacement field. The derivation of the analytical model is outlined below.

4.2.1.1 Geometry

Consider a "biplane beam" structure (Figure 4.3), composed of an inboard biplane region $(0 \le x \le r_j)$ and an outboard monoplane region $(r_j \le x \le R)$. The inboard biplane region is made up of two beams separated by a gap g: the "upper biplane" (UB) beam and the

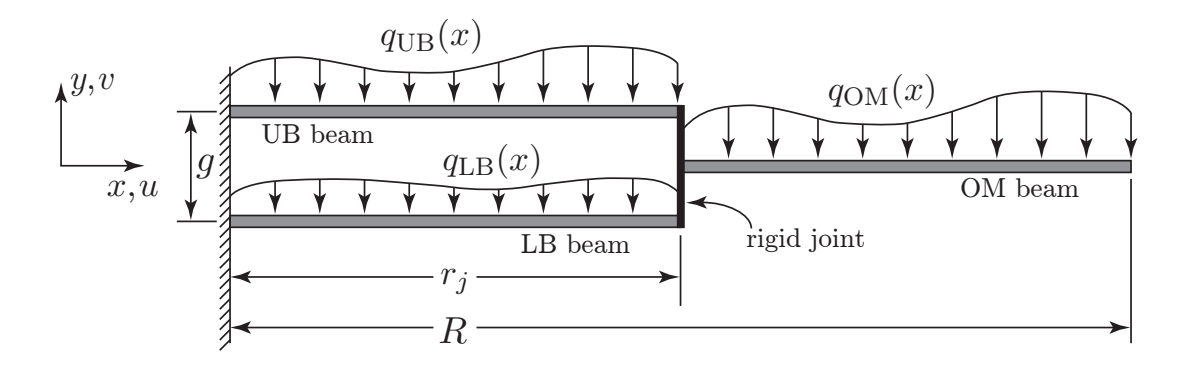


Figure 4.3: Schematic of the biplane beam structure used for the analytical model.

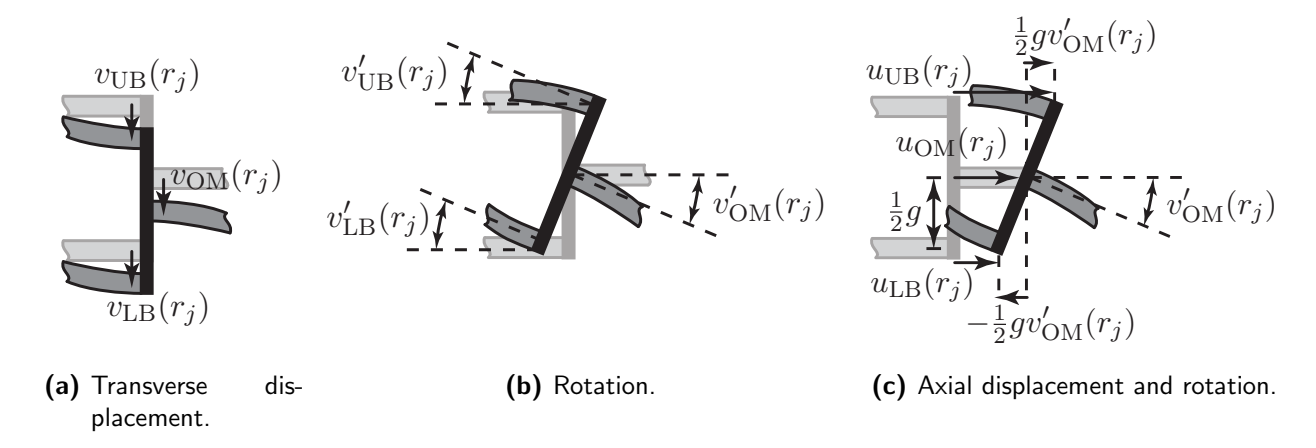


Figure 4.4: Schematics for the kinematic assumptions at the rigid joint $(x = r_j)$ used for the analytical model.

"lower biplane" (LB) beam. The UB and LB beams are both cantilevered at x=0 and both affixed to a rigid joint at $x=r_j$. This joint is assumed to be very thin compared to the span R. The outboard monoplane region is made of one beam: the "outboard monoplane" (OM) beam. The OM beam is affixed to the rigid joint at $x=r_j$, and free at x=R.

4.2.1.2 Loads

Three transverse distributed loads $(q_{UB}(x), q_{LB}(x), and q_{OM}(x))$ are applied to the UB, LB, and OM beams, respectively. To approximate the flapwise bending moment (the primary load on wind turbine blades [51]), the transverse distributed loads were assumed to be constant along each of the spans of the OM, UB, and LB beams. The constant load distribution approximates an "instantaneous snapshot" of a gust load on a wind turbine blade. These

gust loads often lead to the worst-case scenario of all the design load cases suggested by international certification standards of wind turbine blades [82], as was shown in [9]. The magnitude of the inboard distributed loads was assumed to be half of the magnitude of the outboard distributed load (Eqs. (4.1)). In other words, the constant load distribution that would normally be present on the inboard region of a conventional monoplane blade was equally distributed among the UB and LB beams.

$$q_{\text{OM}}(x) = q_0$$

 $q_{\text{UB}}(x) = \frac{1}{2}q_0$ (4.1)
 $q_{\text{LB}}(x) = \frac{1}{2}q_0$.

The transverse distributed loads only simulate flapwise bending loads on the biplane spar. Consider a "full" biplane blade, with airfoils added over a biplane spar. The flapwise bending response of a full biplane blade is unlikely to be much different from the flapwise response of a biplane spar, so flapwise loads are considered in the present study. However, edgewise loads and torsional response will likely be different in the full biplane blade, so they were not investigated here with the analytical model for the biplane spar.

4.2.1.3 Engineering properties

Each beam is assumed to be made of an isotropic, linear elastic material. The UB beam has bending stiffness $EI_{UB}(x)$ and extension stiffness $EA_{UB}(x)$. Similarly, the LB and OM beams have stiffnesses $EI_{LB}(x)$, $EA_{LB}(x)$, $EI_{OM}(x)$, and $EA_{OM}(x)$.

In order to make the analytical model tractable, some assumptions were made for the engineering properties and loads on the biplane beam, leading to simpler equilibrium equations and natural boundary conditions. It was assumed that EA and EI were constant along each of the spans of the OM, UB, and LB beams. Furthermore, the inboard biplane properties

were scaled to the outboard monoplane properties with constants α and β , such that

$$\alpha = \frac{EA_{\rm UB}}{EA_{\rm OM}} = \frac{EA_{\rm LB}}{EA_{\rm OM}}$$

$$\beta = \frac{EI_{\rm UB}}{EI_{\rm OM}} = \frac{EI_{\rm LB}}{EI_{\rm OM}}.$$
(4.2)

4.2.1.4 Kinematic assumptions

The UB, LB, and OM beams were modeled with Euler-Bernoulli beam theory. In addition to transverse bending, all beams were allowed to stretch axially.

The rigid joint has three degrees of freedom: transverse displacement, rotation, and axial displacement (Figure 4.4). The joint effectively links the movement of all three beams at $x = r_j$. At the joint, the transverse displacements and rotations of all three beams must be equal. Additionally, at the joint, the axial displacements of the UB and LB beams are related to the axial displacement of the OM beam and the rotation of the OM beam.

$$u_{\rm UB}(r_j) = u_{\rm OM}(r_j) + \frac{1}{2}gv'_{\rm OM}(r_j)$$

$$u_{\rm LB}(r_j) = u_{\rm OM}(r_j) - \frac{1}{2}gv'_{\rm OM}(r_j)$$
(4.3)

4.2.1.5 Solution for transverse and axial displacements

An expression for the total potential energy of the structure and applied loads was developed and minimized [83, 84]. Then, the minimum total potential energy was used to obtain the equilibrium equations and boundary conditions. Python-based software (the symbolic math package SymPy 0.7.2. [85] and the web-based notebook environment of IPython 0.13 [86]) was used to help derive the solution to these equilibrium equations and boundary conditions. The resulting analytical solution is given below.

The transverse displacements are

$$v_{\text{UB}}(x) = \frac{q_0 x^4}{48EI\beta} - \frac{Rq_0 x^3}{12EI\beta}$$

$$+ \frac{q_0 x^2 \left(3AR\alpha g^2 r_j - A\alpha g^2 r_j^2 + 12IR^2\beta\right)}{24EI\beta \left(A\alpha g^2 + 4I\beta\right)}$$

$$v_{\text{LB}}(x) = \frac{q_0 x^4}{48EI\beta} - \frac{Rq_0 x^3}{12EI\beta}$$

$$+ \frac{q_0 x^2 \left(3AR\alpha g^2 r_j - A\alpha g^2 r_j^2 + 12IR^2\beta\right)}{24EI\beta \left(A\alpha g^2 + 4I\beta\right)}$$

$$v_{\text{OM}}(x) = \frac{q_0 x^4}{24EI} - \frac{Rq_0 x^3}{6EI} + \frac{R^2 q_0 x^2}{4EI}$$

$$+ \frac{q_0 r_j x}{6EI \left(A\alpha g^2 + 4I\beta\right)} \left(-3AR^2 \alpha g^2 + 3AR\alpha g^2 r_j - A\alpha g^2 r_j^2\right)$$

$$-12IR^2\beta + 6IR^2 + 12IR\beta r_j - 6IRr_j - 4I\beta r_j^2 + 2Ir_j^2\right)$$

$$+ \frac{q_0 r_j^2}{48EI\beta \left(A\alpha g^2 + 4I\beta\right)} \left(12AR^2 \alpha \beta g^2 - 16AR\alpha \beta g^2 r_j\right)$$

$$+ 2AR\alpha g^2 r_j + 6A\alpha \beta g^2 r_j^2 - A\alpha g^2 r_j^2 + 48IR^2\beta^2$$

$$-24IR^2\beta - 64IR\beta^2 r_j + 32IR\beta r_j + 24I\beta^2 r_j^2 - 12I\beta r_j^2\right).$$
(4.4c)

The axial displacements are

$$u_{\rm UB}(x) = \frac{gq_0x \left(3R^2 - 3Rr_j + r_j^2\right)}{6E\left(A\alpha q^2 + 4I\beta\right)}$$
(4.5a)

$$u_{\rm LB}(x) = -\frac{gq_0x \left(3R^2 - 3Rr_j + r_j^2\right)}{6E \left(A\alpha q^2 + 4I\beta\right)}$$
(4.5b)

$$u_{\rm OM}(x) = 0. \tag{4.5c}$$

Compare Equations (4.4) and (4.5) to the analytical solution for a cantilever beam of length R, with uniform axial stiffness EA and bending stiffness EI, under a constant distributed load q_0 [87]; here, this reference beam is referred to as a "monoplane beam".

$$v_{\text{monoplane}}(x) = \frac{q_0 R^4}{24EI} \left[\left(\frac{x}{R} \right)^4 - 4 \left(\frac{x}{R} \right)^3 + 6 \left(\frac{x}{R} \right)^2 \right]$$
(4.6a)

$$u_{\text{monoplane}}(x) = 0 \tag{4.6b}$$

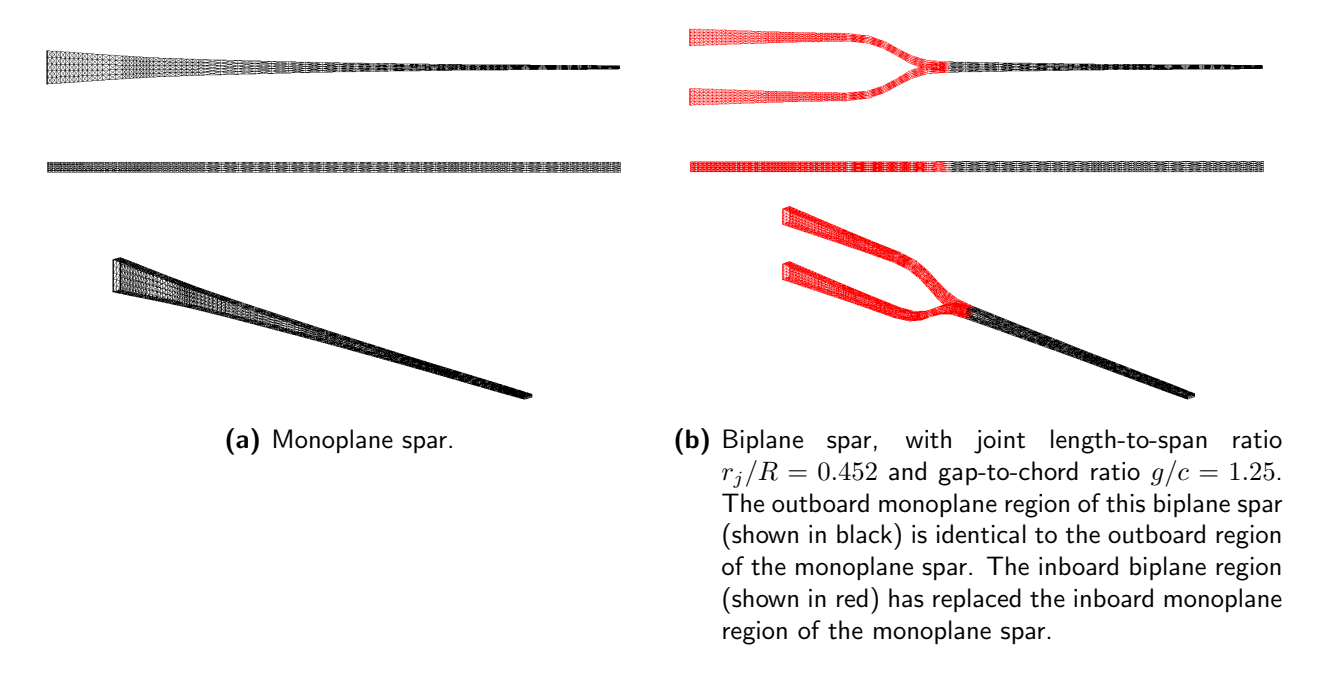


Figure 4.5: Surface geometry of spars used for the computational model. Three views are shown for each spar: edgewise (top), flapwise (middle), and isometric (bottom).

4.2.2 Computational model

Computational models (Figure 4.5) were constructed to include some more complex design features of the biplane spar that could not be included in the analytical model (such as tapering of the spar from root to tip, a smooth biplane-monoplane transition at the joint, and anisotropic composite cross-sections). A computational model of a monoplane spar was also constructed for benchmark comparisons against these biplane spars. These computational models more accurately represent the real structures inside biplane blades and conventional blades than the analytical models used in Section 4.2.1. The computational models were analyzed with 1D beam finite elements and 2D cross-sectional analysis (described further in Section 4.2.2.4). An approximate buckling analysis was used to verify that compressive loads in the inboard region do not exceed critical buckling loads.

The first step of the structures-first approach centers around the design and analysis of spars (Figure 4.2). The 100-meter Sandia research blade [9] was used as a template to design these spars. The Sandia blade was chosen because many details of its design were made publicly available, including its cross-section geometries, composite layup, and material

properties. The Sandia blade is an open platform that can be modified to create new blade designs, making it ideal for this investigation.

4.2.2.1 Assumptions

The main assumption behind the structures-first approach is that the structural performance of a spar is representative of the structural performance of an entire blade. This assumption is reasonable because the spar is the primary load-bearing component in the blade [88, 89]. Furthermore, to the authors' best knowledge, the airfoil shells on the Sandia blade are not intended to be load-bearing; they merely transfer the aerodynamic loads from the wind to the internal spar structure. The spar is composed of spar caps on the top and bottom, and shear webs on the left and right. The spar caps are made of the primary load-carrying unidirectional fibers, and the shear webs stabilize the spar caps under shear forces; this creates a closed-box section.

In this analysis, the spar is defined to include the following structural components from the Sandia blade: the two principal shear webs, the two spar caps, and the portion of the root buildup that is adjacent to the spar caps (Figure 4.6). The root buildup was included because the spar caps are very thin near the spar root, and the root buildup is needed to provide more stiffness in the root structure. All other components in the Sandia blade were neglected.

Three other assumptions were made to simplify the geometry of all spars. First, a rectangular cross-section was assumed for all spars (Figure 4.7). In other words, the curvature of the spar caps and root buildup was neglected. The maximum thickness of each airfoil profile was used to determine the height of each rectangular cross-section in the spar. Second, twist of the cross-section along the span of the spar was not considered (i.e. the spar had zero twist from root to tip). Third, the cylindrical root shown in Figure 4.1 was neglected to limit the number of design parameters in this analysis; future studies will be necessary to quantify its effect on structural performance.

To evaluate the validity of these assumptions, the spanwise properties of the monoplane

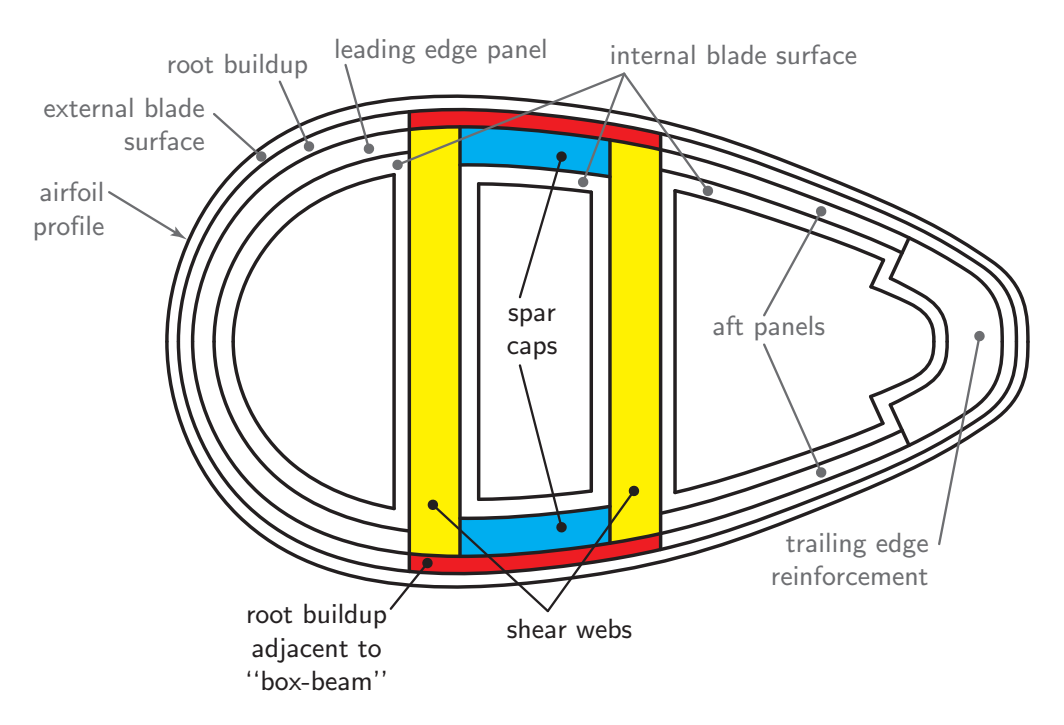


Figure 4.6: The spar is defined to include the two spar caps, the two primary shear webs, and the root buildup adjacent to the "box-beam" formed by the spar caps and shear webs. Note: figure is not to scale.

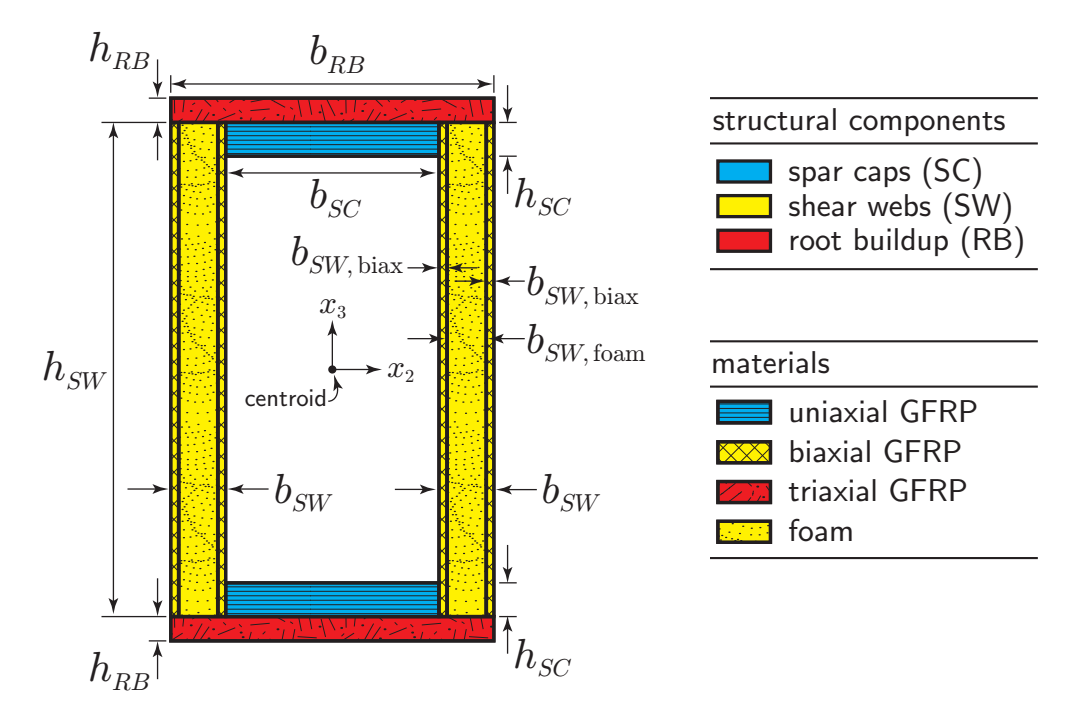


Figure 4.7: All spars were assumed to have rectangular cross-sections, made of the components and materials shown above. Glass fiber reinforced plastics (GFRP) and structural foam were used to construct all spar cross-sections. Note: figure is not to scale.

spar (Table C.2) and the Sandia blade (stations 7–30, reported in Table 2 of Ref. [90]) were compared to each other. In the flapwise direction, these properties match well everywhere except near the root where, as expected, the monoplane spar is less stiff than the full Sandia blade. The monoplane spar root has a lower stiffness because it neglects triaxial laminates in the leading and trailing edges of the root buildup, which provide additional flapwise stiffness. In the edgewise and torsional directions, the properties of the monoplane spar across its entire span have similar distributions, but are about 1-2 orders of magnitude smaller than the Sandia blade. This result is expected, since the leading edge panel and trailing edge reinforcement (which provide edgewise stiffness) and the airfoil shells (which provide torsional stiffness) were neglected from the monoplane spar.

Based on these results, the monoplane spar is an acceptable structural approximation of the Sandia blade in the flapwise direction. It is clear that the monoplane spar is not a good approximation in the edgewise and torsional directions, which is a limitation of the first step in the structures-first approach. Nevertheless, in the absence of the detailed aerodynamic exterior, the monoplane spar is a useful 1st-order characterization of the Sandia blade's structural interior. Bearing this in mind, the monoplane spar can be used as a 1st-order baseline for comparisons against biplane spars in this study to examine the impacts of the biplane blade design.

4.2.2.2 Design of spars

A monoplane spar was designed to approximate the Sandia blade and 15 biplane spars were designed to approximate different biplane blade configurations. Material properties (Table 4.2) and laminate dimensions of all spars were based on the Sandia blade [9]. The material properties of the glass fabrics and epoxy resin materials are also described in more detail in the DOE/MSU Composite Material Fatigue Database [91, 92]. Because weight is one of the important limiting parameters that determines the length of wind turbine blades [19], all monoplane and biplane spars had equal cross-sectional areas at a given spanwise station (Figure 4.8), and hence, equal mass per unit span. This allowed for a self-consistent

Table 4.2: Material property data for glass fiber reinforced plastic (GFRP) composites and structural foam [91, 92, 9].

material	fabric/resin	lay-up	E_1 (GPa)	E_2 (GPa)	G_{12} (GPa)	ν_{12}	ρ (kg/m ³)
uniaxial GFRP	E-LT-5500/EP-3	$[0]_2$	41.8	14.0	2.63	0.28	1920
biaxial GFRP	Saertex/EP-3	$[\pm 45]_4$	13.6	13.3	11.8	0.49	1780
triaxial GFRP	SNL Triax	$[\pm 45]_4[0]_2$	27.7	13.65	7.2	0.39	1850
foam	-	-	0.256	0.256	-	0.3	200

comparison between their structural performance.

Monoplane spar: Figure 4.9 summarizes the procedure used to design and analyze the monoplane spar (Figure 4.5(a)). First, the geometry, layup, and materials of the Sandia blade were used to construct a monoplane spar. Second, the cross-sectional dimensions of the spar caps, shear webs, and root buildup were defined. Third, each cross-section in the spar was meshed and analyzed to compute its stiffness properties. Fourth, a beam finite element model for the monoplane spar was defined. Fifth, a simulated load case was applied to the beam model. Finally, the analysis results were postprocessed to obtain the 1D deflections, 1D bending moments, 1D axial force resultants, and 2D cross-sectional stresses. See Section 4.2.2.4 for details on the software and analyses used in this procedure.

Table B.1 lists the laminate dimensions for each of the monoplane cross-sections (Figure 4.7) that make up the monoplane spar. The monoplane spar (Figure 4.5(a)) had a span of 91.9 m, and a maximum height of 5.3 m at the root. Although the spar was derived from the 100-meter Sandia blade, the spar is slightly shorter because it begins just past the blade root (spar station 1 corresponds to 2.4% span along the Sandia blade) and terminates just before the blade tip (spar station 24 corresponds to 94.3% span along the Sandia blade) [9]. Table C.2 lists the spanwise properties for the monoplane spar, which were calculated with 2D cross-sectional analysis as described later in Section 4.2.2.4.

Biplane spar: Figure 4.10 summarizes the procedure used to design and analyze the biplane spar (one configuration is shown in Figure 4.5(b)), which is similar to the procedure used for the monoplane spar. First, the geometry, layup, and materials of the monoplane spar (which were derived from the Sandia blade) were used to construct a biplane spar. The outboard monoplane region of the biplane spar was left unchanged from the monoplane spar.

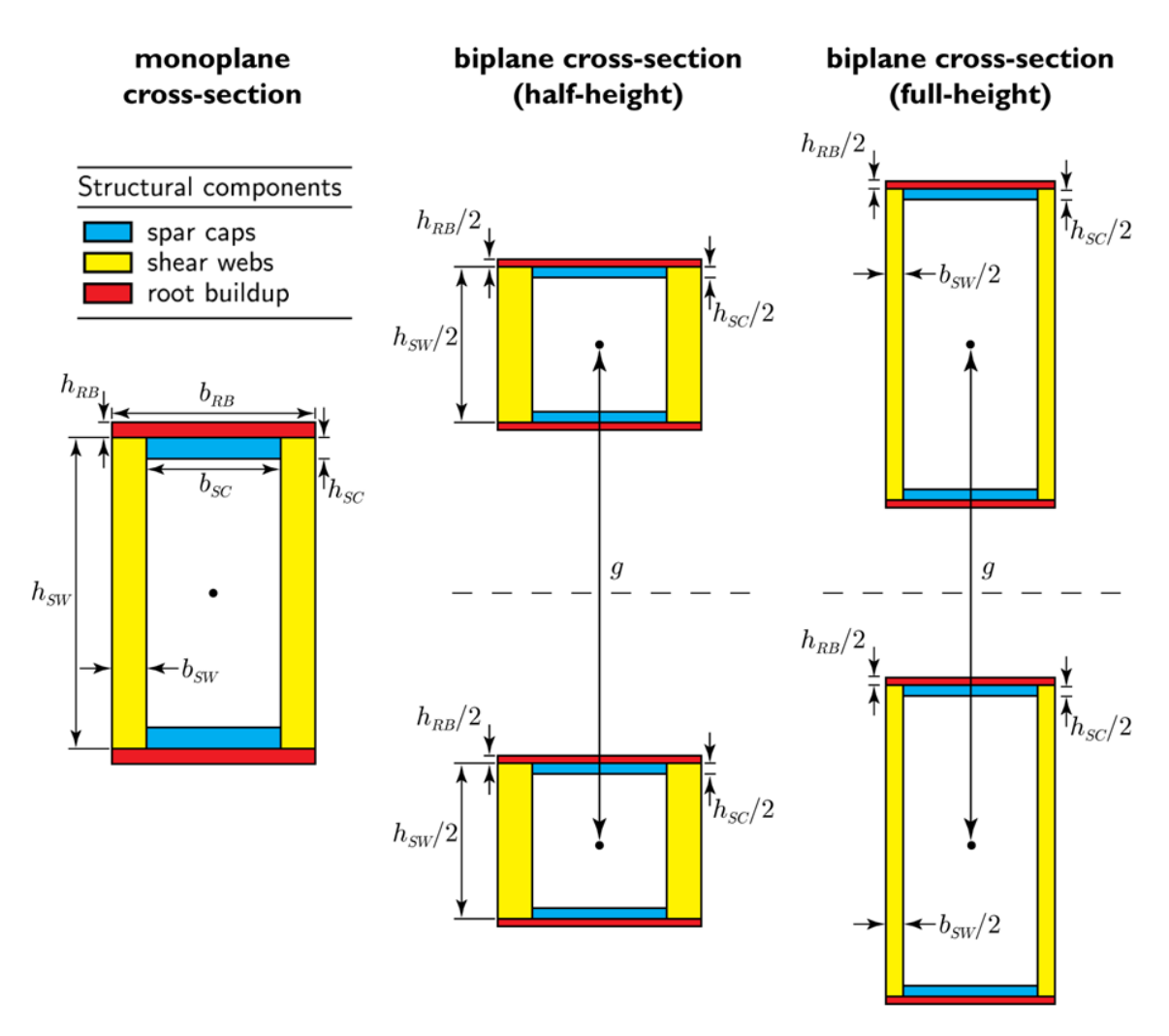


Figure 4.8: All cross-sections had equal areas, so all spars had the same mass per unit span. Note: figure is not to scale.

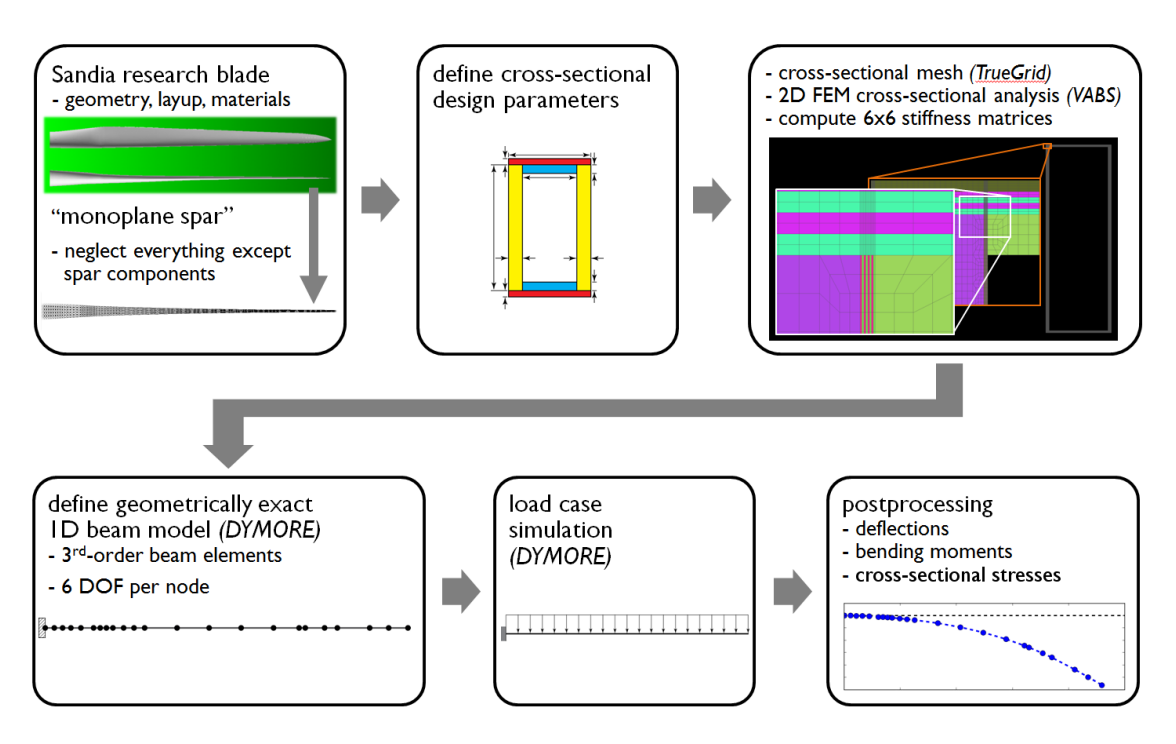


Figure 4.9: Design and analysis procedure for the monoplane spar. The software used in this procedure (*TrueGrid* for cross-sectional mesh generation, *VABS* for 2D cross-sectional analysis, and *DYMORE* for 1D beam finite element analysis) is typeset in italics. The surface geometry of the Sandia blade was taken from [9].

The inboard monoplane region of the monoplane spar was replaced with an inboard biplane region in order to construct a biplane spar [93]. Second, the cross-sectional design parameters were defined. The biplane cross-section included an upper and lower element, which were assumed to be identical in this study. Third, each cross-section in the spar was meshed and analyzed to compute its stiffness properties. Only the upper element of each biplane cross-section was meshed and analyzed, because it was identical to the lower element. Fourth, a beam finite element model was defined, which included the inboard biplane region of the biplane spar. Fifth, a simulated load case was applied to the beam model. An equivalent load was defined for the inboard biplane region so that the total load on the biplane spar was the same as the monoplane spar. Finally, the analysis results for the biplane spar were postprocessed to obtain the same quantities that were obtained for the monoplane spar. See Section 4.2.2.4 for details on the software and analyses used in this procedure.

Two types of biplane cross-sections (Figure 4.8) were constructed to bound the design space for biplane spars. A "half-height" biplane cross-section was constructed, so that the

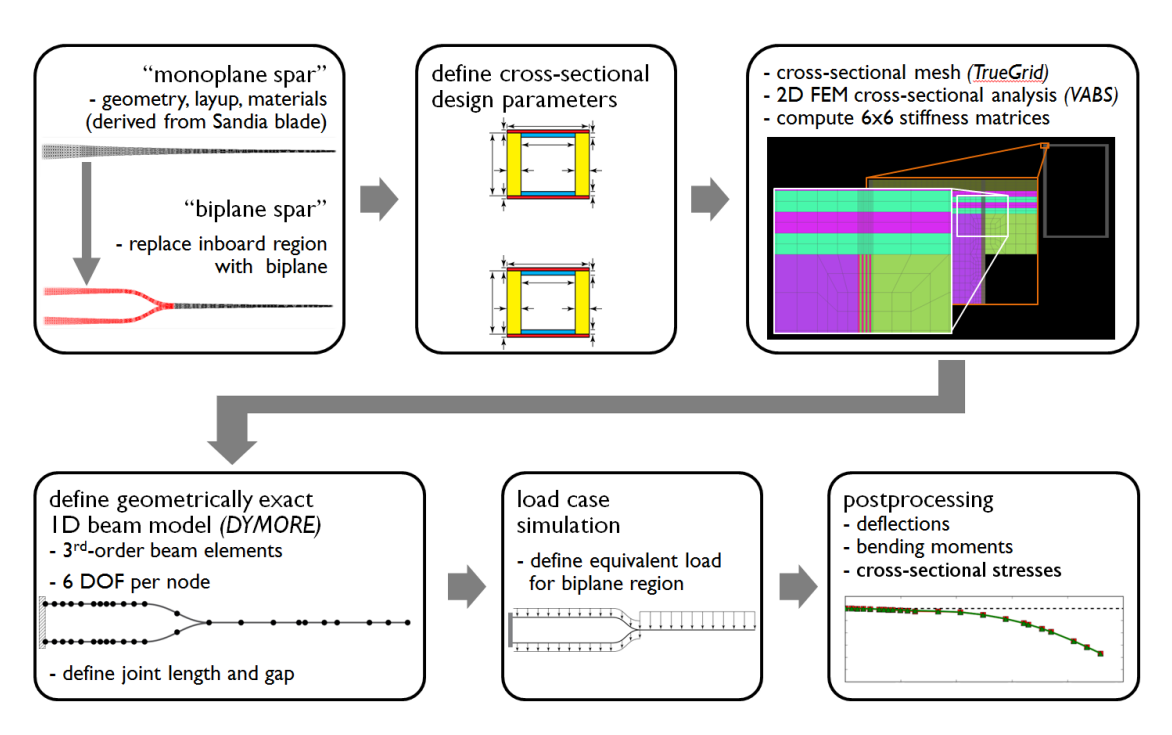


Figure 4.10: Design and analysis procedure for the biplane spar. The software used in this procedure (*TrueGrid* for cross-sectional mesh generation, *VABS* for 2D cross-sectional analysis, and *DYMORE* for 1D beam finite element analysis) is typeset in italics.

upper and lower elements of the biplane cross-section were half as tall as the monoplane cross-section. A "full-height" biplane cross-section was also constructed, so that the upper and lower elements of the biplane cross-section were the same height as the monoplane cross-section. Overall, the upper and lower elements of the full-height biplane cross-section are thinner-walled versions of the monoplane cross-section.

Figure 4.11 illustrates the edgewise views of two sample biplane spars constructed from half-height and full-height biplane cross-sections. The half-height cross-sections form a more slender inboard biplane region than the full-height cross-sections. Once airfoils are fitted over each of these spars, the half-height cross-sections will offer more of an aerodynamic benefit, while the full-height cross-sections will offer more of a structural benefit. No attempt was made in this study to find the optimum biplane cross-section height. Rather, these two configurations bound the design space for the biplane spar, and the optimum configuration is somewhere in between.

Table B.2 lists the laminate dimensions for a biplane spar made with half-height biplane

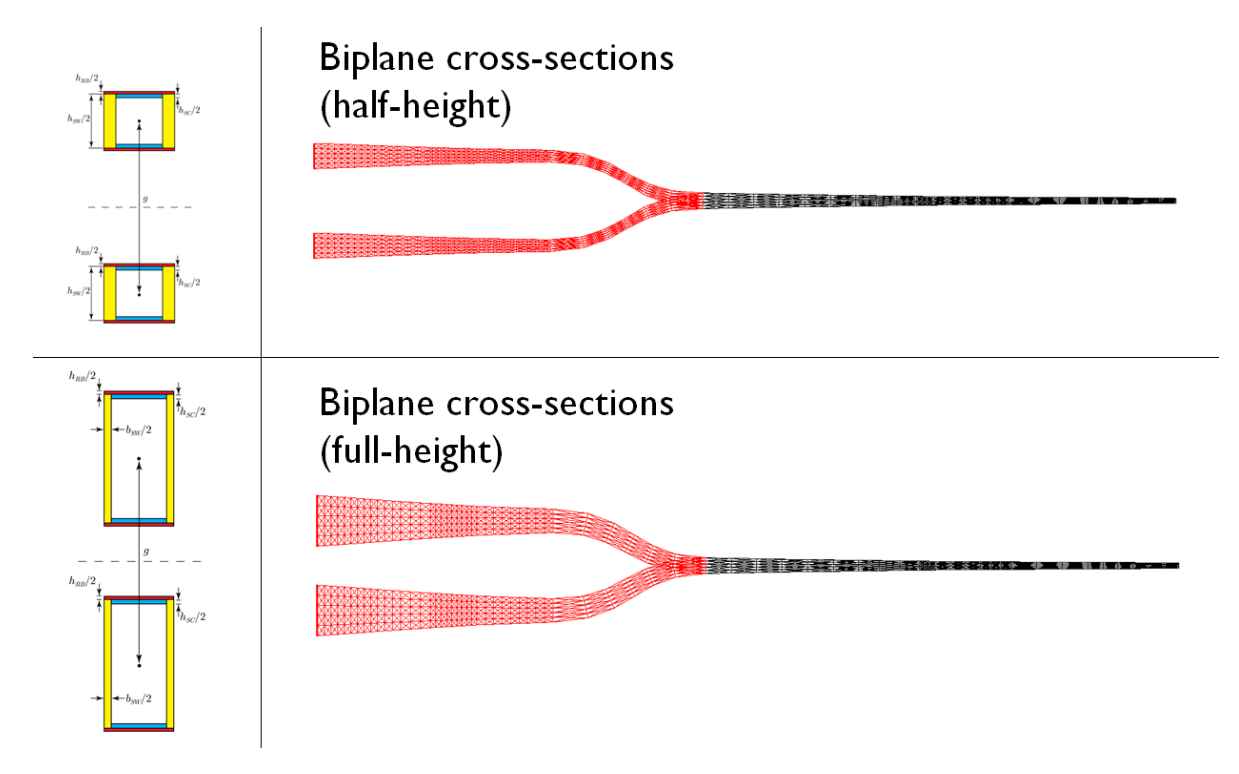


Figure 4.11: Edgewise views of two biplane spars constructed with half-height biplane cross-sections (top) and full-height biplane cross-sections (bottom). Both biplane spars have a joint length-to-span ratio of $r_j/R=0.452$ and a gap-to-chord ratio of g/c=1.25.

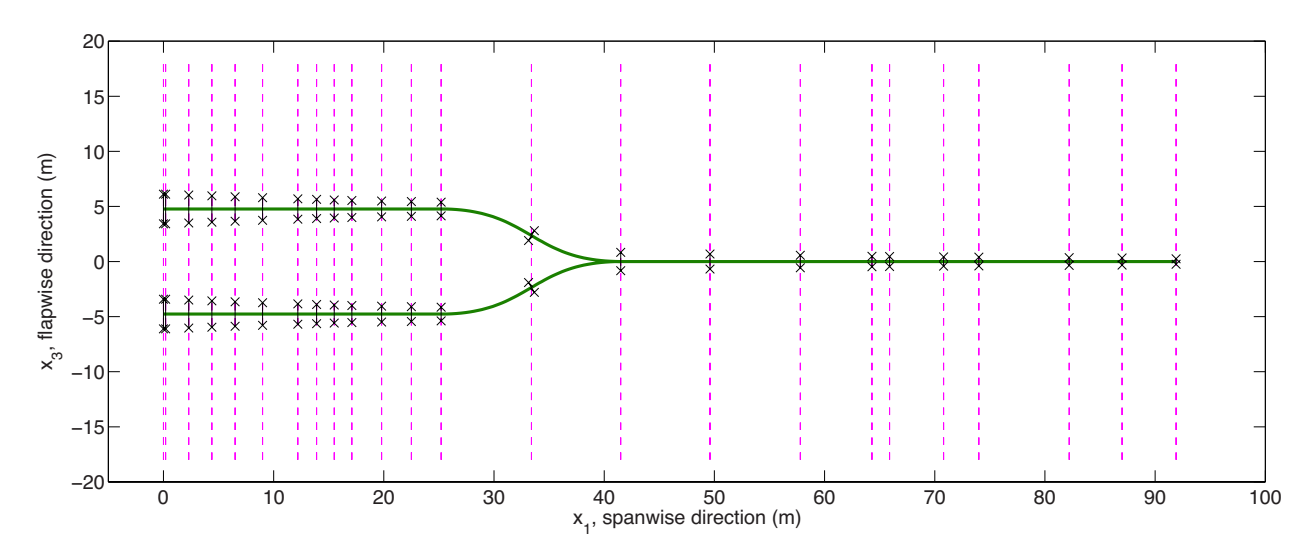
cross-sections. Figure 4.12(a) shows how these cross-sections are distributed along the biplane spar in the spanwise direction (x_1) and the flapwise direction (x_3) . Table C.3 lists the spanwise properties of this biplane spar, which were calculated with 2D cross-sectional analysis, as described later in Section 4.2.2.4. Table B.3, Figure 4.12(b), and Table C.4 give the corresponding details for a biplane spar made with full-height biplane cross-sections.

In order to evaluate the effect of joint length and gap on the structural performance of biplane spars, 15 configurations of the inboard biplane region were made (Figure 4.13). Each configuration had a different value for the joint length-to-span ratio ($r_j/R = 0.245$, 0.274, 0.452, 0.540, and 0.629) and gap-to-chord ratio (g/c = 0.75, 1.00, and 1.25). The procedure in Figure 4.10 was repeated for each different pair of values for r_j/R and g/c. The span (R = 91.9 m) and reference chord (c = 7.628 m, taken to be the maximum chord in the Sandia blade) were held constant for each configuration. Each configuration used "full-height" biplane cross-sections. The location of the biplane-monoplane transition region varied, depending on the configuration.

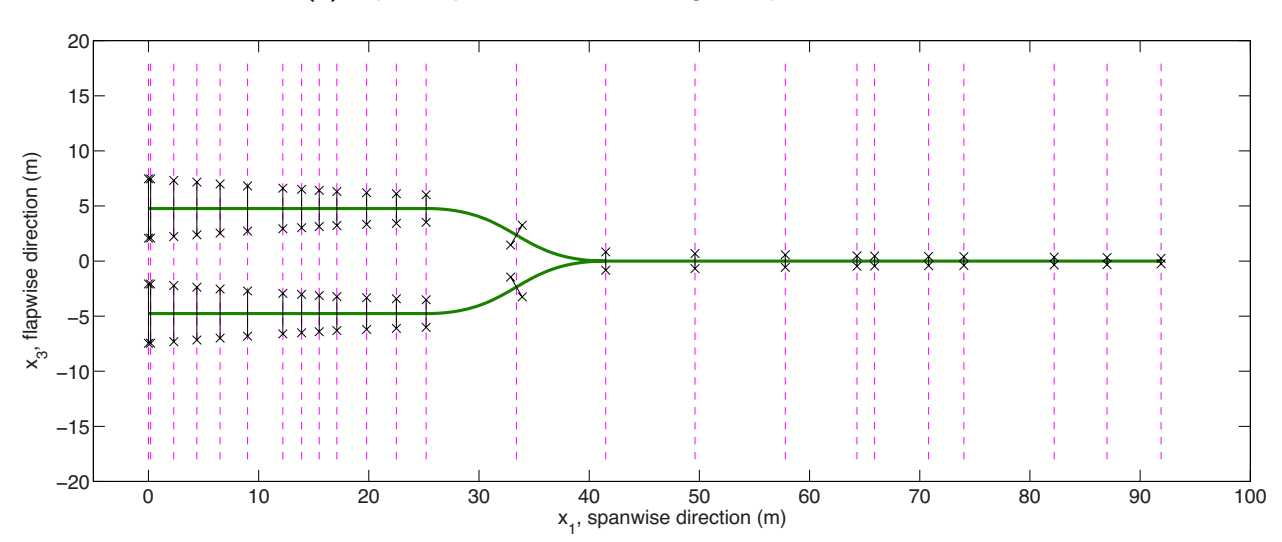
4.2.2.3 Load profiles and boundary conditions

Simple flapwise loads were used to compare the structural performance of biplane spars and the monoplane spar, following the same argument used in the analytical model (Section 4.2.1.2). A constant load distribution was statically applied to each spar (Figure 4.14). The maximum magnitude of the constant load distribution was 1000 N/m. To load the monoplane spar and the biplane spar in an equivalent manner, it was assumed that the loads on the biplane inboard region of the biplane spar were equally distributed among the upper and lower elements (Figure 4.14(b)). All spars were cantilevered at the root ($x_1 = 0$ m) and free at the tip ($x_1 = R = 91.9$ m). These flapwise constant load distributions were also used to estimate the structural efficiency of biplane spars (Section 4.2.2.6).

Static tip loads were also used to estimate the structural efficiency of biplane spars. Two load cases were considered: a flapwise tip load and a torsional tip load (Figure 4.15). Again, both spars were cantilevered at the root and free at the tip. The magnitude of the flapwise



(a) Biplane spar made of "half-height" biplane cross-sections.



(b) Biplane spar made of "full-height" biplane cross-sections.

Figure 4.12: One-dimensional representations of biplane spars with a joint length-to-span ratio $r_j/R=0.452$ and gap-to-chord ratio g/c=1.25. One-dimensional reference lines are plotted as thick solid green lines. Spar station locations are plotted with dashed magenta lines. The solid black lines with x-symbols show the height of each spar cross-section (cross-section height $=h_{SW}+2h_{RB}$) at each spar station.

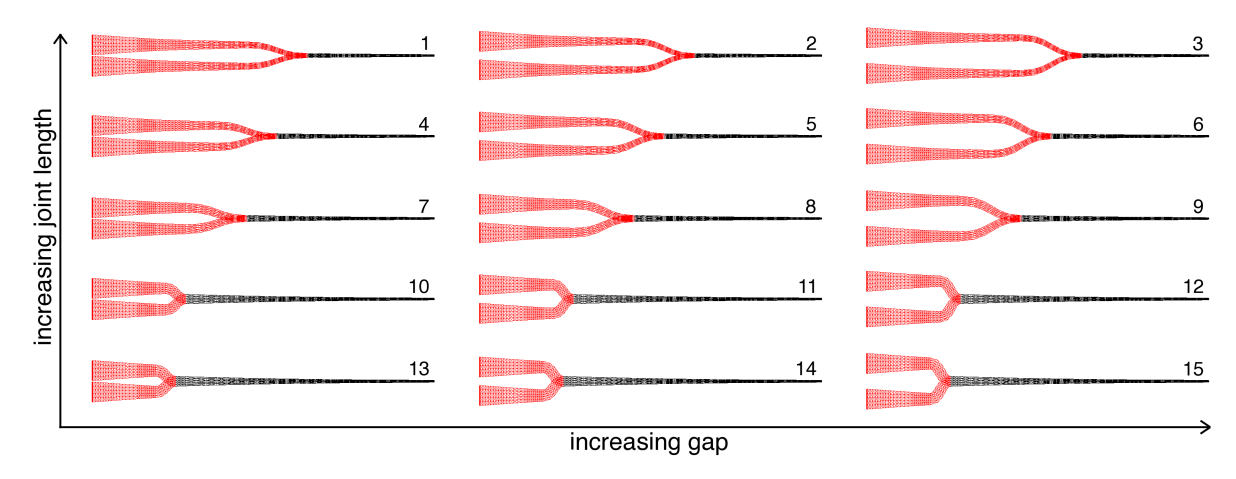
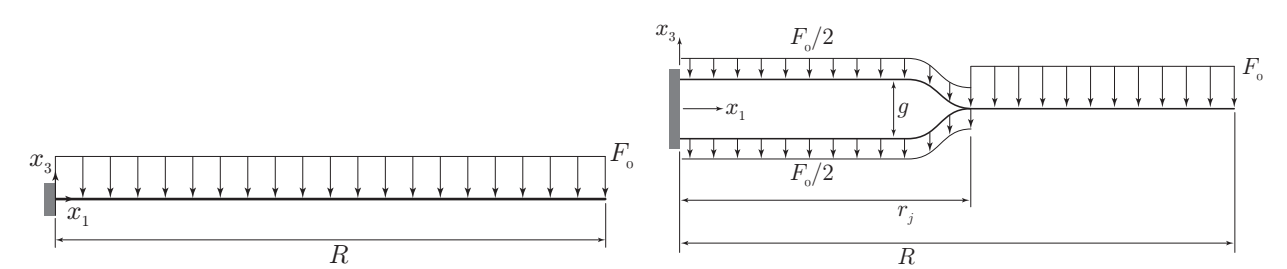


Figure 4.13: Fifteen biplane spar configurations were designed and analyzed in this study.



(a) Flapwise constant load distribution, monoplane spar. (b) Equivalent flapwise constant load distribution, biplane spar.

Figure 4.14: Load profiles applied to spars.

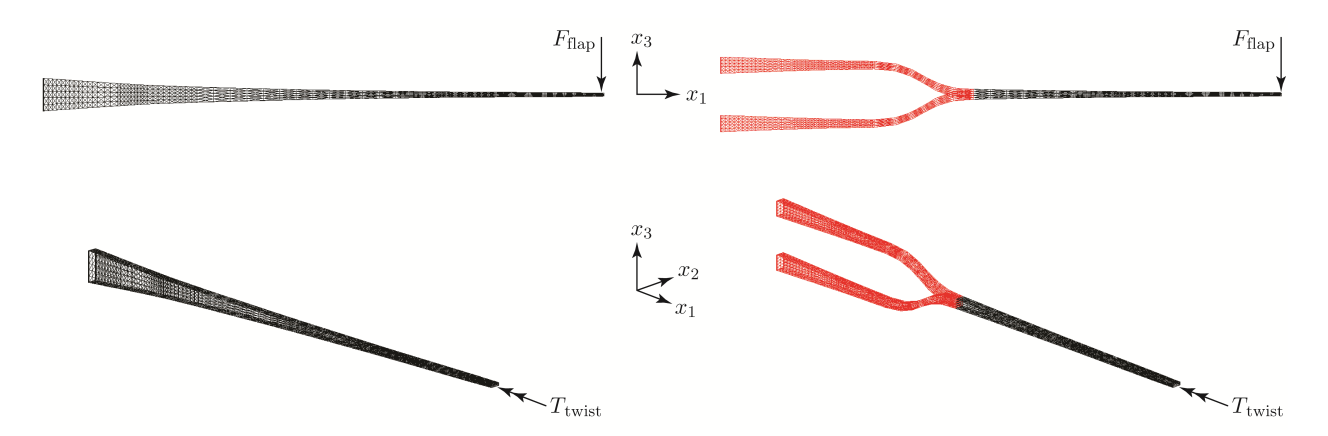


Figure 4.15: Tip loads applied to spars: flapwise (top) and torsional (bottom).

tip load was varied between 1000 N $< F_{\rm flap} < 100,000$ N, and flapwise deflections were calculated. The magnitude of the torsional tip load was varied between 1000 N-m $< T_{\rm twist} < 100,000$ N-m, and both twist angles and edgewise deflections were calculated.

This paper did not investigate biplane spars under edgewise loading. While edgewise loads are important for large blades, they are beyond the scope of this paper because the airfoil shells have been neglected. The airfoil shells contain reinforcements along the leading and trailing edges (Figure 4.6), which help resist edgewise loads. Therefore, it would be inappropriate to load biplane spars in the edgewise direction without the additional support of the reinforcements in the airfoil shells. Edgewise load cases will be considered in future studies that include both the biplane spar and the airfoil shells to model the complete biplane blade. This paper also did not model the dynamic response of biplane spars, but this should be considered in the future for fatigue analyses.

4.2.2.4 1D beam models and 2D cross-sectional analysis

Each spar was modeled with geometrically exact beam finite elements [71] in DYMORE 3.0, a flexible multibody dynamics finite element program [61, 62]. These elements were 3rd-order elements, and were based on a generalized Timoshenko beam model with six degrees of freedom per node [67]. DYMORE performed a nonlinear static analysis to solve for the deformed configuration of each spar under loading.





- (a) Monoplane spar discretized with 1D beam finite elements.
- (b) Biplane spar discretized with 1D beam finite elements.

Figure 4.16: Computational meshes used for finite element analysis. (Note: mid-element nodes not shown)

Figure 4.16 compares the 1D beam models for the monoplane spar and a biplane spar. The spanwise location of the end-nodes was chosen to match the spanwise locations of the blade stations defined for the Sandia blade [9]. In the outboard monoplane regions, the monoplane and biplane spar meshes are identical. However, in the inboard region, the biplane spar mesh has an upper and lower assembly of beam elements, which merge together into one node at the biplane-monoplane joint. Non-Uniform Rational B-Spline (NURBS) curves were used to construct the curved beam elements in the biplane-monoplane transition region.

The 2D cross-sectional properties of all beam elements were calculated with the VABS 3.6 software [63, 64], also known as Variational Asymptotic Beam Sectional analysis. VABS uses the variational asymptotic method [65, 66] to calculate the mass and stiffness matrices for arbitrary beam cross-sections. This work used VABS for cross-sectional analysis in the same manner as in the authors' earlier investigations [31, 35], except some additional features of VABS were used here that were not used earlier. The curvature and pre-twist corrections were considered to calculate the mass and stiffness matrices for cross-sections that belonged to the curved beam elements, and then the 1D beam analysis results from DYMORE were used in VABS to recover the cross-sectional stresses [64].

DYMORE and VABS were selected as structural analysis tools because they are fast and accurate, when compared to three-dimensional finite element analysis (3D FEA) [67, 68]. This was a major requirement in order to conduct a parametric analysis of all fifteen biplane spar configurations. While it is true that 3D FEA is highly accurate, it was judged to be too time consuming to set up the models and compute the results. DYMORE and VABS were also selected because they have successfully modeled helicopter blades [61, 69, 70] and wind turbine blades [68, 71, 72, 73]. This 1D modeling technique has also been previously validated

against 3D FEA for biplane spar structures [31, 35]. Furthermore, several researchers have also used 1D beam finite elements to model a joined wing [94, 74, 75, 76, 77]; which has a joint that resembles the joint of the biplane blade.

4.2.2.5 Buckling analysis

As a result of the approach to conserve mass per unit span, the biplane spar cross-sections have thinner walls than the monoplane spar cross-sections (Figure 4.8), motivating a buckling analysis of the biplane spar. Analytical formulas and representative structures were used to estimate two critical buckling criteria: (1) a "global" beam buckling load, and (2) a "local" plate buckling stress.

The global beam buckling load was estimated with the Euler buckling formula for a simply supported beam under uniaxial compression (Equation (4.7)), where P_{critical} is the buckling load, EI is the flapwise bending stiffness and l is the length of the beam [95]. The lower biplane element in the biplane spar is subjected to the largest axial compressive loads. Therefore, this analysis finds the critical buckling load for a representative beam similar to the lower biplane element.

$$P_{\text{critical}} = \frac{\pi^2 EI}{l^2} \tag{4.7}$$

The local plate buckling stress was estimated with the buckling formula for a simply supported orthotropic plate under uniaxial compression (Equation (4.8)) [95, 96]. Here, $\sigma_{x,\text{critical}}$ is the buckling stress; m is the number of longitudinal half waves; h is the plate thickness; R = a/b is the ratio of plate length a to width b; D_{11} and D_{22} are the bending rigidities about the x and y axes, respectively; D_{66} is the twisting rigidity; and D_{12} is related to the Poisson's ratio ν_{21} . It is assumed that the smallest buckling load occurs when the buckled plate has only one transverse half wave. The lower flange in the lower biplane element of the biplane spar is subjected to the largest axial compressive loads. Therefore, this analysis finds the critical buckling stress for a representative plate similar to the lower flange.

$$\sigma_{x,\text{critical}} = \frac{\pi^2}{hm^2a^2} \left[D_{11}m^4 + 2(D_{12} + 2D_{66})m^2R^2 + D_{22}R^4 \right], \tag{4.8}$$

where

$$R = a/b,$$

$$D_{11} = \frac{E_1 h^3}{12(1 - \nu_{12}\nu_{21})},$$

$$D_{22} = \frac{E_2 h^3}{12(1 - \nu_{12}\nu_{21})},$$

$$D_{12} = \frac{E_2\nu_{21}h^3}{12(1 - \nu_{12}\nu_{21})}, \text{ and}$$

$$D_{66} = G_{12}\frac{h^3}{12}.$$

4.2.2.6 Structural efficiency

The monoplane spar and biplane spars considered all had the same length and mass per unit span. Therefore, the deflections of each spar can be directly compared to each other, in order to estimate the structural efficiency of biplane spars. A factor ϕ was defined as the ratio of the monoplane and biplane spar tip deflections (under a flapwise load) or as the ratio of tip twist angles (under a torsional load).

$$\phi_{\text{flap}} = \frac{v_{\text{tip,monoplane}}}{v_{\text{tip,biplane}}}, \quad \text{or} \quad \phi_{\text{twist}} = \frac{\theta_{\text{tip,monoplane}}}{\theta_{\text{tip,biplane}}}$$
(4.9)

If $\phi > 1$, then the biplane spar is more structurally efficient than the monoplane spar; conversely, if $\phi < 1$, then the biplane spar is less efficient. This definition of a structural efficiency factor is somewhat similar to the stiffness shape factor described in Ref. [97], which compares the curvature of a shaped cross-section to that of a reference beam with the same area. Instead of considering curvatures of cross-sections, this work considers tip deflections of the entire spar structure.

Table 4.3: Scaling factors for the engineering properties of the biplane beam, used in the analytical model.

Biplane cross-section	α	β
half-height	1/2	1/8
full-height	1/2	1/2

4.3 Results

4.3.1 Analytical model: comparison of biplane beam and monoplane beam

The displacement fields for two variants of the biplane beam (Equations (4.4) and (4.5)) and the monoplane beam (Equation (4.6)) were used to compare their structural performance. Two variants of the biplane beam were analyzed, a biplane beam with "full-height" biplane cross-sections, and a biplane beam with "half-height" biplane cross-sections. Both variants of the biplane beam had a joint length-to-span ratio of $r_j/R = 0.45$ and a gap-to-chord ratio of g/c = 1.31. However, each variant used different values of the scaling factors α and β in Equations (4.4) and (4.5); Table 4.3 summarizes the values that were chosen.* These variants were constructed to bound the design space for biplane beams, similar to the design space used for biplane spars (Section 4.2.2.2).

Along with the scaling factors in Table 4.3, nominal values were substituted into Equations (4.4) and (4.6), and the resulting expressions for flapwise (transverse) displacements, bending moments, and axial force resultants were plotted (Figure 4.17). These nominal values were assumed to be R=100 m, $r_j=45$ m, g=10 m, $q_0=1000$ N/m, $E=40.0\times10^9$ Pa, A=1.5 m², and I=4.5 m⁴.

The tip deflection of the biplane beam with half-height cross-sections is about 62% less than the tip deflection of the monoplane beam (Figure 4.17(a)). The tip deflection of the biplane beam with full-height cross-sections is about 77% less than the monoplane beam. In the inboard region (5 m $\lesssim x \lesssim 35$ m), the half-height biplane beam deflects slightly more

^{*}The values of α and β depend on the geometry of the biplane cross-section. In order to choose these values for both biplane beams, the analytical model used the same cross-sections illustrated in Figure 4.8, assuming nominal values of $b_{RB}=1.81$ m, $h_{SW}=4.84$ m, $b_{SW}=0.10$ m, $h_{SC}=0.15$ m, $h_{RB}=0$ m, and $E=40.0\times10^9$ Pa. These nominal values were used to calculate EA and EI for each cross-section, which together with Equation (A.20) give the appropriate values for α and β .

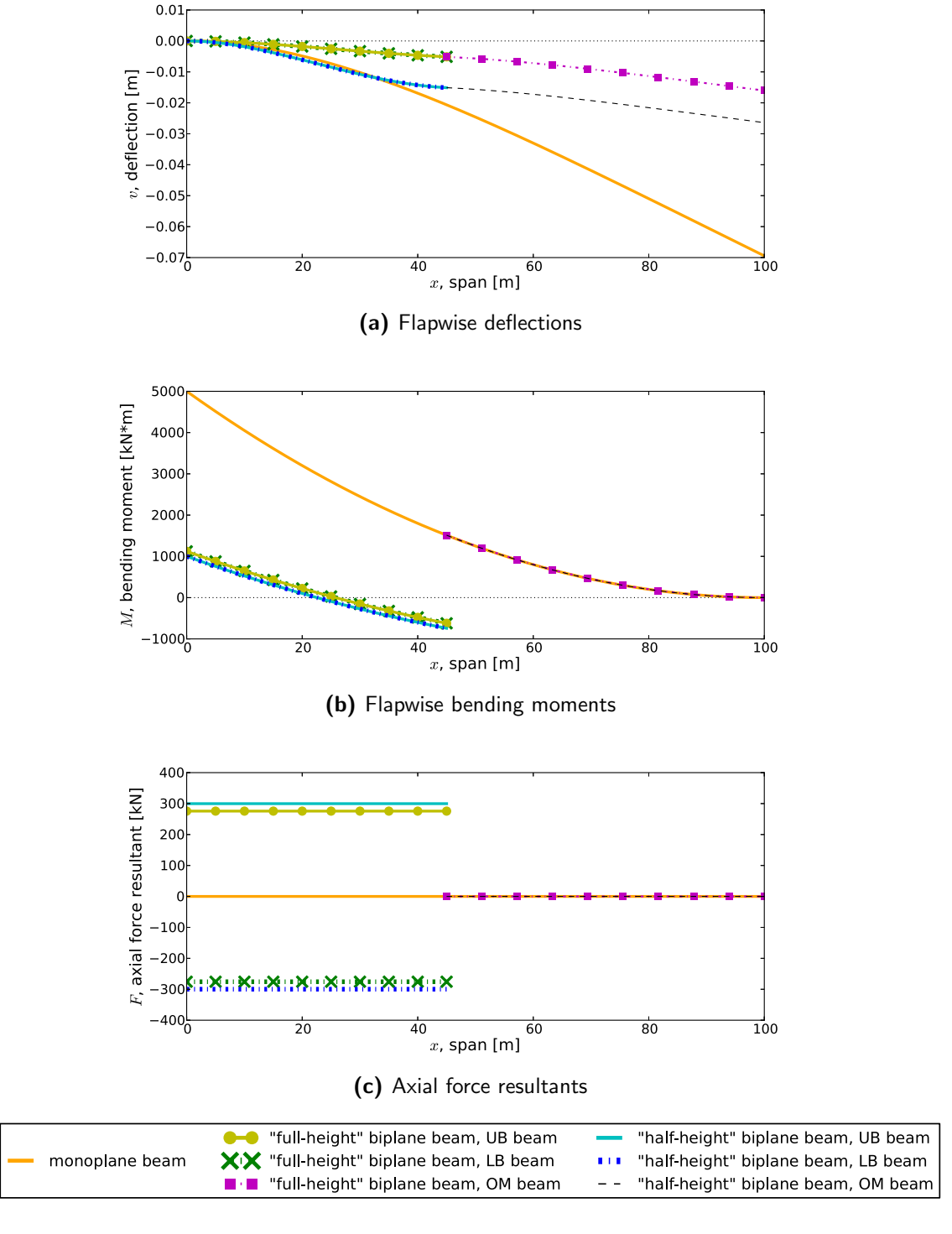


Figure 4.17: Comparison of beam deflections, bending moments, and axial force resultants under equivalent flapwise constant load distributions, calculated with the analytical model: a monoplane beam, a biplane beam with "full-height" biplane cross-sections, and a biplane beam with "half-height" biplane cross-sections. Both biplane beams had design parameters of $r_j/R=0.45$ and g/c=1.31, and were composed of an "upper biplane" (UB) beam, a "lower biplane" (LB) beam, and an "outboard monoplane" (OM) beam.

than the monoplane beam, while the full-height biplane beam does not.

The maximum root bending moment of both biplane beams are about 80% less than the root bending moment of the monoplane beam (Figure 4.17(b)). Past the root of both biplane beams, the bending moment changes sign; this occurs at $x \approx 22$ m for the half-height biplane beam, and at $x \approx 25$ m for the full-height biplane beam. The bending moments in both biplane beams continue to decrease until they reach a minimum at the rigid joint (x = 45 m). At the rigid joint, there is a discontinuity in the bending moment of both biplane beams. Outboard of the joint (45 m $\leq x \leq 100$ m), the bending moments of both biplane beams are identical to the bending moment of the monoplane beam.

The axial force resultants of both biplane beams are constant and nonzero in the inboard biplane region, where the upper biplane element is under tension, and the lower biplane element is under compression (Figure 4.17(c)). Outboard of the joint, the axial force returns to zero in both biplane beams. The axial force is zero everywhere in the monoplane beam.

4.3.2 Computational model

4.3.2.1 Comparison of biplane spar and monoplane spar

The monoplane spar, a biplane spar with "full-height" biplane cross-sections, and a biplane spar with "half-height" biplane cross-sections were analyzed to compare their structural performance under the constant load distribution described in Section 4.2.2.3. Both biplane spars had a joint length-to-span ratio of $r_j/R = 0.452$ and a gap-to-chord ratio of g/c = 1.25.

Cross-sectional Properties: Figure 4.18 shows the flapwise bending stiffness distributions for all three spars. In the inboard region, the biplane spars have larger effective stiffnesses than the monoplane spar, which was a key motivation to investigate the biplane blade concept. In the outboard region, all spars have identical stiffnesses because they each use identical monoplane cross-sections.

Cross-sectional analysis (VABS) was used to calculate the flapwise stiffness at each cross-section in the monoplane spar. For the biplane spars, biplane cross-sections are made of an

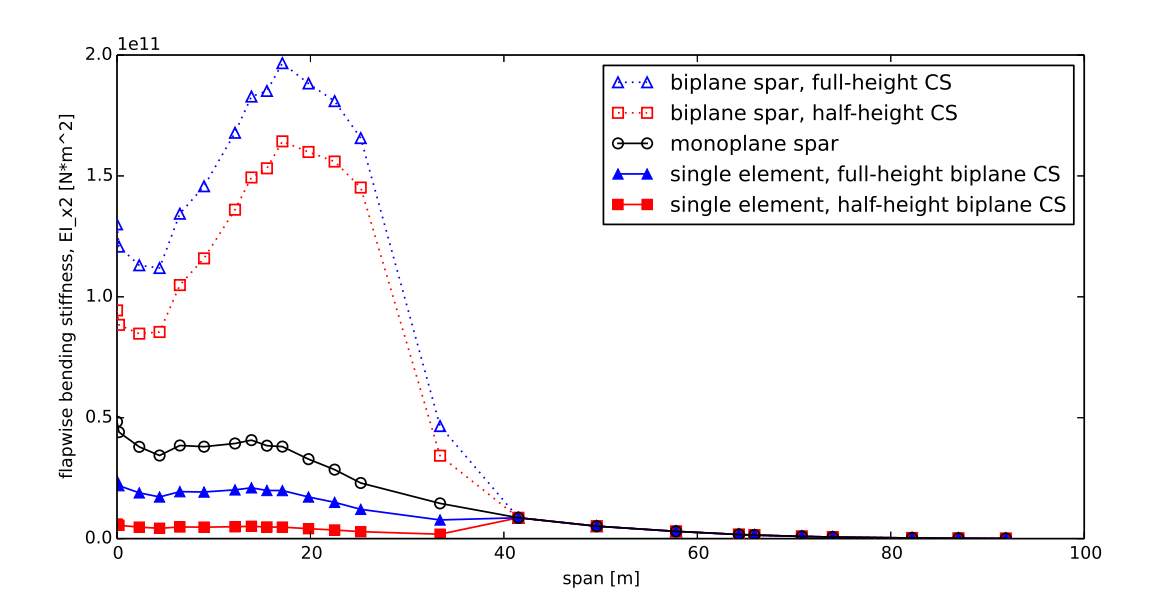


Figure 4.18: Flapwise bending stiffness distributions for a monoplane spar, a biplane spar with "full-height" biplane cross-sections, and a biplane spar with "half-height" cross-sections. Both biplane spars had design parameters of $r_j/R=0.452$ and g/c=1.25. Cross-sectional analysis (VABS) was used to calculate stiffnesses for the monoplane spar. VABS was also used to calculate stiffnesses of "single" elements in full-height and half-height biplane cross-sections. The parallel axis theorem was used with the stiffnesses of "single" elements to approximate the effective flapwise stiffness distributions for both biplane spars.

upper and lower element. VABS was used to calculate the individual stiffnesses of each *single* element (i.e. the stiffness of only the upper element of the biplane cross-sections shown in Figure 4.8, not the effective stiffness of the upper and lower elements as a collective whole). Then, the parallel axis theorem was used to approximate an effective stiffness for the entire biplane cross-section (upper and lower elements). Since the upper and lower elements of the inboard biplane cross-sections are not attached together in the biplane spar, this analysis is a 1st-order approximation of the bending stiffness. As will be shown later, the inboard region of the biplane spar also supports axial loads that play a major role in improving the effective bending stiffness of the entire structure. Nevertheless, the qualitative result in Figure 4.18 still holds: in the inboard region, the biplane spars have larger effective stiffnesses than the monoplane spar.

1D beam analysis: Figure 4.19 shows the flapwise deflections, bending moments, and axial force resultants calculated by the 1D beam finite element analysis from DYMORE. The tip deflection of the biplane spar with half-height cross-sections is about 25% less than the tip deflection of the monoplane spar (Figure 4.19(a)). The tip deflection of the biplane spar with full-height cross-sections is about 35% less than the monoplane spar. The maximum root bending moment of both biplane spars is about 75% less than the root bending moment of the monoplane spar (Figure 4.19(b)). The axial force resultants of both biplane spars are constant and nonzero in the inboard biplane region.

Structural efficiency: Table 4.4 lists the structural efficiency factors of both biplane spars from Equation (4.9), using the tip deflections and tip twist angles calculated by DY-MORE for each of the three load cases (Figures 4.14 and 4.15). For the two tip loads, the structural efficiency factors remained constant across the range of load magnitudes that were considered, because the deflections and twist angles of all spars scaled linearly with the load applied. Both flapwise load cases show that both biplane spars are more structurally efficient (with $1.148 < \phi < 1.528$) at reducing flapwise tip deflections than the monoplane spar.

The torsional tip load shows that the biplane spars have about the same structural efficiency (with $\phi \approx 1.06$) as the monoplane spar in the torsional direction. For the largest torsional tip load (100,000 N-m), all tip twist angles were about 5–6 degrees. While these

Table 4.4: Structural efficiency factors for biplane spars under three different load cases, calculated with Equation (4.9). Both biplane spars have a joint length-to-span ratio of $r_j/R = 0.452$ and a gap-to-chord ratio of g/c = 1.25.

Load case	Structural efficiency, ϕ , of biplane spar				
Loau Case	half-height cross-sections	full-height cross-sections			
flapwise constant load distribution	1.315	1.528			
flapwise tip load	1.148	1.234			
torsional tip load	1.057	1.059			

twist angles were small, in both biplane spars, torsional motions at the joint caused edgewise deflections in the inboard region (Figure 4.20). The largest deflections occurred just inboard of the joint, with a magnitude of about 0.012 m. Conversely, the monoplane spar had little edgewise deflection under the torsional load.

Cross-sectional stresses: Figure 4.21 compares the cross-sectional stresses of both biplane spars and the monoplane spar. The normal components of pointwise stress fields, $\sigma_{11}(x_2, x_3)$, were calculated for cross-sections at each spar station. Maximum values in each cross-section (which correspond to tensile stresses) were plotted above, while minimum values (which correspond to compressive stresses) were plotted below. The maximum and minimum values of stress change for different cross-sections; some jumps in the stress results are observed in the root and joint regions. Section 4.4.2 discusses the possible sources of these jumps in the data.

For the inboard region (0-42 m), the full-height biplane spar tended to have larger maximum normal stresses than the monoplane spar. In the inboard region, the half-height biplane spar tended to have smaller maximum normal stresses than the monoplane spar, except for the stresses in the upper biplane region in between spans of 26-42 m.

For the minimum normal stresses in the inboard region, the magnitude of stresses in the full-height biplane spar tended to be smaller than the monoplane spar. The half-height also tended to have smaller stress magnitudes than the monoplane spar in the inboard region, except for the stresses in the lower biplane region at spans of 0-6 m and 25 m, as well as stresses in the upper biplane region at 4 m.

Contour plots of the normal stresses in selected cross-sections of the monoplane spar

and both biplane spars (Figures 4.22 to 4.24) were plotted with Tecplot 10.0 [98]. In the monoplane spar, the maximum normal stresses are concentrated in the upper spar caps of each cross-section, while the minimum normal stresses are concentrated in the lower spar caps; the stresses in the shear webs are near zero. For the half-height biplane spar (Figure 4.23), in the inboard region (cross-sections A-C), the maximum normal stresses are concentrated in the upper spar caps of the upper biplane region (near $x_3 = 6.1$ m (A), 5.5 m (B), and 5.3 m (C)), while the minimum normal stresses are concentrated in the lower spar caps of the lower biplane region (near $x_3 = -6.1$ m (A), -5.5 m (B), and -5.3 m (C)). In the outboard region (cross-sections D and E), the normal stresses in the half-height biplane spar are identical to the monoplane spar (Figure 4.24). Stresses in the half-height biplane spar (Figure 4.24) show similar behaviors.

4.3.2.2 Buckling analysis

Analytical formulas given in Section 4.2.2.5 were used to estimate two critical buckling criteria: (1) a "global" beam buckling load, and (2) a "local" plate buckling stress.

"Global" beam buckling load: This analysis considered a representative beam similar to the lower biplane element of the biplane spar. The representative beam had a length l=25.2 m, and a flapwise bending stiffness $EI=2.876\times 10^9$ N-m². Substituting these values into Equation (4.7) gives a critical buckling load of $P_{\rm critical}=44700$ kN. Figure 4.19(c) shows that the largest compressive load occurs in the lower biplane element of the half-height biplane spar, and has a magnitude of 269 kN $\ll P_{\rm critical}$. Therefore, the compressive load is far below the critical value.

The representative beam's length was chosen to be the straight length of the lower biplane element, from spar stations 1 to 13 (Table B.2). Since the bending stiffness varies along the span of the biplane spar (Figure 4.18), the representative beam's stiffness was chosen to be uniformly equal to the smallest value that occurs in the lower biplane element; this value occurs at 25.2 m span in the single element of a half-height biplane cross-section. It was expected that the values chosen for l and EI in Equation (4.7) would give a conservative

buckling load.

"Local" plate buckling stress: This analysis considered a representative plate similar to the lower flange in the lower biplane element of the biplane spar. The representative plate had a length a = 25.2 m, width b = 1.5 m, thickness h = 0.0275 m, and material properties equal to those for uniaxial GFRP (Table 4.2). Substituting these values into Equation (4.8) gives a critical buckling stress of $\sigma_{x,\text{critical}} = 17.4$ MPa, which occurs when m = 13. Figure 4.21 shows that the largest compressive stress occurs in the lower biplane element of the half-height biplane spar, and has a magnitude of 5.4 MPa $\sigma_{x,\text{critical}}$. Therefore, the compressive stress is well below the critical value.

The representative plate's length was chosen to be the straight length of the lower biplane element. The width was chosen to be the spar cap width, $b_{SC} = 1.5$ m. Since the flange thickness varies along the span of the biplane spar (Table B.2), the representative plate's thickness was chosen to be uniformly equal to the smallest thickness that occurs in the lower flange; this thickness occurs at spar station 4 ($h = h_{RB} + h_{SC} = 0.0125$ m + 0.0150 m). According to Table B.2, the lower flange is made of both uniaxial GFRP (the spar cap) and triaxial GFRP (the root buildup) between spar stations 1 and 6 (35.7% of the length of the representative plate). However, for this analysis, it was assumed that the representative plate was made entirely of uniaxial GFRP. These material properties (along with the other chosen values) gave the most conservative buckling stress.

The plate buckling stress of the monoplane spar was also calculated with Equation (4.8) as 69.6 MPa, for comparison against the plate buckling stress of the biplane spar. The representative plate for the monoplane spar was identical to the plate for the biplane spar, except that it had a thickness of h = 0.55 m (see spar station 4 in Table B.1, where $h = h_{RB} + h_{SC} = 0.025$ m + 0.030 m). The buckling stress of the plate for the monoplane spar (69.6 MPa) is four times larger than the plate for the biplane spar (17.4 MPa), because the plate for the monoplane spar is twice as thick.

4.3.2.3 Parametric analysis of different biplane spar configurations

Fifteen biplane spar configurations (Figure 4.13) with "full-height" biplane cross-sections were analyzed to compare their structural performance under the constant load distribution described in Section 4.2.2.3. In particular, the effect of two non-dimensional design parameters (joint length-to-span ratio r_j/R , and gap-to-chord ratio g/c) on the tip deflections and root bending moments of each spar was evaluated (Figure 4.25). Overall, tip deflections decrease as the joint length-to-span ratio r_j/R increases (Figure 4.25(a)). For a given joint length-to-span ratio r_j/R , tip deflections always decrease as the gap-to-chord ratio g/c increases. The joint length-to-span ratio r_j/R has a stronger effect on the tip deflection than the gap-to-chord g/c ratio. The biplane spar configuration with the smallest tip deflection has a joint length-to-span ratio of $r_j/R = 0.629$ and a gap-to-chord ratio of g/c = 1.25 (configuration 3 in Figure 4.13).

Similarly, root bending moments also tend to decrease as the joint length-to-span ratio r_j/R increases, as long as $r_j/R \lesssim 0.50$ (Figure 4.25(b)). For a given joint length-to-span ratio r_j/R , root bending moments tend to increase as the gap-to-chord ratio g/c increases, provided that $r_j/R \lesssim 0.40$. If the joint length-to-span ratio grows too large $(r_j/R \gtrsim 0.50)$, the root bending moments begin to increase if the gap-to-chord ratio is large $(g/c \gtrsim 1.0)$. The biplane spar configuration with the smallest root bending moment has a joint length-to-span ratio of $r_j/R = 0.540$ and a gap-to-chord ratio of g/c = 1.25 (configuration 6 in Figure 4.13).

4.4 Discussion

4.4.1 Comparison of results from analytical and computational models

This paper develops analytical and computational models to analyze the structural performance of biplane spars for 100-meter biplane blades. Results from both the analytical model (Figure 4.17) and the computational model (Figure 4.19) in this investigation show similar performance trends for tip deflections and bending moments of biplane beams and spars.

The tip deflections of biplane beams and spars are much smaller than the monoplane beam and spar, respectively. However, if the inboard region is too flexible (as in the half-height biplane beam and spar), inboard deflections of the biplane beam and spar can be slightly larger than the monoplane beam and spar. These inboard deflections can be tuned by adjusting β (the ratio of flapwise bending stiffness in the outboard region to the inboard region) in the analytical model (Equation (4.4)). The root bending moment of biplane beams and spars is also much smaller than the monoplane beam and spar.

Inboard of the joint, bending moments are reduced by a countering moment produced by axial forces in the biplane region (Figures 4.17(c) and 4.19(c)) and reaction forces at the joint. As the analytical model shows in Figure 4.17(b), the root bending moments for the biplane beam ($\approx 1000 \text{ kN-m}$ for the UB beam, and $\approx 1000 \text{ kN-m}$ for the LB beam) do not add up to the root bending moment of the monoplane beam ($\approx 5000 \text{ kN-m}$). The computational model shows a similar behavior in Figure 4.19(b). The countering moment also explains why the bending moments decrease inboard of the joint, in the biplane-monoplane transition region. Inboard of the transition region, the bending moments increase again and reach a local maximum near the root. The bending moments in the biplane beam (Figure 4.17(b)) also decrease at the joint, albeit abruptly, because the joint was assumed to be rigid and the analytical model did not include a biplane-monoplane transition region. Reduced inboard bending moments are also seen in joined wings [94], where the tail is connected to the wing to produce similar axial forces and reaction forces inboard of the joint.

Past the root of the biplane beam, the bending moment changes sign (Figure 4.17(b)) because there is an inflection point in the deflection curve, which is 4th-order in x (Equation (4.4)). This sign reversal in the bending moment is also seen in the biplane spar (Figure 4.19(b)). In the inboard region of both biplane beams, the bending moment curves also have the same shape (Figure 4.17(b)); the curve for the full-height biplane beam is merely shifted up from the half-height biplane beam by a constant, which depends upon β (Equation (4.4)). This behavior is also seen in the bending moments for both biplane spars (Figure 4.19(b)).

Overall, many of the features in the deflection, bending moment, and axial force resultant

curves from the computational model also exist in the analytical model, indicating good qualitative agreement between the two models. This suggests that the analytical model reveals some of the underlying mechanisms for the structural performance of biplane spars, and may be useful as a preliminary design tool for future work.

4.4.2 Cross-sectional stresses

While the biplane spar improved the tip deflections and inboard bending moments, inboard stresses were not always improved. The magnitude of inboard cross-sectional stresses can sometimes be larger in the biplane spar than in the monoplane spar (Figure 4.21). However, some of these large stresses can be explained by jumps in the data, as the maximum and minimum values of stress change for different cross-sections. The jumps near the root are seen in the monoplane spar, as well as both biplane spars. There are also jumps near the joint of both biplane spars, where the biplane transitions into a monoplane. All jumps in the data are confined to the root and joint regions.

For both biplane spars and the monoplane spar, the jumps in the data near the root are due to different mesh geometries and sizes in both the 1D beam models and the 2D cross-sectional models; these jumps are confined to the root region (at spans of 0-15 m, highlighted in green). For example, the length of the 1D beam element between stations 1 and 2 is only 0.2 meters, while the length of the 1D beam element between stations 2 and 3 is 2.1 meters (Tables B.1 to B.3). Within a 2D cross-section mesh, the sizes of the 2D quadrilateral elements sometimes varied greatly between materials. In particular, the biaxial GFRP laminate was much thinner than the rest of the laminates. Considering spar station 1, the biaxial GFRP laminate thickness was 0.003 meters in the shear web, compared to 0.013 meters for the uniaxial GFRP laminate (the next thinnest material) in the spar cap. At the sharp inside corners of the cross-section, these two materials are adjacent to each other (Figure 4.7). Transition quadrilateral elements (a feature provided in TrueGrid) were used to minimize the size differences between elements in different materials in the cross-section, but Figure 4.21 shows that jumps in the results still exist.

For both biplane spars, the jumps in the data near midspan are due to the discontinuity in the flapwise load profile applied near the joint (Figure 4.14(b)); these jumps are confined to the joint region (at spans of 25-42 m, highlighted in purple), where the load profile abruptly changes from a magnitude of $F_0/2$ in the biplane region to F_0 in the monoplane region. In particular, the lower biplane region has large compressive stresses just inboard of the joint (at a span of 33 m).

Large inboard stresses can be further explained by the contour plots of normal stresses in cross-sections A-C of the biplane spars (Figures 4.23 and 4.24); thin walls in these biplane cross-sections likely concentrate stresses and lead to larger stress magnitudes. Note, however, that these biplane spars were not optimized designs. Instead, they were simply designed to have the same mass per unit span as the monoplane spar (which lead to thinner-walled cross-sections) to demonstrate some preliminary structural benefits. Therefore, these stress results present an opportunity for improvements that are needed in future designs.

4.4.3 Buckling analysis

The estimated buckling criteria given in Section 4.3.2.2 showed that the biplane spar does not buckle under the applied loads (given in Section 4.2.2.3). The simply supported boundary conditions chosen for the buckling analysis are conservative, since it is expected that the boundary conditions are somewhat stiffer than simple supports. Nevertheless, the thinner walls in the biplane cross-sections greatly reduced the critical buckling stress, compared to thicker walls in the monoplane cross-sections. This suggests that the possibility of weight reductions from thinner walls in the biplane spar may be limited by the buckling stability of its thinner walls.

4.4.4 Structural efficiency

Table 4.4 shows that biplane spars are more efficient than the monoplane spar at supporting flapwise loads, which arise from the incoming wind. This is a desirable and significant improvement, since wind turbine blades need adequate clearance from the tower to operate

safely. For the same mass as a monoplane spar, the biplane spar reduced tip deflections, which suggests that weight reductions are possible with a realistic biplane blade design.

Under a torsional tip load, the biplane spars performed similarly to the monoplane spar, twisting about 5–6 degrees under a 100,000 N-m torque. However, the torsional and edgewise motions are coupled in biplane spars (Figure 4.20), because the upper and lower biplane elements are offset from the twist axis (Figure 4.8), and twist at the joint induces edgewise deflections in the biplane inboard region. Conversely, in the monoplane spar, the twist axis is centered inside each of its cross-sections, so there are no edgewise deflections under torsional loads. The torsional-edgewise coupling in biplane blades is a unique structural challenge that must be considered carefully in future studies.

4.4.5 Parametric analysis of different biplane spar configurations

A parametric analysis of different biplane spar configurations shows that the joint length-to-span ratio has a strong influence on structural performance (Figure 4.25). Tip deflections of biplane spars are reduced overall as both the joint length-to-span ratio r_j/R and gap-to-chord ratio g/c are increased, but tip deflections depend more strongly on r_j/R than g/c. However, this does not imply that the inboard biplane region should extend out along the entire span of the spar; the results for root bending moments should also be considered. The parametric analysis shows that root bending moments of biplane spars tend to decrease as joint length-to-span ratio increases, but only up to a point. If the joint length-to-span ratio grows too large $(r_j/R \gtrsim 0.50)$ when the gap-to-chord ratio is also large $(1.0 \lesssim g/c < 1.25)$, the root bending moments begin to increase. For the range of parameters examined in this study, $r_j/R \approx 0.5$ and $g/c \approx 1.0$ give an optimal biplane spar design, with both small tip deflections and small root bending moments.

4.4.6 Outlook & future work

The structural benefits described above suggest that the biplane blade may be an attractive design for the next generation of large wind turbine blades. For a uniform distributed load,

biplane spars were shown to deflect less and to have smaller root bending moments than the monoplane spar. These results suggest the same conclusion from past work: for a monoplane spar of fixed length, it is likely possible to construct a *lighter* biplane spar with an *equal* tip deflection. Within the limits of buckling considerations, these benefits can lead directly to weight reductions for large blades that can reduce the cost of the blades, the gravitational loads on the blades, as well as the inertial loads on the rest of the wind turbine. Thus, it is likely that this design will have significant structural benefits for large (3-7 megawatt) and ultra-large (8-10 megawatt) turbines for both land-based and offshore applications.

The analytical and computational models developed here were created to be a platform for future research of biplane blades. Many opportunities exist for improved biplane blade designs, particularly to mitigate large inboard stresses and improve buckling resistance. The analytical model may also be a useful tool for future preliminary designs. While the 1D FEA used in this paper was sufficiently accurate to compare biplane spars to each other with a parametric analysis, 3D FEA should be used for future studies of the two biplane spars that performed best (configurations 3 and 6 in Figure 4.13). This will increase the fidelity of the model, especially near the joint of the biplane spar.

While the results from this investigation suggest that blade weight may be reduced with the biplane blade design, more load cases are necessary to confirm this observation. Once the airfoils have been added over the biplane spar (step 2 of the "structures-first" approach) to form a "full" biplane blade, then actual IEC design load cases [82] will be used. Additionally, future studies will investigate the torsional and edgewise bending response of the inboard biplane region, since these two responses may be coupled. Although manufacturing considerations were outside the scope of this paper, it is important to note that the manufacture of the joint will require some consideration and needs to be addressed in future efforts. The ultimate goal of this research is to design a biplane blade with airfoils, and perform a direct comparison to a monoplane blade. This will require aeroelastic simulations, a fatigue analysis, and a more detailed buckling analysis.

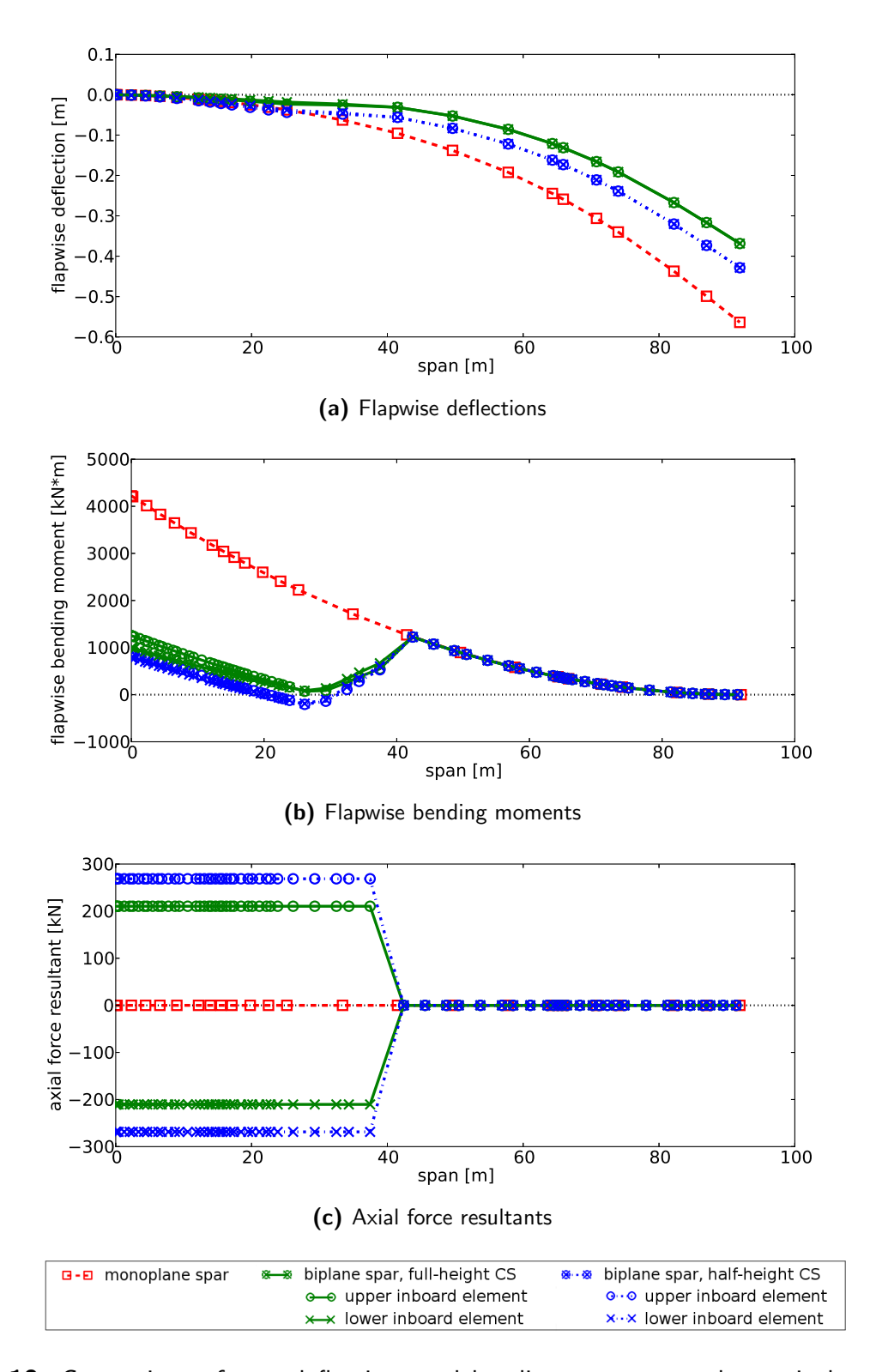


Figure 4.19: Comparison of spar deflections and bending moments under equivalent flapwise constant load distributions, calculated with the computational model (DYMORE): a monoplane spar, a biplane spar with "full-height" biplane cross-sections, and a biplane spar with "half-height" biplane cross-sections. Both biplane spars had design parameters of $r_j/R=0.452$ and g/c=1.25.

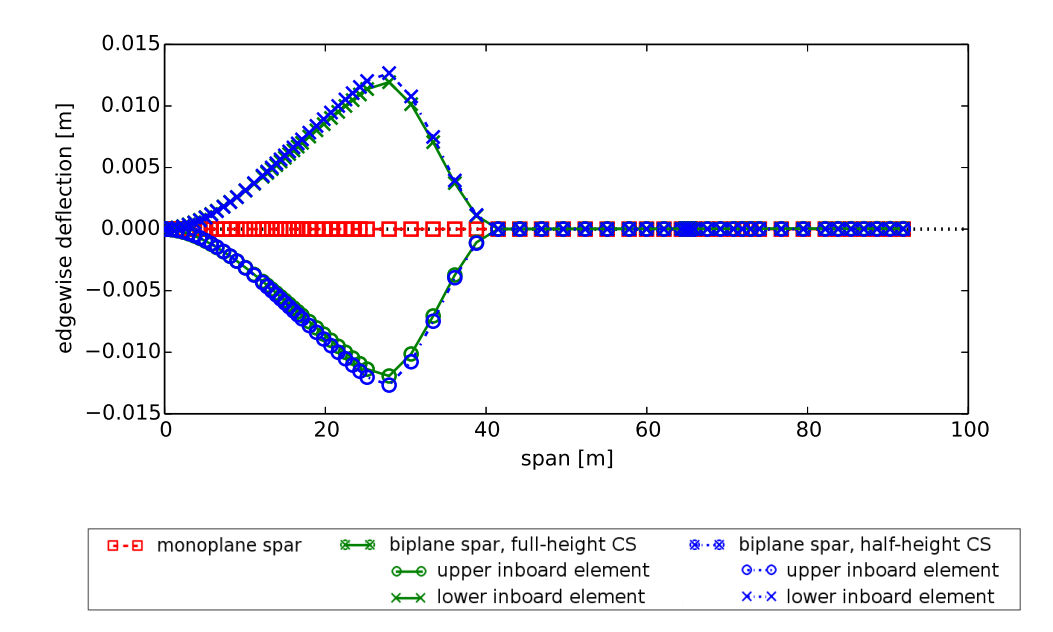


Figure 4.20: Comparison of edgewise deflections of spars under a 100,000 N-m torsional tip load, calculated with DYMORE: a monoplane spar, a biplane spar with "full-height" biplane cross-sections, and a biplane spar with "half-height" biplane cross-sections. Both biplane spars had design parameters of $r_j/R=0.452$ and g/c=1.25.

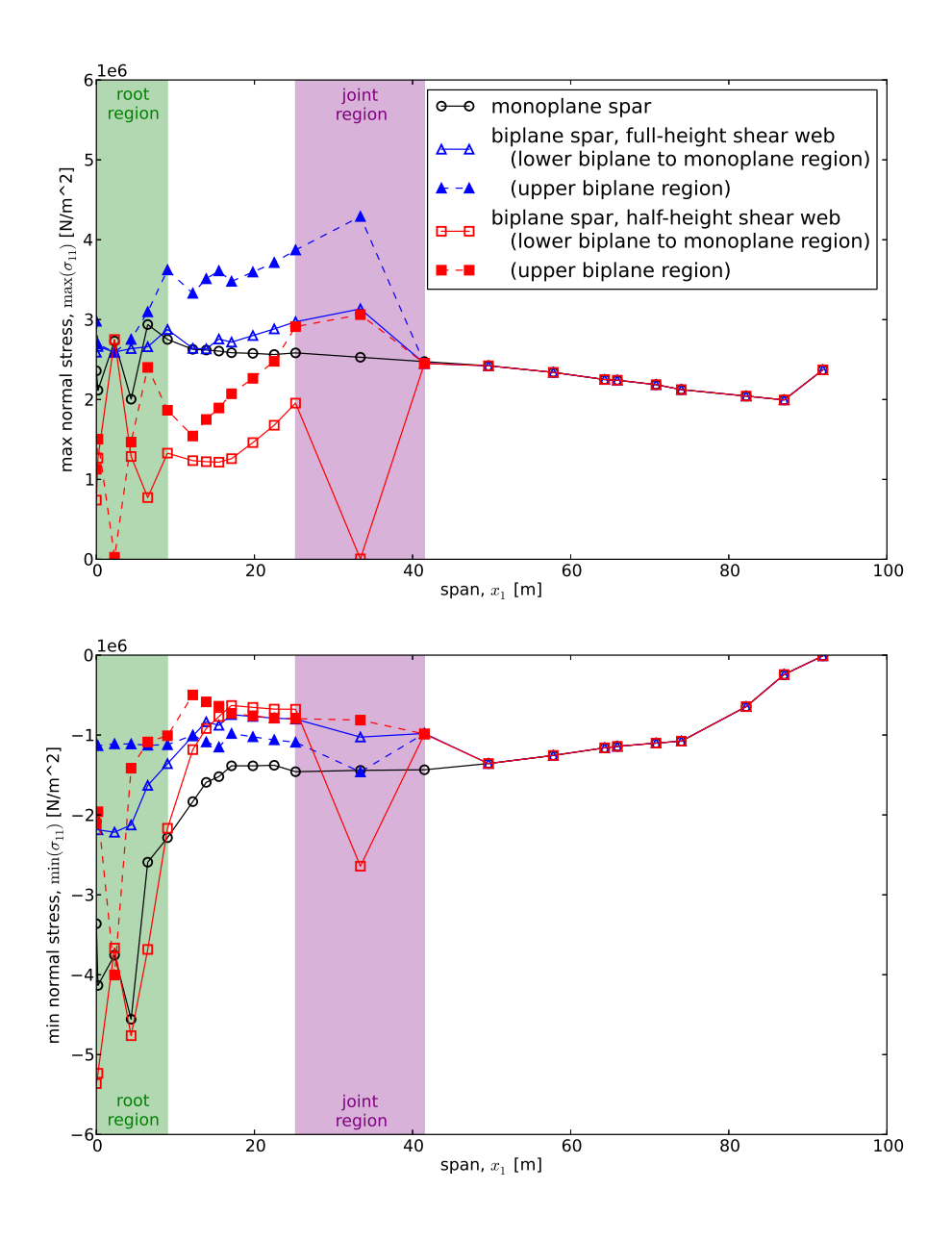
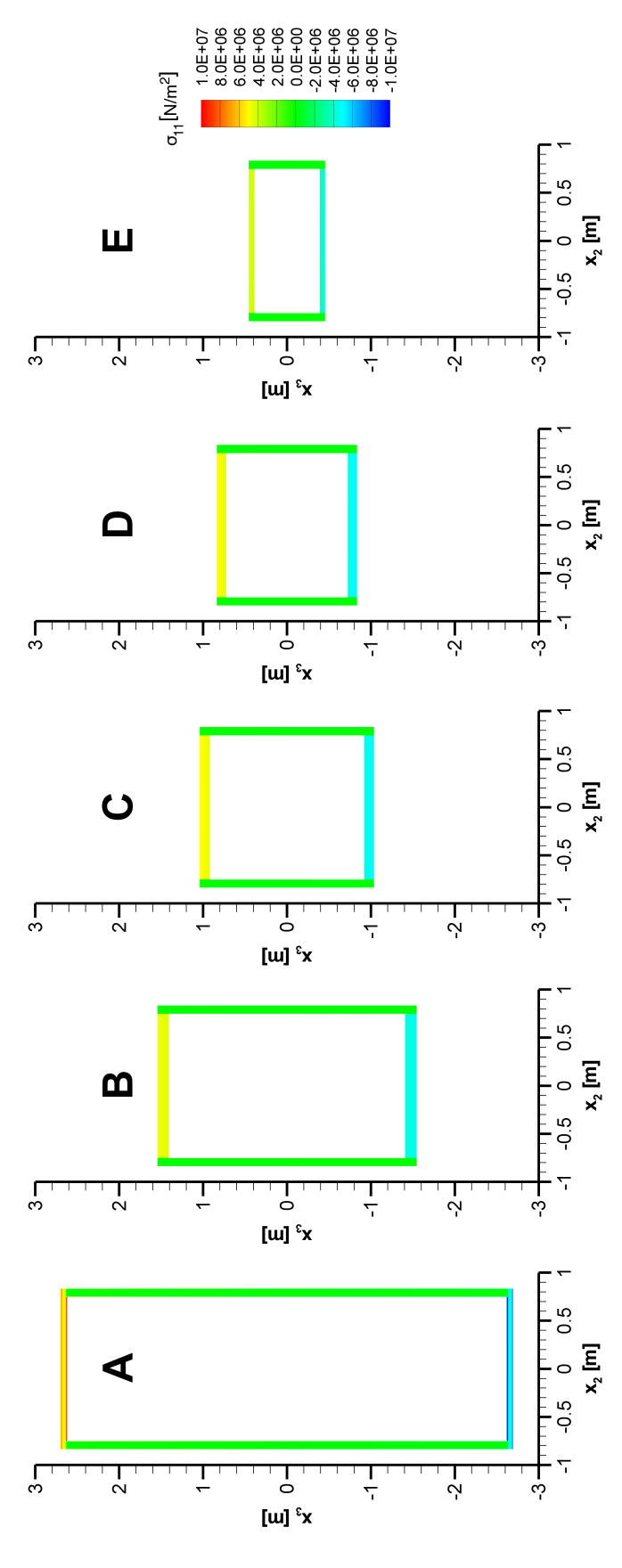
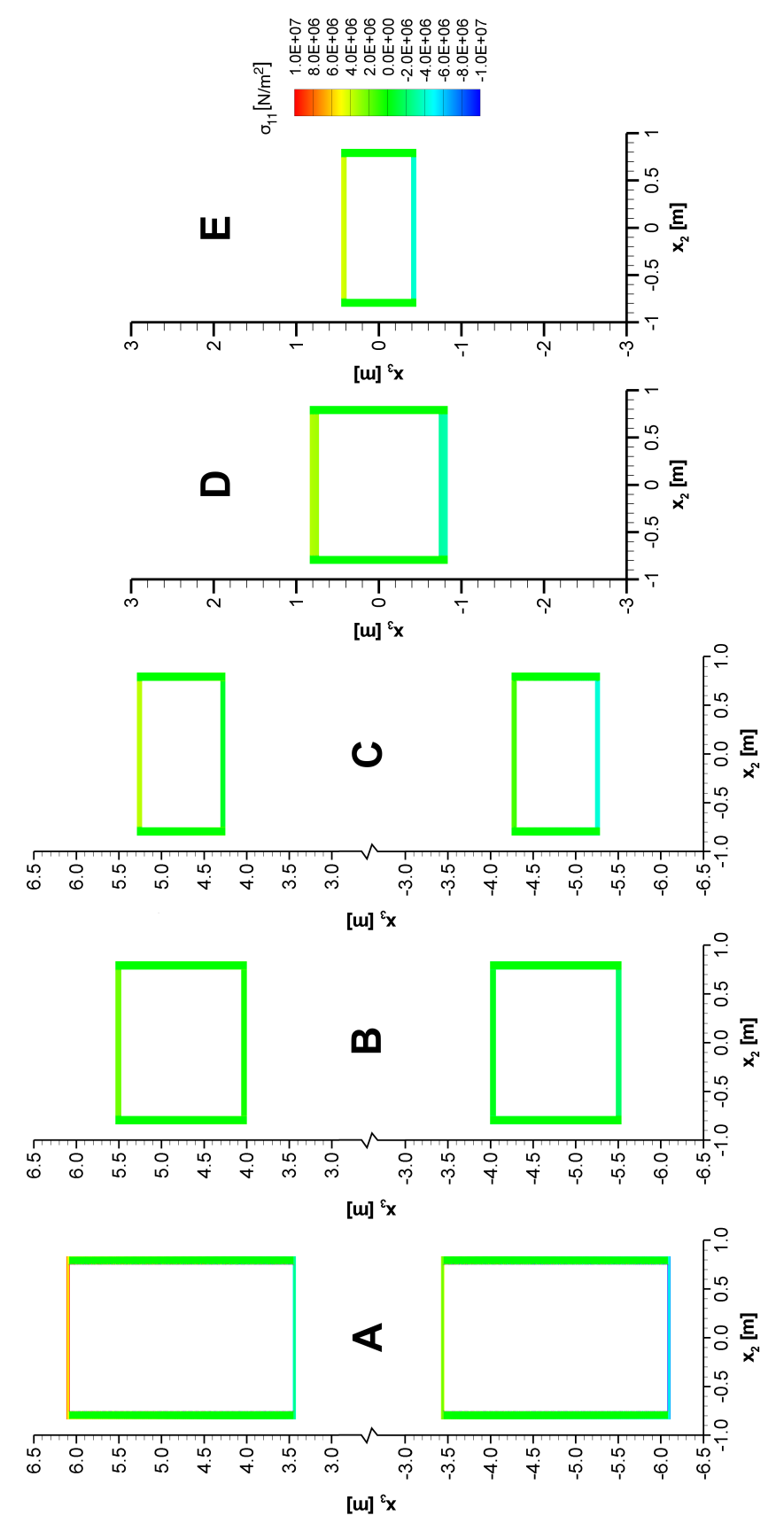


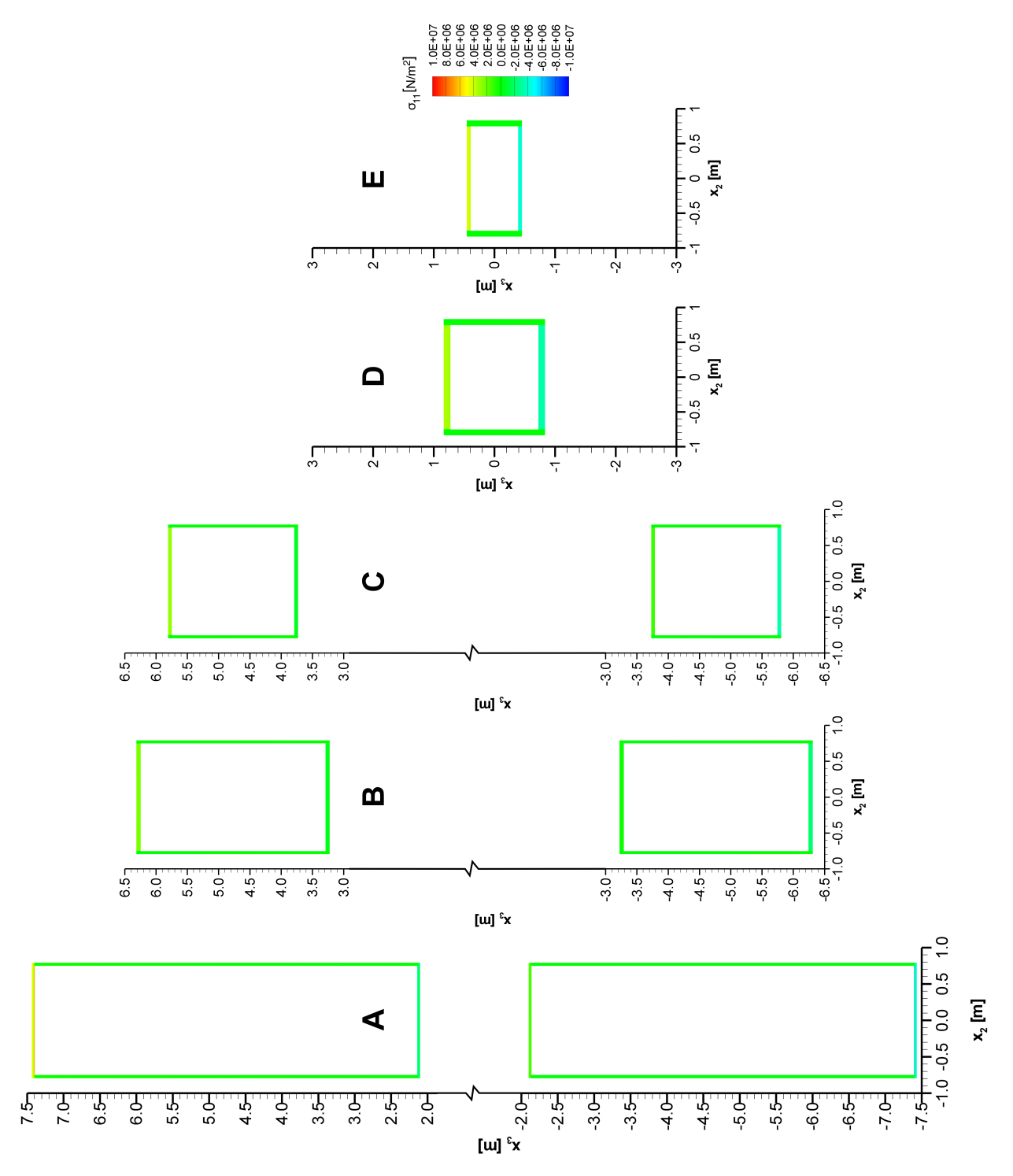
Figure 4.21: Comparison of cross-sectional stresses along the span of three spars under equivalent flapwise constant load distributions, calculated by VABS. Maximum/tensile (top) and minimum/compressive (bottom) normal stress components are compared for a monoplane spar, a biplane spar with "full-height" biplane cross-sections, and a biplane spar with "half-height" biplane cross-sections. The jumps in the data are confined to the root and joint regions. Both biplane spars had design parameters of $r_j/R=0.452$ and g/c=1.25.



A: 0% span (root, station 1), B: 18.6% span (max chord location on Sandia blade, station 10), C: 36.3% span (station **Figure 4.22:** Normal stresses $\sigma_{11}(x_2,x_3)$ in selected cross-sections of the monoplane spar under a flapwise constant load distribution. 14), **D**: 45.2% span (station 15), **E**: 71.7% span (station 19).



under a flapwise constant load distribution. A: 0% span (root, station 1), B: 18.6% span (max chord location on Sandia **Figure 4.23:** Normal stresses $\sigma_{11}(x_2,x_3)$ in selected cross-sections of the "half-height" biplane spar $(r_j/R=0.452$ and g/c=1.25)blade, station 10), **C**: 36.3% span (station 14), **D**: 45.2% span (joint, station 15), **E**: 71.7% span (station 19)



under a flapwise constant load distribution. A: 0% span (root, station 1), B: 18.6% span (max chord location on Sandia **Figure 4.24:** Normal stresses $\sigma_{11}(x_2,x_3)$ in selected cross-sections of the "full-height" biplane spar $(r_j/R=0.452$ and g/c=1.25)blade, station 10), **C**: 36.3% span (station 14), **D**: 45.2% span (joint, station 15), **E**: 71.7% span (station 19)

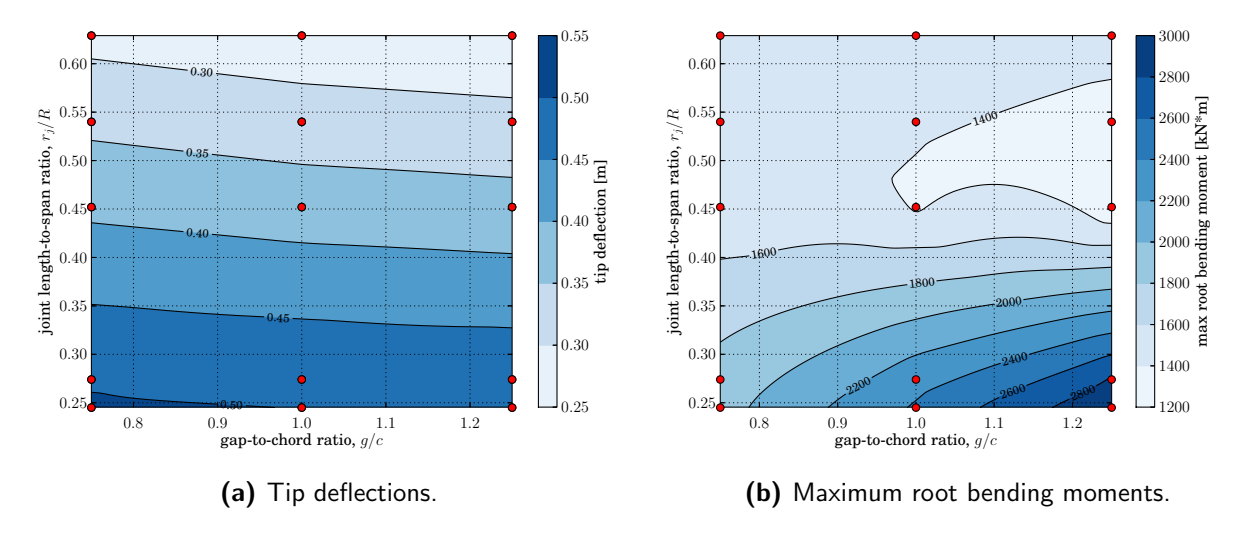


Figure 4.25: Effect of two design parameters (joint length-to-span ratio r_j/R , and gap-to-chord ratio g/c) on the structural performance of a biplane spar under a flapwise constant load distribution. Lighter filled contours show smaller tip deflections and smaller root bending moments. Red points show the location (r_j/R) and g/c0 of each biplane spar configuration on the contour plot.

CHAPTER 5

Aero-structural analysis of a full 100-meter biplane wind turbine blade

5.1 Introduction

Chapters 3 and 4 described earlier studies of the biplane blade, which focused on the design of its internal spar. In Chapter 3, a simple aero-structural investigation was conducted on a 50-meter biplane spar, which was made of isotropic materials and constructed with uniform cross-sections along its span. This investigation validated the approach of modeling the spar with 1D beam finite elements against the modeling approach of 3D tetrahedral finite elements. Finally, a parametric study of nearly 800 biplane spar configurations revealed the basic shape of the biplane spar that gave the smallest tip deflections: the inboard biplane region should extend to about 50% span. (This was considered to be the near-optimal configuration.) The main limitations of this study were: (1) spars were made of isotropic materials, when in reality they are made of composite materials, (2) the spar geometry was highly simplified, since it used uniform cross-sections along the span, when in reality spars taper in thickness from root to tip, and (3) only flapwise static loads were considered, when in reality wind turbine blades must support dynamic loads in multiple directions (although flapwise loads are the primary design driver, edgewise loads* from blade weight may become the design driver for very large 100-meter blade designs).

In Chapter 4, a more complex structural investigation was conducted on a 100-meter biplane spar, which was made of composite materials and constructed with realistic cross-

^{*}As mentioned earlier in Section 2.2, it is important to clearly define the edgewise and flapwise directions, since wind turbine blades are pre-twisted. In this dissertation, the "edgewise" direction refers to the direction that is in-the-rotor-plane. Similarly, the "flapwise" direction refers to out-of-the-rotor-plane.

sections derived from the Sandia reference blade. This addressed the first two limitations of the prior investigation. In addition to static flapwise loads at the tip and distributed along the span, static torsional tip loads were also considered. However, edgewise loads were not considered, since the airfoil exterior (which provides significant edgewise stiffness to support edgewise loads) was negelected from the biplane spar. A parametric study of 15 biplane spar configurations was also conducted, which sought spar geometries that minimzed both tip deflections and root bending moments. This yielded a similar optimal configuration to the prior investigation: the inboard biplane region should extend to about 50% span. The main limitation of this study were: (1) only a few load cases were considered (notably edgewise loads were not considered), and (2) the airfoil exterior was neglected from the biplane spar.

In this study, we can now ask: is the biplane blade more structurally efficient than a conventional 100-meter blade? To answer that question, we need to complete step 2 of the "structures-first" approach: fit the airfoil exterior over the optimized biplane spar from the investigation in Chapter 4. This will allow us to conduct an aero-structural investigation of a *full* biplane blade. This study will only consider a single configuration of the biplane blade, which is symmetric in the flapwise direction, with no stagger in the inboard biplane region.

This investigation's main objective is to study more load cases on a single biplane blade geometry, to further examine the feasibility of the biplane blade design. This will build upon previous work with biplane spars, which neglected several components from the blade geometry to conduct initial analyses. This investigation will include the airfoil exterior, the root joint, and a third shear web, which were all previously neglected.

5.2 Methods

The studies described in Chapters 3 and 4 concentrated on step one of the "structures-first" design approach for a biplane blade: designing the internal biplane spar structure. Here, we complete step two of this approach: fitting the aerodynamic exterior over the biplane spar to construct a "full" biplane blade. A technology stack was developed to manage the

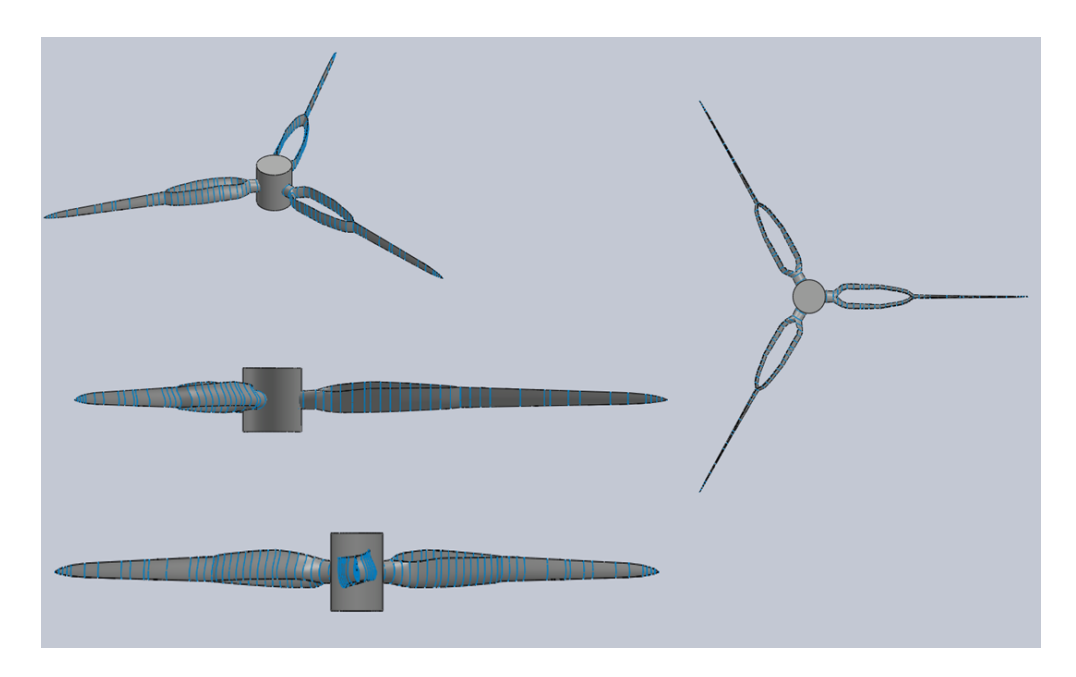


Figure 5.1: CAD rendering of rotor with biplane blades (flapwise symmetric, no stagger configuration). Image credit: Christos Voutsaras.

design and analysis procedures (Figure 5.2). A blade definition spreadsheet served as the main input file that described the blade geometry, laminate schedule, material properties, and 1D beam topology of the biplane blade. These data sets were manipulated with several different software packages to: (1) create a 3D wireframe visualization of the blade geometry (Section 5.2.1); (2) perform 2D cross-section analysis (Section 5.2.2); and (3) construct 1D beam finite element models (Section 5.2.3), apply loads (Section 5.2.4), and predict displacements and forces in the blade.

As described earlier in Chapters 3 and 4, DYMORE and VABS were selected as structural analysis tools because they are fast and accurate, when compared to three-dimensional finite element analysis (3D FEA) [67, 68]. While it is true that 3D FEA is highly accurate, it was judged to be too time consuming to set up the models and compute the results. DYMORE and VABS were also selected because they have successfully modeled helicopter blades [61, 69, 70] and wind turbine blades [68, 71, 72, 73, 99]. This 1D modeling technique has also been previously validated against 3D FEA for biplane spar structures [35]. Furthermore, several researchers have also used 1D beam finite elements to model a joined wing [94, 74, 75, 76, 77]; which has a joint that resembles the joint of the biplane blade.

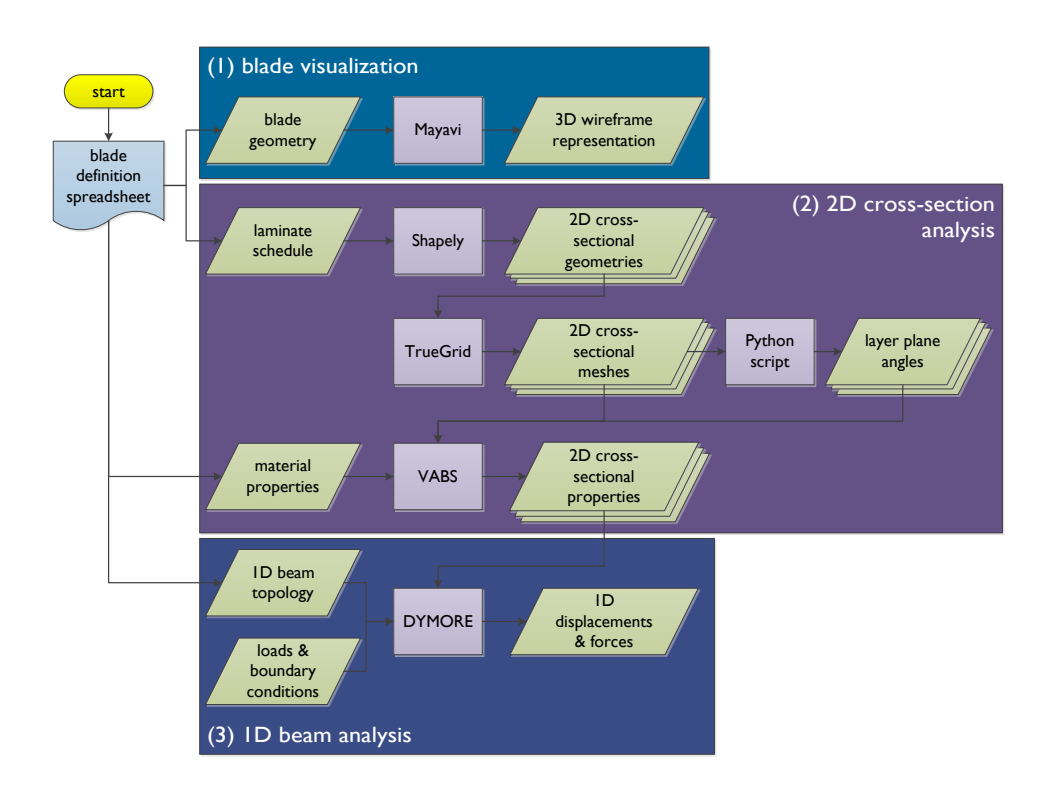


Figure 5.2: Technology stack with design and analysis procedures for a full biplane blade. Blue wavy polygons represent input files, green paralellograms represent data sets, and purple rectangles represent software packages.

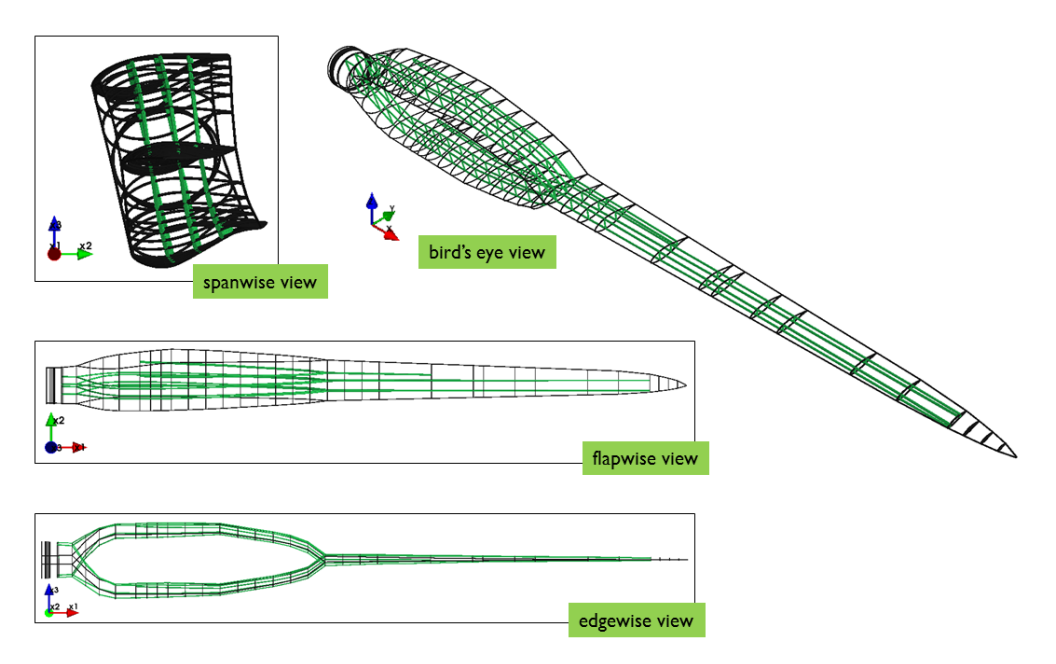


Figure 5.3: Wireframe representation of the full biplane blade. In this configuration, the inboard biplane region is symmetric in the flapwise direction and unstaggered.

5.2.1 Blade geometry

A tool was developed to visualize blade geometries with a wireframe, so that the overall geometry could be quickly edited and verified. Two items were used to define the overall blade geometry: airfoils and shear webs. A spreadsheet[†] was used to define the blade geometry with a series of stations along its span. Each blade station was defined by its spanwise location, airfoil profile, chord length, twist angle, pitch axis fraction, and chordwise locations of shear webs. Then, a wireframe representation of the blade geometry was drawn with Python-based software (the 3D visualization package Mayavi 4.3.1 [101]), so it could be visually checked. If the geometry needed to be edited, the spreadsheet could be modified and a new wireframe representation could be generated.

Two spreadsheets were developed: one to define the Sandia blade, and another to define a biplane blade (Figure 5.3). The Sandia blade spreadsheet was populated with geometry data for 34 stations from [9]. The biplane blade spreadsheet reused geometry data from the Sandia blade in its root region and its monoplane outboard region (stations 1-9 and 21-34,

 $^{^{\}dagger}$ This blade definition spreadsheet was parsed with Python-based software (the data analysis library, pandas 0.12.0 [100]).

respectively, in Table 18 of [9]). New geometry data was developed for the biplane inboard region (Table D.1) based on the design guidelines developed in earlier studies (Chapters 3 and 4), which suggested using 50% thinner biplane airfoils with a gap-to-chord ratio of about 1.0–1.2, and placing the mid-blade joint near 50% span. The root joint was placed at 4.7% span, slightly outboard from the start of the primary shear webs (2.4% span). In this blade configuration, none of the biplane airfoils were staggered. For simplicity, the upper and lower airfoils were identical. In order to provide more resolution of the geometry near the mid-blade joint, 6 new stations were added at 30.3%, 33.1%, 38.5%, 41.2%, 46.6%, and 49.3% span. New transition airfoils for these stations were developed by blending the coordinates of airfoils at adjacent stations. However, no attempt was made to aerodynamically characterize these transition airfoils. Finally, the biplane blade used the same twist distribution[‡] as the Sandia blade [9].

5.2.2 2D cross-sectional analysis

5.2.2.1 Cross-sectional geometry and laminate thicknesses

Once an overall blade geometry was verified, the cross-sectional geometry of the internal blade structure was defined at each station. For a given station, laminate thicknesses were chosen for each of the parts in the internal structure (spar caps, shear webs, leading edge panel, aft panel, trailing edge reinforcement, root buildup) to define its cross-sectional geometry. These laminate thicknesses were added to the same spreadsheet described in Section 5.2.1. Then, each cross-section geometry was drawn with Python-based software (the 2D polygon manipulation package Shapely 1.2.17 [102]), which represented each structural part with polygons.

The Sandia blade spreadsheet was populated with laminate thickness data for 34 stations from [9]. As before, the biplane blade spreadsheet reused laminate thickness data from the Sandia blade (Figure 5.4) in its root region and monoplane outboard region, so that the cross-sectional properties would be identical between each blade. New laminate thicknesses

[‡]Note: all previous work with biplane spars in Chapters 3 and 4 neglected twist.

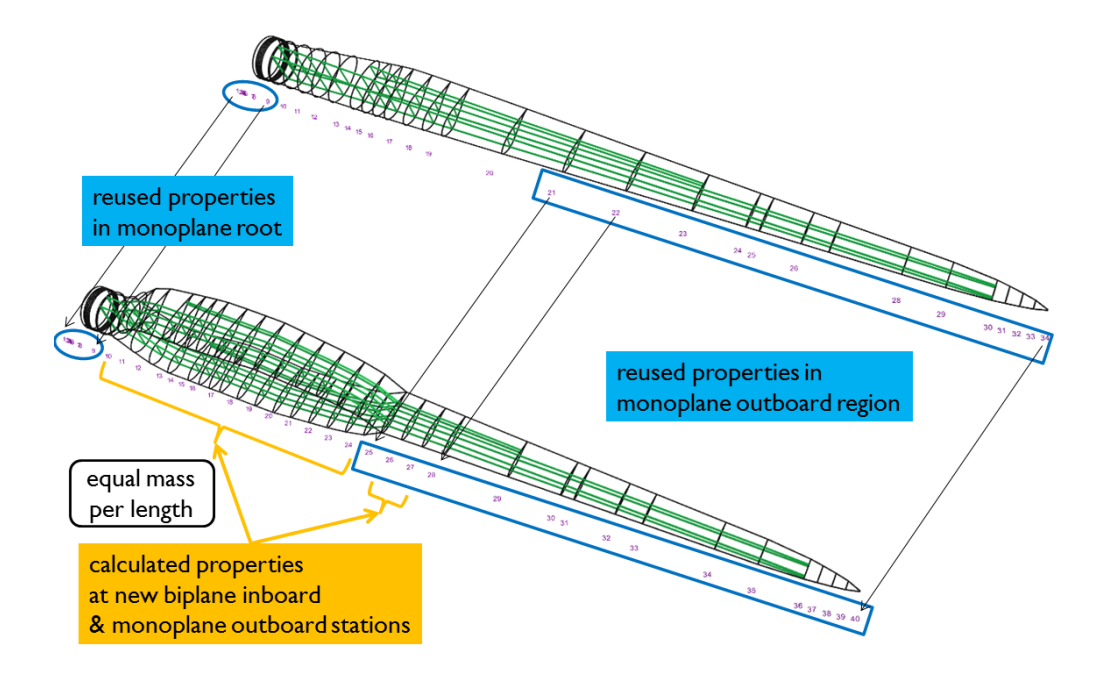


Figure 5.4: The biplane blade reused cross-section properties from the Sandia blade in its monoplane root and monoplane outboard regions. A new biplane inboard region was designed to have equal mass per length as the Sandia blade. New cross-section properties were calculated at these new biplane inboard stations, as well as at two new monoplane outboard stations just outboard of the joint.

were developed for the biplane inboard region (Table D.2) so that the biplane blade and the Sandia blade each had the same mass per unit span. For example, the biplane station at 19.5% span in the biplane blade had the same mass per unit length as the monoplane station at 19.5% span in the Sandia blade.

Four steps were taken to choose the laminate thicknesses for each of the biplane stations. First, all of the main structural part thicknesses were cut in half (spar caps, leading edge panel, trailing edge reinforcement, aft panels). Second, the shear web heights were also cut in half, since each of the biplane stations used $\approx 50\%$ thinner airfoils than the original monoplane stations. Third, some of the material thicknesses for the external and internal surfaces were altered. The triax layer of the external surface was cut to 2.5 mm in the biplane station (from 5 mm in the original monoplane station). The gelcoat layer of the external surface was left unaltered at 0.6 mm, since it represents a thin layer of paint that cannot be realistically manufactured any thinner. The triax layer of the internal surface was cut to 3

mm in the biplane station (from 5 mm in the original monoplane station). Fourth, the spar cap thicknesses were either thickened or thinned until the mass of each corresponding station matched within $\pm 0.5\%$. The spar caps were altered because, out of all the structural parts, the spar caps accounted for the largest mass fraction (20-30%) at each station. Therefore, altering the spar cap thickness was the quickest way to match the masses of each station. No attempt was made to alter the thicknesses of other parts further.

5.2.2.2 Mesh generation and cross-sectional properties

As before in earlier studies (Chapters 3 and 4), the 2D cross-sectional properties at each blade station were calculated with VABS 3.6 [63, 64]. VABS uses the variational asymptotic method [65, 66] to calculate the mass and stiffness matrices for arbitrary beam cross-sections. Three sets of data are needed for the cross-sectional analysis: (1) a mesh of the cross-sectional geometry, (2) material properties for each element in the mesh, and (3) the layer plane angle[§] for each element in the mesh. Using this information, VABS creates a finite element representation of the cross-section to calculate mass and stiffness matrices, which represent the cross-section's Timoshenko beam properties.

Once the cross-section geometries were created, TrueGrid [103, 104] was used to generate meshes for each cross-section. Python scripts were developed to assign the appropriate material properties and layer plane angle to each element in the mesh. The biplane blade and the Sandia blade used the same material properties (Table 5.1). Figure 2.9 shows the materials used for each structural part.

[§]The layer plane angle is the angle between the horizontal axis and the material ply plane of an element in the mesh. See Figure 4 in [64] for more details.

[¶]One caveat about the meshes: some corners of the internal surface that wrapped around right angles at the edge of aft panel 2 were neglected (see lower inset in Figure 5.5), to facilitate the creation of cross-sectional meshes. This was expected to have a negligible effect on cross-sectional properties. However, if VABS is used to recover cross-sectional stresses, it is likely that stress concentrations will be located near these neglected corners. A large amount of time was needed to construct each cross-section mesh, due to its complex geometry, so the corners neglected from the mesh were judged to be an acceptable compromise.

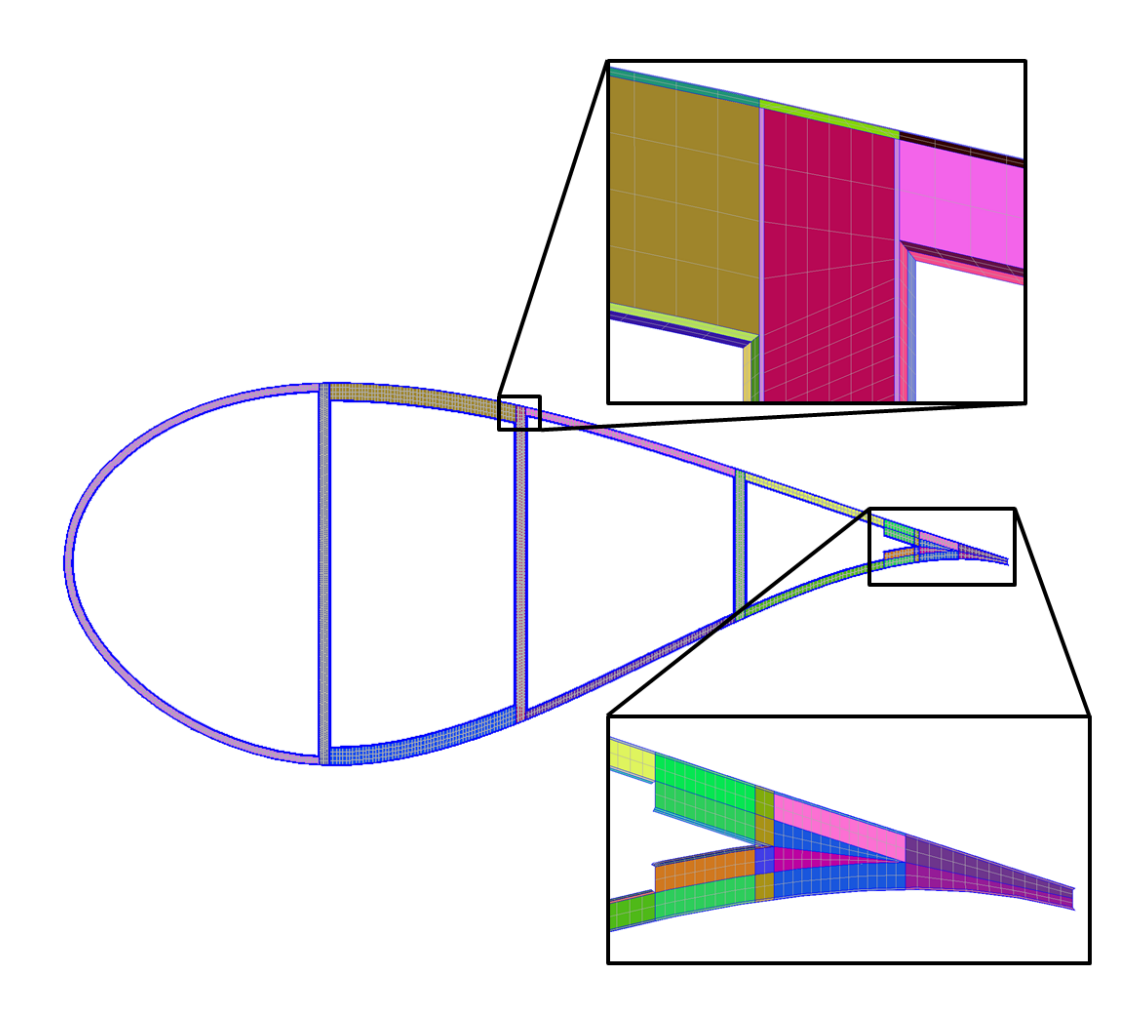


Figure 5.5: Example cross-sectional mesh for station 16 (19.5% span) of the Sandia blade, generated with TrueGrid [103, 104]. Colors denote individual mesh blocks with the same material properties. Each of these blocks have been merged into a single mesh for this entire cross-section.

Table 5.1: Material property data for full blade: glass fiber reinforced plastic (GFRP) composites, structural foam, gelcoat, and resin [91, 92, 9].

material	fabric/resin	lay-up	E_1 (GPa)	E_2 (GPa)	G_{12} (GPa)	ν_{12}	$\rho (kg/m^3)$
uniaxial GFRP	E-LT-5500/EP-3	$[0]_2$	41.8	14.0	2.63	0.28	1920
biaxial GFRP	Saertex/EP-3	$[\pm 45]_4$	13.6	13.3	11.8	0.49	1780
triaxial GFRP	SNL Triax	$[\pm 45]_4[0]_2$	27.7	13.65	7.2	0.39	1850
foam	-	-	0.256	0.256	-	0.3	200
gelcoat	-	-	3.44	3.44	-	0.3	1235
resin	-	-	3.50	3.50	-	0.3	1100

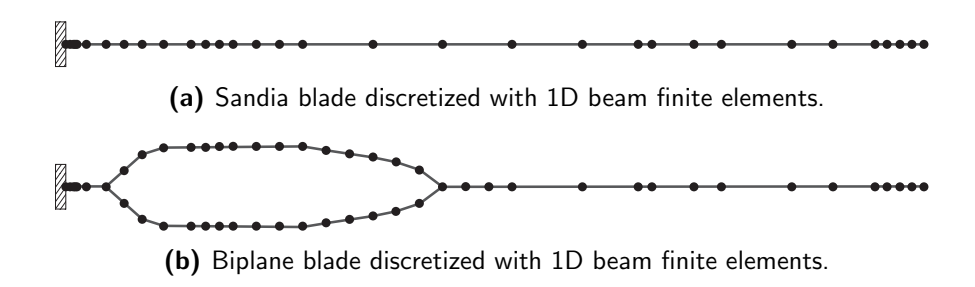


Figure 5.6: Computational meshes used for finite element analysis. (Note: mid-element nodes not shown. Only every 3rd node is shown.)

5.2.3 1D beam finite element models

Each blade was modeled with geometrically exact beam finite elements [71] in DYMORE 3.0, a flexible multibody dynamics finite element program [61, 62]. These elements were 3rd-order elements, and were based on a generalized Timoshenko beam model with six degrees of freedom per node [67]. DYMORE performed a nonlinear static analysis to solve for the deformed configuration of each blade under loading. In this study, DYMORE was also used to perform an modal analysis to solve for the natural frequencies and mode shapes of each blade.

Figure 5.6 compares the 1D beam models for the Sandia blade and the biplane blade. The spanwise location of the end-nodes were chosen to match the spanwise locations of the blade stations defined for the Sandia blade [9]. In the outboard monoplane regions, the Sandia and biplane blade meshes are identical. However, in the inboard region, the biplane blade mesh has an upper and lower assembly of beam elements, which merge together into one node at the root and mid-blade joints.

To add more realism to the 1D beam model, DYMORE can use the beam cross-sections to plot a 3D exterior mesh over the 1D beam model (Figure 5.7). This exterior mesh is purely graphical; it is not considered in the structural calculations. The coordinate system shown here for the biplane blade was also used for the 1D beam model of the Sandia blade.

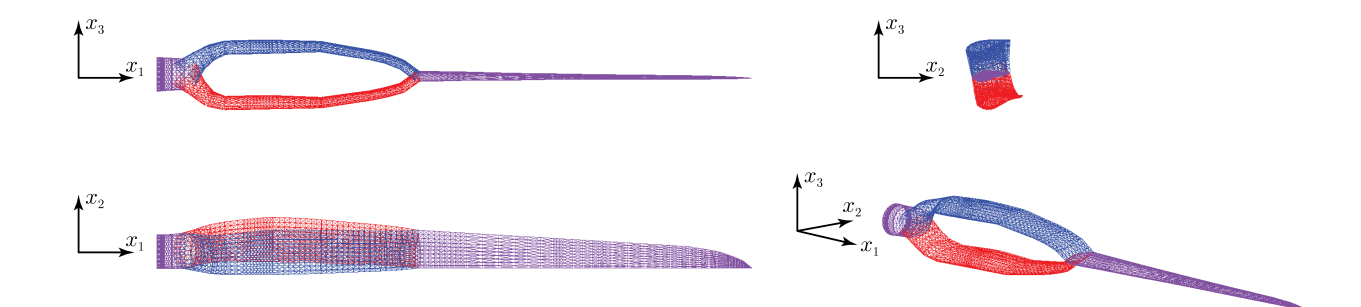


Figure 5.7: Four surface views of the biplane blade: edgewise (top left), spanwise (top right), flapwise (bottom left), and isometric (bottom right). The upper biplane element is blue, the lower biplane element is red, and the outboard monoplane region and the root monoplane regions are both purple.

5.2.4 Load cases

Five static load cases were considered for each blade, so that the structural performance of the full biplane blade could be compared to the Sandia blade. Two of these load cases were simple tip loads: a 10,000 N flapwise tip load, and a 10,000 N edgewise tip load. Two of the load cases were uniform distributed loads with a magnitude of 1,000 N/m: one applied in the flapwise direction, and the other in the edgewise direction. The last load case was a flapwise distributed load predicted by the blade element momentum (BEM) model WT_Perf [105] for the 100-meter Sandia blade operating in a steady wind speed of 11.4 m/s and a rotor rotation rate of 7.44 rpm. Table 5.2 lists the load values versus length of the flapwise distributed load from BEM. All flapwise loads were applied in the $+x_3$ -direction and all edgewise loads were applied in the $+x_2$ -direction (Figure 5.7). For the three distributed load cases, it was assumed that the loads on the biplane inboard region of the biplane spar were equally distributed among the upper and lower elements (for example, as in Figure 4.14(b)).**

In order to inform future designs, a modal analysis was also conducted to model the free vibrations of the blades without applied loads. DYMORE performed an eigenanalysis to calculate the first six natural frequencies and mode shapes for each stationary blade. Now

The edgewise uniform load was selected as a simple load case that could be used to explore the canonical structural behavior of each blade. It was not intended to approximate gravity loads, which would vary along the blade span, with the largest loads at the root, and smallest loads at the tip, in accordance with the mass distribution of the blade.

^{**}This was the same assumption made in Chapters 3 and 4.

Table 5.2: Flapwise distributed load (thrust) for the 100-meter Sandia blade operating in 11.4 m/s wind and rotating at 7.44 rpm, calculated by the BEM model WT_Perf [105].

span (m)	thrust (N/m)
0.000	0.000
2.164	243.878
6.611	299.154
11.058	263.065
16.617	2338.315
23.288	3317.554
29.958	4000.739
36.629	4781.188
43.300	5851.984
49.970	6812.364
56.641	8020.803
63.312	9184.607
69.982	9815.452
76.653	10768.313
83.323	11609.353
88.882	12088.440
93.329	11811.550
97.776	8551.274
100.000	0.000

that the mass of the entire blade was represented, this analysis was conducted to provide an initial idea of the dynamic behavior of the biplane blade, and how it may differ from the conventional Sandia blade. For the static load cases and the modal analysis, both blades were cantilevered at the root $(x_1 = 0 \text{ m})$ and free at the tip $(x_1 = R = 100 \text{ m})$.

5.3 Results

5.3.1 Blade geometry

Table D.1 describes the external geometry of the full biplane blade. The beam axis coordinates describe the 1D beam topology of the blade. In a monoplane station, the beam axis coordinates give the position of the pitch axis (Figure 2.5). In a biplane station, the beam axis coordinates give the positions of the upper and lower reference points (Figure 2.14). This table also lists the twist distribution, the chord distribution, and an airfoil schedule. The beam axis-to-chord ratio describes the fractional position of the beam axis along the chord of an airfoil.^{††} The thickness-to-chord ratio decreases sharply from station 9 to 10

^{††}For a monoplane station, this fractional position is ξc in Figure 2.5; for a biplane station, it is $f_{\text{upper}}c_{\text{upper}}$ or $f_{\text{lower}}c_{\text{lower}}$ in Figure 2.14.

at the root joint (4.7% span), where the blade transitions from a thick monoplane airfoil to two thinner biplane airfoils. Similarly, this ratio increases sharply from station 24 to 25 at the mid-blade joint (43.9% span), where the blade transitions from biplane airfoils to a thicker monoplane airfoil. The maximum gap-to-chord ratio is 1.395 at 11.4% span. While the gap-to-chord ratio slightly decreases between 11.4% and 27.6% span because the chord is changing, the dimensional gap distance remains nearly constant at 9.2 meters. Figure D.1 shows the geometry of selected cross-sections of the biplane blade. Along with the external geometry, this figure also plots the internal structural parts.

The laminate thicknesses of the internal structural parts are listed in Table D.2. This table only gives the selected thicknesses along the span: root buildup, spar cap, trailing edge (TE) reinforcement, leading edge (LE) panel, aft panel, internal surface triax, and external surface triax. Some thicknesses are not listed because they remain constant along the span. These constant thicknesses were taken from [9]. All three shear webs are 86 mm thick (80 mm of foam sandwiched between two layers of 3 mm biax). The external surface consists of a gelcoat layer on top of a triax layer; this gelcoat layer is 0.6 mm thick. The internal surface consists of a resin layer on top of a triax layer; this resin layer is 5 mm thick. The two main shear webs start at 2.4% span and end at 94.3% span; along their entire length, they are placed at 0.75 m fore and aft of the pitch axis. The third shear web starts at 14.6% span and ends at 60.2% span; at its start, it is placed at 78% chord and at its end, it is placed at 68% chord.

5.3.2 Cross-sectional analysis

Before calculating the cross-sectional properties of the biplane blade, the methodology in Figure 5.2 was validated for the Sandia blade. Cross-sectional properties of the Sandia blade were calculated by VABS in this work, and compared to values calculated by PreComp [106] reported in [90]. Figures 5.8 and 5.9 show this comparison. The percent difference from average between the two data sets is also plotted, since the values from [90] have not been experimentally verified. Furthermore, PreComp makes use of some a priori assumptions,

such as neglecting cross-sectional warping, which raises some concerns about the accuracy of its calculated cross-sectional properties [68]. However, the values from [90] are still useful as a reference for a sanity check. The major differences in calculated properties between this work and [90] are in edgewise stiffness and edgewise mass moment of inertia, which are both overpredicted in the inboard region, peaking at about 30% at a span of 14.6 meters. This difference is likely due to a slight overprediction of mass (about 10%) in the inboard region. All other cross-sectional properties matched well, with percent differences no larger than 10% in the inboard region, and near zero differences in the outboard region. Therefore, the methodology in Figure 5.2 was considered sufficiently accurate to calculate the cross-sectional properties of the biplane blade (Table D.3).

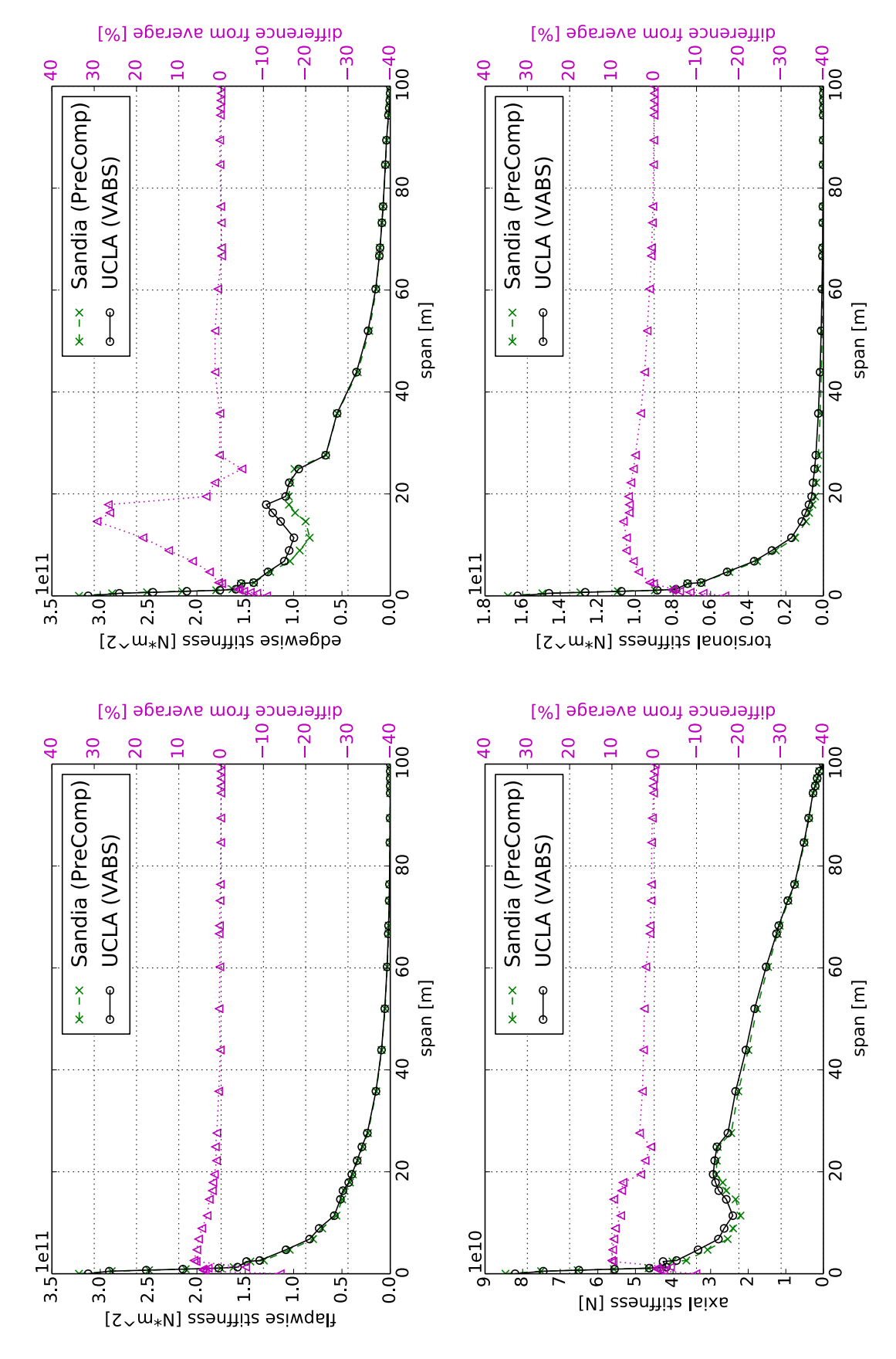
5.3.3 Load cases

5.3.3.1 Flapwise loads

Under each of the flapwise loads, the biplane blade deflects less at the tip than the Sandia blade (Figures 5.10(a), 5.12(a) and 5.14(a)). The displacement of the biplane blade relative to the Sandia blade can be shown more clearly by calculating its structural efficiency (Equation (5.1)), which is defined as the ratio of the Sandia blade displacements ($u(x_1)_{\text{Sandia}}$) and the biplane blade displacements ($u(x_1)_{\text{biplane}}$). Figures 5.11, 5.13 and 5.15 show that, for spans greater than about 25 meters (near the midpoint of the inboard biplane region), the biplane blade is more efficient in the flapwise direction than the Sandia blade. Between 4.7–25 meters, the biplane blade is less efficient. Between 0–4.7 meters, both blades have the same efficiency because they both share the same monoplane root cylinder. At the blade tip (100 meters), the biplane blade is 20–40% more efficient than the Sandia blade, depending on the flapwise load.

$$\phi(x_1) = \frac{u(x_1)_{\text{Sandia}}}{u(x_1)_{\text{biplane}}}$$
(5.1)

The reduced tip deflection of the biplane blade can be further explained by examining its



and torsional (bottom right). Properties calculated by UCLA (using VABS) are compared to those published by Sandia Figure 5.8: Stiffness properties along the span of the Sandia blade: flapwise (top left), edgewise (top right), axial (bottom left), (using PreComp) [90]

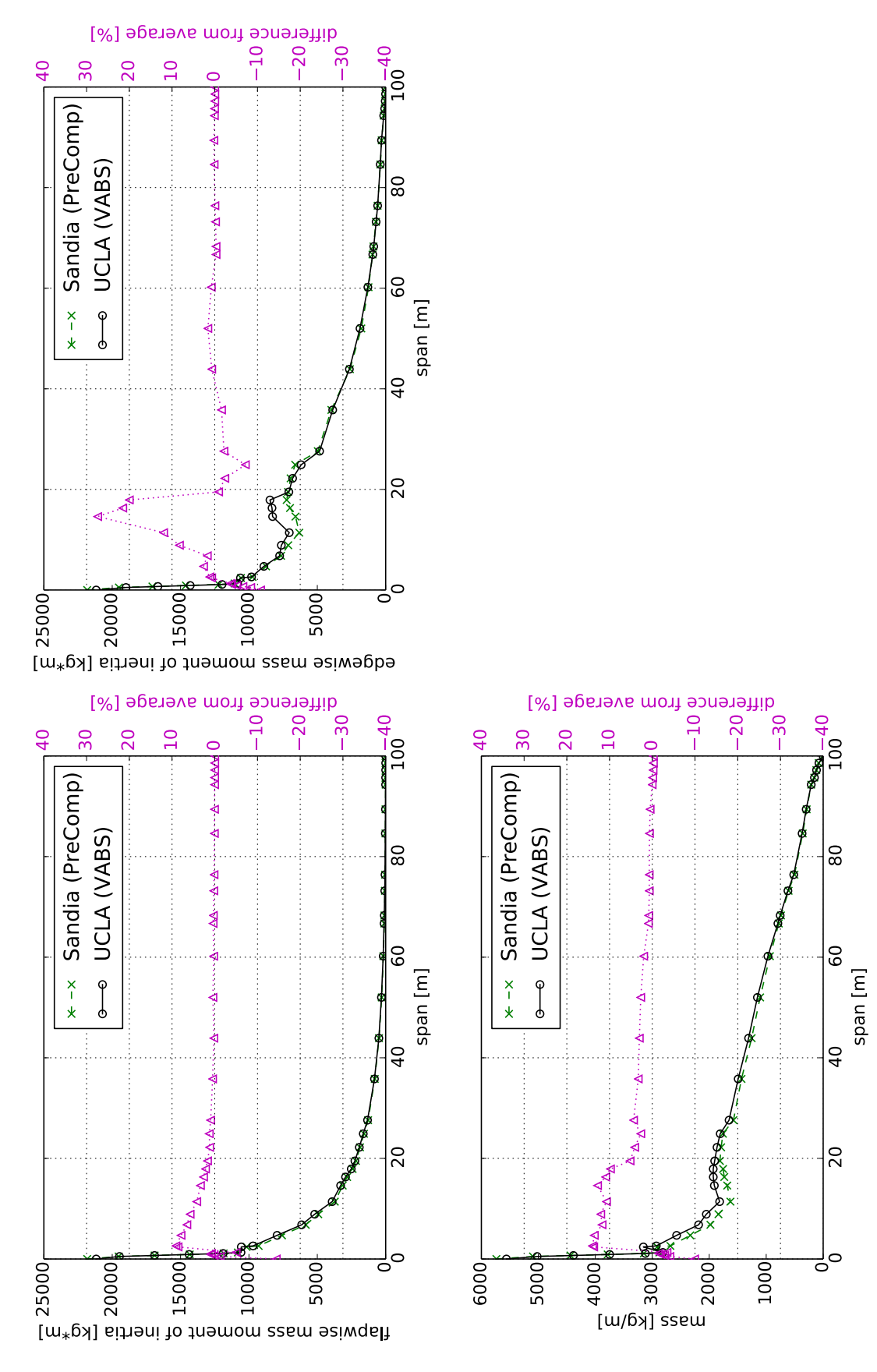


Figure 5.9: Mass properties along the span of the Sandia blade: flapwise mass moment of inertia (top left), edgewise mass moment of inertia (top right), and mass per length (bottom left). Properties calculated by UCLA (using VABS) are compared to those published by Sandia (using PreComp) [90]

moments and rotations. Figures 5.10(d), 5.12(d) and 5.14(d) show that the magnitude of the flapwise bending moment is much smaller in the biplane region. Between a span of about 25–35 meters, the moment changes sign because there is an inflection point in the displacement curve. In other words, the curvature of the deformed biplane blade changes from convex to concave in the biplane region.^{‡‡} The inflection point in the biplane blade's displacements also causes its rotations to remain nearly constant in the biplane region (Figures 5.10(b), 5.12(b) and 5.14(b)). The Sandia blade's rotations steadily increase in magnitude along its span. In short, the inflection point in the biplane blade's displacements is responsible for its reduced tip deflection.

The reduced bending moment in the biplane blade is caused by the mid-blade joint (at a span of 43.9 meters), which converts the bending moment in the outboard monoplane region into axial forces in the inboard biplane region (Figures 5.10(c), 5.12(c) and 5.14(c)). This occurs because of the joint's geometry; under the flapwise loads considered here, the joint tends to rotate about the x_2 -axis, with its upper part moving towards the blade root and its lower part moving towards the blade tip. Therefore, the upper biplane element is in compression (with a negative axial force) and the lower biplane element is in tension (with a positive axial force). At the root joint (span of 4.7 meters), the opposite occurs: the bending moments are restored to the same values as the Sandia blade, and the axial forces vanish.

To check that the flapwise distributed load from BEM was applied correctly, the root bending moment (Figure 5.14(d)) and tip deflection (Figure 5.14(a)) of the Sandia blade were compared to results from a similar load case in Table 13 of [9]: the NWPR (normal wind profile at rated) load case. The normal wind profile is a constant wind speed case with a rated wind speed of 11.3 m/s and a maximum rotation rate of 7.44 rpm. The flapwise root bending moment is 42,519 kN-m in the present study, compared to 43,100 kN-m in [9]. The tip deflection is 6.8 m in the present study, compared to 8.7 m in [9]. While there is only a 1% difference in the flapwise root bending moment, there is a 22% difference in tip deflection. In the NWPR load case, both flapwise and edgewise distributed loads are

^{‡‡}Recall that the curvature of a beam is the second derivative of its displacement, and that the bending moment in a beam is defined as its bending stiffness multiplied by its curvature. Therefore, the bending moment will have the same sign as the curvature.

applied to the Sandia blade. However, in the present study, only a flapwise distributed load from BEM was applied, while the edgewise distributed load was neglected. Since the Sandia blade is twisted, its edgewise and flapwise deflections are coupled, so the additional edgewise distributed load would cause some additional flapwise deflection. This difference in applied loads is likely the cause of the discrepancy in tip deflection. Because the flapwise root bending moments matched well, it was judged that the flapwise distributed load from BEM was applied correctly.

5.3.3.2 Edgewise loads

Under each of the edgewise loads, the biplane blade deflects more at the tip than the Sandia blade (Figures 5.16(a) and 5.18(a)). Figures 5.17 and 5.19 show that, for spans greater than about 5 meters (near the root joint), the biplane blade is less efficient in then edgewise direction than the Sandia blade. Between 0–4.7 meters, both blades have the same efficiency because they both share the same monoplane root cylinder. At the blade tip, the biplane blade is 27–35% less efficient than the Sandia blade, depending on the edgewise load.

The increased tip deflection of the biplane blade can be further explained by examining its moments and rotations. Figures 5.16(d) and 5.18(d) show that the magnitude of the edgewise bending moment is much smaller in the biplane region, but it does not change sign. Therefore, no inflection point exists in the biplane blade's displacements to ultimately limit tip deflection. Furthermore, the biplane blade's rotations at the root joint (span of 4.7 meters) and mid-blade joint (43.9 meters) increase more rapidly than in the Sandia blade (Figures 5.16(b) and 5.18(b)). Both of these results contribute to the increased tip deflection of the biplane blade in the edgewise direction.

Under the edgewise loads considered here, the upper biplane element is in tension and the lower biplane element is in compression (Figures 5.16(c) and 5.18(c)). This occurs because of the blade's twist distribution, which slightly offsets the lower biplane element in the $+x_2$ -direction from the upper biplane element (Figure 5.7). Due to this geometry, edgewise loads tend to rotate the mid-blade joint about the x_3 -axis, placing the lower biplane element in

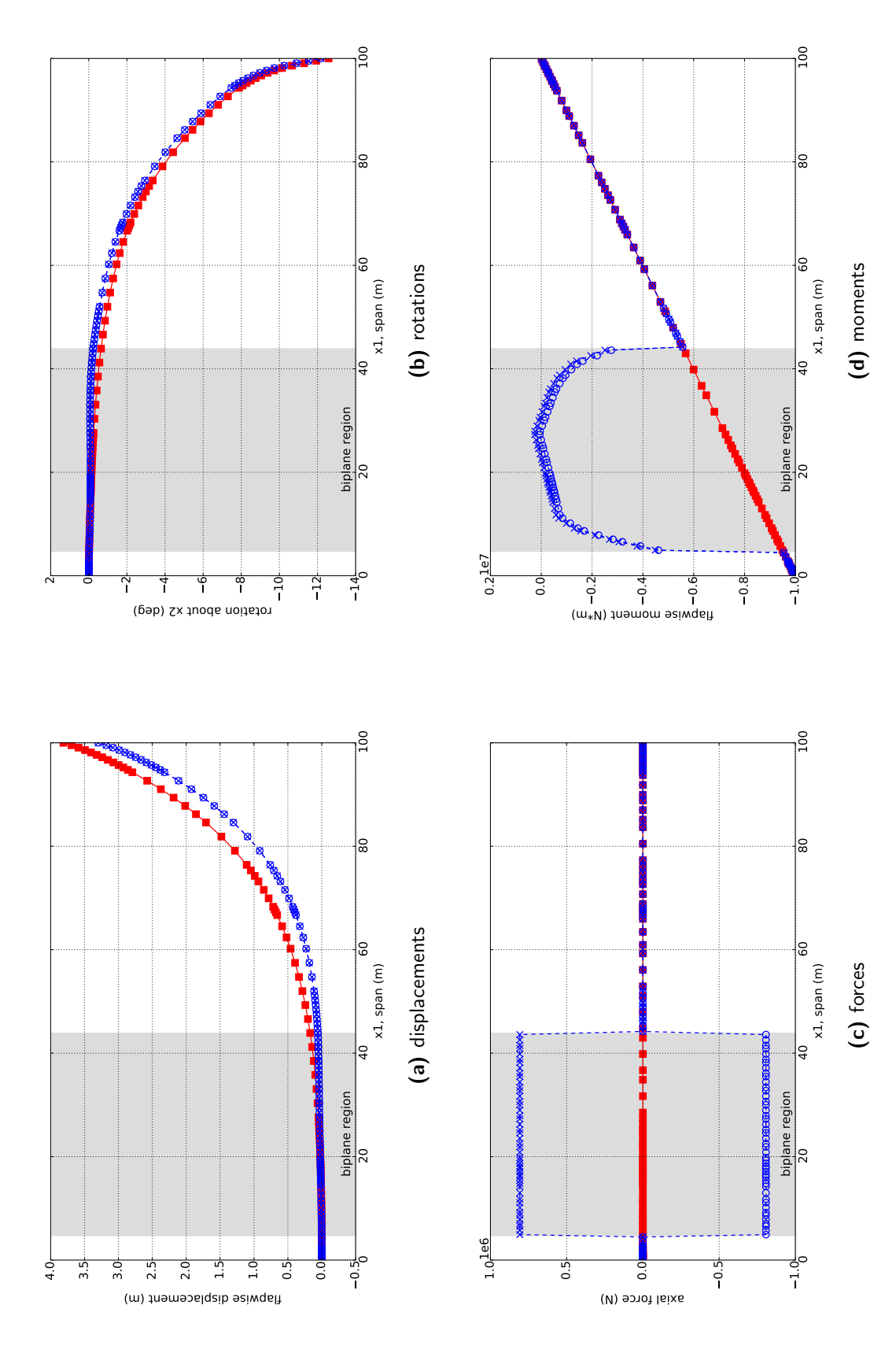


Figure 5.10: Displacements, rotations, forces, and moments computed by DYMORE for the Sandia blade (red squares) and biplane blade (blue circles and crosses) under a 100,000 N flapwise tip load. In the biplane region of the biplane blade, the upper biplane element is plotted with blue circles, while the lower element is plotted with blue crosses.

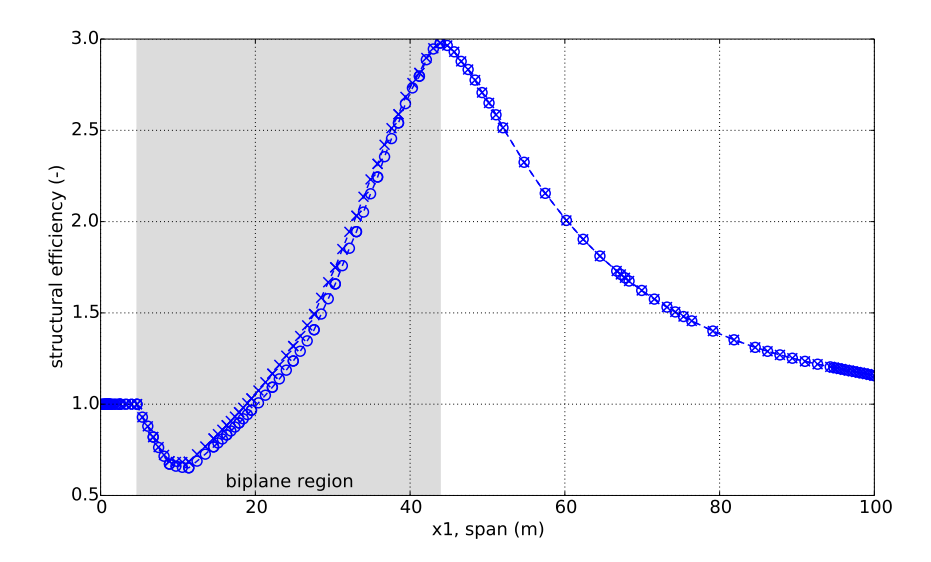
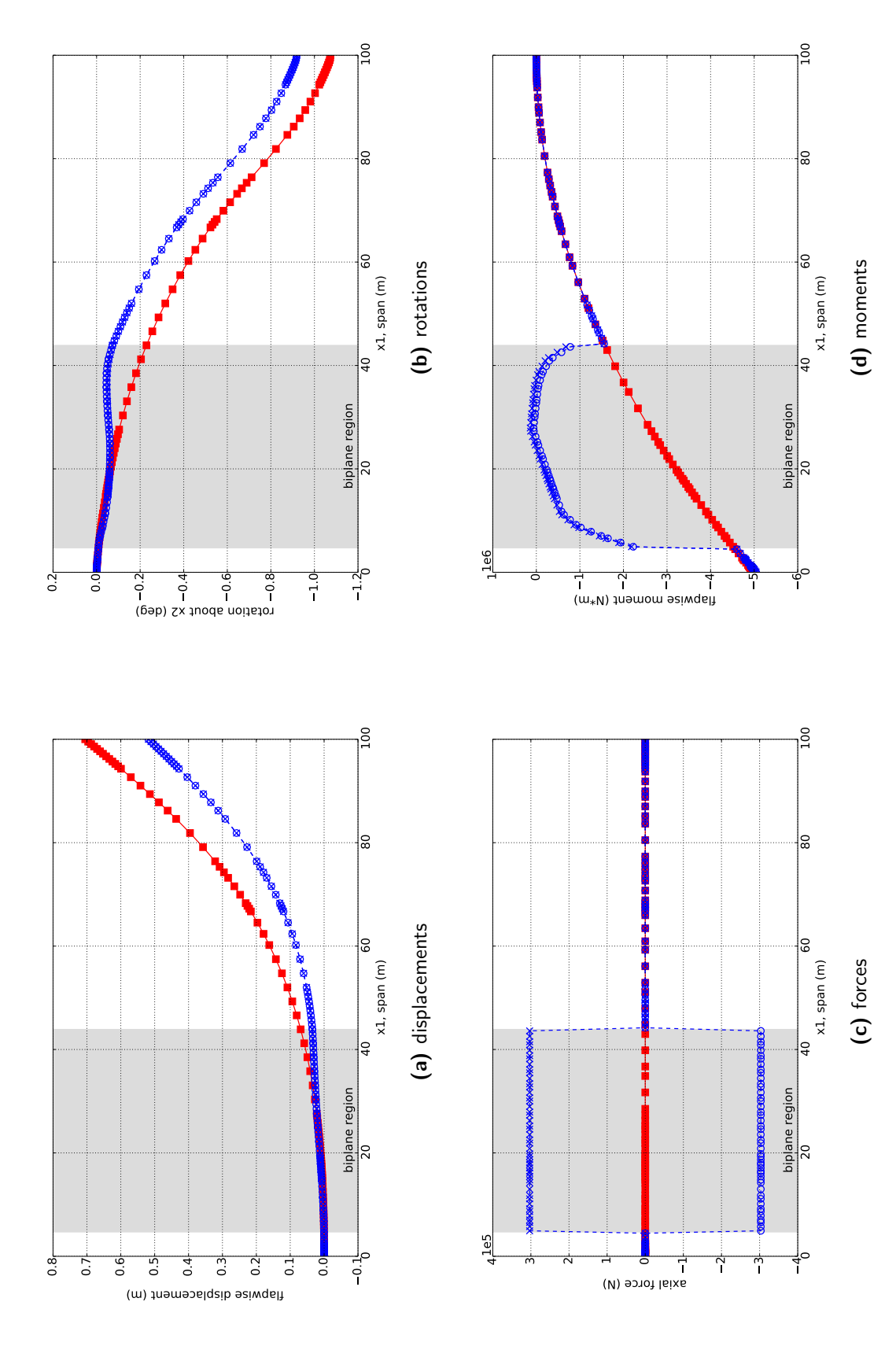


Figure 5.11: Structural efficiency of the biplane blade under a 100,000 N flapwise tip load. In the biplane region of the biplane blade, the upper biplane element is plotted with blue circles, while the lower element is plotted with blue crosses.

compression.

5.3.3.3 Modal analysis

Table 5.3 compares the free vibrations of the biplane and Sandia blades, highlighting the differences in modes 1, 2, and 6, as well as the similarities in modes 3, 4, and 5. In mode 1 (Figure 5.20), the biplane blade vibrates in the edgewise direction, while the Sandia blade vibrates in the flapwise direction as expected. This occurs because the biplane blade has been modified from the Sandia blade by moving mass in the flapwise direction, so that its weak axis is no longer in the flapwise direction, but now in the edgewise direction. As expected, the Sandia blade still has its weak axis in the flapwise direction, and therefore vibrates in the flapwise direction. Furthermore, the first natural frequency of the biplane blade is about 20% larger than the Sandia blade, indicating that slightly more energy is needed to excite the first mode of the biplane blade. In mode 2 (Figure 5.21), this behavior is flipped; now the biplane blade vibrates in flap, while the Sandia blade vibrates in edge. Modes 3–5 have the same shape in both blades, progressing through higher flap and edge modes. The 3rd–5th natural frequencies of the biplane blade are slightly lower than the Sandia blade. In



Displacements, rotations, forces, and moments computed by DYMORE for the Sandia blade (red squares) and biplane blade (blue circles and crosses) under a 1,000 N/m flapwise uniform distributed load. In the biplane region of the biplane blade, the upper biplane element is plotted with blue circles, while the lower element is plotted with blue crosses. Figure 5.12:

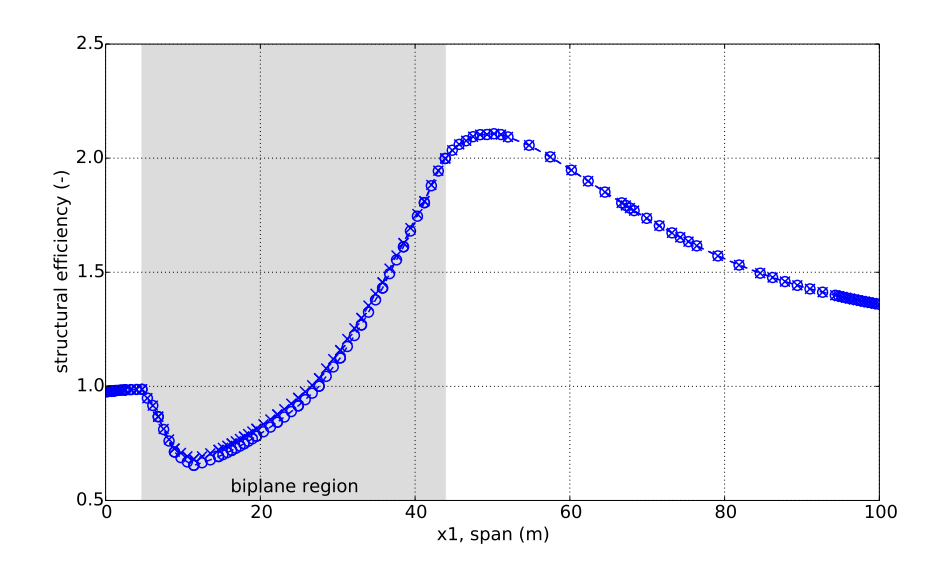


Figure 5.13: Structural efficiency of the biplane blade under a 1,000 N/m flapwise uniform distributed load. In the biplane region of the biplane blade, the upper biplane element is plotted with blue circles, while the lower element is plotted with blue crosses.

Table 5.3: Modal analysis to inform future designs

mode #	biplan	e blade	Sandia blade		
	natural freq. (Hz)	name	natural freq. (Hz)	name	
1	3.227	1st edge	2.697	1st flap	
2	3.471	1st flap	4.337	1st edge	
3	7.337	2nd flap	7.470	2nd flap	
4	12.165	2nd edge	13.916	2nd edge	
5	14.091	3rd flap	15.902	3rd flap	
6	24.689	1st opp. edge/flap	26.757	4th flap	

mode 6 (Figure 5.22), the biplane blade shows coupled torsion and edgewise motions. The monoplane outboard region vibrates in flap, while torsion in the mid-blade joint produces edgewise motions in the biplane inboard region. For comparison, the Sandia blade simply vibrates in a higher flap mode. This highlights an important difference in the dynamical behavior of the biplane blade at higher modes: torsion/edgewise coupling with the mid-board joint and the biplane inboard region.

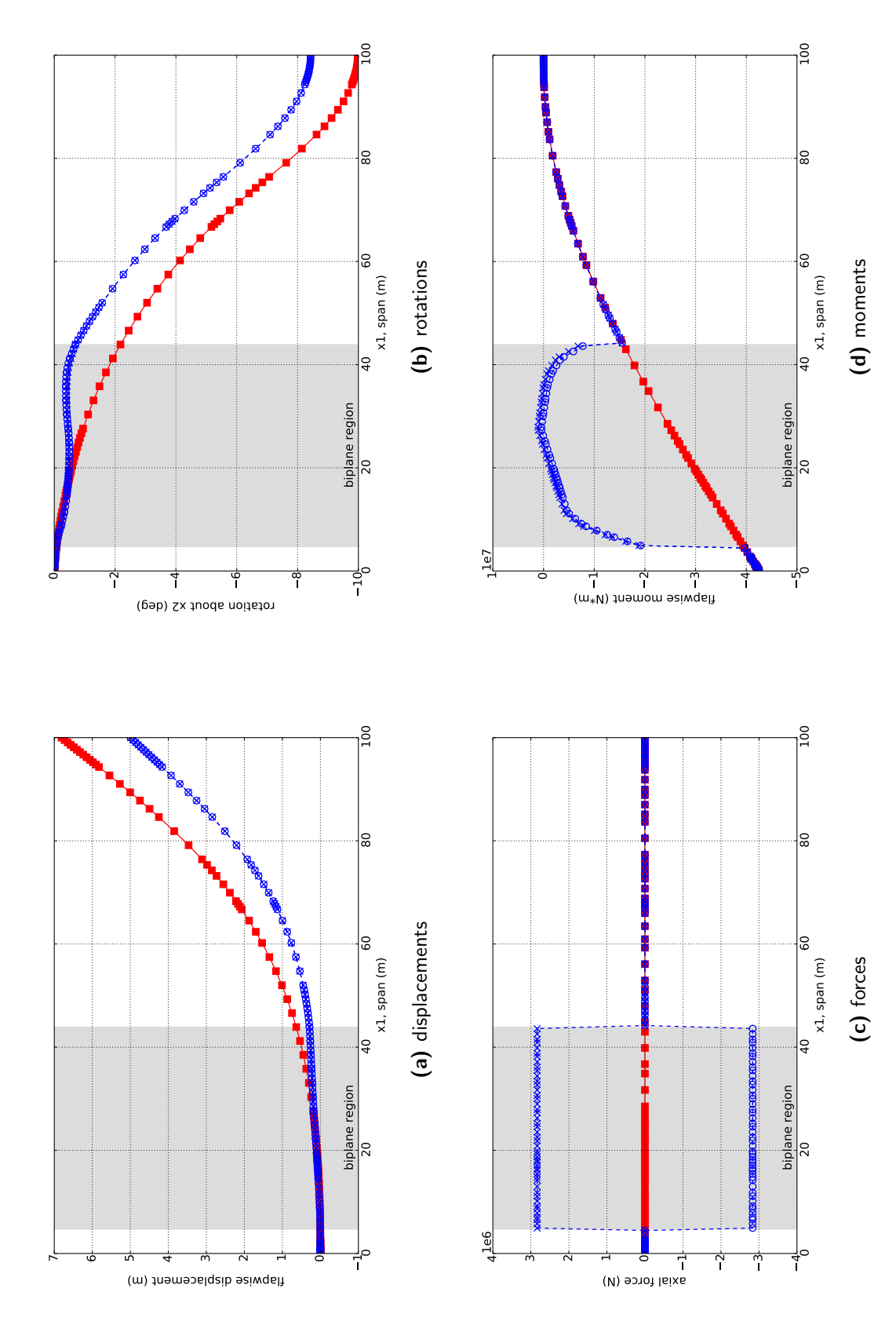


Figure 5.14: Displacements, rotations, forces, and moments computed by DYMORE for the Sandia blade (red squares) and biplane blade (blue circles and crosses) under a flapwise distributed load calculated by WT_Perf [105], a BEM model, for 11.4 m/s wind speed and 7.44 rpm rotor rotation rate. In the biplane region of the biplane blade, the upper biplane element is plotted with blue circles, while the lower element is plotted with blue crosses.

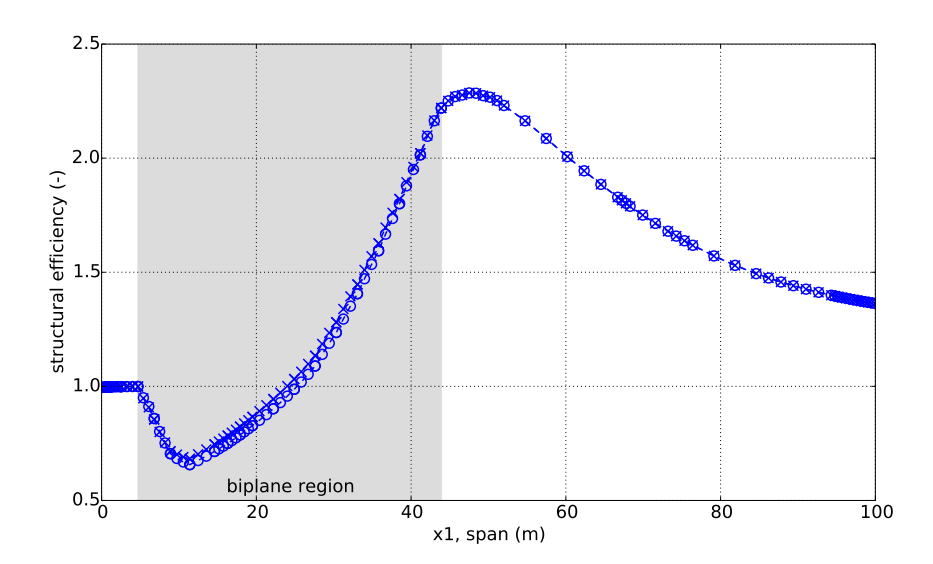


Figure 5.15: Structural efficiency of the biplane blade under a flapwise distributed load calculated by WT_Perf [105], a BEM model, for 11.4 m/s wind speed and 7.44 rpm rotor rotation rate. In the biplane region of the biplane blade, the upper biplane element is plotted with blue circles, while the lower element is plotted with blue crosses.

5.4 Discussion

This study presents a blade definition for a full 100-meter biplane blade. By adding the airfoil exterior over the structurally optimized biplane spar from earlier studies (Chapter 4), this blade definition represents the completion of step 2 in the "structures-first" approach. This full biplane blade design includes the root joint and monoplane root cylinder, which were both neglected from earlier studies.

This study also presents a framework and a technology stack for the design and analysis of biplane blades, which can be used by future researchers. The methodology in this framework was first validated by calculating the cross-sectional properties of the Sandia blade and comparing them to results in [90]. Then, the methodology was used to calculate additional cross-sectional properties for the inboard biplane region of the biplane blade. Finally, a 1D beam finite element model of the biplane blade was constructed, and several flapwise and edgewise load cases were applied.

All of the results for flapwise loads in Section 5.3.3.1 are consistent with the findings

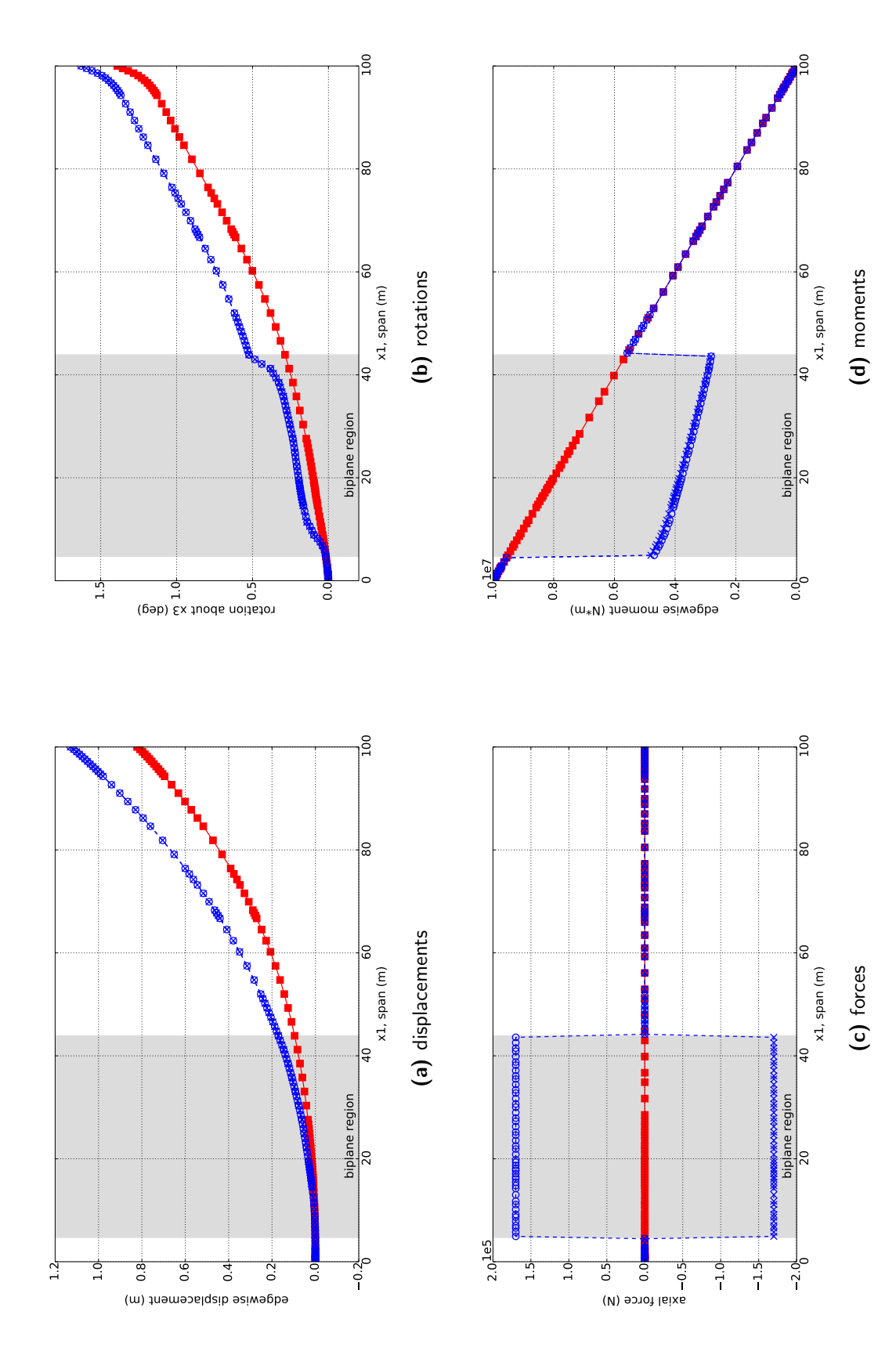


Figure 5.16: Displacements, rotations, forces, and moments computed by DYMORE for the Sandia blade (red squares) and biplane blade (blue circles and crosses) under a 100,000 N edgewise tip load. In the biplane region of the biplane blade, the upper biplane element is plotted with blue circles, while the lower element is plotted with blue crosses.

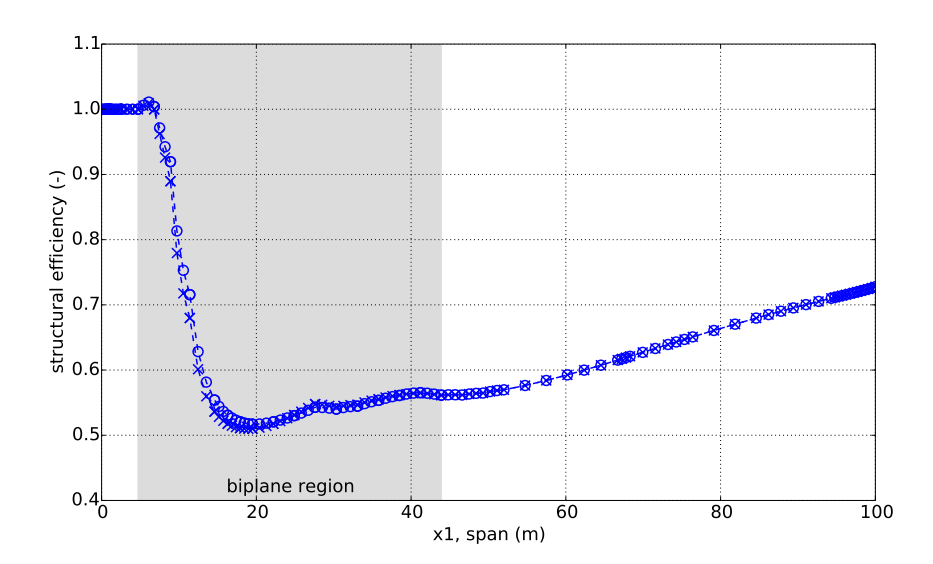
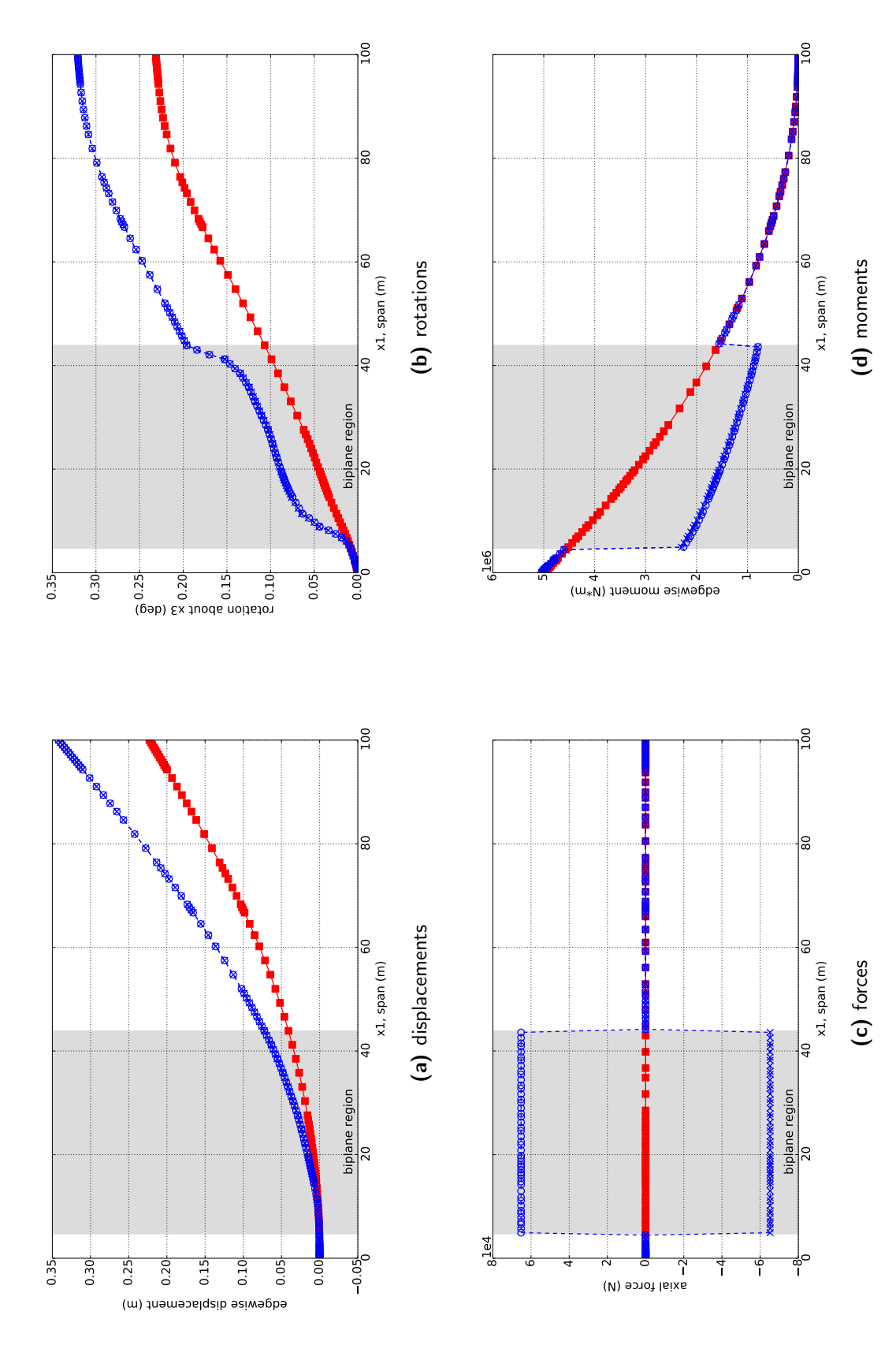


Figure 5.17: Structural efficiency of the biplane blade under a 100,000 N edgewise tip load. In the biplane region of the biplane blade, the upper biplane element is plotted with blue circles, while the lower element is plotted with blue crosses.

presented earlier in Chapters 3 and 4. In the biplane region of the biplane blade, an inflection point in displacements arises because the flapwise bending moment changes sign, resulting in reduced tip deflections. At the tip, the biplane blade is 20–40% more efficient than the Sandia blade, depending on the flapwise load. Axial forces are sustained in the biplane region, which raises concerns about buckling under compressive forces. Chapter 4 showed that buckling was not an issue for biplane spars, but this needs to be verified again for the biplane blade design presented here.

Results for edgewise loads in Section 5.3.3.2 show that the biplane blade deflects more than the Sandia blade. At the tip, the biplane blade is 27–35% less efficient than the Sandia blade, depending on the edgewise load. Compared to the Sandia blade, the biplane blade uses thinner biplane airfoils in the inboard biplane region. These biplane airfoils have sharp trailing edges, which cannot fit trailing edge reinforcements that are as large as the Sandia blade to provide edgewise stiffness in the inboard region. In particular, more edgewise stiffness is needed near the root joint (span of 4.7 meters), where its structural efficiency reaches a minimum of 50%. Future designs of the biplane blade should investigate ways to mitigate this challenge.



Displacements, rotations, forces, and moments computed by DYMORE for the Sandia blade (red squares) and biplane blade (blue circles and crosses) under a $1,000~\mathrm{N/m}$ edgewise uniform distributed load. In the biplane region of the biplane blade, the upper biplane element is plotted with blue circles, while the lower element is plotted with blue crosses. Figure 5.18:

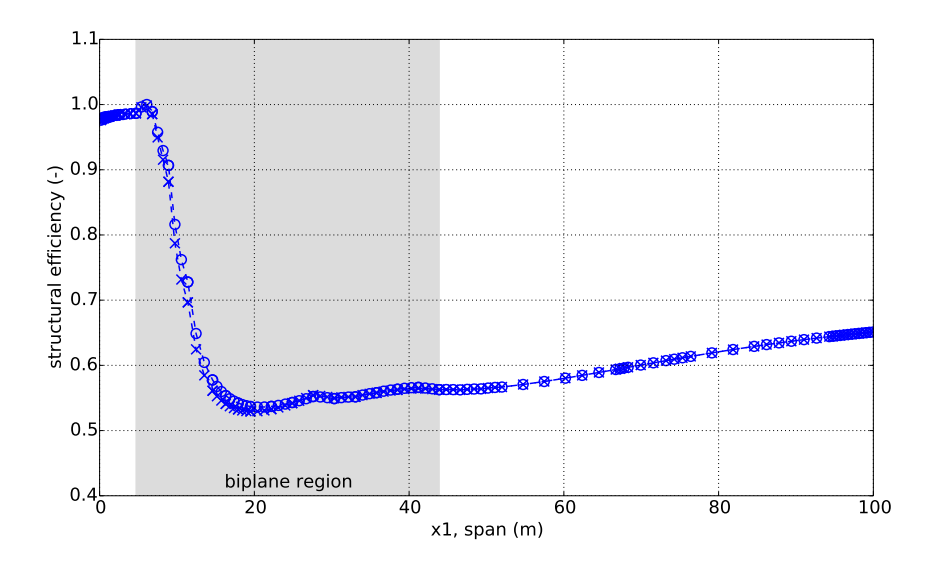


Figure 5.19: Structural efficiency of the biplane blade under a 1,000 N/m edgewise uniform distributed load. In the biplane region of the biplane blade, the upper biplane element is plotted with blue circles, while the lower element is plotted with blue crosses.

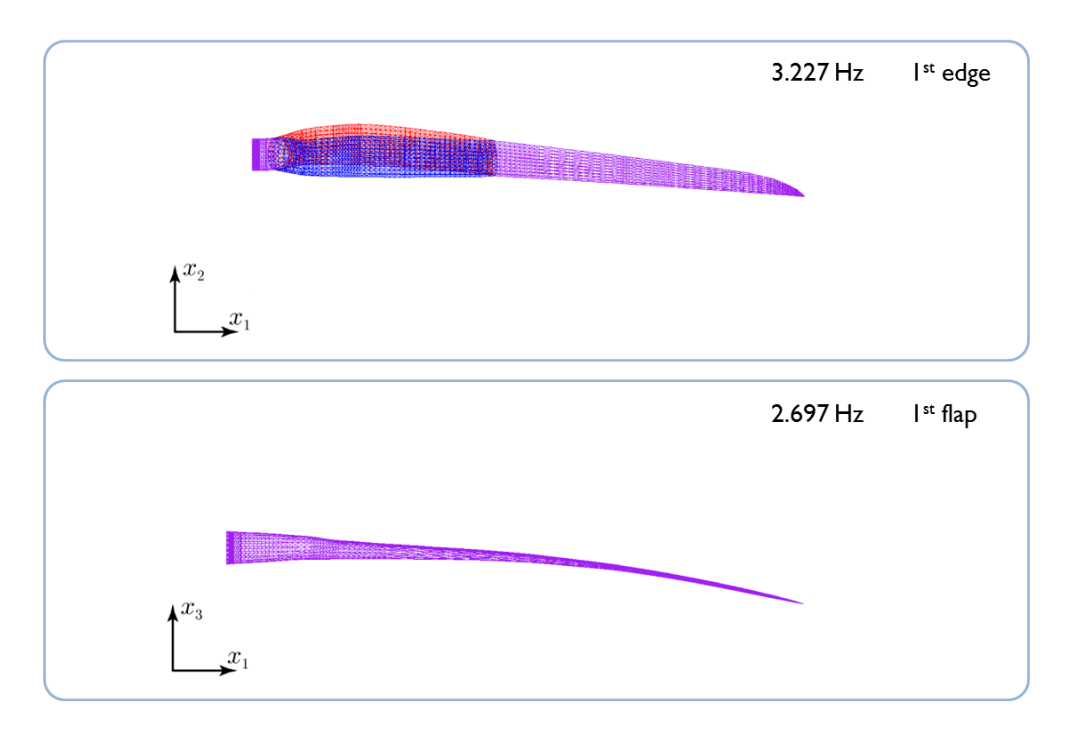


Figure 5.20: Mode 1: The biplane blade vibrates in edge, while the Sandia blade vibrates in flap. To illustrate this, the biplane blade is shown in a flapwise view (top), while the Sandia blade is shown in an edgewise view (bottom).

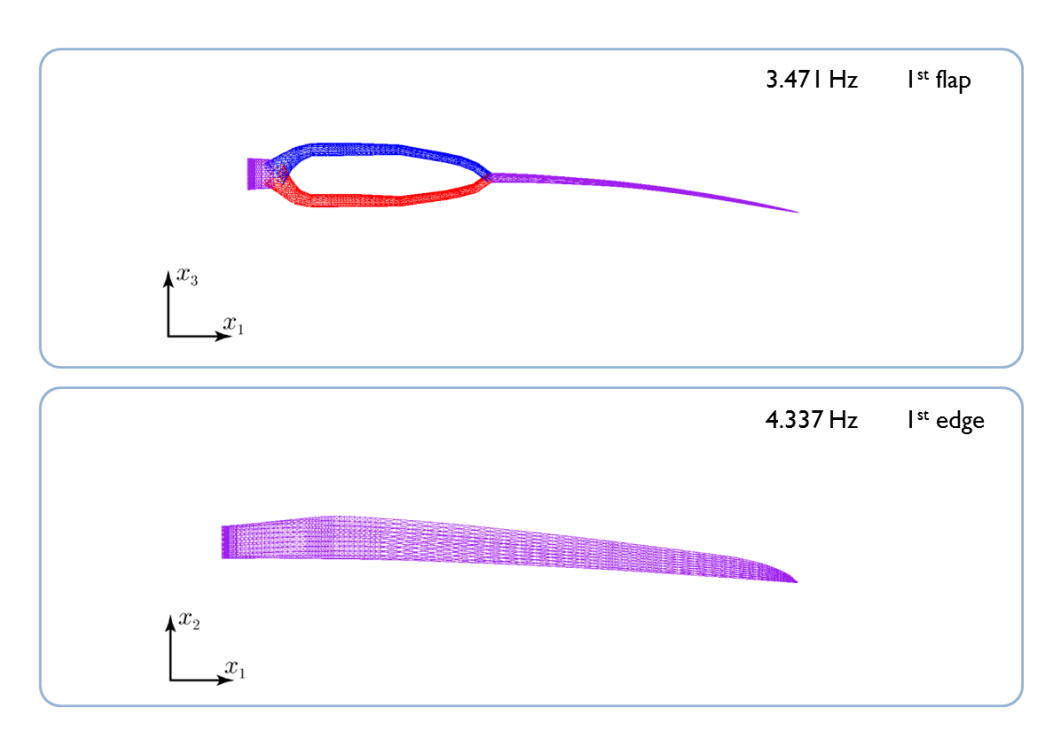


Figure 5.21: Mode 2: The biplane blade vibrates in flap, while the Sandia blade vibrates in edge. To illustrate this, the biplane blade is shown in an edgewise view (top), while the Sandia blade is shown in a flapwise view (bottom).

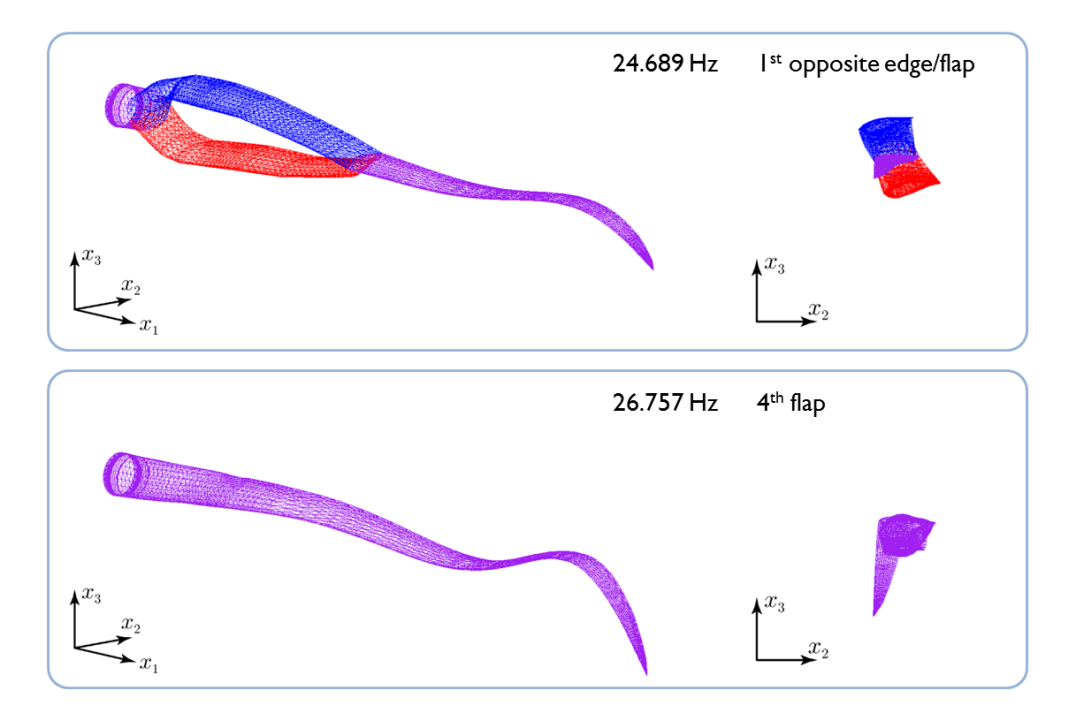


Figure 5.22: Mode 6: The biplane blade shows torsion/edgewise coupling. Two views are shown of each blade: isometric (left), and spanwise looking down the blade from tip to root (right).

The modal analysis in Section 5.3.3.3 sought to identify important design considerations for future studies. This analysis shows that the first mode shape of the biplane blade is edgewise, not flapwise as in the Sandia blade. This should be considered further in future studies, since gravitational fatigue loads act in the edgewise direction. This analysis also revealed that in mode 6, the biplane blade showed torsion/edgewise coupling. This will be an important consideration for future studies of the design of the mid-blade joint against fatigue. Finally, this analysis did not consider centrifugal force, since all blades were modeled as stationary. However, in operation, centrifugal forces will arise from the rotation of the rotor, which will likely stiffen the blade and change its dynamical behavior. Therefore, future studies of biplane blade dynamics should include centrifugal forces.

CHAPTER 6

Conclusions and recommendations

This dissertation used three design studies for the biplane blade, each in order of increasing complexity, to analyze its aerodynamic and structural performance. Considering the results of each of these studies, the biplane blade appears to be a feasible design. Two-dimensional aerodynamic simulations showed that biplane airfoils improved the maximum lift coefficient and lift-to-drag ratio, compared to thick monoplane airfoils. These aerodynamic improvements can have benefits for blade design. The structural behavior of a biplane beam was reasonably predicted with a 1D beam model, compared to results from a 3D model. This indicates that 1D beam models can be accurately used for design studies. An analytical model for biplane beams gave further insights about how the biplane blade supports loads. Axial forces in the biplane inboard region reduce bending moments at the joint. These bending moments are reduced far enough to change sign and create an inflection point in the displacements of the biplane region. This inflection point ultimately reduces tip deflections and improves the flapwise structural efficiency of the biplane blade. An approximate buckling analysis shows that compressive axial loads in the biplane inboard region do not exceed buckling loads. However, the buckling stability of the biplane region needs to be considered in all future designs of the biplane blade.

Parametric studies were used to (1) examine how the dimensions of the biplane inboard region affect blade performance, and (2) identify optimal biplane inboard configurations. These studies found that the most important dimensions of the biplane inboard region are the gap-to-chord ratio (g/c) and the joint length-to-span ratio (r_j/R) . Results of this work show that 1.0 < g/c < 1.2 and $r_j/R \approx 0.5$ give good aero-structural performance. Within these constraints, the transition length-to-joint length ratio (r_t/r_j) had little effect on structural

performance.

Early on in this work, it was known that the 2D aerodynamic performance of biplane airfoils was better than a thick monoplane airfoil. This motivated a "structures-first" approach to design the biplane blade by first focusing on optimizing the structure. No objective function was explicitly defined within a formal optimization methodology, but the parametric studies in this work were used to minimize two structural parameters: tip deflection and root bending moment. At first, this suggests that this was a purely structural optimization. However, this is only half true, since the biplane inboard structure was also expected to improve aerodynamic performance, based on the results from 2D aerodynamic studies. Moving forward, a more closely-coupled aero-structural design approach would further improve the blade design.

Qualitatively, a joint length-to-span ratio of 0.5 is best for two reasons. First, the outboard part of the blade has already been aerodynamically optimized in conventional blades over many years of development. Second, there is not enough material in the outboard half of the blade to split up into a biplane, since the blade thickness tapers from root to tip. Furthermore, the gap-to-chord ratio should be limited to about 1.2 to prevent the biplane inboard region from striking the tower under load, even before the tip would strike the tower.

The flapwise structural performance of the biplane blade is significantly improved over a conventional monoplane blade of the same length and mass. On the other hand, the edgewise structural performance of the biplane blade configuration examined in Chapter 5 was decreased, compared to a monoplane blade. These edgewise stiffness considerations should be investigated further in future designs, since gravitational fatigue loads are important in the edgewise direction for large blades.

While this work looked at an isolated blade in order to develop a design, future studies could build upon this work by considering the entire wind turbine. The structural interactions between the blades and all of the downstream components (e.g. hub, gearbox, tower) will be important to investigate, especially considering that the biplane blade is a stiffer structure in the flapwise direction, compared to a conventional blade. When the biplane

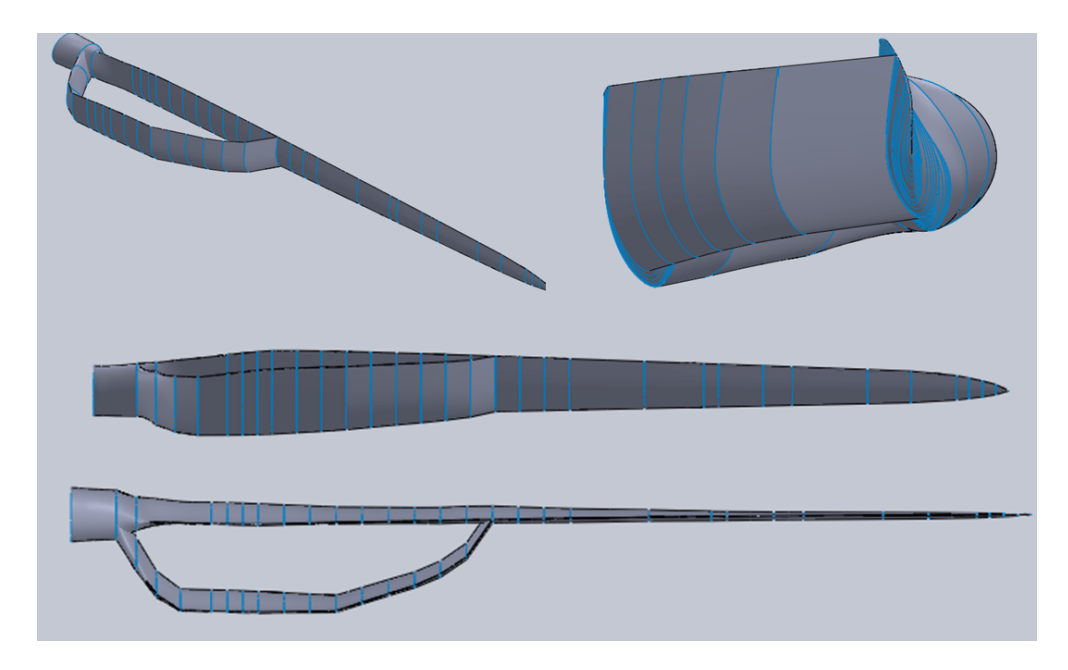


Figure 6.1: CAD rendering of biplane blade, alternate configuration 1 (flapwise asymmetric, no stagger). Image credit: Christos Voutsaras.

blade is under inertial loading, more of the energy from these loads will likely be passed on to these downstream components, resulting in larger stresses that may reduce their lifetime.

There are many opportunities for future work. Much of this work focused on optimizing the structure of the biplane blade, especially in the flapwise direction. Going forward, the aerodynamic shape of the blade should be optimized, with an eye towards its effect on edgewise structural performance. For example, staggering the biplane airfoils in the inboard region could improve aerodynamic performance by delaying stall and creating gentler stall characteristics. Stagger could help improve the blade's edgewise structural efficiency, but may also degrade its flapwise structural efficiency by inclining the weak bending axis of the blade to an angle between the flapwise and edgewise directions. These aerodynamic and structural phenomena could be explored by investigating three alternate configurations of the biplane blade (Figures 6.1 to 6.3). Flapwise asymmetric configurations might be considered if, under loading, the clearance between one of the inboard biplane elements and the tower becomes a more important design driver than the clearance between the blade tip and the tower. Near the root joint, it would be interesting to use biplane flatback airfoils to see if they could improve the edgewise structural efficiency of the blade.

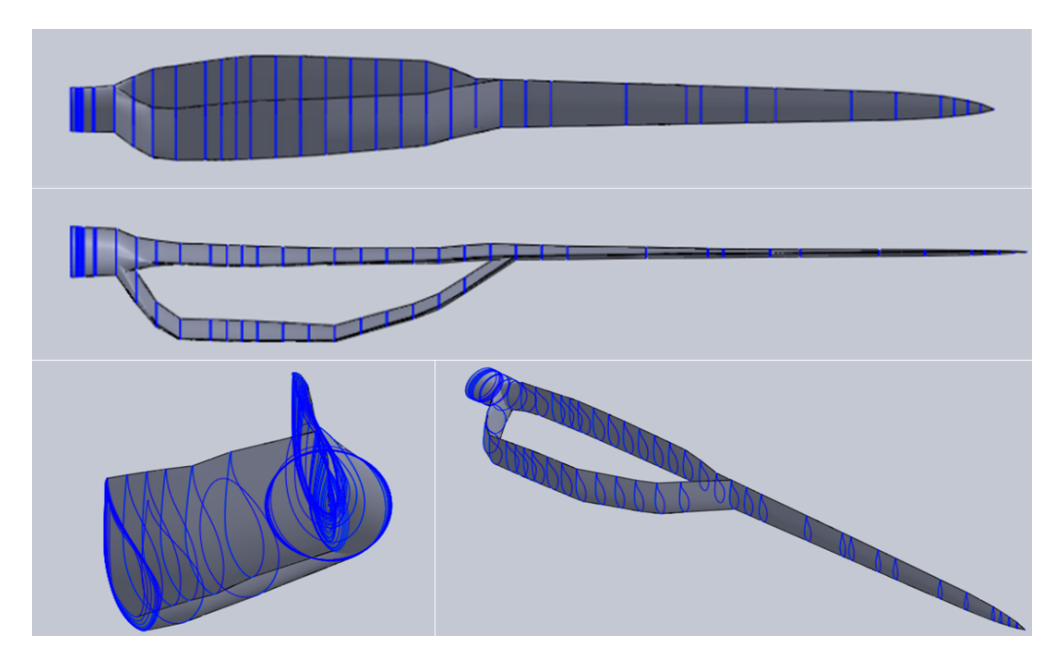


Figure 6.2: CAD rendering of biplane blade, alternate configuration 2 (flapwise asymmetric, staggered). Image credit: Christos Voutsaras.

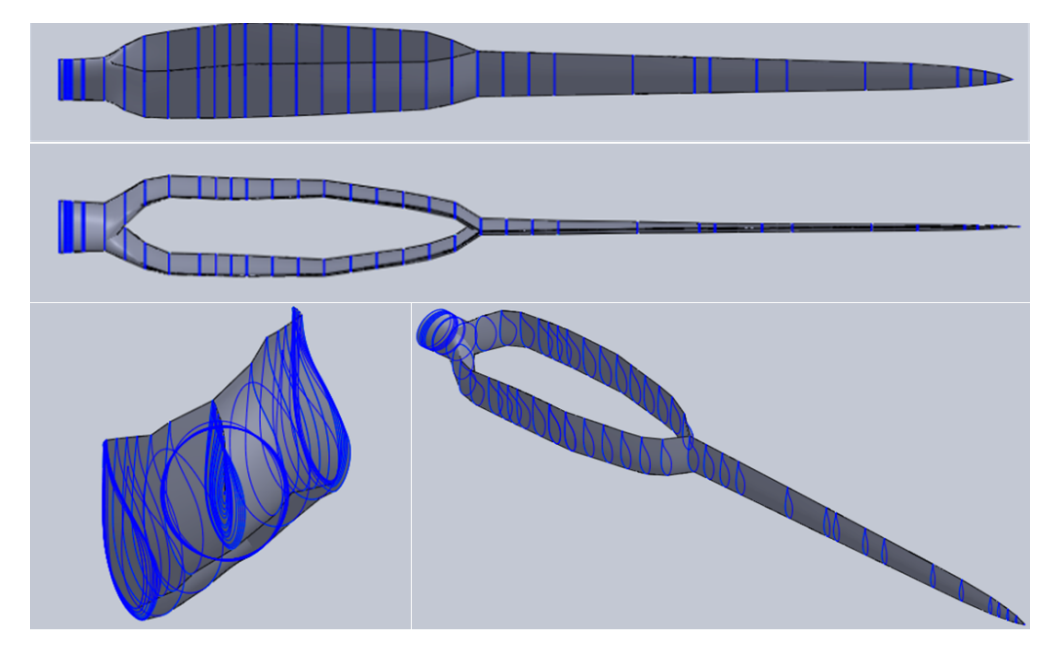


Figure 6.3: CAD rendering of biplane blade, alternate configuration 3 (flapwise symmetric, staggered). Image credit: Christos Voutsaras.

After performing an aerodynamic shape optimization, a full blade analysis should be carried out with higher order models for both aerodynamics and structures. Shell or brick finite element models should be used to investigate the stresses near the mid-blade and root joints more closely. Once these models were constructed, they could be compared to the beam models in this dissertation to further assess their accuracy. Dynamic simulations, torsion/edgewise response, improved buckling analyses, and 3D CFD should also be conducted with the full biplane blade. Aeroelastic and fatigue simulations need to be carried out to compare the stability limits and fatigue lifetime of the biplane blade to the Sandia reference blade. Experimental studies on a small-scale rotor with biplane blades could also be carried out in the future with a "truck test" [107]. Lastly, manufacturing and cost considerations need to be implemented into the biplane blade design.

APPENDIX A

Derivation of analytical model for biplane beams

Section 4.2.1 developed an analytical model for biplane beams. This appendix gives more details about the derivation steps between Sections 4.2.1.3 and 4.2.1.5.

A.1 Kinematic assumptions and essential boundary conditions

The UB, LB, and OM beams were modeled with Euler-Bernoulli beam theory. In addition to transverse bending, all beams were allowed to stretch axially. Euler-Bernoulli beam theory makes the following kinematic assumptions about the displacement fields [81]:

$$u(x,y) = u(x) - yv'(x)$$

$$v(x,y) = v(x)$$
(A.1)

Eqs. (A.1) can be rewritten for the UB, LB, and OM beams as:

$$u_{\rm UB}(x,y) = u_{\rm UB}(x) - yv'_{\rm UB}(x)$$

$$v_{\rm UB}(x,y) = v_{\rm UB}(x)$$

$$u_{\rm LB}(x,y) = u_{\rm LB}(x) - yv'_{\rm LB}(x)$$

$$v_{\rm LB}(x,y) = v_{\rm LB}(x)$$

$$u_{\rm OM}(x,y) = u_{\rm OM}(x) - yv'_{\rm OM}(x)$$

$$v_{\rm OM}(x,y) = v_{\rm OM}(x)$$

Since the UB and LB beams are both cantilevered at x = 0, their axial displacements

(u), transverse displacements (v), and cross-section rotations (v') must all be zero.

$$u_{\rm UB}(0) = 0$$
 $u_{\rm LB}(0) = 0$
 $v_{\rm UB}(0) = 0$
 $v_{\rm LB}(0) = 0$
 $v'_{\rm UB}(0) = 0$
 $v'_{\rm LB}(0) = 0$

The rigid joint has three degrees of freedom: transverse displacement, rotation, and axial displacement (Figure 4.4). The joint effectively links the movement of all three beams at $x = r_j$. At the joint, the transverse displacements and rotations of all three beams must be equal.

$$v_{\text{UB}}(r_j) = v_{\text{OM}}(r_j)$$

$$v_{\text{LB}}(r_j) = v_{\text{OM}}(r_j)$$

$$v'_{\text{UB}}(r_j) = v'_{\text{OM}}(r_j)$$

$$v'_{\text{LB}}(r_j) = v'_{\text{OM}}(r_j)$$
(A.3)

Additionally, at the joint, the axial displacements of the UB and LB beams are related to the axial displacement of the OM beam and the rotation of the OM beam.

$$u_{\rm UB}(r_j) = u_{\rm OM}(r_j) + \frac{1}{2}gv'_{\rm OM}(r_j)$$

 $u_{\rm LB}(r_j) = u_{\rm OM}(r_j) - \frac{1}{2}gv'_{\rm OM}(r_j)$ (A.4)

A.2 Potential energy

Strain energy: Considering the kinematic assumptions in Eqs. (A.1), the only nonzero strain component is

$$\varepsilon_{xx} = \frac{\partial u}{\partial x} = u' - yv''. \tag{A.5}$$

Each beam is assumed to be made of an isotropic, linear elastic material. With this assumption, Hooke's Law gives the constitutive stress-strain relations as

$$\sigma_{xx} = E\varepsilon_{xx},\tag{A.6}$$

where E is the Young's modulus of the material. The strain energy of a linear elastic structure can be written in general form as

$$\mathcal{U} = \int_{\mathcal{B}} \frac{1}{2} \sigma_{ij} \varepsilon_{ij} dV. \tag{A.7}$$

Substituting the constitutive relations (Equation (A.6)) and strains (Equation (A.5)) for a beam into the strain energy (Equation (A.7)), we obtain the strain energy of a single Euler-Bernoulli beam with axial stretch as

$$\mathcal{U}_{\text{beam}} = \int_0^L \left[\frac{1}{2} E A(u')^2 + \frac{1}{2} E I(v'')^2 \right] dx.$$

Hence, the total strain energy for all three beams in the biplane beam structure must be

$$\mathcal{U} = \int_{0}^{r_{j}} \left[\frac{1}{2} E A_{\mathrm{UB}} (u'_{\mathrm{UB}})^{2} + \frac{1}{2} E I_{\mathrm{UB}} (v''_{\mathrm{UB}})^{2} \right] dx$$

$$+ \int_{0}^{r_{j}} \left[\frac{1}{2} E A_{\mathrm{LB}} (u'_{\mathrm{LB}})^{2} + \frac{1}{2} E I_{\mathrm{LB}} (v''_{\mathrm{LB}})^{2} \right] dx$$

$$+ \int_{r_{j}}^{R} \left[\frac{1}{2} E A_{\mathrm{OM}} (u'_{\mathrm{OM}})^{2} + \frac{1}{2} E I_{\mathrm{OM}} (v''_{\mathrm{OM}})^{2} \right] dx.$$
(A.8)

Potential energy of applied loads: The potential energy of all three distributed transverse loads is

$$\mathcal{V} = \int_0^{r_j} q_{\mathrm{UB}} v_{\mathrm{UB}} dx + \int_0^{r_j} q_{\mathrm{LB}} v_{\mathrm{LB}} dx + \int_{r_i}^R q_{\mathrm{OM}} v_{\mathrm{OM}} dx. \tag{A.9}$$

Total potential energy: Now, Equations (A.8) and (A.9) can be combined to write

the total potential energy $(\Pi = \mathcal{U} - \mathcal{V})$ as

$$\Pi = \int_{0}^{r_{j}} \left[\frac{1}{2} E A_{\mathrm{UB}} (u'_{\mathrm{UB}})^{2} + \frac{1}{2} E I_{\mathrm{UB}} (v''_{\mathrm{UB}})^{2} - q_{\mathrm{UB}} v_{\mathrm{UB}} \right] dx
+ \int_{0}^{r_{j}} \left[\frac{1}{2} E A_{\mathrm{LB}} (u'_{\mathrm{LB}})^{2} + \frac{1}{2} E I_{\mathrm{LB}} (v''_{\mathrm{LB}})^{2} - q_{\mathrm{LB}} v_{\mathrm{LB}} \right] dx
+ \int_{r_{j}}^{R} \left[\frac{1}{2} E A_{\mathrm{OM}} (u'_{\mathrm{OM}})^{2} + \frac{1}{2} E I_{\mathrm{OM}} (v''_{\mathrm{OM}})^{2} - q_{\mathrm{OM}} v_{\mathrm{OM}} \right] dx.$$
(A.10)

A.3 Minimum total potential energy

The total potential energy is minimized by taking the first variation of Π in Equation (A.10) and setting it equal to zero ($\delta\Pi=0$). The variational operator $\delta(\cdot)$ behaves similarly to the chain rule; therefore, the first variation can be written as

$$\begin{split} \delta\Pi &= \frac{\partial\Pi}{\partial u'_{\mathrm{UB}}} \delta u'_{\mathrm{UB}} + \frac{\partial\Pi}{\partial v''_{\mathrm{UB}}} \delta v''_{\mathrm{UB}} + \frac{\partial\Pi}{\partial u'_{\mathrm{LB}}} \delta u'_{\mathrm{LB}} + \frac{\partial\Pi}{\partial v''_{\mathrm{LB}}} \delta v''_{\mathrm{LB}} \\ &+ \frac{\partial\Pi}{\partial u'_{\mathrm{OM}}} \delta u'_{\mathrm{OM}} + \frac{\partial\Pi}{\partial v''_{\mathrm{OM}}} \delta v''_{\mathrm{OM}} \\ \Rightarrow 0 &= \int_0^{r_j} \left[EA_{\mathrm{UB}} u'_{\mathrm{UB}} \delta u'_{\mathrm{UB}} + EI_{\mathrm{UB}} v''_{\mathrm{UB}} \delta v''_{\mathrm{UB}} - q_{\mathrm{UB}} \delta v_{\mathrm{UB}} \right] dx \\ &+ \int_0^{r_j} \left[EA_{\mathrm{LB}} u'_{\mathrm{LB}} \delta u'_{\mathrm{LB}} + EI_{\mathrm{LB}} v''_{\mathrm{LB}} \delta v''_{\mathrm{LB}} - q_{\mathrm{LB}} \delta v_{\mathrm{LB}} \right] dx \\ &+ \int_{r_j}^{R} \left[EA_{\mathrm{OM}} u'_{\mathrm{OM}} \delta u'_{\mathrm{OM}} + EI_{\mathrm{OM}} v''_{\mathrm{OM}} \delta v''_{\mathrm{OM}} - q_{\mathrm{OM}} \delta v_{\mathrm{OM}} \right] dx. \end{split}$$

Integration by parts eliminates the derivatives on the δ -terms.

$$\begin{split} 0 &= \left[EA_{\mathrm{UB}}u'_{\mathrm{UB}}\delta u_{\mathrm{UB}}\right]_{0}^{r_{j}} + \left[EI_{\mathrm{UB}}v''_{\mathrm{UB}}\delta v'_{\mathrm{UB}}\right]_{0}^{r_{j}} - \left[\left(EI_{\mathrm{UB}}v''_{\mathrm{UB}}\right)'\delta v_{\mathrm{UB}}\right]_{0}^{r_{j}} \\ &+ \int_{0}^{r_{j}} \left(\left[\left(EI_{\mathrm{UB}}v''_{\mathrm{UB}}\right)'' - q_{\mathrm{UB}}\right]\delta v_{\mathrm{UB}} - \left[EA_{\mathrm{UB}}u'_{\mathrm{UB}}\right]'\delta u_{\mathrm{UB}}\right)dx \\ &+ \left[EA_{\mathrm{LB}}u'_{\mathrm{LB}}\delta u_{\mathrm{LB}}\right]_{0}^{r_{j}} + \left[EI_{\mathrm{LB}}v''_{\mathrm{LB}}\delta v'_{\mathrm{LB}}\right]_{0}^{r_{j}} - \left[\left(EI_{\mathrm{LB}}v''_{\mathrm{LB}}\right)'\delta v_{\mathrm{LB}}\right]_{0}^{r_{j}} \\ &+ \int_{0}^{r_{j}} \left(\left[\left(EI_{\mathrm{LB}}v''_{\mathrm{UB}}\right)'' - q_{\mathrm{LB}}\right]\delta v_{\mathrm{LB}} - \left[EA_{\mathrm{LB}}u'_{\mathrm{LB}}\right]'\delta u_{\mathrm{LB}}\right)dx \\ &+ \left[EA_{\mathrm{OM}}u'_{\mathrm{OM}}\delta u_{\mathrm{OM}}\right]_{0}^{r_{j}} + \left[EI_{\mathrm{OM}}v''_{\mathrm{OM}}\delta v'_{\mathrm{OM}}\right]_{0}^{r_{j}} - \left[\left(EI_{\mathrm{OM}}v''_{\mathrm{OM}}\right)'\delta v_{\mathrm{OM}}\right]_{0}^{r_{j}} \\ &+ \int_{r_{j}}^{R} \left(\left[\left(EI_{\mathrm{OM}}v''_{\mathrm{OM}}\right)'' - q_{\mathrm{OM}}\right]\delta v_{\mathrm{OM}} - \left[EA_{\mathrm{OM}}u'_{\mathrm{OM}}\right]'\delta u_{\mathrm{OM}}\right)dx \end{split}$$

Evaluating the boundary terms gives

$$0 = EA_{\mathrm{UB}}(r_{j})u'_{\mathrm{UB}}(r_{j})\delta u_{\mathrm{UB}}(r_{j}) - EA_{\mathrm{UB}}(0)u'_{\mathrm{UB}}(0)\delta u_{\mathrm{UB}}(0)$$

$$+ EI_{\mathrm{UB}}(r_{j})v''_{\mathrm{UB}}(r_{j})\delta v'_{\mathrm{UB}}(r_{j}) - EI_{\mathrm{UB}}(0)v''_{\mathrm{UB}}(0)\delta v'_{\mathrm{UB}}(0)$$

$$- (EI_{\mathrm{UB}}v''_{\mathrm{UB}})'\big|_{r_{j}}\delta v_{\mathrm{UB}}(r_{j}) + (EI_{\mathrm{UB}}v''_{\mathrm{UB}})'\big|_{0}\delta v_{\mathrm{UB}}(0)$$

$$+ EA_{\mathrm{LB}}(r_{j})u'_{\mathrm{LB}}(r_{j})\delta u_{\mathrm{LB}}(r_{j}) - EA_{\mathrm{LB}}(0)u'_{\mathrm{LB}}(0)\delta u_{\mathrm{LB}}(0)$$

$$+ EI_{\mathrm{LB}}(r_{j})v''_{\mathrm{LB}}(r_{j})\delta v'_{\mathrm{LB}}(r_{j}) - EI_{\mathrm{LB}}(0)v''_{\mathrm{LB}}(0)\delta v'_{\mathrm{LB}}(0)$$

$$- (EI_{\mathrm{LB}}v''_{\mathrm{LB}})'\big|_{r_{j}}\delta v_{\mathrm{LB}}(r_{j}) + (EI_{\mathrm{LB}}v''_{\mathrm{LB}})'\big|_{0}\delta v_{\mathrm{LB}}(0)$$

$$+ EA_{\mathrm{OM}}(R)u'_{\mathrm{OM}}(R)\delta u_{\mathrm{OM}}(R) - EA_{\mathrm{OM}}(r_{j})u'_{\mathrm{OM}}(r_{j})\delta u_{\mathrm{OM}}(r_{j})$$

$$+ EI_{\mathrm{OM}}(R)v''_{\mathrm{OM}}(R)\delta v'_{\mathrm{OM}}(R) - EI_{\mathrm{OM}}(r_{j})v''_{\mathrm{OM}}(r_{j})\delta v'_{\mathrm{OM}}(r_{j})$$

$$- (EI_{\mathrm{OM}}v''_{\mathrm{OM}})'\big|_{R}\delta v_{\mathrm{OM}}(R) + (EI_{\mathrm{OM}}v''_{\mathrm{OM}})'\big|_{r_{j}}\delta v_{\mathrm{OM}}(r_{j})$$

$$+ \int_{0}^{r_{j}} \left(\left[(EI_{\mathrm{UB}}v''_{\mathrm{UB}})'' - q_{\mathrm{UB}} \right]\delta v_{\mathrm{UB}} - \left[EA_{\mathrm{UB}}u'_{\mathrm{UB}} \right]'\delta u_{\mathrm{UB}} \right) dx$$

$$+ \int_{0}^{r_{j}} \left(\left[(EI_{\mathrm{LB}}v''_{\mathrm{DM}})'' - q_{\mathrm{LB}} \right]\delta v_{\mathrm{CM}} - \left[EA_{\mathrm{LB}}u'_{\mathrm{LB}} \right]'\delta u_{\mathrm{CM}} \right) dx$$

$$+ \int_{r_{j}}^{R} \left(\left[(EI_{\mathrm{CM}}v''_{\mathrm{OM}})'' - q_{\mathrm{OM}} \right]\delta v_{\mathrm{OM}} - \left[EA_{\mathrm{OM}}u'_{\mathrm{OM}} \right]'\delta u_{\mathrm{OM}} \right) dx.$$

Several of the boundary terms in Equation (A.11) can be eliminated or combined by satisfying the essential boundary conditions at the root (Equation (A.2)) and the rigid joint

(Equations (A.3) and (A.4)). Eqs. (A.2) imply that

$$\delta u_{\rm UB}(0) = 0$$

$$\delta u_{\rm LB}(0) = 0$$

$$\delta v_{\rm UB}(0) = 0$$

$$\delta v_{\rm LB}(0) = 0$$

$$\delta v'_{\rm UB}(0) = 0$$

$$\delta v'_{\rm LB}(0) = 0$$

$$\delta v'_{\rm LB}(0) = 0.$$

Similarly, Eqs. (A.3) imply that

$$\delta v_{\rm UB}(r_j) = \delta v_{\rm OM}(r_j)$$

$$\delta v_{\rm LB}(r_j) = \delta v_{\rm OM}(r_j)$$

$$\delta v'_{\rm UB}(r_j) = \delta v'_{\rm OM}(r_j)$$

$$\delta v'_{\rm LB}(r_j) = \delta v'_{\rm OM}(r_j)$$

$$\delta v'_{\rm LB}(r_j) = \delta v'_{\rm OM}(r_j)$$
(A.13)

Finally, Eqs. (A.4) imply that

$$\delta u_{\rm UB}(r_j) = \delta u_{\rm OM}(r_j) + \frac{1}{2}g\delta v'_{\rm OM}(r_j)$$

$$\delta u_{\rm LB}(r_j) = \delta u_{\rm OM}(r_j) - \frac{1}{2}g\delta v'_{\rm OM}(r_j)$$
(A.14)

Substituting Equations (A.12) to (A.14) into Equation (A.11) gives

$$0 = EA_{\text{UB}}(r_{j})u'_{\text{UB}}(r_{j}) \left[\delta u_{\text{OM}}(r_{j}) + \frac{1}{2}g\delta v'_{\text{OM}}(r_{j}) \right]$$

$$+ EI_{\text{UB}}(r_{j})v''_{\text{UB}}(r_{j})\delta v'_{\text{OM}}(r_{j})$$

$$- (EI_{\text{UB}}v''_{\text{UB}})' \Big|_{r_{j}}\delta v_{\text{OM}}(r_{j})$$

$$+ EA_{\text{LB}}(r_{j})u'_{\text{LB}}(r_{j}) \left[\delta u_{\text{OM}}(r_{j}) - \frac{1}{2}g\delta v'_{\text{OM}}(r_{j}) \right]$$

$$+ EI_{\text{LB}}(r_{j})v''_{\text{LB}}(r_{j})\delta v'_{\text{OM}}(r_{j})$$

$$- (EI_{\text{LB}}v''_{\text{LB}})' \Big|_{r_{j}}\delta v_{\text{OM}}(r_{j})$$

$$+ EA_{\text{OM}}(R)u'_{\text{OM}}(R)\delta u_{\text{OM}}(R) - EA_{\text{OM}}(r_{j})u'_{\text{OM}}(r_{j})\delta u_{\text{OM}}(r_{j})$$

$$+ EI_{\text{OM}}(R)v''_{\text{OM}}(R)\delta v'_{\text{OM}}(R) - EI_{\text{OM}}(r_{j})v''_{\text{OM}}(r_{j})\delta v'_{\text{OM}}(r_{j})$$

$$- (EI_{\text{OM}}v''_{\text{OM}})' \Big|_{R}\delta v_{\text{OM}}(R) + (EI_{\text{OM}}v''_{\text{OM}})' \Big|_{r_{j}}\delta v_{\text{OM}}(r_{j})$$

$$+ \int_{0}^{r_{j}} \left(\left[(EI_{\text{UB}}v''_{\text{UB}})'' - q_{\text{UB}} \right] \delta v_{\text{UB}} - \left[EA_{\text{UB}}u'_{\text{UB}} \right]' \delta u_{\text{UB}} \right) dx$$

$$+ \int_{0}^{r_{j}} \left(\left[(EI_{\text{LB}}v''_{\text{UB}})'' - q_{\text{LB}} \right] \delta v_{\text{OM}} - \left[EA_{\text{UB}}u'_{\text{UB}} \right]' \delta u_{\text{OM}} \right) dx$$

$$+ \int_{r_{j}}^{R} \left(\left[(EI_{\text{OM}}v''_{\text{OM}})'' - q_{\text{OM}} \right] \delta v_{\text{OM}} - \left[EA_{\text{OM}}u'_{\text{OM}} \right]' \delta u_{\text{OM}} \right) dx .$$

Collecting all the δ -terms gives the expression for minimum total potential energy given in Equation (A.15). After integration of parts and manipulation of the boundary terms, the

expression for minimum total potential energy becomes

$$0 = EA_{\rm OM}(R)u'_{\rm OM}(R)\delta u_{\rm OM}(R) - (EI_{\rm OM}v''_{\rm OM})'|_{R}\delta v_{\rm OM}(R) + EI_{\rm OM}(R)v''_{\rm OM}(R)\delta v'_{\rm OM}(R) + [EA_{\rm UB}(r_{j})u'_{\rm UB}(r_{j}) + EA_{\rm LB}(r_{j})u'_{\rm LB}(r_{j}) - EA_{\rm OM}(r_{j})u'_{\rm OM}(r_{j})]\delta u_{\rm OM}(r_{j}) + [(EI_{\rm OM}v''_{\rm OM})'|_{r_{j}} - (EI_{\rm UB}v''_{\rm UB})'|_{r_{j}} - (EI_{\rm LB}v''_{\rm LB})'|_{r_{j}}]\delta v_{\rm OM}(r_{j}) + [EI_{\rm UB}(r_{j})v''_{\rm UB}(r_{j}) + EI_{\rm LB}(r_{j})v''_{\rm LB}(r_{j}) - EI_{\rm OM}(r_{j})v''_{\rm OM}(r_{j}) + \frac{1}{2}gEA_{\rm UB}(r_{j})u'_{\rm UB}(r_{j}) - \frac{1}{2}gEA_{\rm LB}(r_{j})u'_{\rm LB}(r_{j})]\delta v'_{\rm OM}(r_{j}) + \int_{0}^{r_{j}} [(EI_{\rm UB}v''_{\rm UB})'' - q_{\rm UB}]\delta v_{\rm UB}dx - \int_{0}^{r_{j}} (EA_{\rm UB}u'_{\rm UB})'\delta u_{\rm UB}dx + \int_{0}^{r_{j}} [(EI_{\rm LB}v''_{\rm LB})'' - q_{\rm LB}]\delta v_{\rm LB}dx - \int_{0}^{r_{j}} (EA_{\rm LB}u'_{\rm LB})'\delta u_{\rm LB}dx + \int_{r_{j}}^{R} [(EI_{\rm OM}v''_{\rm OM})'' - q_{\rm OM}]\delta v_{\rm OM}dx - \int_{r_{j}}^{R} (EA_{\rm OM}u'_{\rm OM})'\delta u_{\rm OM}dx.$$

A.4 Equilibrium equations

In order for Equation (A.15) to be equal to zero, each of the individual terms on the right hand side must vanish. In the integral terms, $\delta u_{\rm UB}$, $\delta u_{\rm LB}$, $\delta u_{\rm OM}$, $\delta v_{\rm UB}$, $\delta v_{\rm LB}$, and $\delta v_{\rm OM}$ are all arbitrary. By the fundamental lemma of the calculus of variations [81], each of the integrands must vanish, thereby giving six equilibrium equations.

$$(EI_{\mathrm{UB}}v_{\mathrm{UB}}'')'' = q_{\mathrm{UB}}, \qquad 0 \le x \le r_j \tag{A.16a}$$

$$(EI_{LB}v_{LB}'')'' = q_{LB}, \qquad 0 \le x \le r_j \tag{A.16b}$$

$$(EI_{\text{OM}}v_{\text{OM}}'')'' = q_{\text{OM}}, \qquad r_j \le x \le R$$
(A.16c)

$$(EA_{\mathrm{UB}}u'_{\mathrm{UB}})' = 0, \qquad 0 \le x \le r_j \tag{A.16d}$$

$$(EA_{LB}u'_{LB})' = 0, \qquad 0 \le x \le r_j \tag{A.16e}$$

$$(EA_{\text{OM}}u'_{\text{OM}})' = 0, \qquad r_j \le x \le R \tag{A.16f}$$

A.5 Natural boundary conditions

Each of the boundary terms must also vanish in order for Equation (A.15) to be equal to zero. Because the terms $\delta u_{\rm OM}$, $\delta v_{\rm OM}$, and $\delta v'_{\rm OM}$ are all arbitrary, each of their leading coefficients must vanish. Hence, six natural boundary conditions are obtained. Three of the natural boundary conditions are at the joint $(x = r_j)$.

$$EA_{\rm UB}(r_j)u'_{\rm UB}(r_j) + EA_{\rm LB}(r_j)u'_{\rm LB}(r_j) - EA_{\rm OM}(r_j)u'_{\rm OM}(r_j) = 0$$
 (A.17a)

$$(EI_{\rm OM}v_{\rm OM}'')'|_{r_i} - (EI_{\rm UB}v_{\rm UB}'')'|_{r_i} - (EI_{\rm LB}v_{\rm LB}'')'|_{r_i} = 0$$
 (A.17b)

$$EI_{\text{UB}}(r_j)v_{\text{UB}}''(r_j) + EI_{\text{LB}}(r_j)v_{\text{LB}}''(r_j) - EI_{\text{OM}}(r_j)v_{\text{OM}}''(r_j) + \frac{1}{2}gEA_{\text{UB}}(r_j)u_{\text{UB}}'(r_j) - \frac{1}{2}gEA_{\text{LB}}(r_j)u_{\text{LB}}'(r_j) = 0$$
(A.17c)

The other three natural boundary conditions are at the tip (x = R).

$$EA_{\rm OM}(R)u'_{\rm OM}(R) = 0 \tag{A.18a}$$

$$\left(EI_{\rm OM}v_{\rm OM}''\right)'\big|_{R} = 0 \tag{A.18b}$$

$$EI_{\rm OM}(R)v_{\rm OM}''(R) = 0 \tag{A.18c}$$

Together, the equilibrium equations (Equation (A.16)) and boundary conditions (Equations (A.2) to (A.4), (A.17) and (A.18)) form a general solution that can be used to model the structural response of the biplane beam under static loading.

A.6 Assumptions for engineering properties

In order to make the analytical model tractable, some assumptions were made for the engineering properties and loads on the biplane beam, leading to simpler equilibrium equations and natural boundary conditions. It was assumed that EA and EI were constant along each of the spans of the OM, UB, and LB beams. Furthermore, the inboard biplane properties

were scaled to the outboard monoplane properties with constants α and β , such that

$$EA_{\mathrm{OM}}(x) = EA$$

$$EI_{\mathrm{OM}}(x) = EI$$

$$EA_{\mathrm{UB}}(x) = \alpha EA$$

$$EI_{\mathrm{UB}}(x) = \beta EI$$

$$EA_{\mathrm{LB}}(x) = \alpha EA$$

$$EI_{\mathrm{LB}}(x) = \beta EI,$$
(A.19)

or, expressed another way

$$\alpha = \frac{EA_{\rm UB}}{EA_{\rm OM}} = \frac{EA_{\rm LB}}{EA_{\rm OM}}$$

$$\beta = \frac{EI_{\rm UB}}{EI_{\rm OM}} = \frac{EI_{\rm LB}}{EI_{\rm OM}}.$$
(A.20)

To approximate the flapwise bending moment (the primary load on wind turbine blades [51]), the transverse distributed loads were assumed to be constant along each of the spans of the OM, UB, and LB beams. The constant load distribution approximates an "instantaneous snapshot" of a gust load on a wind turbine blade. These gust loads often lead to the worst-case scenario of all the design load cases suggested by international certification standards of wind turbine blades [82], as was shown in [9]. The magnitude of the inboard distributed loads were assumed to be half of the magnitude of the outboard distributed load (Eqs. (A.21)). In other words, the constant load distribution that would normally be present on the inboard region of a conventional monoplane blade was equally distributed among the UB and LB beams.

$$q_{\text{OM}}(x) = q_0$$

$$q_{\text{UB}}(x) = \frac{1}{2}q_0$$

$$q_{\text{LB}}(x) = \frac{1}{2}q_0.$$
(A.21)

The assumptions in Equations (4.1) and (A.19) simplify the equilibrium equations (Equa-

tion (A.16)) as

$$\beta E I v_{\text{UB}}^{""} = \frac{1}{2} q_0, \qquad 0 \le x \le r_j$$
 (A.22a)

$$\beta E I v_{\text{LB}}^{""} = \frac{1}{2} q_0, \qquad 0 \le x \le r_j$$
 (A.22b)

$$EIv_{OM}^{""} = q_0, \qquad r_i \le x \le R$$
 (A.22c)

$$\alpha E A u_{\text{UB}}^{"} = 0, \qquad 0 \le x \le r_j \tag{A.22d}$$

$$\alpha E A u_{\rm LB}^{"} = 0, \qquad 0 \le x \le r_j \tag{A.22e}$$

$$EAu''_{OM} = 0, r_j \le x \le R$$
 (A.22f)

and the natural boundary conditions at the joint (Equation (A.17)) as

$$\alpha E A u'_{\text{UB}}(r_j) + \alpha E A u'_{\text{LB}}(r_j) - E A u'_{\text{OM}}(r_j) = 0$$
(A.23a)

$$EIv_{\text{OM}}^{""}(r_j) - \beta EIv_{\text{UB}}^{""}(r_j) - \beta EIv_{\text{LB}}^{""}(r_j) = 0$$
(A.23b)

$$\beta E I v_{\text{UB}}''(r_j) + \beta E I v_{\text{LB}}''(r_j) - E I v_{\text{OM}}''(r_j)$$
$$+ \frac{1}{2} g \alpha E A u_{\text{UB}}'(r_j) - \frac{1}{2} g \alpha E A u_{\text{LB}}'(r_j) = 0$$
(A.23c)

and the natural boundary conditions at the tip (Equation (A.18)) as

$$EAu'_{OM}(R) = 0 (A.24a)$$

$$EIv_{\rm OM}^{\prime\prime\prime}(R) = 0 \tag{A.24b}$$

$$EIv''_{OM}(R) = 0. (A.24c)$$

A.7 Solution of equilibrium equations

The simplified equilibrium equations and boundary conditions form a boundary value problem that can now be solved analytically. The method of undetermined coefficients [108] was used to solve the nonhomogeneous ordinary differential equations in Equation (A.22), subject to the boundary conditions in Equations (A.2) to (A.4), (A.23) and (A.24). Python-based software was used to help derive the solution to this boundary value problem. The symbolic math package SymPy 0.7.2 [85] was used inside the web-based notebook environment of IPython 0.13 [86] to record each step of the derivation. Because the derivation is lengthy, it is omitted here; refer to [109, 110] for more details. The resulting analytical solution is given in Equations (4.4) and (4.5).

APPENDIX B

Laminate schedules for spars

The tables in this appendix list the laminate thicknesses of composite materials used to construct three spars: a monoplane spar derived from the Sandia SNL100-00 blade (Figure 4.5(a)), a biplane spar with half-height cross-sections (Figure 4.11 (top)), and a biplane spar with full-height cross-sections (Figure 4.11 (bottom)). Each spar has the same length and mass.

Table B.1: Laminate schedule for the monoplane spar. All spar stations use monoplane cross-sections. Note: the coordinate x_1 is in the spanwise direction, pointing from the spar root to the spar tip.

spar	spar	coordinate	root b	root buildup	spar	spar cap		shear web	
station	fraction (-)	x_1 (m)	b_{RB} (m)	h_{RB} (m)	b_{SC} (m)	h_{SC} (m)	bSW,foam (m)	$b_{SW, \text{biax}}$ (m)	h_{SW} (m)
1	0.000	0.0	1.672	0.063	1.500	0.013	0.080	0.003	5.266
2	0.002	0.2	1.672	0.055	1.500	0.013	0.080	0.003	5.265
က	0.025	2.3	1.672	0.040	1.500	0.020	0.080	0.003	5.009
4	0.048	4.4	1.672	0.025	1.500	0.030	0.080	0.003	4.741
2	0.071	6.5	1.672	0.015	1.500	0.051	0.080	0.003	4.425
9	0.098	0.6	1.672	0.005	1.500	0.068	0.080	0.003	4.091
7	0.133	12.2	0.000	0.000	1.500	0.094	0.080	0.003	3.680
œ	0.151	13.9	0.000	0.000	1.500	0.111	0.080	0.003	3.480
6	0.169	15.5	0.000	0.000	1.500	0.119	0.080	0.003	3.285
10	0.186	17.1	0.000	0.000	1.500	0.136	0.080	0.003	3.089
11	0.215	19.8	0.000	0.000	1.500	0.136	0.080	0.003	2.882
12	0.245	22.5	0.000	0.000	1.500	0.136	0.080	0.003	2.696
13	0.274	25.2	0.000	0.000	1.500	0.128	0.080	0.003	2.498
14	0.363	33.4	0.000	0.000	1.500	0.119	0.080	0.003	2.077
15	0.452	41.5	0.000	0.000	1.500	0.111	0.080	0.003	1.672
16	0.540	49.6	0.000	0.000	1.500	0.102	0.080	0.003	1.360
17	0.629	57.8	0.000	0.000	1.500	0.085	0.080	0.003	1.138
18	0.700	64.3	0.000	0.000	1.500	0.068	0.080	0.003	0.954
19	0.717	62.9	0.000	0.000	1.500	0.064	0.080	0.003	0.910
20	0.770	70.8	0.000	0.000	1.500	0.047	0.080	0.003	0.832
21	0.805	74.0	0.000	0.000	1.500	0.034	0.080	0.003	0.796
22	0.894	82.2	0.000	0.000	1.500	0.017	0.080	0.003	0.707
23	0.947	87.0	0.000	0.000	1.500	600.0	0.080	0.003	0.651
24	1.000	91.9	0.000	0.000	1.500	0.005	0.080	0.003	0.508

gap-to-chord ratio g/c=1.25. Spar stations 1-14 use "half-height" biplane cross-sections; stations 15-24 use monoplane cross-sections. **Table B.2:** Laminate schedule for a biplane spar with "half-height" cross-sections, joint length-to-span ratio $r_j/R=0.452$, and

snar	snar	Coord	coordinates	root	root building	Spar	snar can		shear weh	
station	fraction (-)	x ₁ (m)	x3 (m)	b_{RB} (m)	h_{RB} (m)	b_{SC} (m)	h_{SC} (m)	$b_{SW, \text{foam}}$ (m)	bSW,biax (m)	h_{SW} (m)
1	0.000	0.0	±4.768	1.672	0.0315	1.500	0.0065	0.080	0.003	2.6330
2	0.002	0.2	± 4.768	1.672	0.0275	1.500	0.0065	0.080	0.003	2.6325
က	0.025	2.3	± 4.768	1.672	0.0200	1.500	0.0100	0.080	0.003	2.5045
4	0.048	4.4	± 4.768	1.672	0.0125	1.500	0.0150	0.080	0.003	2.3705
2	0.071	6.5	± 4.768	1.672	0.0075	1.500	0.0255	0.080	0.003	2.2125
9	0.098	0.6	± 4.768	1.672	0.0025	1.500	0.0340	0.080	0.003	2.0455
7	0.133	12.2	± 4.768	0.000	0.000	1.500	0.0470	0.080	0.003	1.8400
∞	0.151	13.9	± 4.768	0.000	0.000	1.500	0.0555	0.080	0.003	1.7400
6	0.169	15.5	± 4.768	0.000	0.000	1.500	0.0595	0.080	0.003	1.6425
10	0.186	17.1	± 4.768	0.000	0.000	1.500	0.0680	0.080	0.003	1.5445
11	0.215	19.8	± 4.768	0.000	0.000	1.500	0.0680	0.080	0.003	1.4410
12	0.245	22.5	± 4.768	0.000	0.000	1.500	0.0680	0.080	0.003	1.3480
13	0.274	25.2	± 4.768	0.000	0.000	1.500	0.0640	0.080	0.003	1.2490
14	0.363	33.4	± 2.355	0.000	0.000	1.500	0.0595	0.080	0.003	1.0385
15	0.452	41.5	0.000	0.000	0.000	1.500	0.1110	0.080	0.003	1.6720
16	0.540	49.6	0.000	0.000	0.000	1.500	0.1020	0.080	0.003	1.3600
17	0.629	57.8	0.000	0.000	0.000	1.500	0.0850	0.080	0.003	1.1380
18	0.700	64.3	0.000	0.000	0.000	1.500	0.0680	0.080	0.003	0.9540
19	0.717	62.9	0.000	0.000	0.000	1.500	0.0640	0.080	0.003	0.9100
20	0.770	70.8	0.000	0.000	0.000	1.500	0.0470	0.080	0.003	0.8320
21	0.805	74.0	0.000	0.000	0.000	1.500	0.0340	0.080	0.003	0.7960
22	0.894	82.2	0.000	0.000	0.000	1.500	0.0170	0.080	0.003	0.7070
23	0.947	87.0	0.000	0.000	0.000	1.500	0.0000	0.080	0.003	0.6510
24	1.000	91.9	0.000	0.000	0.000	1.500	0.0050	0.080	0.003	0.5080

gap-to-chord ratio g/c=1.25. Spar stations 1-14 use "full-height" biplane cross-sections; stations 15-24 use monoplane cross-sections. **Table B.3:** Laminate schedule for a biplane spar with "full-height" cross-sections, joint length-to-span ratio $r_j/R=0.452$, and

snar	snar	proor	coordinates	root	root building	snar	snar can		shear weh	
station	fraction (-)	x ₁ (m)	x ₃ (m)	b_{RB} (m)	h_{RB} (m)	b_{SC} (m)	h_{SC} (m)	$b_{SW,\text{foam}}$ (m)	bSW.biax (m)	h_{SW} (m)
П	0.000	0.0	±4.768	1.586	0.03321	1.500	0.0065	0.040	0.0015	5.266
2	0.002	0.2	± 4.768	1.586	0.02899	1.500	0.0065	0.040	0.0015	5.265
က	0.025	2.3	± 4.768	1.586	0.02108	1.500	0.0100	0.040	0.0015	5.009
4	0.048	4.4	± 4.768	1.586	0.01318	1.500	0.0150	0.040	0.0015	4.741
2	0.071	6.5	± 4.768	1.586	0.00791	1.500	0.0255	0.040	0.0015	4.425
9	0.098	0.6	± 4.768	1.586	0.00264	1.500	0.0340	0.040	0.0015	4.091
7	0.133	12.2	± 4.768	0.000	0.0000	1.500	0.0470	0.040	0.0015	3.680
∞	0.151	13.9	± 4.768	0.000	0.0000	1.500	0.0555	0.040	0.0015	3.480
6	0.169	15.5	± 4.768	0.000	0.0000	1.500	0.0595	0.040	0.0015	3.285
10	0.186	17.1	± 4.768	0.000	0.0000.0	1.500	0.0680	0.040	0.0015	3.089
11	0.215	19.8	± 4.768	0.000	0.0000	1.500	0.0680	0.040	0.0015	2.882
12	0.245	22.5	± 4.768	0.000	0.0000	1.500	0.0680	0.040	0.0015	2.696
13	0.274	25.2	± 4.768	0.000	0.0000	1.500	0.0640	0.040	0.0015	2.498
14	0.363	33.4	± 2.355	0.000	0.0000	1.500	0.0595	0.040	0.0015	2.077
15	0.452	41.5	0.000	0.000	0.0000	1.500	0.1110	0.040	0.0015	1.672
16	0.540	49.6	0.000	0.000	0.0000	1.500	0.1020	0.040	0.0015	1.360
17	0.629	57.8	0.000	0.000	0.0000	1.500	0.0850	0.040	0.0015	1.138
18	0.700	64.3	0.000	0.000	0.0000.0	1.500	0.0680	0.040	0.0015	0.954
19	0.717	62.9	0.000	0.000	0.0000	1.500	0.0640	0.040	0.0015	0.910
20	0.770	70.8	0.000	0.000	0.0000	1.500	0.0470	0.040	0.0015	0.832
21	0.805	74.0	0.000	0.000	0.0000	1.500	0.0340	0.040	0.0015	0.796
22	0.894	82.2	0.000	0.000	0.0000.0	1.500	0.0170	0.040	0.0015	0.707
23	0.947	87.0	0.000	0.000	0.0000	1.500	0.0000	0.040	0.0015	0.651
24	1.000	91.9	0.000	0.000	0.0000	1.500	0.0050	0.040	0.0015	0.508

APPENDIX C

Spanwise properties of spars

The tables in this appendix summarize the cross-sectional stiffness and mass properties of the three spars studied in Chapter 4, whose laminate schedules are given in Appendix B. The values presented in these tables were calculated by the 2D cross-sectional analysis tool, VABS [64]. In its analysis, VABS calculates a 6×6 stiffness matrix and a 6×6 mass matrix. Only selected values from these matrices are shown here; a key is provided in Table C.1.

Table C.1: Key for translating column entries in Tables C.2 to C.4 and D.3 to VABS matrix entries in *.K files.

table column entry	VABS entry
flapwise stiffness	K_{55}
edgewise stiffness	K_{66}
torsional stiffness	K_{44}
axial stiffness	K_{11}
mass	M_{11}
flapwise mass moment of inertia	M_{55}
edgewise mass moment of inertia	M_{66}

Table C.2: Spanwise properties for the monoplane spar. These properties were calculated for each of the cross-sections in the spar, using the VABS 3.6 software [64]. All spar stations use monoplane cross-sections.

	700		stiffness	stiffness properties			mass properties	S
spar	fraction	flapwise	edgewise	torsional	axial	37 00	flapwise mass	edgewise mass
station		stiffness	stiffness	stiffness	stiffness	(1:-/-:)	moment of	moment of
	(-)	(N^*m^2)	(N^*m^2)	(N^*m^2)	<u>N</u>	(kg/m)	inertia (kg*m)	inertia (kg*m)
1	0.000	4.834E+10	2.530E+09	9.265E+08	8.073E+09	7.456E+02	3.933E+03	2.818E+02
2	0.002	4.405E + 10	2.393E+09	9.206E + 08	7.485E+09	6.961E + 02	3.573E + 03	2.703E+02
က	0.025	3.796E + 10	2.246E + 09	8.647E+08	7.175E+09	6.299E + 02	2.853E+03	2.476E+02
4	0.048	3.437E+10	2.167E + 09	8.041E + 08	7.237E+09	5.804E+02	2.311E + 03	2.278E+02
S	0.071	3.852E+10	2.421E+09	7.406E+08	9.028E+09	6.227E+02	2.248E+03	2.254E+02
9	0.098	3.803E + 10	2.577E+09	6.686E+08	1.031E+10	6.409E + 02	2.019E + 03	2.181E+02
7	0.133	3.934E + 10	3.013E + 09	5.893E + 08	1.306E + 10	7.378E+02	1.963E + 03	2.252E+02
∞	0.151	4.073E+10	3.369E + 09	5.608E + 08	1.512E + 10	8.251E + 02	2.002E+03	2.368E+02
6	0.169	3.844E + 10	3.515E + 09	5.294E + 08	1.606E + 10	8.607E+02	1.876E + 03	2.389E+02
10	0.186	3.806E + 10	3.872E + 09	5.003E + 08	1.812E + 10	9.482E + 02	1.840E + 03	2.507E+02
11	0.215	3.287E + 10	3.827E + 09	4.641E + 08	1.805E + 10	9.371E + 02	1.584E + 03	2.437E + 02
12	0.245	2.853E + 10	3.786E + 09	4.317E + 08	1.799E + 10	9.272E + 02	1.372E + 03	2.375E+02
13	0.274	2.301E + 10	3.555E + 09	3.948E + 08	1.692E + 10	8.706E+02	1.106E + 03	2.222E+02
14	0.363	1.458E + 10	3.251E + 09	3.189E + 08	1.564E + 10	7.963E + 02	6.976E+02	1.983E + 02
15	0.452	8.629E + 09	2.975E + 09	2.462E + 08	1.450E + 10	7.286E+02	4.109E + 02	1.761E + 02
16	0.540	5.144E + 09	2.695E + 09	1.898E + 08	1.326E + 10	6.601E + 02	2.441E + 02	1.559E + 02
17	0.629	3.004E + 09	2.247E + 09	1.468E + 08	1.105E + 10	5.503E + 02	1.426E + 02	1.300E + 02
18	0.700	1.702E + 09	1.807E + 09	1.105E + 08	8.857E+09	4.426E+02	8.088E+01	1.055E + 02
19	0.717	1.461E + 09	1.703E + 09	1.020E + 08	8.341E + 09	4.172E + 02	6.944E + 01	9.970E + 01
20	0.770	9.257E + 08	1.287E + 09	8.210E + 07	6.182E + 09	3.151E + 02	4.432E + 01	7.872E+01
21	0.805	6.339E + 08	9.730E + 08	6.861E + 07	4.539E+09	2.383E + 02	3.069E + 0.1	6.347E + 01
22	0.894	2.640E+08	5.538E + 08	4.080E+07	2.376E+09	1.356E + 02	1.323E + 01	4.212E + 01
23	0.947	1.242E + 08	3.535E + 08	2.352E+07	1.354E + 09	8.658E + 01	6.569E + 00	3.160E + 01
24	1.000	4.343E + 07	2.283E + 08	9.361E + 06	8.026E+08	5.591E + 01	2.405E+00	2.247E+01

[64]. For spar stations 1-14, properties of the upper and lower biplane elements are reported separately, with respect to the **Table C.3:** Spanwise properties for a biplane spar with "half-height" cross-sections, joint length-to-span ratio $r_j/R=0.452$, and gap-to-chord ratio g/c=1.25. These properties were calculated for each of the cross-sections in the spar, using VABS 1D reference lines in Figure 4.12. For spar station 14, a curvature correction (curvature about the x_2 -axis, $k_2 = 0.0020$ rad/m) was applied to both the upper and lower biplane elements.

	:	upper or		stiffness _l	stiffness properties			mass properties	SS.
spar	spar	lower	flapwise	edgewise	torsional	axial	3300	flapwise mass	edgewise mass
station		biplane	stiffness	stiffness	stiffness	stiffness	(kg/m)	moment of	moment of
	(-)	element	(N^*m^2)	(N^*m^2)	(N^*m^2)	(N)	(KB/III)	inertia (kg*m)	inertia (kg*m)
-	0000	upper	6.043E + 09	1.265E + 09	4.375E+08	4.038E+09	3.728E+02	4.916E + 02	1.409E + 02
-	0.000	lower	6.043E + 09	1.265E + 09	4.375E+08	4.038E+09	3.728E + 02	4.916E + 02	1.409E + 02
c	000	upper	5.521E + 09	1.199E+09	4.321E+08	3.752E + 09	3.486E + 02	4.477E+02	1.353E + 02
7	0.002	lower	5.521E + 09	1.199E+09	4.321E + 08	3.752E+09	3.486E + 02	4.477E+02	1.353E + 02
c	300	upper	4.749E+09	1.124E+09	3.981E + 08	3.590E + 09	3.150E + 02	3.566E + 02	1.238E+02
n	0.023	lower	4.749E+09	1.124E+09	3.981E + 08	3.590E + 09	3.150E + 02	3.566E + 02	1.238E + 02
_	870	upper	4.278E+09	1.081E + 09	3.588E + 08	3.605E + 09	2.896E+02	2.880E+02	1.138E + 02
†	0.040	lower	4.278E+09	1.081E + 09	3.588E+08	3.605E + 09	2.896E + 02	2.880E+02	1.138E+02
ц	0.071	upper	4.823E+09	1.212E+09	3.243E + 08	4.521E + 09	3.120E + 02	2.817E + 02	1.129E + 02
n	0.07 I	lower	4.823E+09	1.212E+09	3.243E + 08	4.521E + 09	3.120E + 02		1.129E + 02
ď	800 0	upper	4.752E+09	1.288E + 09	2.813E + 08	5.154E + 09	3.201E + 02	2.520E + 02	1.090E + 02
o	0.0	lower	4.752E+09	1.288E+09	2.813E + 08	5.154E + 09	3.201E + 02	2.520E + 02	1.090E+02
7	0 133	upper	4.918E + 09	1.506E + 09	2.427E+08	6.530E + 09	3.689E + 02	2.453E + 02	1.126E + 02
-	0.10	lower	4.918E + 09	1.506E + 09	2.427E+08	6.530E + 09	3.689E + 02	2.453E + 02	1.126E + 02
0	151	upper	5.091E + 09	1.685E + 09	2.332E+08	7.562E+09	4.125E + 02	2.503E + 02	1.184E + 02
0	101.0	lower	5.091E + 09	1.685E + 09	2.332E+08	7.562E+09	4.125E + 02	2.503E + 02	1.184E+02
c	0 160	upper	4.804E+09	1.757E+09	2.197E + 08	8.030E+09	4.304E+02	2.345E + 02	1.195E + 02
n	0.10	lower	4.804E + 09	1.757E+09	2.197E + 08	8.030E+09	4.304E+02	2.345E + 02	1.195E + 02
1	186	upper	4.852E + 09	1.942E + 09	2.183E + 08	9.218E+09	4.741E+02	2.300E + 02	1.253E + 02
2	201.0	lower	4.852E + 09	1.942E + 09	2.183E + 08	9.218E+09	4.741E+02	2.300E + 02	1.253E + 02
-1	0.215	upper	4.108E + 09	1.913E + 09	1.907E + 08	9.026E+09	4.686E+02	1.980E + 02	1.219E + 02
1	0.213	lower	4.108E + 09	1.913E + 09	1.907E+08	9.026E+09	4.686E + 02	1.980E + 02	1.219E + 02
12	0.245	upper	3.567E + 09	1.893E + 09	1.752E+08	8.994E+09	4.636E + 02	1.715E + 02	1.187E + 02
71	54.0	lower	3.567E + 09	1.893E + 09	1.752E + 08	8.994E+09	4.636E + 02	1.715E + 02	1.187E + 02
73	0.274	upper	2.876E + 09	1.777E+09	1.568E + 08	8.458E + 09	4.353E+02	1.382E+02	1.111E + 02
2	1	lower	2.876E + 09	1.777E+09	1.568E + 08	8.458E+09	4.353E+02	1.382E + 02	1.111E + 02
14	0.363	upper	1.820E + 09	1.621E + 09	1.204E + 08	7.689E+09	3.981E + 02	8.720E + 01	9.916E + 01
+	0000	lower	1.820E + 09	1.621E + 09	1.204E + 08	7.689E+09	3.981E + 02	8.720E+01	9.916E + 01
15	0.452	1	8.629E + 09	2.975E+09	2.462E + 08	1.450E + 10	7.286E+02	4.109E+02	1.761E+02
16	0.540	1	5.144E + 09	2.695E + 09	1.898E + 08	1.326E + 10	6.601E + 02	2.441E+02	1.559E + 02
17	0.629	1	3.004E + 09	2.247E+09	1.468E + 08	1.105E + 10	5.503E + 02	1.426E + 02	1.300E+02
18	0.700	ı	1.702E + 09	1.807E+09	1.105E + 08	8.857E+09	4.426E+02	8.088E+01	1.055E + 02
19	0.717	1	1.461E + 09	1.703E + 09	1.020E + 08	8.341E + 09	4.172E + 02	6.944E + 01	9.970E+01
20	0.770	1	9.257E + 08	1.287E+09	8.210E+07	6.182E + 09	3.151E + 02	4.432E+01	7.872E+01
21	0.805	1		9.730E+08	6.861E + 07	4.539E+09	2.383E + 02	3.069E + 01	6.347E+01
22	0.894	ı	2.640E + 08	5.538E+08	4.080E+07	2.376E+09	1.356E + 02	1.323E + 01	4.212E+01
23	0.947	1	1.242E + 08	3.535E+08	2.352E+07	1.354E + 09	8.658E + 01	6.569E + 00	3.160E + 01
24	1.000		4.343E+07	2.283E+08	9.361E+06	8.026E+08	5.591E+01	2.405E+00	2.247E+01

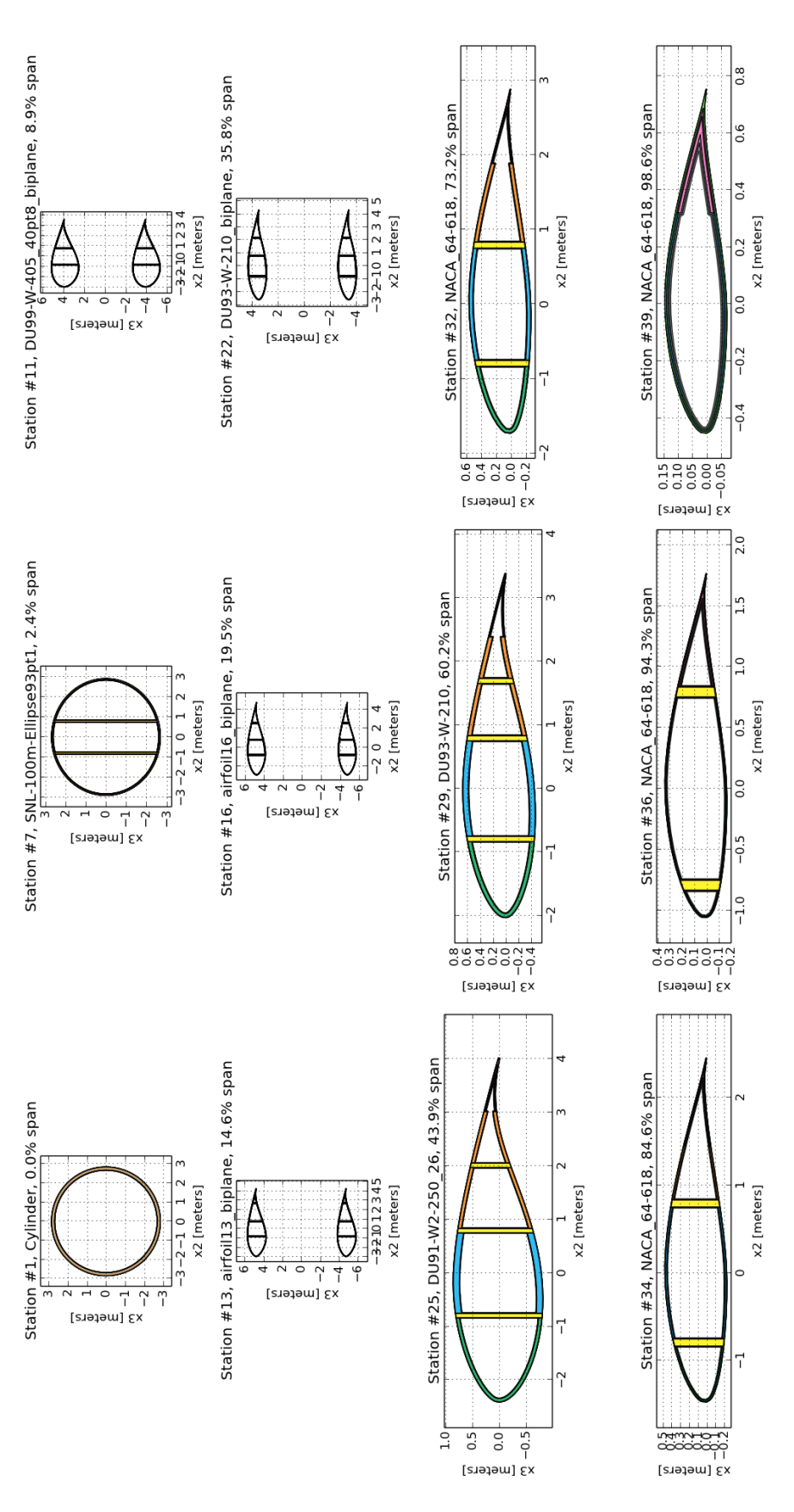
[64]. For spar stations 1-14, properties of the upper and lower biplane elements are reported separately, with respect to the **Table C.4:** Spanwise properties for a biplane spar with "full-height" cross-sections, joint length-to-span ratio $r_j/R=0.452$, and gap-to-chord ratio g/c=1.25. These properties were calculated for each of the cross-sections in the spar, using VABS 1D reference lines in Figure 4.12. For spar station 14, a curvature correction (curvature about the x_2 -axis, $k_2 = 0.0020$ rad/m) was applied to both the upper and lower biplane elements.

	:	upper or		stiffness _l	stiffness properties			mass properties	es
spar	spar	lower	flapwise	edgewise	torsional	axial	3300	flapwise mass	edgewise mass
station		biplane	stiffness	stiffness	stiffness	stiffness	(kg/m)	moment of	moment of
	(-)	element	(N^*m^2)	(N^*m^2)	(N^*m^2)	(N)	(KB/III)	inertia (kg*m)	inertia (kg*m)
-	0000	upper	2.399E + 10	1.180E + 09	4.330E+08	4.037E+09	3.728E+02	1.951E + 03	1.315E + 02
-	0.000	lower	2.399E + 10	1.180E + 09	4.330E+08	4.037E+09	3.728E + 02	1.951E + 03	1.315E + 02
c	000	upper	2.190E + 10	1.118E + 09	4.311E + 08	3.745E + 09	3.481E + 02	1.776E + 03	1.263E + 02
7	0.002	lower	2.190E + 10	1.118E + 09	4.311E + 08	3.745E+09	3.481E + 02	1.776E+03	1.263E + 02
c	300	upper	1.894E + 10	1.059E + 09	4.063E+08	3.588E+09	3.151E + 02	1.422E+03	1.163E + 02
n	0.023	lower	1.894E + 10	1.059E + 09	4.063E + 08	3.588E + 09	3.151E + 02	1.422E+03	1.163E + 02
_	870	upper	1.724E + 10	1.034E+09	3.791E + 08	3.620E + 09	2.904E + 02	1.157E + 03	1.078E+02
4	0.040	lower	1.724E + 10	1.034E+09	3.791E + 08	3.620E+09	2.904E + 02	1.157E + 03	1.078E+02
ц	0.071	upper	1.942E + 10	1.171E + 09	3.502E+08	4.513E + 09	3.113E + 02	1.131E + 03	1.076E+02
n	0.07 I	lower	1.942E + 10	1.171E + 09	3.502E+08	4.513E + 09	3.113E + 02	1.131E + 03	1.076E+02
ď	800 0	upper	1.928E + 10	1.259E+09	3.179E + 08	5.151E + 09	3.202E + 02	1.022E + 03	1.049E + 02
o	0.0	lower	1.928E + 10	1.259E + 09	3.179E + 08	5.151E + 09	3.202E + 02	1.022E + 03	1.049E + 02
7	0 133	upper	2.017E + 10	1.484E + 09	2.832E+08	6.531E + 09	3.689E + 02	1.004E + 03	1.092E + 02
-	0.10	lower	2.017E + 10	1.484E + 09	2.832E+08	6.531E + 09	3.689E + 02	1.004E + 03	1.092E + 02
o	151	upper	2.101E+10	1.664E + 09	2.693E + 08	7.562E+09	4.125E + 02	1.031E + 03	1.152E + 02
0	101.0	lower	2.101E+10	1.664E + 09	2.693E + 08	7.562E+09	4.125E + 02	1.031E + 03	1.152E + 02
c	0 160	upper	1.992E + 10	1.738E+09	2.542E + 08	8.030E+09	4.304E+02	9.703E+02	1.164E + 02
n	0.10	lower	1.992E + 10	1.738E + 09	2.542E + 08	8.030E+09	4.304E+02	9.703E + 02	1.164E + 02
7	186	upper	1.988E + 10	1.917E + 09	2.399E+08	9.062E+09	4.741E+02	9.593E + 02	1.225E + 02
2	201.0	lower	1.988E + 10	1.917E + 09	2.399E + 08	9.062E+09	4.741E+02	9.593E + 02	1.225E+02
-1	0.215	upper	1.723E + 10	1.896E + 09	2.228E+08	9.026E+09	4.686E+02	8.288E+02	1.192E + 02
1	0.213	lower	1.723E + 10	1.896E + 09	2.228E+08	9.026E+09	4.686E + 02	8.288E+02	1.192E + 02
12	0.245	upper	1.501E + 10	1.877E+09	2.074E+08	8.994E+09	4.636E + 02	7.200E+02	1.163E + 02
71	54.0	lower	1.501E + 10	1.877E + 09	2.074E+08	8.994E+09	4.636E + 02	7.200E+02	1.163E + 02
73	0.274	upper	1.211E + 10	1.762E + 09	1.903E+08	8.458E + 09	4.353E+02	5.808E+02	1.088E+02
2	1	lower	1.211E + 10	1.762E + 09	1.903E + 08	8.458E+09	4.353E+02	5.808E+02	1.088E+02
14	0.363	upper	7.710E+09	1.602E + 09	1.548E + 08	7.422E+09	3.981E + 02	3.688E + 02	9.726E + 01
•	0	lower	7.710E+09	1.602E + 09	1.548E + 08	7.422E+09	3.981E + 02	3.688E + 02	9.726E + 01
15	0.452	1	8.629E + 09	2.975E + 09	2.462E + 08	1.450E + 10	7.286E+02	4.109E+02	1.761E + 02
16	0.540	1	5.144E + 09		1.898E + 08	1.326E + 10	6.601E + 02	2.441E+02	1.559E + 02
17	0.629	1	3.004E + 09	2.247E+09	1.468E + 08	1.105E + 10	5.503E + 02	1.426E + 02	1.300E+02
18	0.700	ı	1.702E + 09	1.807E+09	1.105E + 08	8.857E+09	4.426E+02	8.088E+01	1.055E + 02
19	0.717	1	1.461E + 09	1.703E + 09	1.020E + 08	8.341E + 09	4.172E + 02	6.944E + 01	9.970E+01
20	0.770	1	9.257E + 08	1.287E+09	8.210E + 07	6.182E + 09	3.151E + 02	4.432E+01	7.872E+01
21	0.805	1	6.339E + 08		6.861E + 07	4.539E+09	2.383E + 02	3.069E + 01	6.347E + 01
22	0.894	ı	2.640E + 08	5.538E + 08	4.080E+07	2.376E+09	1.356E + 02	1.323E + 01	4.212E+01
23	0.947	1	1.242E + 08	3.535E + 08	2.352E+07	1.354E + 09	8.658E + 01	6.569E + 00	3.160E + 01
24	1.000		4.343E+07	2.283E+08	9.361E+06	8.026E+08	5.591E+01	2.405E+00	2.247E+01

APPENDIX D

Blade definition for 100-meter biplane blade

These figures and tables define the geometry of the full 100-meter biplane blade studied in Chapter 5. The external (aerodynamic) geometry is described by the airfoil, chord, and twist schedules presented in Table D.1. The laminate schedule for the internal structure is given in Table D.2. Lumped structural properties for blade cross-sections (calculated by VABS) are given in Table D.3. Only selected values from VABS are shown here; a key is provided in Table C.1.



modules Shapely [102] and Matplotlib [111]. Colors denote different structural parts: spar caps (blue), shear webs Figure D.1: Selected cross-sections of the biplane blade (flapwise symmetric, no stagger configuration), plotted with the Python internal surfaces (grey), and external surfaces (light green). Note: each station is plotted with a different scale, but all (yellow), leading edge panel (dark green), aft panels (orange), trailing edge reinforcement (pink), root buildup (brown), plots have a 1:1 aspect ratio.

Table D.1: Geometry of a full 100-meter biplane blade, which is symmetric in the flapwise direction and uses biplane airfoils with zero stagger. The root joint is located at blade station 9 (4.7% span), and the mid-blade joint is located at blade station 25 (43.9% span).

blade	upper or lower		axis coord		twist	chord	beam axis-to-	thickness- to-chord	airfoil	gap-to- chord
station	biplane element	x_1 (m)	x_2 (m)	x_3 (m)	(deg)	(m)	chord ratio	ratio	anton	ratio
1	-	0.000	0.000	0.000	13.308	5.694	0.500	1.000	Cylinder	-
2	-	0.500	0.000	0.000	13.308	5.694	0.500	1.000	Cylinder	-
3	-	0.700	0.000	0.000	13.308	5.694	0.500	0.993	SNL-100m-0pt007	-
1	-	0.900	0.000	0.000	13.308	5.694	0.500	0.985	SNL-100m-0pt009	-
5	-	1.100	0.000	0.000	13.308	5.694	0.500	0.978	SNL-100m-0pt011	-
5	-	1.300	0.000	0.000	13.308	5.694	0.500	0.970	SNL-100m-Ellipse97	-
7	-	2.400	0.000	0.000	13.308	5.792	0.499	0.931	SNL-100m-Ellipse93pt1	-
3	-	2.600	0.000	0.000	13.308	5.811	0.498	0.925	SNL-100m-Ellipse92pt5	-
)	-	4.700	0.000	0.000	13.308	6.058	0.483	0.840	SNL-100m-Transition84	-
	upper	6.800	-0.508	2.147	13.308	6.304	0.468	0.532	SNL-100m-Transition53pt2	0.700
10	lower	6.800	0.508	-2.147	13.308	6.304	0.468	0.532	SNL-100m-Transition53pt2	0.700
	upper	8.900	-0.905	3.825	13.308	6.551	0.453	0.408	DU99-W-405_40pt8	1 000
11	lower	8.900	0.905	-3.825	13.308	6.551	0.453	0.408	DU99-W-405_40pt8	1.200
	upper	11.400	-1.097	4.639	13.308	6.835	0.435	0.300	DU97-W-300	
12	lower	11.400	1.097	-4.639	13.308	6.835	0.435	0.300	DU97-W-300	1.395
	upper	14.600	-1.098	4.641	13.308	7.215	0.410	0.255	UCLA-100m-Transition-255	
13	lower	14.600	1.098	-4.641	13.308	7.215	0.410	0.255	UCLA-100m-Transition-255	1.322
	upper	16.300	-1.087	4.643	13.177	7.404	0.400	0.235	UCLA-100m-Transition-235	
.4	lower	16.300	1.087	-4.643	13.177	7.404	0.400	0.235	UCLA-100m-Transition-235	1.288
	upper	17.900	-1.077	4.646	13.046	7.552	0.390	0.218	UCLA-100m-Transition-218	
L 5	lower	17.900	1.077	-4.646	13.046	7.552	0.390	0.218	UCLA-100m-Transition-218	1.263
		19.500	-1.066	4.647	12.915	7.628	0.380	0.218	UCLA-100m-Transition-203	
.6	upper		1.066		12.915	7.628	0.380	0.203	UCLA-100m-Transition-203	1.250
	lower	19.500		-4.647 4.661		7.585			UCLA-100m-Transition-203	
.7	upper	22.200	-1.002	4.661	12.133		0.378	0.190		1.257
	lower	22.200	1.002	-4.661	12.133	7.585	0.378	0.190	UCLA-100m-Transition-190	
18	upper	24.900	-0.939	4.677	11.350	7.488	0.377	0.180	UCLA-100m-Transition-180	1.274
	lower	24.900	0.939	-4.677	11.350	7.488	0.377	0.180	UCLA-100m-Transition-180	
19	upper	27.600	-0.874	4.687	10.568	7.347	0.375	0.204	DU93-W-210_20pt4	1.298
	lower	27.600	0.874	-4.687	10.568	7.347	0.375	0.204	DU93-W-210_20pt4	
20	upper	30.333	-0.758	4.257	10.101	7.206	0.375	0.206	DU93-W-210_20pt6	1.200
	lower	30.333	0.758	-4.257	10.101	7.206	0.375	0.206	DU93-W-210_20pt6	
21	upper	33.067	-0.650	3.830	9.633	7.064	0.375	0.208	DU93-W-210_20pt8	1.100
	lower	33.067	0.650	-3.830	9.633	7.064	0.375	0.208	DU93-W-210_20pt8	1.100
22	upper	35.800	-0.551	3.417	9.166	6.923	0.375	0.210	DU93-W-210	1.000
	lower	35.800	0.551	-3.417	9.166	6.923	0.375	0.210	DU93-W-210	1.000
23	upper	38.500	-0.433	2.839	8.673	6.758	0.375	0.226	DU93-W-210_22pt6	0.850
-5	lower	38.500	0.433	-2.839	8.673	6.758	0.375	0.226	DU93-W-210_22pt6	0.050
24	upper	41.200	-0.281	1.958	8.181	6.594	0.375	0.243	DU91-W2-250_24pt3	0.600
	lower	41.200	0.281	-1.958	8.181	6.594	0.375	0.243	DU91-W2-250_24pt3	0.000
25	-	43.900	0.000	0.000	7.688	6.429	0.375	0.260	DU91-W2-250_26	-
26	-	46.600	0.000	0.000	7.185	6.258	0.375	0.251	UCLA-100m-Transition-251	-
27	-	49.300	0.000	0.000	6.683	6.086	0.375	0.241	UCLA-100m-Transition-241	-
28	-	52.000	0.000	0.000	6.180	5.915	0.375	0.230	DU93-W-210_23	-
29	-	60.200	0.000	0.000	4.743	5.417	0.375	0.210	DU93-W-210	-
30	_	66.700	0.000	0.000	3.633	5.019	0.375	0.190	NACA 64-618 ₋ 19	-
31	-	68.300	0.000	0.000	3.383	4.920	0.375	0.185	NACA 64-618 ₋ 18pt5	-
2	_	73.200	0.000	0.000	2.735	4.621	0.375	0.180	NACA 64-618	-
3	_	76.400	0.000	0.000	2.348	4.422	0.375	0.180	NACA 64-618	-
34	_	84.600	0.000	0.000	1.380	3.925	0.375	0.180	NACA 64-618	_
35	_	89.400	0.000	0.000	0.799	3.619	0.375	0.180	NACA 64-618	_
36	-	94.300	0.000	0.000	0.280	2.824	0.375	0.180	NACA 64-618	_
37	_	95.700	0.000	0.000	0.210	2.375	0.375	0.180	NACA 64-618	_
38	_	97.200	0.000	0.000	0.210	1.836	0.375	0.180	NACA 64-618	_
39	-	98.600	0.000	0.000	0.140	1.208	0.375	0.180	NACA 64-618	_
	_	90.000	0.000	0.000	0.070	1.200	0.313	0.100	INUCU 04-010	-

Table D.2: Laminate schedule for a full 100-meter biplane blade.

blade station	x_1 (m)	upper or lower biplane	root buildup,	spar cap, uniax	TE rein- forcement,	TE rein- forcement,	LE panel, foam (m)	aft panel, foam	internal surface,	external surface,
Station	()	element	triax (m)	(m)	uniax (m)	foam (m)	rouni (m)	(m)	triax (m)	triax (m)
1	0.00	-	0.16000						0.00500	0.00500
2	0.50	-	0.14000	0.01300	0.00100				0.00500	0.00500
3	0.70	-	0.12000	0.01300	0.00200				0.00500	0.00500
4	0.90	-	0.10000	0.01300	0.00300				0.00500	0.00500
5	1.10	-	0.08000	0.01300	0.00500				0.00500	0.00500
5	1.30	-	0.07000	0.01300	0.00700		0.00100	0.00100	0.00500	0.00500
7	2.40	-	0.06300	0.01300	0.00800		0.00350	0.00350	0.00500	0.00500
3	2.60	_	0.05500	0.01300	0.00900		0.01300	0.01300	0.00500	0.00500
9	4.70	_	0.04000	0.02000	0.01300		0.03000	0.10000	0.00500	0.00500
	6.80	upper	0.01100	0.02000	0.00900		0.02500	0.05000	0.00300	0.00250
10		lower	0.01100	0.02000	0.00900		0.02500	0.05000	0.00300	0.00250
	8.90	upper	0.00900	0.03500	0.01250	0.03000	0.03000	0.05000	0.00300	0.00250
11	0.50	lower	0.00900	0.03500	0.01250	0.03000	0.03000	0.05000	0.00300	0.00250
	11.40	upper	0.00500	0.04200	0.01650	0.03000	0.03000	0.05000	0.00300	0.00250
12	11.10	lower	0.00500	0.04200	0.01650	0.03000	0.03000	0.05000	0.00300	0.00250
	14.60	upper	0.00300	0.04200	0.02000	0.03000	0.03000	0.05000	0.00300	0.00250
13	14.00	lower		0.06300	0.02000	0.03000	0.03000	0.05000	0.00300	0.00250
	16.30	upper		0.06400	0.02500	0.03000	0.03000	0.03000	0.00300	0.00250
14	10.50				0.02500	0.03000	0.03000	0.03000	0.00300	0.00250
	17.00	lower		0.06400						
15	17.90	upper		0.05950	0.03000	0.03000	0.03000	0.03000	0.00300	0.00250
	10.50	lower		0.05950	0.03000	0.03000	0.03000	0.03000	0.00300	0.00250
16	19.50	upper		0.05700	0.03000	0.03000	0.03000	0.03000	0.00300	0.00250
		lower		0.05700	0.03000	0.03000	0.03000	0.03000	0.00300	0.00250
17	22.20	upper		0.05600	0.03000	0.03000	0.03000	0.03000	0.00300	0.00250
		lower		0.05600	0.03000	0.03000	0.03000	0.03000	0.00300	0.00250
18	24.90	upper		0.05500	0.03000	0.03000	0.03000	0.03000	0.00300	0.00250
10		lower		0.05500	0.03000	0.03000	0.03000	0.03000	0.00300	0.00250
19	27.60	upper		0.05300	0.01500	0.02000	0.03000	0.03000	0.00300	0.00250
19		lower		0.05300	0.01500	0.02000	0.03000	0.03000	0.00300	0.00250
20	30.33	upper		0.04970	0.01500	0.01650	0.03000	0.03000	0.00300	0.00250
20		lower		0.04970	0.01500	0.01650	0.03000	0.03000	0.00300	0.00250
21	33.07	upper		0.04630	0.01500	0.01350	0.03000	0.03000	0.00300	0.00250
Z I		lower		0.04630	0.01500	0.01350	0.03000	0.03000	0.00300	0.00250
00	35.80	upper		0.04300	0.01500	0.01000	0.03000	0.03000	0.00300	0.00250
22		lower		0.04300	0.01500	0.01000	0.03000	0.03000	0.00300	0.00250
22	38.50	upper		0.03900	0.01250	0.00850	0.03000	0.03000	0.00300	0.00250
23		lower		0.03900	0.01250	0.00850	0.03000	0.03000	0.00300	0.00250
	41.20	upper		0.03600	0.01000	0.00650	0.03000	0.03000	0.00300	0.00250
24	=	lower		0.03600	0.01000	0.00650	0.03000	0.03000	0.00300	0.00250
25	43.90	-		0.11100	0.01500	0.01000	0.06000	0.06000	0.00500	0.00500
26	46.60	_		0.10800	0.01300	0.01000	0.06000	0.06000	0.00500	0.00500
27	49.30	_		0.10500	0.01000	0.01000	0.06000	0.06000	0.00500	0.00500
28	52.00	_		0.10200	0.00800	0.01000	0.06000	0.06000	0.00500	0.00500
29	60.20	_		0.10200	0.00400	0.01000	0.06000	0.06000	0.00500	0.00500
30	66.70	-		0.06800	0.00400	0.01000	0.06000	0.06000	0.00500	0.00500
31	68.30	-		0.06400	0.00400	0.01000	0.05500	0.05500	0.00500	0.00500
32	73.20			0.04700	0.00400	0.01000	0.05500	0.03500	0.00500	0.00500
	73.20 76.40	-			0.00400			0.04500		0.00500
33		-		0.03400		0.01000	0.03000		0.00500	
34	84.60	-		0.01700	0.00400	0.01000	0.01500	0.01500	0.00500	0.00500
35	89.40	-		0.00900	0.00400	0.01000	0.01000	0.01000	0.00500	0.00500
36	94.30	-		0.00500	0.00400	0.01000	0.00500		0.00500	0.00500
37	95.70	-		0.00500	0.00400	0.01000	0.00500		0.00500	0.00500
38	97.20	-		0.00500	0.00400	0.01000	0.00500		0.00500	0.00500
39	98.60	-		0.00500	0.00400	0.01000	0.00500		0.00500	0.00500
40	100.00	-							0.00125	0.00500

Table D.3: Spanwise properties for a full biplane blade.

		upper or			properties			mass propertie	
blade	x_1	lower	flapwise	edgewise	torsional	axial	mass	flapwise mass	edgewise mass
station	(m)	biplane	stiffness	stiffness	stiffness	stiffness	(kg/m)	moment of	moment of
		element	(N*m ²)	(N*m ²)	(N*m ²)	(N)		inertia (kg*m)	inertia (kg*m)
1	0.00	-	3.125E+11	3.125E+11	1.627E+11	8.201E+10	5.561E+03	2.117E+04	2.117E+04
2	0.50	-	2.907E+11	2.802E+11	1.460E+11	7.450E+10	5.021E+03	1.947E+04	1.899E+04
3	0.70	-	2.524E+11	2.455E+11	1.267E+11	6.503E+10	4.384E+03	1.691E+04	1.666E+04
4	0.90	-	2.145E+11	2.105E+11	1.075E+11	5.556E+10	3.748E+03	1.437E+04	1.430E+04
5	1.10	-	1.775E+11	1.763E+11	8.836E+10	4.630E+10	3.122E+03	1.189E+04	1.197E+04
6	1.30	-	1.580E+11	1.598E+11	7.845E+10	4.178E+10	2.814E+03	1.058E+04	1.082E+04
7	2.40	-	1.487E+11	1.542E+11	7.228E+10	4.265E+10	3.156E+03	1.056E+04	1.062E+04
8	2.60	-	1.351E+11	1.414E+11	6.507E+10	3.907E+10	2.930E+03	9.704E+03	9.811E+03
9	4.70	-	1.079E+11	1.265E+11	5.119E+10	3.335E+10	2.573E+03	7.942E+03	8.908E+03
10	6.80	upper	1.978E + 10	4.185E+10	9.565E+09	1.289E+10	1.093E+03	1.510E + 03	3.211E+03
	0.00	lower	1.978E + 10	4.185E+10	9.565E+09	1.289E+10	1.093E+03	1.510E + 03	3.211E+03
11	8.90	upper	1.110E + 10	3.614E+10	4.432E+09	1.317E + 10	1.025E+03	7.645E + 02	2.837E+03
	0.50	lower	1.110E + 10	3.614E+10	4.432E+09	1.317E + 10	1.025E+03	7.645E + 02	2.837E+03
12	11.40	upper	6.315E+09	3.452E+10	2.190E+09	1.223E+10	9.095E+02	4.123E+02	2.612E+03
	11.70	lower	6.315E+09	3.452E+10	2.190E+09	1.223E+10	9.095E+02	4.123E+02	2.612E+03
13	14.60	upper	7.725E+09	3.788E+10	1.671E+09	1.343E+10	9.529E+02	4.626E+02	2.864E+03
10	11.00	lower	7.725E+09	3.788E+10	1.671E + 09	1.343E+10	9.529E+02	4.626E+02	2.864E+03
14	16.30	upper	7.874E + 09	4.651E+10	1.708E+09	1.396E+10	9.676E + 02	4.670E + 02	3.267E+03
17	10.50	lower	7.874E+09	4.651E+10	1.708E+09	1.396E+10	9.676E+02	4.670E+02	3.267E+03
15	17.90	upper	7.405E+09	5.515E+10	1.691E + 09	1.375E + 10	9.636E+02	4.448E+02	3.733E+03
10	11.50	lower	7.405E+09	5.515E+10	1.691E + 09	1.375E+10	9.636E+02	4.448E+02	3.733E+03
16	19.50	upper	6.936E+09	5.828E+10	1.635E+09	1.344E+10	9.509E+02	4.193E+02	3.931E+03
10	13.50	lower	6.936E+09	5.828E+10	1.635E+09	1.344E+10	9.509E+02	4.193E+02	3.931E+03
17	22.20	upper	6.020E + 09	5.771E+10	1.458E + 09	1.321E+10	9.306E+02	3.638E+02	3.871E+03
	0	lower	6.020E+09	5.771E+10	1.458E + 09	1.321E + 10	9.306E+02	3.638E+02	3.871E+03
18	24.90	upper	5.137E+09	5.592E+10	1.271E+09	1.295E+10	9.056E+02	3.101E + 02	3.727E+03
10	24.50	lower	5.137E+09	5.592E+10	1.271E+09	1.295E+10	9.056E+02	3.101E+02	3.727E+03
19	27.60	upper	4.257E+09	3.714E+10	1.079E+09	1.152E+10	8.283E+02	2.577E + 02	2.846E+03
-5	21.00	lower	4.257E+09	3.714E+10	1.079E+09	1.152E+10	8.283E+02	2.577E + 02	2.846E+03
20	30.33	upper	3.962E+09	3.548E+10	1.032E+09	1.105E+10	8.015E+02	2.417E+02	2.702E+03
20	50.55	lower	3.962E+09	3.548E+10	1.032E+09	1.105E+10	8.015E+02	2.417E+02	2.702E+03
21	33.07	upper	3.665E+09	3.383E+10	9.836E+08	1.057E + 10	7.739E+02	2.257E+02	2.561E+03
	00.01	lower	3.665E+09	3.383E+10	9.836E+08	1.057E + 10	7.739E+02	2.257E+02	2.561E+03
22	35.80	upper	3.380E + 09	3.224E+10	9.351E+08	1.011E+10	7.467E+02	2.102E+02	2.424E+03
	00.00	lower	3.380E+09	3.224E+10	9.351E+08	1.011E + 10	7.467E+02	2.102E+02	2.424E+03
23	38.50	upper	3.475E+09	2.796E+10	9.863E+08	9.423E+09	7.179E+02	2.203E+02	2.188E+03
	00.00	lower	3.475E+09	2.796E+10	9.863E+08	9.423E+09	7.179E+02	2.203E+02	2.188E+03
24	41.20	upper	3.376E+09	2.342E+10	9.827E+08	8.811E+09	6.874E+02	2.147E+02	1.905E+03
		lower	3.376E+09	2.342E+10	9.827E+08	8.811E+09	6.874E+02	2.147E + 02	1.905E+03
25	43.90	-	9.082E+09	3.497E+10	1.792E+09	2.061E+10	1.310E + 03	4.968E+02	2.655E+03
26	46.60	-	7.800E+09	3.107E+10	1.575E+09	1.987E+10	1.259E+03	4.260E+02	2.397E+03
27	49.30	-	6.672E+09	2.650E+10	1.374E+09	1.905E+10	1.206E+03	3.641E+02	2.114E+03
28	52.00	-	5.699E+09	2.301E+10	1.193E+09	1.829E+10	1.155E+03	3.110E+02	1.879E+03
29	60.20	-	3.304E+09	1.512E+10	7.666E+08	1.524E+10	9.701E+02	1.806E+02	1.302E+03
30	66.70	-	2.101E+09	1.132E+10	5.068E + 08	1.248E+10	7.948E+02	1.167E + 02	9.421E+02
31	68.30	-	1.810E+09	1.063E+10	4.513E+08	1.187E+10	7.548E+02	1.006E+02	8.730E+02
32	73.20	-	1.182E+09	8.673E+09	3.383E+08	9.479E+09	6.187E+02	6.725E+01	6.975E+02
33	76.40	-	8.561E+08	7.462E+09	2.809E+08	7.693E+09	5.167E+02	5.023E+01	5.869E+02
34	84.60	-	4.157E+08	5.121E+09	1.772E+08	5.173E+09	3.702E+02	2.626E+01	3.950E+02
35	89.40	-	2.448E+08	3.942E+09	1.274E+08	3.929E+09	2.983E+02	1.672E+01	3.045E+02
36	94.30	-	9.691E + 07	1.884E+09	5.751E+07	2.761E + 09	2.099E+02	6.787E+00	1.442E+02
37	95.70	-	5.649E+07	1.031E+09	3.045E+07	2.175E+09	1.535E+02	3.845E+00	7.385E+01
38	97.20	-	2.541E+07	4.529E+08	1.363E+07	1.658E + 09	1.168E + 02	1.722E+00	3.232E+01
39	98.60	-	6.808E+06	1.174E + 08	3.616E+06	1.061E + 09	7.433E+01	4.571E-01	8.271E+00
40	100.00	-	6.513E+02	1.224E+04	5.208E+02	2.528E+07	1.885E+00	4.956E-05	9.354E-04

REFERENCES

- [1] U.S. Energy Information Administration, "Electricity Net Generation: Total (All Sectors)." http://www.eia.gov/totalenergy/data/monthly/pdf/sec7_5.pdf, 2014. Accessed: 2014-05-12.
- [2] N. Horner, I. Azevedo, and D. Hounshell, "Effects of government incentives on wind innovation in the United States," *Environmental Research Letters*, vol. 8, p. 044032, Dec. 2013.
- [3] U.S. Department of Energy, "20% Wind Energy by 2030: Increasing Wind Energy's Contribution to U.S. Electricity Supply," tech. rep., U.S. Department of Energy, Energy Efficiency and Renewable Energy, Oak Ridge, TN, 2008.
- [4] Executive Office of the President, "The President's Climate Action Plan." http://www.whitehouse.gov/sites/default/files/image/president27sclimateactionplan.pdf, 2013. Accessed: 2014-05-30.
- [5] California Public Utilities Commission, "California Renewables Portfolio Standard (RPS)." http://www.cpuc.ca.gov/PUC/energy/Renewables/index.htm, 2014. Accessed: 2014-05-29.
- [6] R. Wiser and M. Bolinger, "2012 Wind Technologies Market Report," tech. rep., U.S. Department of Energy, Berkeley, CA, 2013.
- [7] J. Wilkes, J. Moccia, and M. Dragan, "Wind in power: 2011 European statistics." http://www.ewea.org/fileadmin/files/library/publications/statistics/Wind_in_power_2011_European_statistics.pdf, 2012. Accessed: 2014-05-30.
- [8] SSP Technology A/S, "83.5 m. blade (7MW)." http://www.ssptech.com/solutions/83-5-m--blade-(7mw).aspx, 2013. Accessed: 2014-05-28.
- [9] D. T. Griffith and T. D. Ashwill, "The Sandia 100-meter All-glass Baseline Wind Turbine Blade: SNL100-00," tech. rep., Sandia National Laboratories, Albuquerque, NM, 2011.
- [10] UpWind, "Design limits and solutions for very large wind turbines A 20 MW turbine is feasible," tech. rep., EWEA, 2011.
- [11] B. C. Larsen, "Østerild National Test Centre for Large Wind Turbines." http://www.vindenergi.dtu.dk/English/About/Oesterild.aspx, 2014. Accessed: 2014-05-15.
- [12] Renewable Energy World Editors, "Meet The New World's Biggest Wind Turbine." http://www.renewableenergyworld.com/rea/news/article/2014/02/meet-the-new-worlds-biggest-wind-turbine, 2014. Accessed: 2014-05-15.

- [13] Wind-turbine-models.com, "Samsung S7.0-171 7.000,0 kW Turbine." http://en.wind-turbine-models.com/turbines/285-samsung-s7.0-171, 2012. Accessed: 2014-05-15.
- [14] 4C Offshore, "Offshore Wind Turbine: S7.0-171, Samsung Heavy Industries." http://www.4coffshore.com/windfarms/turbine-samsung-heavy-industries-shi-7-mw-tid37.html, 2014. Accessed: 2014-05-15.
- [15] ENERCON GmbH, "E-126 / 7,580 kW ENERCON." http://www.enercon.de/en-en/66.htm, 2014. Accessed: 2014-05-15.
- [16] G. Hatch, "Why Are Wind Turbines Getting Bigger?." http://www.terramagnetica.com/2009/08/01/why-are-wind-turbines-getting-bigger/, 2009. Accessed: 2014-05-15.
- [17] P. Brøndsted, H. Lilholt, and A. Lystrup, "Composite Materials for Wind Power Turbine Blades," *Annual Review of Materials Research*, vol. 35, pp. 505–538, Aug. 2005.
- [18] D. A. Griffin, "Blade System Design Studies Volume I: Composite Technologies for Large Wind Turbine Blades," tech. rep., Sandia National Laboratories, Kirkland, WA, 2002.
- [19] P. S. Veers, T. D. Ashwill, H. J. Sutherland, D. L. Laird, D. W. Lobitz, D. A. Griffin, J. F. Mandell, W. D. Musial, K. J. Jackson, M. Zuteck, A. Miravete, S. W. Tsai, and J. L. Richmond, "Trends in the Design, Manufacture and Evaluation of Wind Turbine Blades," Wind Energy, vol. 6, pp. 245–259, July 2003.
- [20] P. Jamieson, *Innovation in Wind Turbine Design*. Chichester, UK: John Wiley & Sons, Ltd, Aug. 2011.
- [21] E. Lantz, M. Hand, and R. Wiser, "The Past and Future Cost of Wind Energy," in 2012 World Renewable Energy Forum, (Denver, CO), pp. 1–10, National Renewable Energy Laboratory, 2012.
- [22] Danish Energy Agency (DEA), "Wind Power in Denmark: Technologies, Policies, and Results," tech. rep., Danish Energy Agency, 1999.
- [23] J. Lemming, P. E. Morthorst, N.-E. Clausen, and P. H. Jensen, "Contribution to the Chapter on Wind Power Technology Perspectives 2008," tech. rep., Risø DTU National Laboratory for Sustainable Energy, Roskilde, Denmark, 2008.
- [24] W. A. Timmer and R. P. J. O. M. van Rooij, "Summary of the Delft University Wind Turbine Dedicated Airfoils," *Journal of Solar Energy Engineering*, vol. 125, no. 4, pp. 488–496, 2003.
- [25] E. Hau and H. von Renouard, Wind Turbines. Berlin/Heidelberg: Springer-Verlag, 2 ed., 2006.

- [26] C. P. van Dam, E. A. Mayda, D. D. Chao, and D. E. Berg, "Computational Design and Analysis of Flatback Airfoil Wind Tunnel Experiment," tech. rep., Sandia National Laboratories, Albuquerque, NM, 2008.
- [27] F. Grasso, "Development of thick airfoils for wind turbines," in 50th AIAA Aerospace Sciences Meeting, (Nashville, TN), pp. 1–12, AIAA, 2012.
- [28] K. J. Jackson, M. D. Zuteck, C. P. van Dam, K. J. Standish, and D. Berry, "Innovative Design Approaches for Large Wind Turbine Blades," Wind Energy, vol. 8, pp. 141–171, Apr. 2005.
- [29] C. E. Lynch, Advanced CFD Methods for Wind Turbine Analysis. Ph.D. Dissertation, Georgia Institute of Technology, 2011.
- [30] Siemens AG, "SWT-2.3-113." http://www.energy.siemens.com/us/pool/hq/power-generation/wind-power/SWT-2.3-113-product-brochure_EN.pdf, 2011. Accessed: 2014-05-30.
- [31] P. Roth-Johnson and R. E. Wirz, "Aero-structural investigation of biplane wind turbine blades," Wind Energy, vol. 17, no. 3, pp. 397–411, 2014. doi: 10.1002/we.1583.
- [32] S. Narsipur, Computational analysis of multielement airfoils for wind turbines. M.S. Thesis, University of Illinois at Urbana-Champaign, May 2012.
- [33] F. Zahle, M. Gaunaa, N. N. Sørensen, and C. Bak, "Multiple-Element Airfoil Optimization for a Next-Generation Light Rotor," in *The Science of Making Torque from Wind*, (Oldenburg, Germany), ForWind Center for Wind Energy Research, 2012.
- [34] R. E. Wirz, "USPTO International Application No. PCT/US11/26367: Advanced Aerodynamic and Structural Blade and Wing Design," 2011.
- [35] R. E. Wirz and P. M. Johnson, "Aero-Structural Performance of Multiplane Wind Turbine Blades," in 29th AIAA Applied Aerodynamics Conference, (Honolulu, HI), pp. 1–15, AIAA, 2011.
- [36] P. Roth-Johnson, R. E. Wirz, and E. Lin, "Structural design of 100-m biplane wind turbine blades," *Renewable Energy*, 2014. doi: 10.1016/j.renene.2014.05.030.
- [37] P. Chiu and R. E. Wirz, "Aerodynamic Performance of Biplane Airfoils for Wind Turbine Blades," in *AWEA Windpower*, (Atlanta, GA), pp. 1–22, 2012.
- [38] P. Grabau, "US 8,177,517 B2. Blade for a wind turbine rotor," 2012.
- [39] M. Brødsgaard, Biplane Wing Sections for Wind Turbines: Investigation of wind turbine rotor with biplane wing sections. M.S. Thesis, Technical University of Denmark, 2012.
- [40] M. Gaunaa, N. Sørensen, and C. Bak, "Thick airfoils & High lift," in *Research in Aeroelasticity EFP-2007-II* (T. Buhl, ed.), ch. 10, pp. 103–113, Roskilde, Denmark: Risø National Laboratory, 2009.

- [41] A. M. Ragheb and M. S. Selig, "Multi-Element Airfoil Configurations for Wind Turbines," in 29th AIAA Applied Aerodynamics Conference, (Honolulu, HI), pp. 1–13, AIAA, 2011.
- [42] M. Gaunaa, F. Zahle, N. N. Sørensen, and C. Bak, "Quantification of the Effects of Using Slats on the Inner Part of a 10MW Rotor," in *EWEA 2012*, (Copenhagen, Denmark), pp. 1–12, EWEA, 2012.
- [43] E. Hau, Wind Turbines, vol. W. Berlin, Heidelberg: Springer Berlin Heidelberg, 3 ed., 2013.
- [44] M. Hansen, Aerodynamics of wind turbines. Golden, CO: Earthscan/James & James, Feb. 2008.
- [45] P. L. Fuglsang, C. Bak, M. Gaunaa, and I. Antoniou, "Design and Verification of the Risø-B1 Airfoil Family for Wind Turbines," *Journal of Solar Energy Engineering*, vol. 126, pp. 1002–1010, Nov. 2004.
- [46] J. Tangler and D. Somers, NREL Airfoil Families for HAWTs. National Renewable Energy Laboratory, 1996.
- [47] P. L. Fuglsang and C. Bak, "Development of the Risø Wind Turbine Airfoils," Wind Energy, vol. 7, pp. 145–162, Apr. 2004.
- [48] W. Timmer and R. van Rooy, "Thick airfoils for HAWTs," Journal of Wind Engineering and Industrial Aerodynamics, vol. 39, no. 1-3, pp. 151–160, 1992.
- [49] D. Somers, "Design and Experimental Results for the S809 Airfoil," tech. rep., National Renewable Energy Laboratory, Golden, CO, Jan. 1997.
- [50] C. Bak, P. L. Fuglsang, J. Johansen, and I. Antoniou, "Wind Tunnel Tests of the NACA 63-415 and a Modified NACA 63-415 Airfoil," tech. rep., Risø National Laboratory, Roskilde, Denmark, Aug. 2008.
- [51] M. Hansen, J. Sørensen, S. Voutsinas, N. Sørensen, and H. Madsen, "State of the art in wind turbine aerodynamics and aeroelasticity," *Progress in Aerospace Sciences*, vol. 42, pp. 285–330, June 2006.
- [52] J. N. Sørensen, "Aerodynamic Aspects of Wind Energy Conversion," *Annual Review of Fluid Mechanics*, vol. 43, pp. 427–448, Jan. 2011.
- [53] V. B. Kaloyanova, Structural Modeling and Optimization of a Joined-Wing Configuration of a High-Altitude Long Endurance (HALE) Aircraft. Ph.D. Thesis, University of Cincinnati, 2009.
- [54] LM Wind Power, "Rotor Blades: Pre-bending." http://www.lmwindpower.com/Rotor-Blades/Products/Features/Standard/Prebending, 2012. Accessed: 2012-07-18.

- [55] T. D. Ashwill, G. Kanaby, K. J. Jackson, and M. Zuteck, "Development of the Swept Twist Adaptive Rotor (STAR) Blade," in 48th AIAA Aerospace Sciences Meeting, (Orlando, FL), pp. 1–13, AIAA, 2010.
- [56] P. L. Fuglsang, I. Antoniou, K. Dahl, and H. Madsen, "Wind tunnel tests of the FFA-W3-241, FFA-W3-301 and NACA 63-430 airfoils," Tech. Rep. December, Risø National Laboratory, Roskilde, Denmark, 1998.
- [57] R. V. Jenkins, A. S. Hill, and E. J. Ray, "Aerodynamic performance and pressure distributions for a NASA SC(2)-0714 airfoil tested in the Langley 0.3-meter transonic cryogenic tunnel," tech. rep., Langley Research Center, Hampton, VA, 1988.
- [58] D. C. Planchard and M. P. Planchard, Engineering Design With Solidworks 2010: A Step-by-step Project Based Approach Utilizing 3D Solid Modeling. SDC Publications, 2010.
- [59] F. Villalpando, M. Reggio, and A. Ilinca, "Assessment of Turbulence Models for Flow Simulation around a Wind Turbine Airfoil," *Modelling and Simulation in Engineering*, vol. 2011, pp. 1–8, 2011.
- [60] P. R. Spalart and S. R. Allmaras, "A one-equation turbulence model for aerodynamic flows," *La Recherche Aerospatiale*, vol. 1, no. 1, pp. 5–21, 1994.
- [61] O. A. Bauchau, C. L. Bottasso, and Y. Nikishkov, "Modeling rotorcraft dynamics with finite element multibody procedures," *Mathematical and Computer Modelling*, vol. 33, no. 10-11, pp. 1113–1137, 2001.
- [62] O. A. Bauchau, *DYMORE User's Manual*. Atlanta, Georgia: Georgia Institute of Technology, 2010.
- [63] W. Yu, D. H. Hodges, X. Hong, and V. V. Volovoi, "Validation of the Variational Asymptotic Beam Sectional Analysis," AIAA Journal, vol. 40, no. 10, pp. 2105–2112, 2002.
- [64] W. Yu, VABS Manual for Users. Logan, Utah: Utah State University, 2011.
- [65] V. Berdichevsky, "Variational-asymptotic method of constructing a theory of shells," *PMM*, vol. 43, no. 4, pp. 664–687, 1979.
- [66] C. Cesnik, V. Sutyrin, and D. H. Hodges, "A Refined Composite Beam Theory Based on the Variational-Asymptotic Method," in AIAA/ASME/ASCE/AHS/ASC Structures, Structural Dynamics, and Materials Conference, 34th and AIAA/ASME Adaptive Structures Forum, (La Jolla, CA), pp. 2710–2720, 1993.
- [67] W. Yu and D. H. Hodges, "Generalized Timoshenko Theory of the Variational Asymptotic Beam Sectional Analysis," *Journal of the American Helicopter Society*, vol. 50, no. 1, pp. 46–55, 2005.

- [68] H. Chen, W. Yu, and M. Capellaro, "A critical assessment of computer tools for calculating composite wind turbine blade properties," *Wind Energy*, vol. 13, no. 6, pp. 497–516, 2009.
- [69] W. Yu, "Efficient High-Fidelity Simulation of Multibody Systems with Composite Dimensionally Reducible Components," *Journal of the American Helicopter Society*, vol. 52, no. 1, pp. 49–57, 2007.
- [70] O. A. Bauchau and J. Ahmad, "Advanced CFD and CSD methods for multidisciplinary applications in rotorcraft problems," in 6th AIAA/NASA/USAF Multidisciplinary Analysis and Optimization Symposium, (Bellevue, WA), pp. 1441–1451, 1996.
- [71] D. H. Hodges and W. Yu, "A rigorous, engineer-friendly approach for modelling realistic, composite rotor blades," *Wind Energy*, vol. 10, no. 2, pp. 179–193, 2007.
- [72] O. A. Bauchau and J. Wang, "Stability Analysis of Complex Multibody Systems," Journal of Computational and Nonlinear Dynamics, vol. 1, no. 1, pp. 1–71, 2006.
- [73] A. D. Otero and F. L. Ponta, "Structural Analysis of Wind-Turbine Blades by a Generalized Timoshenko Beam Model," *Journal of Solar Energy Engineering*, vol. 132, pp. 1–8, Feb. 2010.
- [74] R. Sivaji, S. Marisarla, V. Narayanan, V. Kaloyanova, U. Ghia, and K. Ghia, "Aerodynamic and Structural Analyses of Joined Wings of Hale Aircraft," in New Developments in Computational Fluid Dynamics, vol. 90 of Notes on Numerical Fluid Mechanics and Multidisciplinary Design (NNFM), pp. 152–164, Berlin/Heidelberg: Springer-Verlag, 2005.
- [75] Z. Sotoudeh and D. H. Hodges, "Nonlinear Aeroelastic Analysis of Joined-Wing Aircraft with Fully Intrinsic Equations," in 50th AIAA/ASME/ASCE/AHS/ASC Structures, Structural Dynamics, and Materials Conference, (Palm Springs, CA), pp. 1–14, AIAA, 2009.
- [76] Z. Sotoudeh and D. H. Hodges, "Parametric Study of Joined-Wing Aircraft Geometry," in 51st AIAA/ASME/ASCE/AHS/ASC Structures, Structural Dynamics, and Materials Conference, (Orlando, FL), pp. 1–19, AIAA, 2010.
- [77] Z. Sotoudeh, D. H. Hodges, and C.-S. Chang, "Validation Studies for Aeroelastic Trim and Stability Analysis of Highly Flexible Aircraft," *Journal of Aircraft*, vol. 47, pp. 1240–1247, July 2010.
- [78] COMSOL Multiphysics, Structural Mechanics Module: Verification Models. Stockholm, Sweden: COMSOL AB, 4.0a ed., 2010.
- [79] LM Wind Power, "LM Wind Power's 73.5 meter blades flying on the largest offshore wind turbine in the world." http://www.lmwindpower.com/Media/Media-Kit/ Press-Releases/2012/03/75_3, 2012. Accessed: 2013-01-08.

- [80] Alstom, "Alstom and LM Wind Power develop the worlds largest wind turbine blade." http://moourl.com/m6oa6, 2011. Accessed: 2013-01-08.
- [81] I. H. Shames and C. L. Dym, Energy and finite element methods in structural mechanics. Washington: Hemisphere Pub. Corp., 1985.
- [82] International Electrotechnical Commission, *IEC/TC88*, 61400-1 ed. 3, Wind turbines— Part 1: Design requirements. Geneva, Switzerland: IHS, 3 ed., 2005.
- [83] C. Lanczos, *The Variational Principles of Mechanics*. New York: Dover Publications, 4th ed., 1970.
- [84] L. Komzsik, Applied calculus of variations for engineers. Boca Raton: CRC Press, 2009.
- [85] Sympy Development Team, "SymPy: Python library for symbolic mathematics." http://www.sympy.org, 2012. Accessed: 2014-05-30.
- [86] F. Pérez and B. E. Granger, "IPython: A System for Interactive Scientific Computing," Computing in Science & Engineering, vol. 9, no. 3, pp. 21–29, 2007.
- [87] J. M. Gere and S. P. Timoshenko, *Mechanics of materials*. Boston: PWS Publishing Company, 4 ed., 1997.
- [88] G. A. Lowe and N. Satterly, "Comparison of Coupon and Spar Tests," in *Design of composite structures against fatigue: applications to wind turbine blades* (R. M. Mayer, ed.), ch. 9, pp. 133–148, Bury St Edmunds: MEP, 1996.
- [89] D. Bannister, "Materials technology for the wind energy market JEC Composites." http://www.jeccomposites.com/news/composites-news/materials-technology-wind-energy-market, 2008. Accessed: 2013-01-08.
- [90] D. T. Griffith and B. R. Resor, "Description of Model Data for SNL100-00: The Sandia 100-meter All-glass Baseline Wind Turbine Blade," tech. rep., Sandia National Laboratories, Albuquerque, NM, 2011.
- [91] J. F. Mandell and D. D. Samborsky, "DOE/MSU Composite Material Fatigue Database: March 31, 2010 Update," tech. rep., Sandia National Laboratory, Albuquerque, NM, 2010.
- [92] J. F. Mandell and D. D. Samborsky, "DOE/MSU Composite Material Fatigue Database: Test Methods, Materials, and Analysis," tech. rep., Sandia National Laboratory, Albuquerque, NM, 1997.
- [93] P. Roth-Johnson and R. E. Wirz, "US Patent Application, Wind Turbine Blade with Biplane Section," 2014.
- [94] J. W. Gallman, S. C. Smith, and I. M. Kroo, "Optimization of Joined-Wing Aircraft," *Journal of Aircraft*, vol. 30, no. 6, pp. 897–905, 1993.

- [95] F. Bloom and D. Coffin, *Handbook of thin plate buckling and postbuckling*. Boca Raton, FL: Chapman & Hall/CRC, 2001.
- [96] J. Whitney, Structural analysis of laminated anisotropic plates. Lancaster, PA: Technomic Pub. Co., 1987.
- [97] N. Buckney, A. Pirrera, S. D. Green, and P. M. Weaver, "Structural efficiency of a wind turbine blade," *Thin-Walled Structures*, vol. 67, pp. 144–154, June 2013.
- [98] Tecplot Inc., "Tecplot (Version 10.0-6-012)," 2005.
- [99] I. Fleming and D. Luscher, "A model for the structural dynamic response of the CX-100 wind turbine blade," Wind Energy, vol. 17, pp. 877–900, June 2014.
- [100] W. McKinney, "pandas: Python Data Analysis Library." http://pandas.pydata.org/, 2014. Accessed: 2014-05-11.
- [101] P. Ramachandran and G. Varoquaux, "Mayavi: 3D Visualization of Scientific Data," Computing in Science & Engineering, vol. 13, pp. 40–51, Mar. 2011.
- [102] S. Gillies, A. Bierbaum, K. Lautaportti, and O. Tonnhofer, "Shapely." https://pypi.python.org/pypi/Shapely, 2014. Accessed: 2014-05-08.
- [103] R. Rainsberger, TrueGrid User's Manual, Volume 1, Version 2.3: Introduction, Graphical User Interface, and Parts, vol. 1. XYZ Scientific Applications, Inc., 2006.
- [104] R. Rainsberger, TrueGrid User's Manual, Volume 2, Version 2.3: Geometry, Assembly, Global Properties, and Output, vol. 2. XYZ Scientific Applications, Inc., 2006.
- [105] M. Buhl, "WT_Perf user's guide: Version 3.1," tech. rep., National Renewable Energy Laboratory, Golden, CO, 2004.
- [106] G. S. Bir, "User's guide to PreComp (Pre-Processor for Computing Composite Blade Properties)," tech. rep., National Renewable Energy Laboratory, Golden, CO, 2006.
- [107] S. M. Larwood, B. Acker, and J. Sencenbaugh, "Measurement of Truck Cab Flow in Support of Wind Turbine Testing," tech. rep., National Renewable Energy Laboratory, Golden, CO, 1998.
- [108] E. Kreyszig, Advanced Engineering Mathematics. Hoboken, NJ: Wiley, 9 ed., 2006.
- [109] P. Roth-Johnson, "Extended analytical model with general EI and EA." http://nbviewer.ipython.org/urls/dl.dropbox.com/u/1211947/2012-12-19_extended_analytical_model_genl_EI_EA.ipynb, 2012. Accessed: 2013-01-08.
- [110] P. Roth-Johnson, "Analytical expressions for transverse and axial displacements." http://nbviewer.ipython.org/urls/dl.dropbox.com/u/1211947/2012-12-19_ analytical_exps_transverse_and_axial_disps.ipynb, 2012. Accessed: 2013-01-08.

[111] J. D. Hunter, "Matplotlib: A 2d graphics environment," Computing In Science & Engineering, vol. 9, no. 3, pp. 90–95, 2007.